Liquid-assisted ultrafast growth of superconducting ´lms derived from chemical solutions

Laia Soler Bru

Liquid-assisted ultrafast growth of superconducting films derived from chemical solutions

A dissertation submitted for the degree of

DOCTORATE OF PHILOSOPHY IN MATERIALS SCIENCE

BY

Laia Soler Bru

Supervisors:
Prof. Xavier Obradors Berenguer
Dra. Susagna Ricart Miró

Departament de Materials Superconductors i Nanoestructuració a Gran Escala
Institut de Ciències de Materials de Barcelona - CSIC

Tutor: Prof. Roser Pleixats Rovira
Doctorat en Ciència de Materials
Departament de química- Facultat de Ciències
Universitat Autònoma de Barcelona

January 2019

Memòria que porta per títol **"Liquid-assisted ultrafast growth of superconducting films derived from chemical solutions "** i presentada per aspirar al Grau de Doctor en Ciència de Materials per **Laia Soler Bru**

Autora:
Llic. Laia Soler Bru

amb el vist i plau de: **Prof. Xavier Obradors Berenguer**, Professor d'investigació del Institut de Ciències de Materials de Barcelona (ICMAB-CSIC); **Dra. Susagna Ricart Miró**, Científica Titular del Institut de Ciències de Materials de Barcelona (ICMAB-CSIC) and **Prof. Roser Pleixats Rovira**, catedràtica del Departament de Química Orgànica de la Universitat Autònoma de Barcelona (UAB).
I per a que així consti, signen el present certificat.

Director:	*Directora:*	*Tutora:*
Prof. Xavier Obradors Berenguer	Dra. Susagna Ricart Miró	Prof. Roser Pleixats Rovira

Bellaterra, 22 de gener de 2019

Abstract

The widespread use of High Temperature Superconductors (HTS) into large scale applications is, in part, still limited by the high costs of coated conductors manufacturing. Aiming for a breakthrough to achieve high throughput, in this thesis we have developed a novel technique that combines the low cost benefits of solution processing with the very high growth rates of crystallization from liquid phases. It relies on the growth of $YBa_2Cu_3O_{7-\delta}$ epitaxial films assisted by a transient liquid derived from carboxylate solutions.

In this dissertation, we first explain the basics of the process that leads to $YBa_2Cu_3O_{7-\delta}$ crystallization assisted by a transient liquid and then we elaborate on the results of our investigation about this technique.

The reactions involved in the process are observed with *in situ* measurements. Pyrolysis of the Ba, Cu and Y propionates mixture at low temperatures ($<500°C$) is observed with *in situ* infrared spectroscopy. Then, time resolved X-ray diffraction with synchrotron light is used to reveal the reaction paths to convert the resulting $BaCO_3$, CuO and Y_2O_3 to the final phase, as well as nucleation and growth of the $YBa_2Cu_3O_{7-\delta}$ film from the transient liquid.

To do so, the deposition step is performed with spin coating or Ink Jet printing methodologies. The solutions characteristics have been adapted to the deposition technique and correlated to the resulting film morphology.

Then, several parameters have been investigated to control the rate limiting $BaCO_3$ elimination reaction in order to avoid carbon retention in the final thick epitaxial films.

Afterwards, the basic concepts for understanding the nucleation and growth mechanisms of YBCO with TLAG are set. With the aim of obtaining c-axis epitaxial $YBa_2Cu_3O_{7-\delta}$ films, several strategies are presented to control the driving force for crystallization. The relevant parameters are solution composition, oxygen pressure, heating ramps and growth temperatures. Finally, the crystallization conditions are correlated to the resulting films microstructure and superconducting performances.

Two different paths are presented to reach TLAG. A direct temperature rise at constant oxygen pressure (Temperature-route), or a two step process (P_{O_2}-route). For the latter, $BaCO_3$ elimination is disentangled from $YBa_2Cu_3O_{7-\delta}$

growth by a jump on P_{O_2}.

Additionally, several challenges needed to be addressed depending on the route: liquid reactivity with the substrates due to its highly corrosive nature or improper wettability, are some of them.

Finally, we have succeeded in obtaining highly epitaxial YBCO thin films of 90-500 nm with very high superconducting performances (T_c=90-92 K, J_c up to 5 MA/cm^2 at self-field and 77 K), at growth rates up to 100 nm/s, increased by a factor 100 from those reported with conventional CSD.

Contents

Abstract . . . iii

1 Introduction **1**
1.1 Motivation . . . 1
1.2 Superconducting materials . . . 2
1.3 $YBa_2Cu_3O_{7-\delta}$ structure . . . 5
1.4 Second generation coated conductors and perspectives . . . 6
1.5 Oxide growth techniques for REBCO . . . 8
1.5.1 Liquid mediated growth techniques . . . 9
1.5.2 Chemical Solution Deposition methodology . . . 11
1.6 Objectives and outline of the thesis . . . 14

2 Experimental methodologies **17**
2.1 Experimental procedure . . . 17
2.1.1 Preparation of precursor solutions . . . 17
2.1.2 Deposition on treated substrates . . . 19
2.1.3 Pyrolysis step . . . 22
Single deposition . . . 22
Multi deposition . . . 22
2.1.4 Film crystallization . . . 23
2.1.4.1 Experimental conditions for the low P_{O_2} route 25
2.1.5 Oxygenation . . . 26
2.2 Characterization techniques . . . 27
2.2.1 Precursor solution physiochemical characterizations . . . 28
2.2.2 Thermal decomposition analyses . . . 29
2.2.3 Microscopic techniques . . . 30
2.2.4 X-Ray Diffraction techniques . . . 32
2.2.4.1 High-Resolution X-ray Diffraction . . . 34
2.2.4.2 Two-dimensional X-ray Diffraction . . . 35
2.2.4.3 Quantification analyses . . . 37

2.2.5 *In situ* XRD with synchrotron radiation 39
2.2.6 Fourier Transform Infrared Spectroscopy 42
2.2.7 Physical characterizations of superconducting properties 46

3 Solution processing and intermediate reactions 49
3.1 Solution design towards TLAG 50
3.1.1 Solvent and additive effects on film thickness and morphology 52
3.1.2 Porosity modulation 56
3.2 Pyrolysis process of fluorine free solutions 59
3.2.1 *In situ* FTIR analysis on metal propionates decomposition 61
3.2.2 Nanostructure of calcinated films 70
3.3 Water content influence 73
3.3.1 Solution water content control 73
3.3.2 Thermal decomposition of hydrated solutions 75
3.3.3 Morphologycal and physical consequences 77
3.4 $BaCO_3$ elimination reactions 80
3.4.1 *In situ* XRD studies of the conversion process 82
3.4.2 Towards ultrafast conversion rates in T-route 90
3.4.2.1 P_{O_2} effect 91
3.4.2.2 Heating rate effect 94
3.4.3 CO_2 diffusion 97
3.4.3.1 Thickness dependence 97
3.4.3.2 CO_2 removal towards faster decarbonation . . 100
3.5 Conclusions 103

4 Liquid-assisted nucleation and growth mechanisms 105
4.1 Fundamental aspects on nucleation and growth from solution . 106
4.1.1 Introduction 106
4.1.2 Nucleation 108
4.1.3 Epitaxial growth 112
4.2 Transient Liquid Assisted Growth general characteristics 114
4.2.1 Transient liquid growth principles 114
4.2.2 Working window for YBCO TLAG growth 116

4.2.3 Supersaturation in TLAG as driving force 118
4.2.4 Nucleation competition between $YBa_2Cu_3O_{7-\delta}$ orientations 122
4.2.5 Rate controlling factors for growth 125
4.2.6 Supersaturation and morphology in REBCO techniques 128
4.3 $BaCuO_2$-CuO eutectic reaction 129
4.4 Conclusions 134

5 TLAG Temperature-route **137**
5.1 Supersaturation tuning for epitaxial $YBa_2Cu_3O_{7-\delta}$ nucleation . 138
5.1.1 Nucleation control with temperature and melt composition at ultrafast heating rates 138
5.1.2 Nucleation control with heating rate 143
5.2 YBCO growth 150
5.2.1 *In situ* XRD studies of YBCO growth 150
5.2.1.1 Ultrafast growth of epitaxial $YBa_2Cu_3O_{7-\delta}$ . . 151
5.2.1.2 Growth of randomly oriented $YBa_2Cu_3O_{7-\delta}$. 156
5.2.1.3 Polycrystalline YBCO grains elimination . . . 157
5.2.2 Microstructural evolution 158
5.3 Processes derived from the liquid properties 161
5.3.1 Liquid diffusion 162
5.3.1.1 Control by heating rate 166
5.3.1.2 Film thickness and substrate 169
5.3.1.3 Cation composition effects 172
5.3.1.4 Multilayered structures 174
5.3.2 Interfacial chemical reactivity 176
5.3.2.1 T-P_{O_2} dependence 177
5.3.2.2 Heating ramp dependence 179
5.3.2.3 Local reactivity 180
5.4 Microstructure and physical characterizations of epitaxial YBCO films with T-route 182
5.4.1 Growth regimes and texture quality 183
5.4.1.1 Growth of thick films 188
5.4.2 Films morphology and granularity 190

5.4.3 Nanoscale defects landscape in T-route 195
5.5 Conclusions 198

6 TLAG-P_{O_2} route **201**
6.1 Reaction mechanisms in P_{O_2} route 201
6.2 YBCO crystallization decoupled from $BaCO_3$ elimination . . . 205
6.2.1 *In situ* YBCO growth rate 205
6.2.2 Nucleation control with the processing conditions 209
6.3 Reactivity in P_{O_2} route: $BaTiO_3$ 213
6.4 Structural characterizations 217
6.4.1 Grains morphology 217
6.4.2 Nanoscale defects 218
6.5 Physical characterizations 221
6.5.1 a/b-oriented grains effects 223
6.6 Conclusions 227

7 General conclusions **229**
Future work and outlook 234

Appendix **237**

Glossary **237**

Bibliography **241**

Chapter 1

Introduction

1.1 Motivation

The fight against global warming is the main challenge that society currently needs to face. It involves, among many other necessities, a change of the energy paradigm to stop CO_2 emissions. Therefore, new technologies with enhanced efficiency, smart and clean energy concepts are a necessity.

Any such new device will most likely rely on materials with outstanding functional properties. In particular, the processes of crystal growth, thin film fabrication, and development of nanomaterials lay the foundation of the modern functional materials, low-dimensional structures, microelectronic devices and nanostructured materials with new functionalities [1, 2].

The International Energy Agency stated in their 2018 outlook that electricity is the fastest-growing final form of energy, especially with the increasing electrification of transportation including plug-in vehicles [3]. Cuprate superconductors, are a particular case of functional oxides which can transport large currents without losses, a property that makes them very interesting for energy sustainability applications (efficient, smart and clean power system; transformers, motors, superconducting magnetic energy-storage (SMES) devices, etc).

The development of this material into a flexible conductor with high current transport capabilities is already a reality, so called 2G-coated conductors (CCs). It involves the growth of epitaxial $REBa_2Cu_3O_{7-\delta}$ (REBCO, RE=Rare Earth or Y) layers on top of buffered long length flexible metallic substrates.

However, in most cases, their real applicability now relies on commercial viability. For a widespread use of superconductivity, as for other sustainable energy technologies, new breakthroughs in the manufacturing processes are required. Those should combine high performance with high throughput and

low cost [4, 5, 6, 7, 8]

Chemical Solution Deposition (CSD) techniques have emerged with enormous potential for low cost production of many functional oxide thin films. In the recent years, it has been proven as a unique opportunity for processing high performance, low cost nanostructured $YBa_2Cu_3O_{7-\delta}$ based coated conductors. However, it has an intrinsic limitation on the material growth rate ($< 2\,nm/s$) to achieve high throughputs.

The oxide growth techniques with real potential to go well beyond the present state of the art concerning growth rates, are those using liquid assisted growth. Fast atomic diffusion and high atomic density encompasses a much higher growth rate than in vapour or solid diffusion approaches [9]. Some methodologies for liquid-assisted growth of REBCO material have been developed, but none using low cost CSD approaches.

We propose and develop in this thesis a new approach based on deposition of chemical solutions, but using a transient liquid to assist the epitaxial growth of REBCO: Transient Liquid Assisted Growth (TLAG-CSD). We expect this combination to be a breakthrough on the epitaxial growth of functional oxides at enhanced rates and adaptable to low cost manufacturing. However, many issues have to be addressed, from the understanding of the overall process, to the attainment of epitaxial layers with the required microstructure and properties.

1.2 Superconducting materials

The main property of superconductors is the ability to show zero resistance against electrical current below a critical temperature (T_c). The nature of the superconductivity is unconventional, which can be considered as a macroscopic quantum phenomenon: quantum mechanics on a real-world-sized scale [10]

Superconductivity was first discovered in mercury at 4.2K back in 1911 by Kamerlingh Onnes after being able to liquefy helium [11]. Many expectations arose from this phenomena for both scientific and practical visions. Since then, numerous advances have brought theoretical insights gave rise to several nobel prize laureates (1933 Meissner effect [12]; 1957 BCS theory [13]; 1950 Ginzburg-Landau theory [14]; 1962 Josephson effect [15]), while serendipity has played a

major role to the finding of new class of materials displaying entirely unforeseen properties.

During many years Nb alloys were the champion in terms of performances and applicability. Their properties led to fabrication of high electric field superconducting magnets (>10T) still widely used in magnetic imaging resonance (MRI) and high-energy physics applications.

It was not until 1986 that the discovery of high transition temperatures superconductors (HTS) [16] based on ceramic materials supposed a new breakthrough in the field. With transition temperatures higher than 77 K and up to 92 K, HTS can operate under liquid nitrogen cryogenic systems.

In the last 20 years, other type of superconductors appeared, such as MgB_2 [17] with T_c=39 K and pnictide-based materials [18] of the general formula La-Fe-As-O, with critical temperatures of up to 50 K.

Now, from an engineering point of view, the discovery of higher T_c materials would not make a very large difference in the prospect of widespread use of superconductivity

Instead, the introduction of superconductivity in large scale applications will be driven by exploiting the current-carrying capabilities on cost-effective fabricated superconductors [4]. Of course, the particular requirements are different for each application [7].

The opportunities that superconducting based devices offer are not only based on simple increased efficiency over conventional technologies; they provide unique solutions to challenges that cannot be achieved otherwise (i.e power cables, superconducting magnetic energy-storage (SMES) devices, transformers, fault current limiters and motors) [5].

This transition faces several limitations. For instance, economic constraints are related to the current HTS high costs due to sophisticated, low yields and limited throughput manufacturing processes. Hence, the challenge of producing long length uniform wires of these materials is huge and there is still a need for further research [8].

One of the most relevant parameters for superconducting materials proficiency is critical current density (J_c) performance under external applied magnetic fields, specially important for high magnetic field applications.

All HTS materials are type II superconductors. They present two values of critical fields (H_{c_1} and H_{c_2}). They are schematized in Figure 1.1a. Below H_{c_1}, superconductors are in the Meissner phase [12], by which the material expels applied magnetic field from its interior by generating surface electrical currents, showing a perfect diamagnetic behaviour.

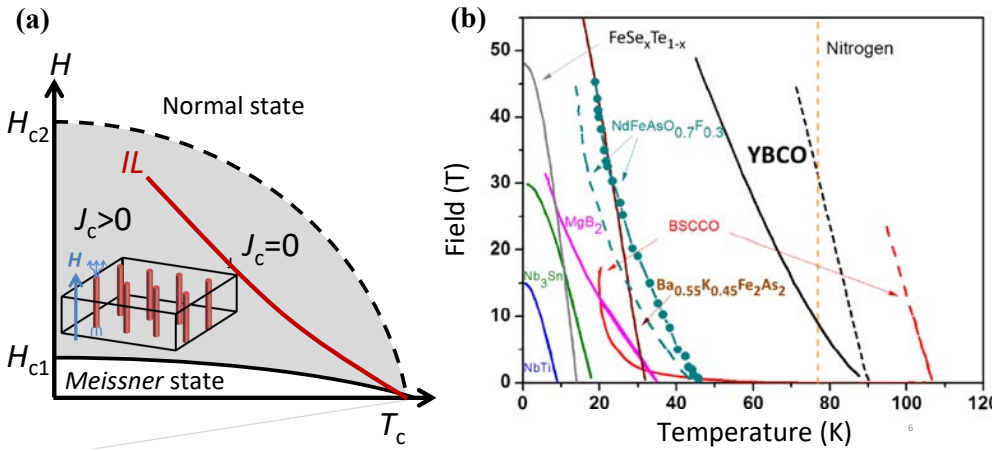

Figure 1.1: (a) Typical magnetic field-temperature diagram for type II superconductors in which different states can be observed. (b) For several superconductors, dashed lines show the upper critical field ($H_{c_2}(T)$) at which superconductivity is destroyed, while solid lines indicate the irreversibility field line (IL) at which the critical current density vanishes. Figure adapted from [19]

For fields between H_{c_1} and H_{c_2} a new state is formed (Mixed state) [20, 21]. Here, the magnetic field penetrates into the material forming quantized cylindrical flux lines called vortices. In this region, the material can carry high currents without destroying superconductivity as long as the vortices are static. At higher temperatures and magnetic fields, vortices movement activated by thermal energy produces current dissipation, and J_c vanishes above the so called irreversibility field (H^*).

Hence, the irreversibility line (continuous line in Fig.1.1) is the relevant pa-

rameter for applications, and not the transition to normal state H_{c2}.

$YBa_2Cu_3O_{7-\delta}$ [22] exhibits the most promising performance suitable for both low/high field and temperature applications. It presents a high T_c at 93 K and the highest field current carrying capacity at liquid nitrogen temperature (77 K). Additionally, the $J_c(H)$ curves at high temperatures can be further pushed by engineering the nanostructure in a way that vortices movement is hindered. Artificial pinning centers (APC) or non-superconducting defects may be generated through synthesis of nanocomposite materials [23, 24].

1.3 $YBa_2Cu_3O_{7-\delta}$ structure

$YBa_2Cu_3O_{7-\delta}$ is commonly termed as YBCO or Y123. Its unit cell structure is displayed in Figure 1.2. It is composed by three pseudocubic elementary perovskite unit cells. A central Y layer, around which are stacked the CuO_2 planes which are thought to be the seat of superconductivity. CuO_2 planes are separated by charge-reservoir interleaved layers which contain CuO chains. Those provide a proper carrier density in the superconducting planes.

The δ value is related to oxygen vacancies that can be disordered or ordered leading to two different lattices: tetragonal ($0.65 < \delta \leq 1$) or orthorhombic ($0 \leq \delta \leq 0.65$). Maximum T_c value ($\sim$ 92 K) is achieved with a δ $\sim$0.07, when the compound presents the orthorhombic phase [25]. In this form, the oxygen atoms occupy the O(1A), while the O(1B) sites are empty, resulting in a one-dimensional CuO chain parallel to the b-axis (Fig. 1.2).

Due to its structure, the current along the CuO_2 planes (or ab planes) is much higher than the current that flows parallel to the c direction. Consequently YBCO (and superconducting cuprates in general) is highly anisotropic. This fact places fundamental restrictions on its properties, especially in polycrystalline form.

It was shown that grain boundaries act as weak links, hence critical current density drops exponentially as the misorientation angle (θ) between crystallites increases [26]. Dimos *et al* demonstrated that this reduction occurs irrespective of the type of grain boundary misorientation: twist, tilt, etc. Thus, to avoid significant grain boundary obstacles to current flow, the material must be tex-

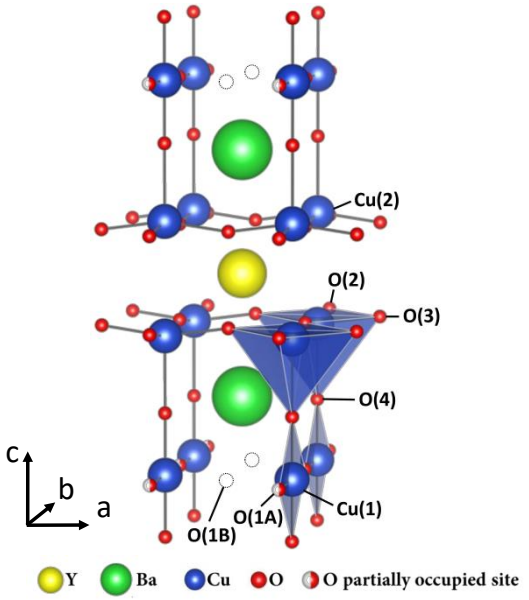

Figure 1.2: orthorhombic phase crystalline structure of $YBa_2Cu_3O_{7-\delta}$

tured biaxially. That is, not just with one axis of texture but the three of them (in plane and out of plane texture) [27].

Therefore, highly epitaxy (θ<4) is required to display the highest superconducting performances [28, 29]. The approach for texturing HTS material biaxially over long lengths is addressed with the coated conductor technology.

1.4 Second generation coated conductors and perspectives

The manufacturing of long, robust and flexible conductor out of anisotropic ceramic materials is a challenging task. Extensive work with contributions from material science, nanotechnology and engineering fields led to the appearance of so called second generation tapes or Coated Conductors (CCs), first demonstrated in 1991 [30].

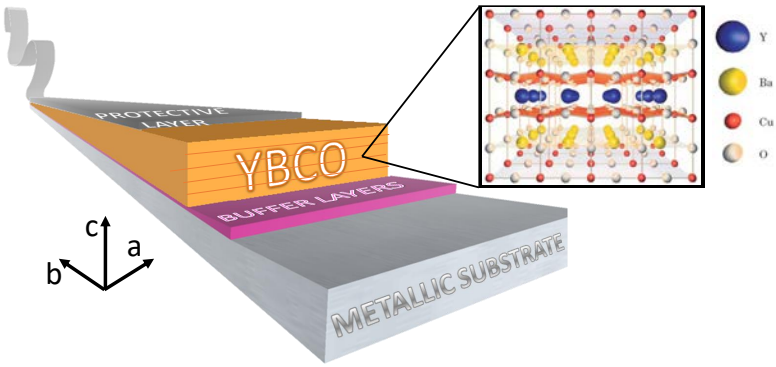

Figure 1.3: Representation of a multilayer architecture of coated conductors (CC). At the inset, biaxially textured nanostructure of the $YBa_2Cu_3O_{7-\delta}$ film

An example of coated conductor architecture is displayed in Figure 1.3. A REBCO thin film is grown biaxially aligned to an oxide buffer layer with similar lattice parameters. Those are at the same time placed on a metallic substrate with good mechanical properties. On top, a protective cap layer is used to cover the superconducting phase. Overall, it composes an heteroepitaxial tape [6, 7]

Several buffer layers may be needed to transfer the biaxial texture from the substrate to REBCO while providing a continuous, smooth and chemically inert surface (avoiding metallic ions diffusion from the substrate). The most used materials are CeO_2, $YSrO_2$ (YSZ), $BaZrO_3$, MgO, $LaAlO_3$ and $SrTiO_3$. The substrates can be textured using RABiTS (Rolling Assisted Biaxially Textured Substrates) or IBAD (Ion Beam Assisted Deposition) reel-to-reel technologies [31].

Currently, CCs tapes are produced by several companies worldwide with lengths up to 500 m [32]. However, the slow growth methods and expensive production still limit the introduction of this technology to a wide market. The key parameter is cost/performance ratio, usually measured in terms of $€/kAm$, using critical current (I_c) at 77 K and self-field [7]. For instance, a value of 10 $€/kAm$ would be required to boost the propagation of CCs in power systems [8]. Requirements imply that production rate of CC should be in the range of 500 km/h. Therefore, for the growth of 2-3 μm thick REBCO

film in 5-10 m long furnaces, growth time should not exceed 30 s.

Coated conductors use only a few per cent of the current-carrying cross section, so J_c of REBCO has to be pushed to its limit [19, 33]. On the other hand, the need of enhancing production speed at low cost requires the development of new material growth methodologies.

1.5 Oxide growth techniques for REBCO

The growth of such complex architecture supposed big challenges [34] that drove to the development of new thin film growth techniques, initially used for semiconductors nanotechnology, for complex oxides.

The deposition of complex perovskite cells in form of high-quality thin films, has prompted oxides applicability to smart and functional devices. These materials are characterized by having strongly correlated electronic and magnetic states [35]. Some of their functionalities are ferroelectricity, magnetoresistance, ionic and electronic conductivity, thermoelectricity, electrochromism, magnetism, piezoelectricity, resistance switching and superconductivity.

Methodologies to prepare epitaxial oxide thin films are very diverse [36]. The most successful techniques for REBCO growth in practical applications, being currently used by CCs manufacturers, are Pulsed Laser Deposition (PLD), Trifluoroacetates based Metal Organic Deposition (TFA-MOD), Metalorganic Chemical Vapour Deposition (MOCVD) and the recently developed reactive co-evaporation and direct reaction (RCE-DR) [5].

The mayor drawbacks of vapour deposition techniques are the high costs and equipment complexity. In recent years, there have been huge developments in engineering that have led to the deposition of large areas in continuous and enhanced throughput [33, 37, 38]

More advantageously, solution deposition methods enable easy continuous deposition over large areas at atmospheric pressure, having a strong potential for achieving the above mentioned cost reductions [39, 40, 7].

Nevertheless, low throughput due to small growth rates still refrains the full development of these classic techniques due to intrinsic growth rate limitations.

In *in situ* vapour deposition techniques, the material flux (atoms$\cdot cm^2 \cdot s^-1$) is

the rate-determining factor for growth. Maximum growth rates reported using PLD [41] and MOCVD [42] are up to 10 nm/s.

In trifluoroacetate chemical solution routes (TFA-CSD), the low solid state diffusion involves growth rates limited to <3 nm/s [43].

Therefore, a liquid phase intermediate may be a necessity to increase production throughput. For instance, Y atomic diffusivity in the liquid is over 100 times higher than in the solid, and atoms concentration on the surface is 5 orders of magnitude higher in solutions than in vapour [44]. This makes liquid assisted processes so much faster.

$(10^{-9} - 10^{-6})$ in the vapour as compared to the liquid in LPE ($\sim 10^{-1}$) [44].

1.5.1 Liquid mediated growth techniques

Melt growth techniques are the most widely used to produce single crystals at the fastest rates (>1 mm/h). It is estimated that the 90% of sintered commercial products involve the formation of a liquid during the process [45].

Another advantage is the high quality of the obtained crystals. One of the major difficulties relies on the corrosive character of melts, that may lead to contamination from the crucibles or seeds. Fundamental aspects on crystallization from liquids are given in chapter 4.

If the material can grow from its own melt, melt growth is the most used approach. However, it requires, among other things, congruent melting. The alternative is growth from high temperate solutions. In this case, the components of the material dissolve in a solvent (flux) which is a low-melting oxide (see Fig.1.4). The flux composition can include, or not, the elements of the final crystal phase. Single crystals are obtained when this solution is supersaturated, usually by cooling. Information from the material phase transformations and solubility curves given in phase diagrams is essential for the design of this methodology. Because it is possible to find a flux for most inorganic materials, high temperature solution growth is used for the synthesis of many oxides, such as garnets [46].

Since $YBa_2Cu_3O_{7-\delta}$ melts incongruently, growth from direct melt can not be performed. For this reason, high temperature solution growth methods have been used.

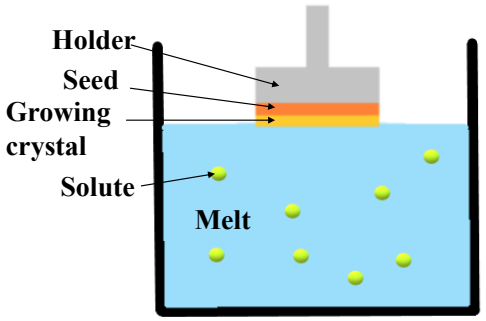

Figure 1.4: Scheme of thin film growth using high temperature solution growth. Particularly, liquid phase epitaxy with a vertical dipping system

Phase diagrams for the Y-Ba-Cu-O system are extremely complex, involving tens of species of different compositions and states [47]. For instance, about 11 melt-involved interactions can be identified only in air [48]. Hence, the possibilities for the design of a flux method for this material are huge, but also very complex. However, its interesting performances as a superconductor drove to an extensive research resulting on abundant data and numerous approaches for its synthesis, that still continuous nowadays.

Liquid mediated growth processes were used in the early years after HTS discovery for the fabrication of bulk HTS materials. First, the so called Melt Textured Growth (MTG) for bulk ceramics was developed taking advantage of the material peritectic decomposition to [BaO-CuO]liquid + Y_2BaCuO_5(211) [49, 50, 51, 52]. Growth is performed when cooling from high temperatures and the 211 particles supersaturate the melt to form REBCO (Fig. 1.4). To do so, a starting composition containing YBCO + 211 phases, is melted followed by a slow cooling process.

For instance, the diffusivity of Y in the [3BaO-5CuO] liquid at 970°C is $4 \cdot 10^{-10} m^2 s^{-1}$ [53], while in the YBCO solid is almost two orders of magnitude lower, of only $8 \cdot 10^{-12} m^2 s^{-1}$ [54]. With MTG, single crystals could be synthesized at rates of 200-800 nm/s and filaments up to 3000 nm/s [49, 55].

With the same idea, other examples were later developed for thin films production. First was Liquid Phase Epitaxy (LPE) [56], widely applied to com-

posite semiconductor materials, in particular to III-V-semiconductors such as GaAs or InP. Growth is performed from a bath of molten flux which is supersaturated either by cooling the melt from the undersaturated region (Fig. 1.4), or by spatial transport of flux through a temperature gradient. REBCO thin film growth rates were up to 50 nm/s [53, 57, 58].

Some LPE limitations were solved with Hybrid Liquid Phase Epitaxy or Tri-phase epitaxy (HLPE, TPE) [59, 60, 61, 62]. They involve deposition and melting of a thin [BaO-xCuO] liquid flux layer, followed by RE introduction to the layer by means of a vapour technique. Rates of around 10-35 nm/s were demonstrated for the growth of epitaxial YBCO thick layers [63].

An outstanding recent development is reactive co-evaporation and direct reaction technique (RCE-DR) [64]. A liquid phase develops at low oxygen partial pressure ($\sim 10^{-8}$ bar) from an amorphous phase deposited by reactive co-evaporation. Then, a fast change on P_{O_2} conditions allows rapid conversion to REBCO. RCE-DR holds the record for throughput per hour (360 m/h) for an industrial CC process.

Though, all just mentioned techniques still require the use of complex implementation schemes; and in many occasions are not flexible enough to induce inclusions of secondary phases for pinning and properties enhancement.

1.5.2 Chemical Solution Deposition methodology

The *ex situ* chemical method Chemical Solution Deposition (CSD) appears to be the most promising methodology for large-scale low cost production.

The development of CSD processes was first made for SiO_2 and TiO_2 optical coatings [65, 66]. Nowadays, CSD has already been proven to succeed in high quality epitaxial growth of oxides and other materials, displaying performances competitive with *in situ* methodologies [67, 68]. Some examples are graphene [69], CeO_2 for catalysis and as buffer layers in superconducting applications [70, 71]. Among complex oxides, some examples are $(Ba,Sr)TiO_3$, $Pb(Zr,Ti)O_3$, $LaNiO_3$, $(La,Sr)MnO_3$, $BiFeO_3$ and $YBa_2Cu_3O_{7-\delta}$.

The general principle is to prepare a homogeneous solution of the necessary cation species that after deposition on a substrate and annealing will compose the crystallized material.

The methodology usually involves four steps (Fig.1.5): (1) synthesis of the precursor solution, (2) solution deposition on the substrate (3) low-temperature heat treatment for drying and/or pyrolosis of organics, and formation of amorphous films (typically 300-500°C), (4) high temperature heat treatment for densification and crystallization (from 600 to 1100 °C) [72, 73, 74].

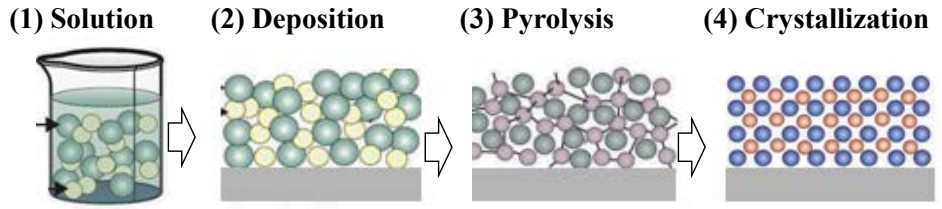

Figure 1.5: Schematic representation of the 4 processing steps in the Chemical Solution Deposition methodology

There are a variety of solution-based approaches depending on the process chemistry [75]:

- Sol-gel mainly using alkoxide precursors that undergo primarily hydrolysis and condensation, with 2-methoxyethanol as reactant and solvent
- Metalorganic decomposition (MOD) based on metal carboxylate compounds
- Hybrid routes or *chelate* utilize both carboxylate and alkoxide precursors, which react to form oligomers or small polymers

MOD main challenges are: i) film susceptibility to cracking and shrinkage due to the excessive volume loss during pyrolysis ii) film porosity and iii) limited control of structural evolution and film microstructure.

CSD for YBCO growth

Until the present, the development of Metal Organic Chemical Solution Deposition (CSD) for $YBa_2Cu_3O_{7-\delta}$ thin films growth has been governed by the so called TFA route (TFA-CSD), proposed by Gupta *et al* [76].

The use of solutions based on trifluoroacetate salts leads to BaF_2 after pyrolysis that react with water vapour to form the $YBa_2Cu_3O_{7-\delta}$ phase [39, 40]. Hence, the growth is driven by a solid-gas reaction that suffers from low growth rates (1 nm/s) [77].

An additional difficulty of the TFA process is the HF release, which is highly corrosive and entails a fine control of the gas flow that also limits the possibilities for parallel growth of tapes. Most recent research is focused on reducing the fluorine content (Low Fluorine route) [78, 79, 80, 81]

TFA-CSD developments and the introduction of artificial pinning centres by the addition of elements in the starting solution, boost HTS materials performance [82, 83].

On the other hand, CSD growth of YBCO films using completely non-fluorinated precursors has been very little studied. The main limitation is a poor control of the decomposition kinetics of $BaCO_3$ [84] (a stable phase produced in a significant amount from non-fluorinated salts decomposition), specially for thick films. This fact has hindered a reliable CSD methodology other than the TFA route.

Some studies were made shortly after the discovery of HTS, but could not obtain good performances [85, 86]. In the most recent years, scarce works from non-fluorine solutions suggested that good quality (1-4 MA/cm^2, 77 K, sf) pristine YBCO films could be grown following similar processing conditions to the ones used for TFA precursors. Different precursors were used: acetylacetonates [87], acetates in propionic acid solvent [88, 89, 90, 91], acetates in aqueous solvent [92], polymer assisted deposition [93, 94], dichloroacetic acid-MOD [95] and Cl doped propionate solutions [96], with different degree of success.

However, many unknowns still exist about the reaction mechanisms to form $YBa_2Cu_3O_{7-\delta}$ and real capability of eliminating carbon in a reproducible way. Until today, any author has reported ultrafast growth rates using fluorine free solutions.

1.6 Objectives and outline of the thesis

We develop along this Thesis a new liquid growth technique approach using chemical solutions deposition (CSD): Transient Liquid Assisted Growth (TLAG-CSD). In this case, the formation of the liquid naturally occurs as an intermediate state at the thermodynamic conditions of the final crystal phase.

For the REBCO superconductor, the forming liquid is composed by the BaO-CuO mixed oxide, while Y or RE are the solute. These are the same phases used in the just described techniques based on growth from liquids.

The key to reach such conditions is the choice of specific solution composition that, after pyrolysis, results on a nanometric mixture of the corresponding cations oxides or carbonates, instead of fluorinated precursors obtained in the TFA-CSD methodology. Additionally, the proper conditions for ultrafast growth have to be reached at very fast rates (i.e using a Rapid Thermal Annealing).

This approach entails a tight control of the intermediate compounds leading to the final desired phase. Then, the growth of epitaxial films with good performances still needs to be optimized by tuning the solubility conditions, which are the driving force for crystallization.

To do so, several issues have to be addressed:

- The design of a stable solution to be deposited and decomposed to obtain a layer of the desired thickness, homogeneity and the adequate precursors
- Enhance the elimination of the intermediate $BaCO_3$ to avoid C retention
- Control the nucleation processes for epitaxial growth with the adequate microstructure to maximize the physical properties
- Determine the growth rate with *in situ* approaches

In this work we report the basis and first investigations of the whole process. It involves from the solution design to the achievement of epitaxial $YBa_2Cu_3O_{7-\delta}$ thin films with excellent superconducting properties and ultrafast growth rates. $YBa_2Cu_3O_{7-\delta}$ growth velocities of 100 nm/s are demonstrated and critical currents up to 5 MA/cm^2 at self-field and 77 K have been achieved, surpassing present technologies.

Chapter 2 is dedicated to describe the experimental procedure for the overall synthesis and the characterization techniques that have been utilized.

In chapter 3, the solution deposition, decomposition and precursors reactions during thermal treatment are addressed. First, it is necessary the design of an adequate and stable solution composed by the carboxylate salts of the respective cations. The next step is the solution deposition on substrates for obtaining the desired thickness and an homogeneous film. Both spin coating and Ink Jet printing deposition methodologies have been applied. After that, the pyrolysis of the dried deposited solution until decomposition of the organics is analysed with *in situ* Infrared spectroscopy measurements.

On the other hand, the resulting morphology at the macro- and nano-scale is also characterized and optimized.

After that, the reactions at higher temperatures of the obtained oxides and $BaCO_3$ are elucidated with *in situ* XRD experiments with synchrotron light. Additionally, experiments at ultrafast heating rates under different atmospheres have been used to enhance decarbonation kinetics.

The basis of the nucleation and growth from the transient liquid will be reported in Chapter 4. Fundamental aspects on nucleation and growth from solution are first summarized and then used to set the bases for crystallization from the transient liquid. Important issues that will be widely used in the next chapters are solution supersaturation, the control of forming YBCO crystal orientation, growth rate limiting factors and the T-P_{O_2} phase diagram.

Chapter 5 is devoted to the $YBa_2Cu_3O_{7-\delta}$ synthesis by directly heating at a constant P_{O_2} to the transient liquid growth conditions for YBCO. Efforts are made to disclose and control the supersaturation conditions for epitaxial growth and maximized superconducting performances. YBCO nucleation and growth rates are disclosed by means of fast acquisition *in situ* XRD and Transmission Electron Microscopy (TEM) analyses. The main difficulties in this approach lie on the control of the dewetting and corrosive character of the transient melt. Both phenomena are deeply investigated in order to propose several solutions. Finally, the resulting films microstructure and physical properties are reported.

Another processing path, the P_{O_2} route, is described in chapter 6. It consists on reaching the liquid growth zone with a P_{O_2} jump at isothermal conditions. This approach overcomes some of the limitations of the previous route. Again,

YBCO nucleation and growth mechanisms are extracted from *in situ* XRD experiments and the resulting microstructure and physical properties correlated to the liquid supersaturation for crystallization.

Finally, the main conclusions of this research and future perspectives are gathered.

This work involves results arisen from strong collaborations with other scientists. First, group co-workers dedicated to: analysis of physical properties and advanced X-ray diffraction (PhD candidate J. Banchewski), growth of nanostructured films using TLAG (PhD candidate J. Jareño), Transmission Electron Microscopy analyses (Dr. R. Guzman), thermal analyses and growth from ultra-high vacuum (PhD candidate S. Rasi) and InK Jet printing (Dr. B. Villarejo and Dr. F. Pino). All this is performed under the framework of the ERC Advanced grant "ULTRASUPERTAPE project: Utrafast growth of ultrahigh performance superconducting tapes "led by Prof. T.Puig.

Involving other research groups, we have collaborated with Dr. P. Roura and Dr. J. Farjas from the GRMT group at University of Girona for thermal decomposition analyses and the phase diagram of YBCO; Dr. C. Mocuta from the Diffabs Beamline in Soleil synchrotron (Paris) with the *in situ*XRD experiments with synchrotron; Dr. M. Kreuzer from the MIRAS Beamline in Alba synchrotron (Bellaterra) with the *in situ* IR experiments; and a 2 months research stay at the University of Cambridge (United Kingdom) under the supervision from Prof. J.MacManus-Driscoll and Dr. A. Kursumovic, provided fundamental understating from the HLPE technique (not reported here) that could be applied to TLAG.

Chapter 2

Experimental methodologies

In this chapter are described the experimental methodologies used in this Thesis to process, analyse and characterize all the steps involved on the transient liquid assisted growth of YBCO thin films from chemical solutions.

2.1 Experimental procedure

The experimental procedure applied for the preparation of YBCO thin films mediating CSD-TLAG is based on the methodologies developed for MOD techniques [67, 68]. The process is carried out through five main steps. Firstly, a metalorganic precursor solution containing the metal salts is prepared (section 2.1.1) and deposited on the substrate (section 2.1.2). Then, the sample is exposed to a low temperature heat treatment for the removal of organic species (section 2.1.3), followed by a higher-temperature heat treatment to crystallize the material (section 2.1.4). Finally, an oxygenation step is necessary to convert the tetragonal phase to the orthorhombic superconducting phase (section 2.1.5). The experimental procedure for each step is detailed hereunder.

2.1.1 Preparation of precursor solutions

Acetate salts of the three cations that comprise YBCO are dissolved in propionic acid and alcohol solvents [88]. In this work, the effects of different cation proportions, total concentration and solvents ratio have been investigated. Is described here the general synthesis procedure.

Commercial $Y(CH_3COO)_3$, $Ba(CH_3COO)_2$ (Aldrich) and $Cu(CH_3COO)_2$) (Alfa-Aesar) are dried in a thermostatic vacuum dryer (Vaciotem-T, from Selecta). It is important to keep water content of synthesized solutions lower

than 2%. Therefore, it is necessary to handle the preparation process under a dry and inert atmosphere such as nitrogen or argon. Special care has to be taken with yttrium acetates due to its hygroscopic behaviour. In contrast, completely anhydrous yttrium acetate is difficult to dissolve. One night at the vacuum dryer and 50°C are the optimal conditions that allow proper dissolution maintaining low water content.

The three salts are then dissolved in propionic acid for four hours at 50°C. After cooled down to room temperature, anhydrous alcohol (methanol or butanol) and additives (typically $5\%_{v/v}$ triethanolamine (TEA)) can be added at this step and the mixture is stirred overnight for a complete dissolution. Finally, the solution is transferred to a volumetric flask to reach the appropriate volume according to the desired concentration. The obtained blue solution (Fig. 2.1) is kept in sealed vials, under argon atmosphere and it is filtrated using syringe filters (Teflon membrane, 0.2 μm of pore size) before usage .

Figure 2.1: Acetates based solution with methanol:propionic acid 1:1 ratio

Typically concentration ranges for the precursors solutions are from 1M to 1.5M in sum of metals salts (Y+Ba+Cu). Two solutions were prepared with the stoichiometric ratio 1:2:3 and 1:2:4.6 for Y:Ba:Cu salts. The resulting stoichiometry is measured by classical volumetric and gravimetric methods so that the weighted quantities are adjusted to these results.

Solutions stability with time depends on concentration, solvent and water content. Since alcohols are hygroscopic and can produce esterification reactions with carboxylic acids, an alternative procedure is used for solvents mixtures. In the first place, a "mother solution" with propionic acid and double concentration of salts is prepared and kept in sealed vials. The addition of alcohol and additive is then performed just before usage. However, due to solubility

restrictions, this methodology can only be used for final concentrations <1M in sum of metals and the Y:Ba:Cu 1:2:3 composition.

2.1.2 Deposition on treated substrates

Deposition of precursor solutions on substrates has mainly been carried out by spin coating (SC) deposition. It is a simple procedure suitable for the synthesis of thin films (<300nm of final film thickness) at a laboratory scale. Additionally, our solutions have also been tested for Ink Jet printing (IJP), which allows single deposition of higher volumes (>300nm of final film thickness) and it is appropriate for continuous long length production or patterning [97].

Both procedures are conducted inside a glove box under a continuous flow of nitrogen in order to keep environmental humidity lower than 10% and minimize impurities inclusion.

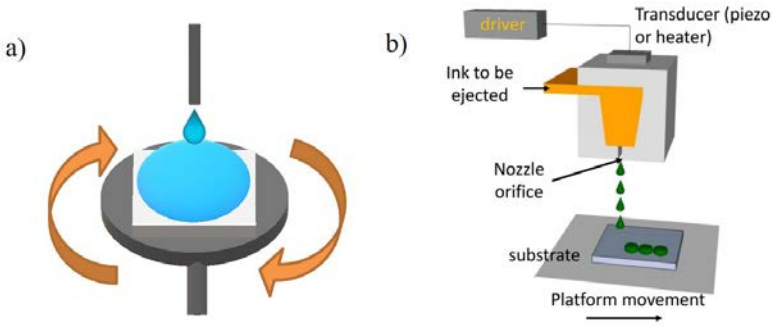

Figure 2.2: Schematic representations of a)spin coater and b)Ink Jet printer (reproduced from [98])

Spin coating

The fluid is spread by centrifugal force on the substrate when a rotary movement is applied (Fig.2.2(a)) [99]. To do so, 15 μL of precursor solution are placed at the centre of the substrate with a Pyrex microsyringe. Then, it is accelerated in 1s at a rate of 6000 rpm and held for 2 min. Just after, the sample is placed in a hot plate at 70°C for 5 min to complete solvent evaporation.

Ink Jet printing

Printing is performed by controlled ejection of picoliters of ink on the surface from a printhead employing a single nozzle (Fig.2.2(b)). The ink is loaded by capillary forces into a hollow glass needle, which is attached to a piezoelectric dispenser. The drop is controlled mediating a bipolar squared wave, by tuning the pulse length, wave pulse width (voltage), and frequency.

In this case, the nozzle is static while a platform where the substrate is placed moves in two perpendicular directions. The thickness will be determined by the drop volume and drop pitch (distance between deposited drops). The last depends on motors velocity and drop frequency.[100, 101].

Ink Jet printed pyrolyzed samples shown in this Thesis have been produced in collaboration with B. Villarejo and F. Pino and in the framework of other thesis and projects [102].

Substrates

Three commercial single crystals have been mainly used as substrates for YBCO growth: (001) $LaAlO_3$ (LAO), (001)$SrTiO_3$ (STO) and the mixed peroviskite (100) $(LaAlO_3)_{0.3}(Sr_2AlTaO_6)_{0.7}$ (LSAT). They are commercially available and 5x5 mm of size. The choice is based on the low mismatch with YBCO lattice parameters (Tab. 2.1). Besides that, other requirements taken into account are thermal expansion, polished surface quality, stability and robustness.

	Structure	Lattice parameters (Å)	Misfit to YBCO (%)
LAO	cubic	3.79	-1.56
STO	cubic	3.91	1.56
LSAT	cubic	3.86	0.26
YBCO	orthorhombic	3.85	0

Table 2.1: Lattice parameters and mismatch with YBCO of substrates. Negative misfit will produce compressive strain, while positive misfit is accounted to tensile strain

Before usage, the surface is cleaned and conditioned to be atomically flat.

The substrates are previously washed with methanol and acetone, removed by means of compressed N_2 flow. Then, a thermal treatment at 900 °C for 5h under 0.5L/min of oxygen flow is applied to reorganize the surface in form of atomically flat terraces (Fig.2.3).

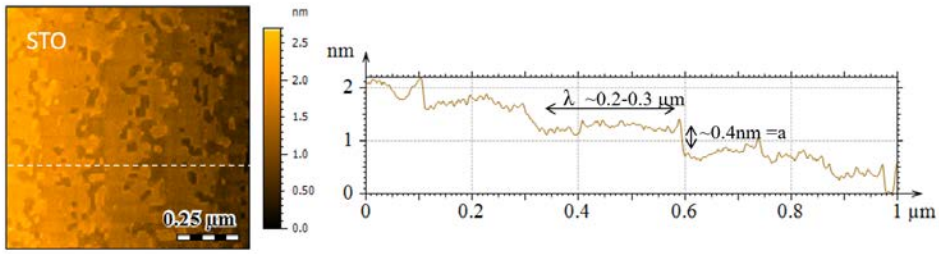

Figure 2.3: AFM image of as-treated STO surface and the corresponding profile

This stair-like morphology is a consequence of the miscut angle θ. From this value, it depends the terrace width (λ):

$$tan\theta = \frac{a}{\lambda} \tag{2.1}$$

Being a the lattice parameter. Terrace steps for (001) surfaces in equilibrium should be separated by a height $(n + 1/2)a$ with n=$1/2, 1, 3/2, 2 \ldots$.

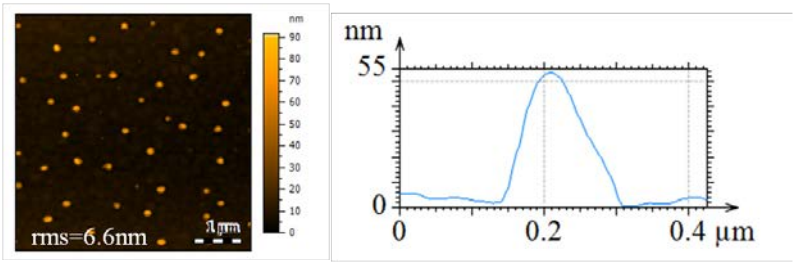

Figure 2.4: AFM image of 50nm YBCO buffer layer grown by PLD and profile of a CuO grain

On the other hand, 50nm thin films of YBCO have been used as buffer

layer for homoepitaxial growth. YBCO is deposited in this case by Pulsed Laser Deposition (PLD) on treated STO substrates. The growth conditions, optimized in previous Thesis of the group, are at 800 °C with a pressure of 0.3 mbar of O_2 and it is deposited at a frequency of 5Hz, 1300 pulses and $2J \cdot cm^{-2}$ of laser fluence. The films surface present no porosity, roughness of $\sim 6nm$ and typical precipitates of copper oxide are $\sim 50nm$ high, as it can be observed in figure 2.4.

2.1.3 Pyrolysis step

During low-temperature heat treatment the dried solution is converted to a nanocrystalline film by decomposition of organic phases, the pyrolysis process. This step was optimized after studying the solution decomposition processes in previous works to ensure that the obtained films are free from organic species.

Thermal treatment is carried out with a tubular furnace placed in a laboratory of controlled humidity (<30%) to prevent hygroscopic processes of as-deposited films [103]. However, when increasing temperature, humid atmosphere is used in order to avoid sublimation of copper(II) acetate at temperatures higher than 110°C [104]. To do so, humidified gas with $P_{H_2O} = 23mbar$ is obtained by passing oxygen through deionized water contained in two flasks in series, prior to entering the furnace. The thermal process is made under oxygen flow ($0.12L \cdot min^{-1}$)

Single deposition Most of the samples deposited by spin coating have been calcinated following the thermal profile presented in figure 2.5. For thicker films deposited by IJP, heating ramps have been modified.

Multi deposition For the achievement of homogeneous thick films by spin coating using our solutions, a process of multideposition has been followed. It consists on subsequent deposition and pyrolysis of several layers until the desired thickness is reached. Intermediate depositions are heated up to 300°C following the heating ramps of the standard process. After the last coating, the standard temperature profile up to 500°C is followed, increasing the dwell time 30min.

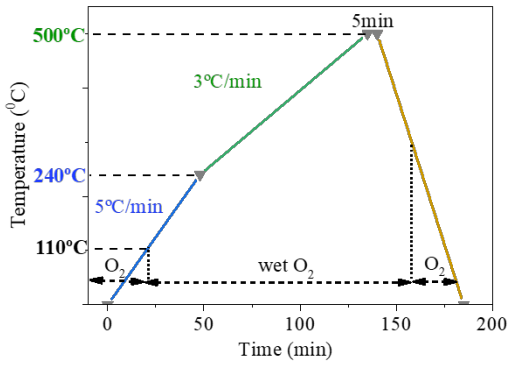

Figure 2.5: Thermal profile for standard pyrolysis

2.1.4 Film crystallization

YBCO phase is crystallized from as-pyrolyzed films over a higher temperature thermal treatment. Several processes take place during this step: decomposition of intermediate phases, formation of a metastable liquid and YBCO nucleation and growth. The understanding and optimization of these processes is one of the main aims of this Thesis. Thus, detailed information regarding experimental conditions has been modified for each experiment and will be detailed with the corresponding discussions. Yet, in this section the characteristics and set up for the thermal treatments performed by means of the different furnaces used will be undertaken.

Typically, heat treatments for CSD have been performed in tubular furnaces with Conventional Thermal Annealing (CTA). For the crystallization step in TLAG, CTA have been used for low heating rates. However, the control of fast liquid mediated growth demands very high ramp rates. This requirement is fulfilled using a Rapid Thermal Annealing (RTA) oven (AS-Micro from Annealsys) that can work at rates up to $250°C{\cdot}s^{-1}$ for heating and $\sim 20°C{\cdot}s^{-1}$ for cooling down.

- **Conventional Thermal Annealing with tubular furnace** uses electric resistive heating. The sample is situated on a crucible in a quartz

tube at the previously calibrated position for the desired temperature profile. The furnace is calibrated to minimize the possible overshoots and it is tested periodically and for every new heat recipe by measuring the real temperatures with a thermocouple type k.

- **Rapid Thermal Annealing furnace** is equipped with an infrared system allowing very fast and precise changes of temperature. It is composed by a quartz tube with infrared halogen lamps on top and bottom side. The lamps are supplied by a special power converter that controls the power applied to the lamps and provides fast power control and high process reproducibility. The sample is placed on a SiC coated graphite susceptor on a quartz holder provided with a thermocouple and its position has been determined in order to give the best temperature uniformity. This susceptor allows maximum speeds of $60°C \cdot s^{-1}$. For faster velocities, a silicon wafer has been used as holder, with less precise temperature control.

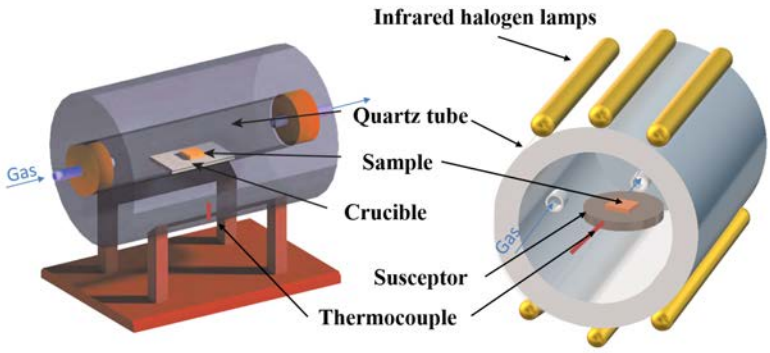

Figure 2.6: Schematic representation of a tubular furnace, at left and a Rapid Thermal Annealer, at right.

In both cases, oxygen partial pressures are achieved mediating the mixture of nitrogen and oxygen, which gas flow speed is set by mass flow controllers. In table 2.2 the operating conditions ranges are summarized for each furnace.

However, the effective flux distribution where the sample is placed is homogeneous in the case of the CTA with a ∼22mm quartz tube, but turbulent and

Parameters	Tubular	RTA
Heating rate ($°C \cdot s^{-1}$)	<0.4	0.4–60
Cooling rate ($°C \cdot s^{-1}$)	0.05–0.5	10–30
P_{O_2} at p_0 (bar)	$2{\cdot}10^{-4}$–10^{-2}	$4{\cdot}10^{-4}$–10^{-2}
Total gas flow ($L \cdot min^{-1}$)	0.6	2

Table 2.2: Range of parameters used for YBCO crystallization with each furnace

low for the RTA due to the bigger dimensions of the chamber compared to the gas inlet and outlet size and position. Thus, total gas flows are not comparable for the two equipments. Most of the experiments have been performed operating with the highest flux that flow controllers permitted.

Other advantage of the tubular furnace is the possibility to work with humid gas, which permits to perform all the annealing steps (pyrolysis, crystallization and oxygenation) in continuous.

In contrast, RTA is provided with a rotary pump and it can operate at reduced total pressures, in contrast our CTA.

During the course of this Thesis, a new tubular furnace with flash heating is being developed in the group to fulfil the requirements of TLAG process. It combines the advantages of having a high and homogeneously distributed gas flow in the tubular tube; with very fast heating ramps by means of a motor that brings mechanically the sample to the desired temperature and speed inside the furnace.

2.1.4.1 Experimental conditions for the low P_{O_2} route

For the low P_{O_2} route, the pyrolyzed sample is first heated up to high temperature (770-840°C) at a $P_{O_2} \sim 10^{-5}$ bar for precursors decomposition below YBCO stability line (step I). Then, YBCO crystallization is produced after a jump on P_{O_2} at a constant temperature to the optimum T-P_{O_2} conditions (step II).

To achieve a P_{O_2} of $\sim 10^{-5}$ bar with our systems, we use the RTA at the minimum total pressure of $2{\cdot}10^{-3}$ bar, previously cleaned using N_2 and vacuum

cycles. For the jump on P_{O_2}, the total pressure is increased to $2 \cdot 10^{-2}$ bar by introducing a flux of gas flow at 2L/min and keeping the rotary pump. A P_{O_2} of $3 \cdot 10^{-4}$ bar, is reached as fast as with 2ms. (Fig. 2.7(b)).

P_{O_2} can be tuned for this step from 10^{-4} bar to $2 \cdot 10^{-2}$ bar by using N_2/O_2 mixtures controlled by massflows. Monitored total pressure and oxygen partial pressure is shown in figure 2.7 for the switch between step I and step II.

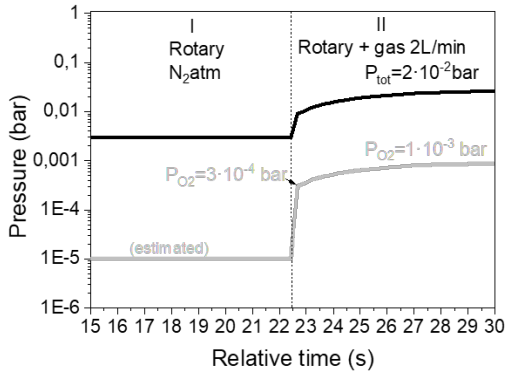

Figure 2.7: Monitored jump in total pressure and oxygen partial pressure for the low P_{O_2} route and final P_{O_2} of 10^{-3} bar.

2.1.5 Oxygenation

A post annealing process is required to oxygenate the resulting YBCO tetragonal phase for its transition to the superconducting orthorhombic crystal orientation. The thermal treatment was optimized and checked by in-situ resistance measurements conducted by A. Stangl (Fig.2.8a). This step is performed at a tubular furnace under an oxygen flow of $0.6L \cdot min^{-1}$.

In the case of samples crystallized in the tubular furnace, the oxygenation has been conducted when cooling down. At 600°C the gas flow is switched to dry oxygen and temperature is decreased at a rate of 2.5 °C$\cdot min^{-1}$ to 450°C and hold for 200min.

For the samples grown in the RTA or other furnaces, the oxygenation process

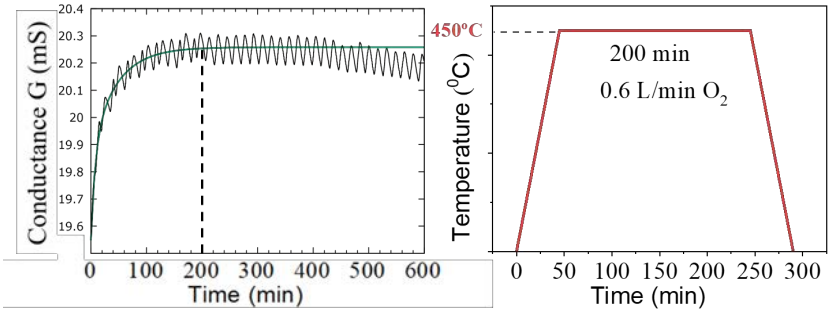

Figure 2.8: At left, time evolution conductance during dwell at 450°C. At right, standard thermal profile for oxygenation

is carried out separately from room temperature, following the profile depicted in Fig. 2.8b.

2.2 Characterization techniques

Phase composition and films structure have been mainly characterized mediating X-Ray Diffraction (XRD) techniques and Transmission Electron Microscopy (TEM). TEM also provides morphological information within the film, as well as Focused Ion Beam (FIB). Organic species and barium carbonate evolution have been also investigated by means of Fourier Transform Infrared Spectroscopy (FTIR).

Surface smoothness and superficial homogeneity of as-pyrolyzed samples have been characterized by Optical Microscopy (OM), while the surface microstructure and phase purity of growth films have been observed using Scanning Electron Microscopy (SEM) with coupled Energy-dispersive X-ray spectroscopy (EDX) and eventually by means of Atomic Force Microscopy (AFM) or Raman spectroscopy.

Finally, film thickness has been measured by TEM, FIB images or by measuring a step with a Profilometer P16 from KLA-Tencor. To do so, half of the

sample is covered using a standard photoresist as protector, while the uncovered material is removed by chemical etching with orthophosphoric acid diluted in distilled water (1:1).

2.2.1 Precursor solution physiochemical characterizations

Physiochemical properties of solutions have an influence on deposition and pyrolysis processes. Further, they serve as a tool to ensure stability and reproducibility of the process. Evaluated parameters are the following:

Viscosity is measured at room temperature with a HAAKE RheoStress RS600 rheometer from Thermo Electron Corporation by the "controlled stress method". A rheometer measures resistance of liquids in response to applied forces. In this case, the shear rate produced by a liquid placed within a rotating and static cylinders can be correlated to viscosity.

Surface tension is determined with the pendant drop method [105] with a DSA 100 analyser from KRÜSS.

Contact angle is a measurement that allows quantification of the wettability that a liquid have on a certain surface. Our solutions are evaluated on LAO substrates from imaging analysis of sessile drops photographs (Fig. 2.9) with a DSA 100 analyser from KRÜSS by using the Axysimmetric Drop Shape Analysis (ADSA) technique [106].

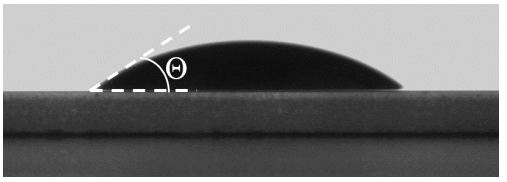

Figure 2.9: Image of a $2\mu L$ digitized sessile drop for contact angle (Θ) analysis with ADSA technique

Water content is measured by Karl Fisher titration with a Crison Tritomatic 1S [107]. Solution water content should be kept <2wt% for obtaining good and reproducible results. Its influence is commented in section 3.3

Stoichiometry Copper and yttrium concentrations are determined with iodimetry and complexometric titrations respectively. Precipitation gravimetry is required in order to determine the barium content.

2.2.2 Thermal decomposition analyses

The thermal decomposition pathway of deposited films is followed by Thermogravimetric Analysis (TGA) and Evolved Gas Analysis (EGA). These analysis have been conducted by the GRMT group at University of Girona (UdG) in collaboration with S. Rasi, Dr. P. Roura and Dr. J. Farjas.

TGA measures weight evolution of the material with temperature, under certain atmospheric conditions. Simultaneous thermogravimetry and differential thermal analysis (DTA) have been performed with a Mettler Toledo thermobalance (TGA/DSC1).

In order to correlate the information provided by TGA measurements with our film decomposition processes, analyses are performed directly on deposited films. Previous studies observed relevant differences if measurements were made on powders, which is more common [108]. Furthermore, experimental conditions are also reproduced. Similar annealing profiles to the standard processes and gas compositions in continuous flow (55ml/min) were possible.

Furthermore, the initial and final mass of the samples (measured with a XS3DU balance) is always compared with that deduced from the TG curve. TG curves are normalized to the mass of the sample once dehydrated, at 150°C [109]. Additionally, the derivative of the mass loss (dTG) is plotted to indicate the main mass loss steps.

EGA permits the detection of gases evolved from a heated sample during decomposition or desorption. For some measurements, EGA was coupled with TG analysis using mass spectroscopy (MS) detection (TG-MS). For that, a steel capillary heated to 200°C connects the TG gas outlet which is at atmospheric pressure; with the MS chamber composed by a quadrupole mass analyser (MKS model Microvision Plus) kept in vacuum. Very thick films ($> 2\mu m$) have to be used for good sensitivity.

2.2.3 Microscopic techniques

Optical Microscopy

OM is used to image the films surface with a maximum magnification of 100x with visible light. On the one hand, it is useful to characterize the global film homogeneity after pyrolysis and identify film defects such as cracks, buckling or precipitates. On the other hand, it shows macroscopic inhomogeneities caused during film growth. Some examples are big secondary phases raising at the surface or film free areas produced by the formation of drops, phase separation or dewetting phenomena of the YBCO film. Mainly two OM equipments have been used during the course of this Thesis: a Leica DM 1750 M and a B-600 MET from OPTIKA.

Scanning Electron Microscopy

SEM provides high resolution information of film surfaces, reaching magnifications up to 10^5x. For our study, it is a crucial to observe features such as microscopic material inhomogeneities, grains size and orientation, phase separation, precipitates on the surface, porosity, etc. A morphological information that is crucial for the understanding of film growth, as well as for its physical properties.

The film is scanned by means of a focused high-energy electron beam that interacts with the atoms of the sample. From this collision, two types of electrons are ejected, besides X-rays: backscattered electrons (BSE) and secondary electrons (SE). One detector collects SE, which are low energy electrons (0-20 eV) produced from inelastic scattering of ionized atoms from the first nanometers. It provides topographic information since the amount of detected electrons depends on the depth, producing an image of different contrasts. The other detector is devoted to BSE, high energy electrons ($\sim$ 50keV) reflected from interactions with atoms nucleus. Those will be proportional to atomic nucleus weight, leading to compositional images of the films.

Images were taken on a field emission FEI Quanta 200 FEG SEM of FEI CompanyTM. High-resolution imaging is performed under high vacuum conditions with an acceleration voltage of $\sim 15kV$. Sample preparation is not

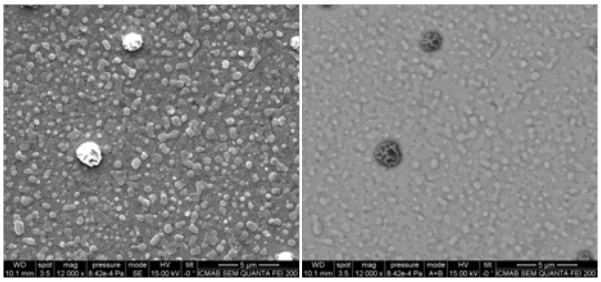

Figure 2.10: SEM images of a grown YBCO film with CuO precipitates on the surface. At left the image is acquired using SE mode and precipitates appear brighter due to their higher thickness. At right, a BSE image in which the grains are darker than the film because of the lower atomic number of CuO

required since the films are electrically conductive after oxygenation. Measurements were carried out by me.

Focused Ion Beam

FIB resembles SEM, with the difference that SEM uses a focused beam of electrons, while FIB uses a focused beam of gallium ions instead. Primary beam currents are used for imaging the sample surface, whereas high beam operation is used to sputter or remove material from the surface (e.g. high-precision milling). This allows the creation of very precise cross sections of a sample for subsequent imaging via SEM.

For this project, the technique is performed for imaging the inner part of the films in order to study the porosity of pyrolyzed films and quantification is performed by image treatment using ImageJ program. FIB images were taken by Dr. R.Guzman and Dr. A. Palau from our group (SUMAN) by using dual beam (SEM, FIB) Zeiss 1560 XB.

Transmission Electron Microscopy

Using TEM is possible to image the internal structure of films at the atomic scale. A beam of electrons is transmitted through a very thin sample. After be-

ing magnified and focused by a series of electromagnetic lenses, the information is gathered in an image or diffraction pattern. Additionally, this information can be complemented with compositional analysis by using attached EELS (Electron Energy Loss Spectrometry) or EDX devices that collect electrons which have been scattered instead. This makes TEM a very powerful tool for both morphological and compositional characterizations of the YBCO matrix, lattice defects, grain orientations or secondary phases.

TEM studies were performed by Dr. Roger Guzman and Bernat Mundet, members of our group (SUMAN). Samples were prepared by FIB or conventional mechanical polishing followed by low-voltage Ar ion milling for the final thinning [110]. Different TEM equipments were chosen depending on the resolution needed for each case of study. For low magnification TEM images, a FEI Tecnai G2 F20 operated at 200KV located at Catalan Institute of Nanoscience and Nanotechnology (ICN2) was used. While high resolution TEM images were obtained using a FEI Titan 60-300 microscope equipped with an X-FEG gun, a CETCOR probe corrector and a Gatan TRIDIEM 866 ERS energy filter operated in STEM mode at 300 kV. This one is placed at the Advanced Microscopy Laboratory (LMA) in Zaragoza.

Scanning transmission electron microscopy (STEM) was performed using the FEI Tecnai F20 S/TEM operated in STEM mode at 300 kV with a Gatan TRIDIEM 866 ERS energy filter.

2.2.4 X-Ray Diffraction techniques

XRD is the most common technique for structural characterizations of materials. In contrast to TEM, it is a nondestructive technique and it probes a large sample volume. With XRD we perform studies on the film composition, crystalline structure, grain orientations, phase quantification, lattice parameters, defects... When a crystalline matrix is irradiated by a monochromatic X-ray beam, this will be scattered with the same wavelength (λ) as the incident beam. For parallel atomic planes of atoms (hkl), with a space d_{hkl} between the planes, constructive interference only occurs when Bragg's law is satisfied:

$$n\lambda = 2d_{hkl}sin\theta \tag{2.2}$$

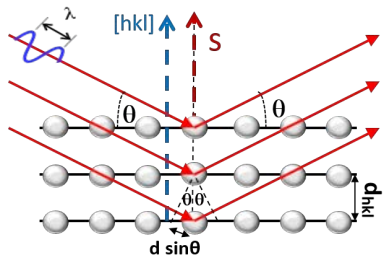

Figure 2.11: Schematic representation of the constructive interference between two incident X-rays on a crystal surface (Bragg's law)

Consequently, a family of planes produces a diffraction peak only at a specific angle θ. In a typical configuration, the diffracted wave intensity is then collected by a detector for each incident angle to build the so called diffraction pattern (I(2θ)). Thus, peak positions are determined by d_{hkl} since λ is fixed by the diffractometer [111]. Additionally, the plane normal [hkl] must be parallel to the diffraction vector s as seen in figure 2.11. Then, the intensities will be affected by the orientation of grain domains within the sample. For polycrystalline samples, in which grains are randomly distributed, the scattered intensity will be constant for the same scattering angle, and distributed in a circle (Debye ring). However, for epitaxial films, only families of hkl planes that are oriented parallel to the surface plane contribute to a Bragg reflection, focused to only a few points in the reciprocal space (Fig.2.12).

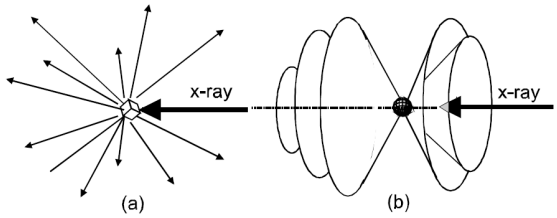

Figure 2.12: Patterns of diffracted X-rays: (a) from a single crystal and (b) from a polycrystalline sample [112]

Multiple information can be gathered by tuning the diffraction configura-

tion. Typical rotating angles are represented in figure 2.13. We have used for the study of our films different scan modes and detectors, involving multiple diffractometers that are presented in this section.

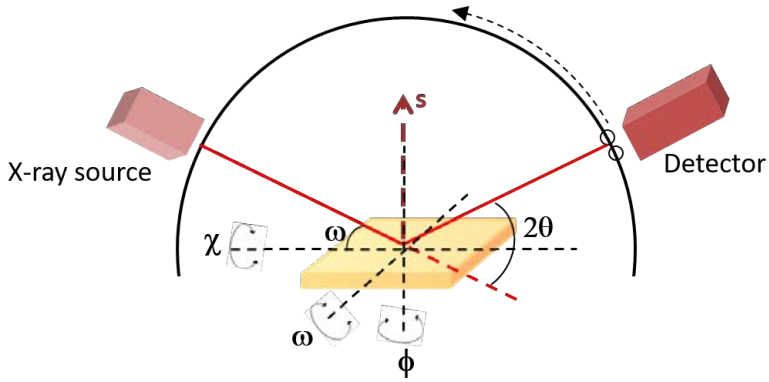

Figure 2.13: Schematic representation of a $\theta - 2\theta$ scan with a typical Bragg Brentano geometry and rotating angles nomenclature.

2.2.4.1 High-Resolution X-ray Diffraction

High-resolution (HRXRD) scans are performed with a Discover D8 Bruker diffractometer (X-ray energy = 8.049 keV) equipped with a Lynxeye XE energy-dispersive 1D detector, using Bragg-Brentano configuration (Fig.2.13). The measurements were conducted by the service technicians A.Crespi, J.Esquius and F.G.Campos, whereas analysis of acquired data was performed by me and in collaboration with J.Banchewski.

- $\theta - 2\theta$ **scans**. Data acquisition is performed in the range of 7°to 100°in 2θ with a step size of 0.02°at a speed of 2s/step. Grain sizes can be calculated from the integral-breadth β applying the Deby Scherrer formula, and non-uniform strain evaluation is determined through semiquantitative Williamson-Hall plots[83].

- **Grazing Incidence-XRD** is needed for compositional identification of polycrystalline phases within the film which intensity may be hidden by

the pronounced enhancement of Bragg reflections from textured phases or the substrate. These include precursor phases, remaining intermediates or products derived from reactivity with the substrate. To do so, ω is fixed at a very low angle $\sim 1^{\circ}$(above the critical angle for total reflection of the film material) while the detector is moved along the 2θ circle. Bragg reflections are found at comparable positions as in a symmetrically measured pattern. However, with grazing incidence geometry the scattering vector s is no longer parallel with the surface, excluding Bragg reflections of our epitaxial phases and single crystal substrates.

- ω **scan** or rocking curves provide information on mosaicity of a particular reflection. A scan in ω is performed at a fixed 2θ position. For the case of YBCO, the chosen 2θ is the corresponding to the (005)YBCO peak. Then, the calculated full width at half maximum (FWHM) of the acquired peak is proportional to the quality of the out-of-plane texture. The narrower the peak, the higher the crystalline quality of the sample.

2.2.4.2 Two-dimensional X-ray Diffraction

Many of the films to be analysed in this study are composed by both textured and random grains of the YBCO phase. Typical $\theta - 2\theta$ scans on these type of samples are not optimal since the diffracted intensities of out-of-plane crystallites is hidden within the enhanced intensity of peaks diffracting from the epitaxial fraction lying parallel to film surface, as explained before. In addition, with rocking curves is possible to measure grains misorientation degree, but it only probes the orientation in ω direction and for a particular reflection. Other plane orientations can be projected by means of pole figures (ϕ scans for each χ), but those are very slow measurements with a point detector and again for only a particular 2θ reflection.

Therefore, it is convenient to perform texture studies using an equipment provided by a two-dimensional detector, which can acquire out-of-plane positions probing a larger volume of reciprocal space within a single collection frame ($\Delta 2\theta$=30°, $\Delta\chi$=70°). The General Area Detector Diffraction System, from now on GADDS, is integrated in a Bruker-AXS D8 Advance diffractometer, operating with CuK_{α} radiation. It is located in ICMAB and it has also

been operated by the XRD service managers.

It uses the same geometry as a conventional four-circle diffractometer. The detector is moving in one circle, while a goniometer is used to rotate the sample as shown in figure 2.14. The resulting patterns are later integrated at the desired angles using a software. A typical scan is shown in figure 2.15.

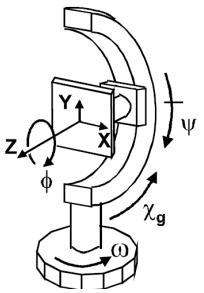

Figure 2.14: Representation of a goniometer and rotation axes (ω, χ, ϕ) and translation axes X, Y, Z [112]

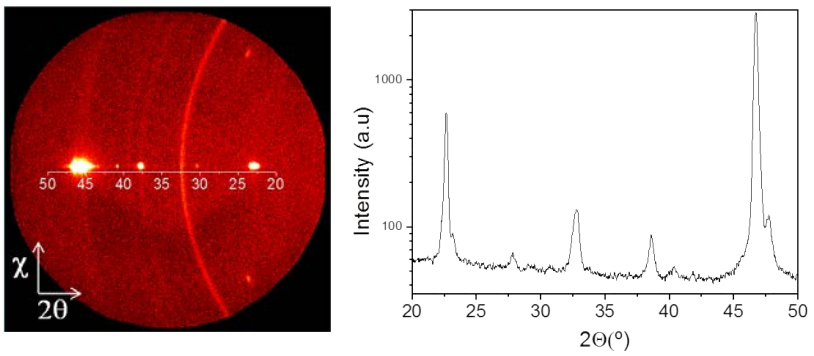

Figure 2.15: At left, typical GADDS frame of a ω-scan and diffraction pattern obtained after χ integration of the full frame, at right. Measurement conditions are ω=10°- 25°, 2θ=35°and detector-sample distance is fixed at $\sim 15cm$

- **Standard scans** $\theta - 2\theta$ range is already defined in the area detector

at a fixed 2θ position. Yet, in order to acquire the full intensity of the epitaxial phases, the measurement is performed by moving the sample in ω to assure Bragg conditions.

For standard scans, ω values range from 10°to 25°during 900s.

- **Secondary phases identification**. For non-quantitative measurements and with the objective of enhancing the intensity of secondary polycrystalline phases, diffraction angles of substrate planes are avoided with an ω range of 12°-23°, during 1800s.

2.2.4.3 Quantification analyses

Data analysis for the quantification of epitaxial and random fractions, c- and a/b-oriented grains are performed with the GADDS detector.

YBCO random fraction

The methodology developed for the random fraction quantification of nanoparticles developed by A.Llordés [113, 24], is now applied to YBCO.

During a GADDS measurement, the acquisition of the diffraction pole (c-axis oriented epitaxial grains) and diffracted ring (randomly oriented grains) is simultaneous. We calculate random fractions from the standard $\theta - 2\theta$ measurements, in which the detector is approximately centred at the (005)YBCO reflection.

The random fraction can be approximated to:

$$\Gamma_{random} = \frac{\nu_{random}}{\nu_{c-grains}} = \frac{I^{exp}_{ring} \cdot (360/\Delta\chi) \cdot 4\pi)}{8 \cdot I^{exp}_{pole}} \tag{2.3}$$

where I is the integrated intensity and ν the volume fraction. The diffracted intensity of the epitaxial contribution is normalized for the equivalent 8 poles by symmetry, while the polycrystalline ring is applied for the whole ring (360°) and the entire solid angle 4π as an approximation.

The integration limits are: $\Delta 2\theta = 1.5$°is the same for both contributions. $\Delta\chi = 7$ for the ring and $\Delta\chi = 3$ for the pole, centred at the respective reflection angles.

Then, the background intensities are subtracted, and the polycrystalline intensity normalized is deducted from the epitaxial one. For instance, $I^{exp}_{pole} = I^{calc}_{pole} - I^{calc}_{back} - (I^{calc}_{ring} \cdot \Delta\chi_{pole}/\Delta\chi_{ring})$. The background integration area is displaced to close 2θ maintaining the same χ, for both reflections. An error of 4% was calculated from the dispersion of results when applying different 2θ integration limits.

ab-oriented YBCO grains fraction

The ab-grains volume percent (ν_{ab}) and fraction were determined by Granozio *et al* [114] using the following relations:

$$\nu_{ab} = \frac{2 \cdot I_a sin(\chi_a)}{2 \cdot I_a sin(\chi_a) + \cdot I_c sin(\chi_c)} \tag{2.4}$$

then,

$$\Gamma_{ab} = \frac{\nu_{ab}}{\nu_c} = \frac{\nu_{ab}}{1 - \nu_{ab}} \tag{2.5}$$

The factor 2 is introduced due to the twofold symmetry of a-grains. Corrections for the scattering factors are not required when comparing intensities from reflection of the same family of planes.

Two 2D-XRD ϕ scans are performed with the GADDS detector on the (104)YBCO reflection centred at a fixed χ to the value of the corresponding maximum intense Bragg peak for each grain (see Fig2.16). $\Delta\phi = 5°$, $2\theta = 28°$, $\omega = 14.\chi_a = 34°$and $\chi_c = 56°$. The acquisition time is 30 min. The intensities I are extracted from the integration of the respective poles, after background subtraction.

c-oriented YBCO grains fraction (epitaxial fraction)

The epitaxial fraction (Γ_c) is referred to the percentage of c-axis oriented grains with respect to the total YBCO orientations. It is calculated after having quantified the contributions of the random (Γ^c_{random}) and ab-grains (Γ^c_{ab}) with respect to the c-grains, using the just exposed methods. Then, the random fraction can be expressed as:

$$\Gamma_c(\%) = (\frac{\nu_c}{\nu_c + \nu_{ab} + \nu_{random}}) \cdot 100 = (\frac{1}{1 + \Gamma^c_{ab} + \Gamma^c_{random}}) \cdot 100 \tag{2.6}$$

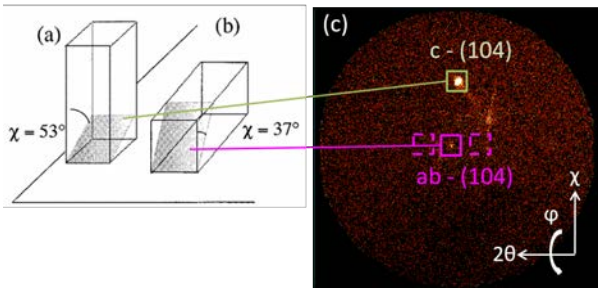

Figure 2.16: Schematics showing the χ angle of the (104) plane in (a)c-axis and (b) a-axis grains. Reproduced from [114] (c) 2D-XRD image of a scan centred on the diffraction pole of the (104) reflection of the a-grains

Taking into account that:

$$\nu_{ab} = \Gamma^{c}_{ab} \cdot \nu_c \text{ and } \nu_{random} = \Gamma^{c}_{random} \cdot \nu_c \tag{2.7}$$

Then

$$\Gamma^{tot}_{random}(\%) = \Gamma^{c}_{random} \cdot \Gamma_c \text{ and } \Gamma^{tot}_{ab}(\%) = \Gamma^{c}_{ab} + \Gamma_c \tag{2.8}$$

2.2.5 *In situ* XRD with synchrotron radiation

In situ XRD growth experiments with fast acquisition times were performed to study reaction paths, growth rates, deduce the presence of the transient liquid phase and characteristic temperatures of all involved phases.

We carried out *in situ* XRD experiments in synchrotron beamline DiffAbs-Soleil, located in Paris. The experiments exposed in this thesis were performed in two runs of 6 full days and were granted under the proposals n°20160881 and n°20170911.

The experiments were conducted by group co-workers and me with the assistance of C. Mocuta. Raw data treatment was performed by J.Banchewski, and I carried out the data analysis of the exposed experiments in this thesis.

The beamline has a DiffAbs-6 circles diffractometer with a heater stage provided, among others, an area detector (X-ray hybrid pixel area detector, XPAD) (Fig.2.17a). The beam energy was maintained at 18 KeV. With such conditions,

the main phases involved in our process diffract within the 2θ range of the 2D detector. Thus, we could extract information regarding all phases at each acquisition point.

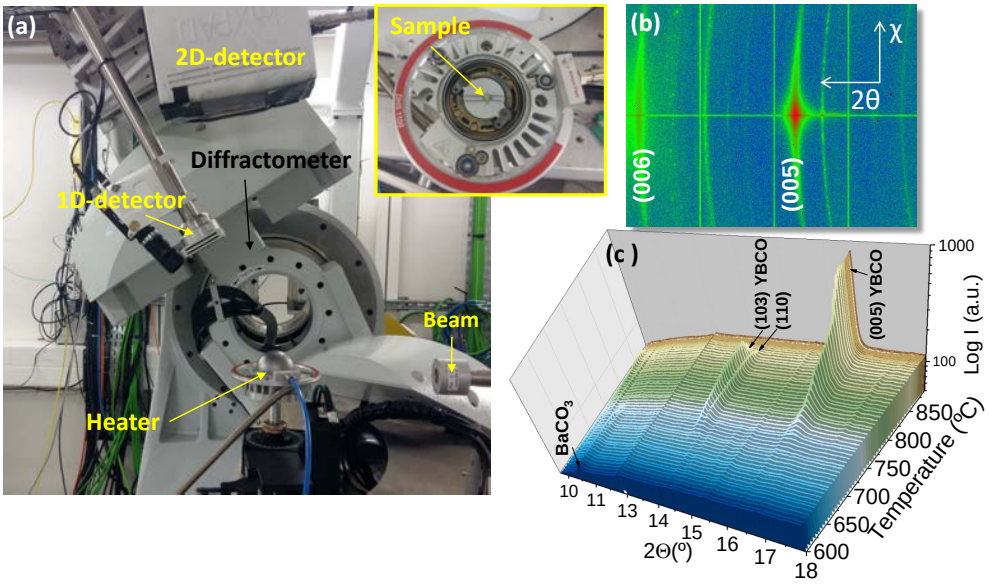

Figure 2.17: (a) Experimental station where the principal components are signalled. The inset shows a detailed view of the sample stage. (b)2D-XRD image. (c)Integrated 2θ diffraction scans with temperature

Acquisition times per data point could be from 50 ms, with better resolution as time increases. Generally, 500 ms were used for phase evolution before YBCO growth and 100 ms for YBCO growth. To follow random phases, grazing XRD scans ($\omega = 4°$) were recorded, while to follow YBCO growth, conditions close to Bragg angle ($\omega = 7.9 - 8.1°$) with the (005) peak were met ($\theta 2\theta$ geometry). Total Bragg configuration could not be used to avoid saturation of the detector.

Two heaters were used. In the first run, a DHS 900 heater allowed heating ramps up to 0.8°C/s. During the 2nd run, a Anton Paar DHS1100 heating stage equiped with a Graphite dome allowed heating rates up to 5°C/s. Slight gas flow was allowed from a gas inlet and being expelled from leaks between

the dome and stage.

Two main configurations were used to meet the requirements for the Temperature-route and the P_{O_2}-route.

Temperature rise

The pyrolyzed samples were placed at the heating stage and heated at rates from 0.4 to 5°C/s at 1 bar of total pressure with different oxygen partial pressures.

P_{O_2} jump

In order to carry out experiments that require a pressure jump with precise P_{O_2} control, a singular purpose experimental setup was designed and implemented with user home equipment.

Fig.2.18 shows a schematic drawing of the setup. Two circuits, one for the lower and one for the upper pressure regulation, are separated by timers/electrovalves and connected to the dome furnance. Two rotary pumps, one turbo pump, needle and butterfly valves allow the independent pressure regulation of both cicuits before the experiment. A P_{O_2} meter and a massflow system were used to adjust a desired oxygen partial pressure. Pressure jumps from 10^{-6} bar to atmospheric pressure with O_2 adjustment down to 10^{-5} bar were realized, allowing us to perform precise P_{O_2} step processes at a given temperature.

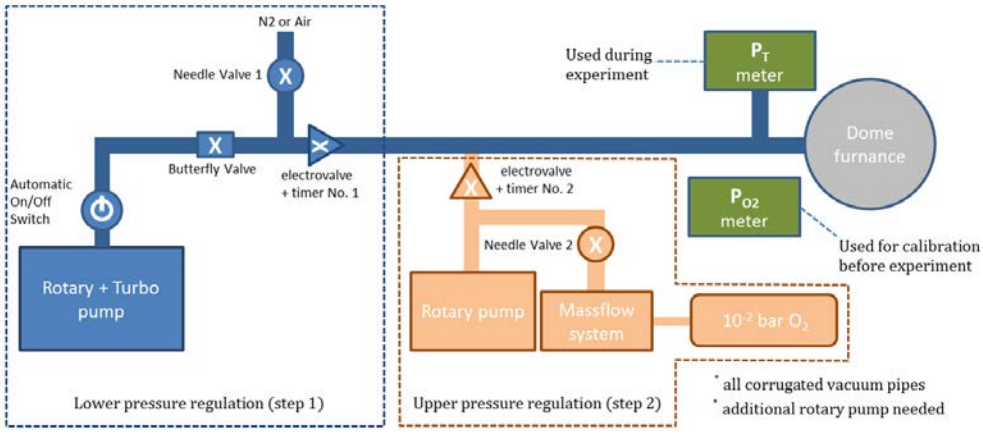

Figure 2.18: Schematic illustration of the circuit to perform a pressure jump from initial to final value with pre-adjusted P_{O_2} partial pressure

These experiments were performed with the Anton Paar DHS1100 heating stage during the second run. Unfortunately, during the pressure jumps the heater temperature suffered an undesired temperature decrease due to the temperature difference of the incoming cold gas and a slow response of the heater.

Data treatment

Each scan conforms a $2\theta-\chi$ image at a fixed ω (Fig.2.17b). Those are integrated in χ to obtain intensity-2θ diffraction patterns (Fig.2.17c).

To follow phases evolution, the main reflections intensities are normalized by their maximum intensity. To do so, first the background is subtracted and then the peak maximum is taken within shifts. Then, we approximate the intensities to be proportional to the phase molar amount. To finish, the normalized intensities are plotted with temperature or time to show each phase evolution.

In some specific experiments, the peaks were fitted to correlate to the molar amount with better precision (not shown here). It showed comparable results with peak intensity.

The slight increase in intensity observed sometimes in the $BaCO_3$ and CuO phases at high temperatures just before decomposition, was justified from fitted results by an increase of particle size [115].

2.2.6 Fourier Transform Infrared Spectroscopy

We use this spectroscopic technique for two main purposes: investigation of organic species during calcination and semi-quantification of carbonate at high temperatures.

Molecules absorb infrared radiation of the same wavelength as the frequency of chemical bonds vibrational or rotational modes. The FTIR spectrum is recorded by passing a beam of infrared radiation through the sample. Then, the amount of transmitted light is detected for each frequency or wavelength. After being submitted to Fourier transform, a transmittance or absorbance spectrum reveals information on the nature of chemical bonds so that it is a fingerprint of the sample chemical composition.

Since our samples are films already deposited on the substrate, measurements are performed on transmittance mode using a holder in which the sample is placed normal to the beam. The detected wavelength range is limited by the

oxides substrate absorption, typically below 1500 cm^{-1} for our substrates, being LAO the one absorbing below the lowest wavelengths (1370 cm^{-1}). A typical scan is conducted in the mid-infrared region, approximately between 4000-1200 cm^{-1}.

In situ FTIR

The analysis of organic specimens evolution through the pyrolysis step is performed by means of *in situ* FTIR. These experiments have been conducted in collaboration with Dr. M. Kreuzer at the facilities of infrared microspectroscopy beamline (MIRAS) of ALBA synchrotron, but working with conventional IR radiation from a Vertex 70 spectrometer. The system is provided by a Linkam temperature controlled sample stage FTIR600 and the detector is coupled with a microscope (Fig. 2.19). The heater is composed by a transparent window and a 3mm hole in the holder that allows the sample to be measured in transmittance mode under continuous gas flow. Additionally, the Hyperion 3000 microscope is used to focus the film area to be measured with a magnification of 15x, while the IR light have a spacial resolution of 33μm. Thus, the

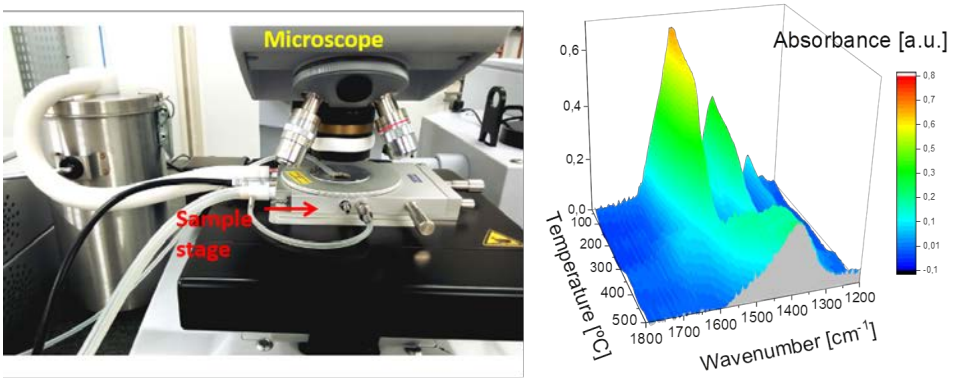

Figure 2.19: At left, temperature Montrolled Microscope Stage used for *in situ* FTIR analysis. At right, time resolved absorbance while heating

equipment allows continuous data acquisition while performing film calcination process under similar conditions to the standard pyrolysis process (See Fig.2.5).

Each spectrum is composed by 64 scans, acquired during 15s. A total of 80 spectrum have been recorded from 50 to 500°C, thus one every 5.6°C. Solutions are previously coated or printed on LAO substrates and dried to 70°C.

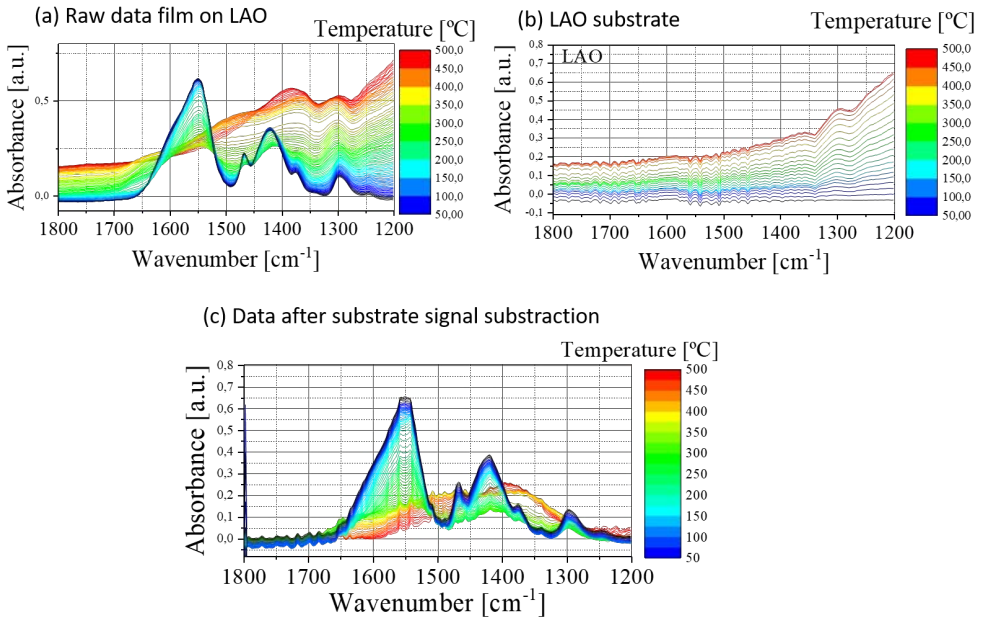

Figure 2.20: *In situ* FTIR scans from 50 to 500°C. Image (a) shows the raw data obtained for a deposited solution. In (b) the scans obtained for LAO substrate alone and (c) the result of data treatment after substrate absorption subtraction

Data treatment is necessary to subtract absorption produced by the substrate, which is increasing at high temperatures and at low wavelengths (See Fig. 2.20). To do so, LAO substrate IR spectrum has been measured without coating along a similar thermal profile. Then, the substrate scans have been interpolated to fit the exact temperature values for each experiment. Once this step is completed, the data can be placed in matrices of the same size. This allows simple subtraction of the substrate absorbance values from the sample raw data with temperature. The result is a corrected spectrum in which only

bands corresponding to the film chemical compounds are present.

Carbonate pseudo-quantification

On the other hand, barium carbonate intermediate decomposition during thermal treatment has been followed by *ex situ* FTIR measurements performed with also a Vertex 70 from Bruker located in ICMAB. Before each measurement, the chamber is filled with N_2 to prevent atmospheric signals. The carbonate absorption band ($\nu_3 \sim 1413cm^{-1}$) is followed for different thermal treatment conditions of the growth stage.

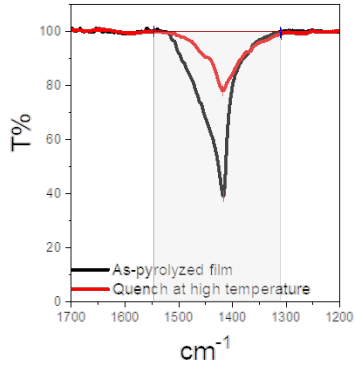

Figure 2.21: Integration range of IR absorption peaks corresponding to carbonate for the calculation of carbon losses

The FTIR spectrum of each film is also recorded after pyrolysis, when all carbonate is present, for normalization. The blanc is subtracted by measuring the LAO substrate without any film deposited on top. A semi quantitative analysis for determining the carbonate content of the samples is performed by normalizing the area of the absorbance bands obtained after treatment with the initial content for each film (Fig.2.21). An area-based method appears preferable to considering peak heights at selected wavenumbers since numerous factors can affect band position, shape and intensity [116]. By Lambert-Beer law (2.9) and assuming ε and b constant values, absorbance is proportional to

concentration.

$$A = \varepsilon bc \tag{2.9}$$

Where A is absorbance, ε is the molar absorptivity with units of $L \cdot mol^{-1} cm^{-1}$, b is the path length in which the sample is contained and c is the concentration of the compound in solution, expressed in $mol \cdot L^{-1}$.

2.2.7 Physical characterizations of superconducting properties

Inductive Measurements: SQUID Magnetometer

DC-magnetometry was used to investigate the electromagnetic response of superconducting YBCO films to provide us an idea about the quality of the samples.

The magnetic moment of the films can be measured in a non destructive way with a commercial superconducting quantum interference device (SQUID) magnetometer from Quantum Design equipped with a superconducting magnet of 7 T. The sensor can resolve magnetic moments in the order of 10^{-6} emu and since it is placed inside a helium cryostat, measurements between 5K and room temperature are possible.

and then cooled down under Zero Field Cooled (ZFC) conditions (no magnetic field is applied during the cooling process) to 10 K.

In order to extract J_c, the sample is cooled down under Zero Field Cooled (ZFC) conditions (no magnetic field is applied during the cooling process) to 5K. Then, the magnetic moment of the sample is saturated at 5K by applying a constant magnetic field of 3T parallel to its c-axis, that is then removed again. For J_c(T), the sample magnetization is measured as temperature increases.

To measure J_c(H), after ZFC, the magnetic field is increased up to a maximum of 7 T while the magnetization values are being measured at a constant temperature and then, decreased to close the hysteresis loop.

According to the Bean model[117], we can obtain the critical current density (J_c) from the magnetization values m obtained by using the following equation:

$$J_c = \frac{3m}{\pi r^3 t} \tag{2.10}$$

where t is the sample thickness and r the radius. r is approximated to 2.57 mm for $5x5mm^2$ squared samples.

Electrical transport measurements

Superconducting characterizations can also be performed from electrical transport measurements. The transport measurements of the YBCO films have been performed at ICMAB by J. Banchewski.

When the applied current exceeds I_c, the resistance becomes non-zero and a drop in voltage is measured. Transport measurements of patterned samples have been applied to determine the critical current density on tracks of the YBCO films in the presence of an applied magnetic field H as a function of the angle θ and at different temperatures.

Electrical transport measurements were carried out with a Physical Properties Measurement System (PPMS) from Quantum Design at ICMAB. The system essentially consists of a 9T superconducting magnet and a helium cryostat. Precise control of temperature within the range 1.8-400 K can be achieved.

Critical temperatures (T_c) were determined using the PPMS Quantum Design system using the Van der Pauw method determined with the derivative criterion (highest slope at the transition).

Chapter 3

Solution processing and intermediate reactions

The combination of liquid-assisted growth with solution processing many join of the advantages required for low cost, high throughput and high performance production of CCs. Chemical solution deposition (CSD) demands low capital investment and low cost production, while liquid assisted growth would enhance film growth rate as compared to the TFA-CSD approach.

Here we report an investigation which has as objective the development of solution derived precursors suitable for transient liquid assisted growth (TLAG). Morphological properties, thickness, composition, and consequently, performance of the crystalline film can be tuned by modifying the characteristics of precursor solution and all processing steps.

The first requirement is the design of an adequate solution so that after deposition and decomposition of organic matter (pyrolysis) results in homogeneous films. At the macroscale, the films should be continuous, without cracking or buckling.

Film thickness control depends on the deposition technique. This process is compatible with well known methodologies (e.g. spin coating, dip coating or web coating) in which thickness depends on rheological properties and solution concentration. But also novel drop-on-demand Ink Jet printing (IJP) can be applied. The advantage rely on thickness control mediating drop volume and spacing, making it suitable for large volumes deposition and large scale applications. However, the issue of increasing film thickness in CSD still remains a complex problem.

Regarding composition, it is of essential importance for TLAG growth that the nature of phases after pyrolysis is the adequate to form the transient liquid

at higher temperatures. For REBCO growth, the liquid phase is the [BaO-CuO] eutectic melt.

This rules out the possibility to use trifluoroacetate solutions, which BaF_2 intermediate only decomposes with the presence of water through a solid-gas reaction forming YBCO [76, 40].

Instead, decomposition of fluorine free organometallic solutions lead to the formation of the metal oxides or barium carbonate. Early studies showed the impossibility to eliminate residual carbon at the grain boundaries resulting from a non complete $BaCO_3$ decomposition which was shown to be detrimental on the superconducting properties [84]. Nowadays, many unknowns still exist about the real capability of eliminating carbon, specially for thick films ($> 300nm$), as well as about the reaction pathway to form YBCO. For this reason, a careful study on precursors evolution, with special focus on the $BaCO_3$ elimination, is essential to achieve high performance YBCO films through TLAG.

In this chapter we will address the two main decomposition processes, from both a morphological and compositional point of view: firing of the deposited organic solution at low temperatures and $BaCO_3$ evolution at higher temperatures. Additionally, we will follow the reactions by means of *in situ* experiments performed using Infrared Spectroscopy and X-ray diffraction with synchrotron light, respectively for both processes.

3.1 Solution design towards TLAG

Chemical solution deposition is a very versatile technique for tuning films characteristics through changes on solution chemistry and deposition parameters, while maintaining a control of the stoichiometry on a molecular level.

Precursor composition, concentration, rheological characteristics and deposition technique have a direct influence on the film thickness and homogeneity, on the thermal decomposition pathway, resulting porosity and, in the last instance on the crystallization processes.

In this section we correlate starting solutions and their properties with the morphological and compositional characteristics of the resulting pyrolysed films.

For the precursor solution design, we choose fluorine free metalorganic based solutions composed by short alkyl chain carboxylates dissolved in carboxylic acids and polar solvents such as methanol. The advantages of using carboxylates are the following: they are stable, commercially available and easy to prepare. Additionally, low carbon backbone organics are preferred to avoid large releases of carbon dioxide that could lead to increased porosity in the films, residual carbon or cracks [68, 118].

A screening on stability of various salts, solvents and additives was performed in previous studies [88]. As a result, solutions composed by metal acetates dissolved in mixtures of propionic acid and methanol are stable for 4 weeks and allow maximum concentrations of 1.5M in sum of metals salts (Y+Ba+Cu). Moreover, the addition of small quantities of aminoalcohols such us triethanolamine (TEA) or diethanolamine (DEA) is investigated with the objective of increasing solution stability [119], thickness or mechanical properties during decomposition.

After having obtained stable solutions, their rheological properties have to be suitable for the deposition technique in order to obtain homogeneous films of the desired thickness. For *ex situ* techniques, the quantity of material obtained will be determined by the thickness achieved at the deposition step and metal concentration of the initial solution.

Deposition	Thickness (nm)	Conc.(M)	Solvent	Additive
SC	90-300	$1-1.5$	Propionic acid/Methanol	$5\%_{v/v}$ TEA
IJP	400-800	0.5	Propionic acid/Butanol	$0.5\%_{v/v} DEA$

Table 3.1: Characteristics of precursor solutions used in this Thesis for each deposition technique. Thickness is referred to final film after YBCO growth

Typical final film thickness achieved by Spin Coating (SC) are in the range of 90-300nm, linked to solution rheological properties. Most of the studies for this Thesis have been performed with films of this thickness range.

However, it is also of big interest for applications the achievement of thicker

films. With this objective, we have performed either spin coated multidepositions or single deposition by Ink Jet printing.

In table 3.1 typical solutions composition adapted for each deposition technique are presented.

3.1.1 Solvent and additive effects on film thickness and morphology

Spin coated solutions

The effects that solvent and additives of spin coated solutions have to film uniformity and thickness are investigated.

Solutions composed by acetate salts with different solvents mixture of propionic acid-methanol and with-without $5\%_{v/v}$ TEA have been spin coated on LAO treated substrates and pyrolyzed until 500°C under wet oxygen flow with the standard thermal treatment. Total salts concentrations were fixed at 1.5M and thickness were measured after growth by profilometry after chemical etching (Fig.3.1(a)).

Considerable differences on final film thickness are observed depending on both solvent mixture and additive. The spin coating process can theoretically be expressed using a modified Navier-Stokes equation (3.1.1) [67] that correlates film thickness (h) with deposited solution physical parameters:

$$h = \frac{c}{2\omega\rho_s}\left(\frac{3\eta\rho_l}{t}\right)^{1/2} \tag{3.1}$$

Where η is the viscosity, c the mass concentration (weight of solid film/weight of solution) and ρ_s and ρ_l are the solid and liquid densities respectively, while ω and t refers to the angular velocity and spinning time.

To provide insight into this matter, viscosities and solutions wettability with the substrate have been measured (Fig.3.1b,c).

The addition of organic additives is a well known strategy for thickness enhancement by increasing solution viscosity. For the studied solutions, viscosity values are doubled by addition of $5\%_{v/v}$TEA and also contact angle increases respect to solutions without additive. These two factors contribute on enhancing final film thickness. For instance, the thickness of a deposited propionic

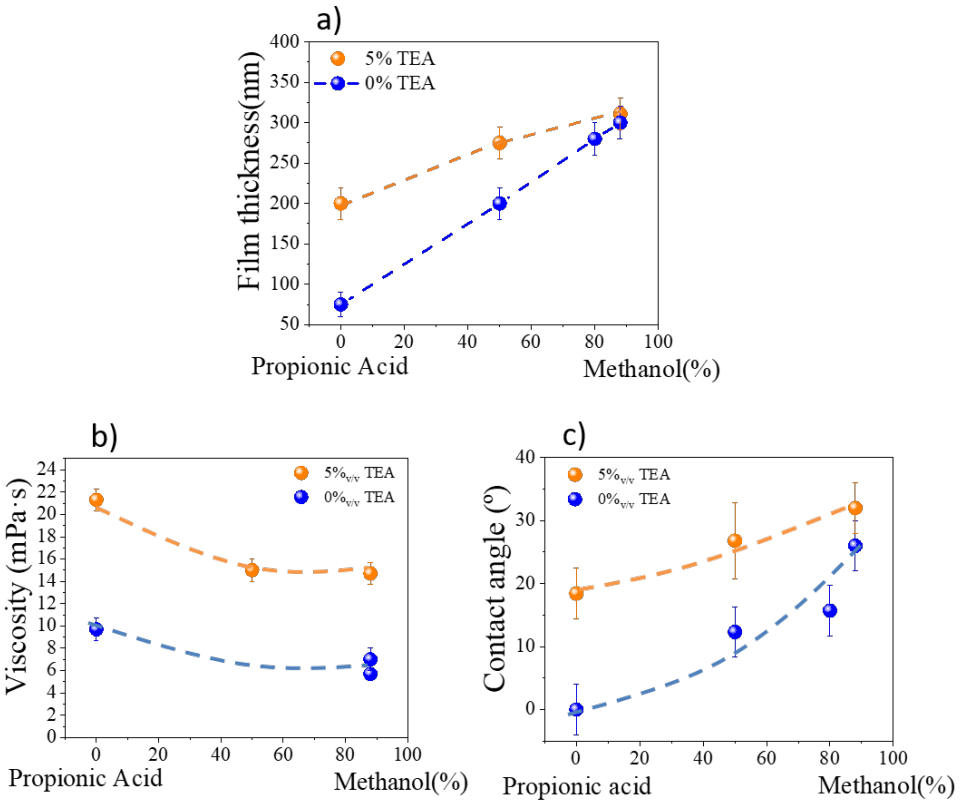

Figure 3.1: Characteristics of different precursor solutions containing different ratio of methanol-propionic acid solvent and possible addition of $5\%_{v/v}$ TEA. (a) Thickness of final YBCO film obtained measured by profilometry. (b)Viscosity values and (c) Solution contact angle θ with LAO substrate

acid solution can be increased from 70nm to 200nm by the addition of TEA. Nonetheless, the extent of this increase is less relevant for methanol solutions, which contact angle values do not differ in respect to the solution without additive.

Additionally, high viscous solutions trend to produce non-uniform distributions of liquid resulting in inhomogeneous or irreproducible pyrolysis [80]. This

fact limits the possibilities to increase the additive amounts and use this strategy to enhance film thickness even more. In our screening, the solution presenting the highest viscosity ($20 mPa \cdot s$) has a final thickness of 200 nm and pyrolysis is completely homogeneous.

Still, a major effect on film thickness enhancement is observed by solvent formulation when increasing the proportion of methanol. Despite the fact that methanol viscosity is lower than for propionic acid, a trend that can also be observed in Figure 3.1(b), solution contact angle on LAO substrate increase very significantly with methanol, leading to much thicker films. For instance, methanol based solution which contact angle is 20°, produce 300 nm thick films, while propionic based solution that have complete wettability results on only 70 nm thick films.

Thus, the effect of wettability seems to have a major contribution than viscosity. Being surface tension very similar for both solvents (25.5mN/m for the propionic acid and 24.5 for methanol), we attribute the differences on wettability to distinct interaction between the functional groups and the substrate surface.

Another effect to take into account is the low volatility of methanol (boiling point of 64.7°C), that may cause the evaporative drying step to happen very early during spinning. That may result in the coating being dried before the peak speed is reached, thus creating thicker than expected films [120].

Composition effects in terms of coating homogeneity are presented in Figure 3.2. Thickness have been adjusted to 200nm after growth by diluting proportionally the salts concentration of solutions named as:

Solution	Propionic acid- Methanol(%)	TEA ($\%_{v/v}$)	Concentration (M)
D	0	5	1.5
B	50	5	1
E	88	0	0.75

Table 3.2: Solutions nomenclature

While solutions with $< 50\%$ of methanol are completely homogeneous, Solution E with a 88% presents stritations already observed just after deposition. These defects are thickness ondulations along the fluid flow direction during

Figure 3.2: 2.5x optical microscope images of pyrolyzed films deposited with solutions containing different proportions of methanol-propionic acid, being the methanol content 88%, 50% and 0%

spinning. This phenomena is also accounted to fast evaporation processes. It leads to unbalanced capillary forces that develops into thicker or thinner areas depending on local surface tension deviations [67].

Although epitaxial films of YBCO presenting very good properties ($3MA/cm^2$, T-route) were obtained using Solution E, homogeneity problems in pyrolysis are a source of irreproducible results and thus solutions containing a maximum of 50% of methanol have mostly been used for the films growth.

Ink Jet Printed solutions

IJP allows deposition of huge controlled volumes, leading to thicker films with a single deposition. Moreover, it is appropriate for continuous long length production or patterning.

Preliminary studies on solution design and pyrolysis of big deposited volumes were carried out with collaboration with B. Villarejo within our group. As a result, it has been demonstrated that modified fluorine free solutions (table 3.1)) are also compatible to deposition by IJP, although much effort has to be done in order to control decomposition without cracking or buckling phenomena.

Extensive studies are presented elsewhere [102] compared with IJP deposition of low fluorine solutions. Both solutions only differ from the Yttrium salt, being trifluoroacetate instead of acetate. This leads to a content of 20% in F. The lack of trifluoroacetate molecules produces films more susceptible to stress release, leading to higher probabilities to buckle.

The use of coordinating ligands such us diethanolamine (DEA) showed me-

chanical resistance improvement towards obtaining bucking and cracks as seen in Figure 3.3. A $0.5\%_{v/v}$ of DEA in a 0.5%M YBCO solution, corresponds to a 10.4% mol DEA/mol M(Y+Ba+Cu).

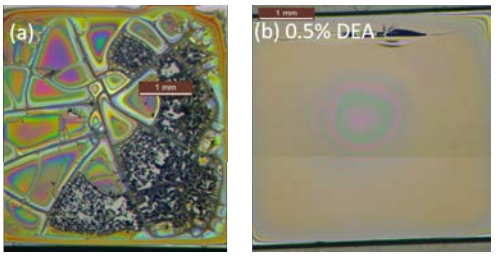

Figure 3.3: 2.5x optical microscope images of pyrolyzed films deposited by Ink Jet printing deposition. Solution are composed by propionic acid solvent and (b) has a 0.5% of DEA. Nominal thickness is 500nm. Films were heated respectively at a rate of 0.2°C/min and 1°C/min at the critical temperature range of 160-300°C. Figure (a) presents cracks and delamination, while film of Figure (b) is homogeneous

In situ monitoring by optical microscope during film annealing show buckling is produced between 180-240°C, while cracks appear from 240°C to 300°C. A comparison of buckling in films with and without additive is illustrated in Figure 3.4. Decomposition of the film without additive arise irreversible buckling starting at 180°C and delamination at $\sim$ 210°C. In contrast, stress release of the sample containing DEA ligands generates smaller buckling at 180°C, that is reversed after 10°C, leading to a homogeneous film at 200°C.

Still, reproducibility is low due to inhomogeneities caused by liquid movement during deposition. It leads to solution accumulations causing thicker areas where cracks are prone to form. Thus, more effort has to be done on fixing the liquid, for example by UV curing.

3.1.2 Porosity modulation

Solvent removal from the forming gels of particles has to go through several structural rearrangement processes while a large fraction of volume is eliminated. As a result, internal stress is generated and a from of relaxation is

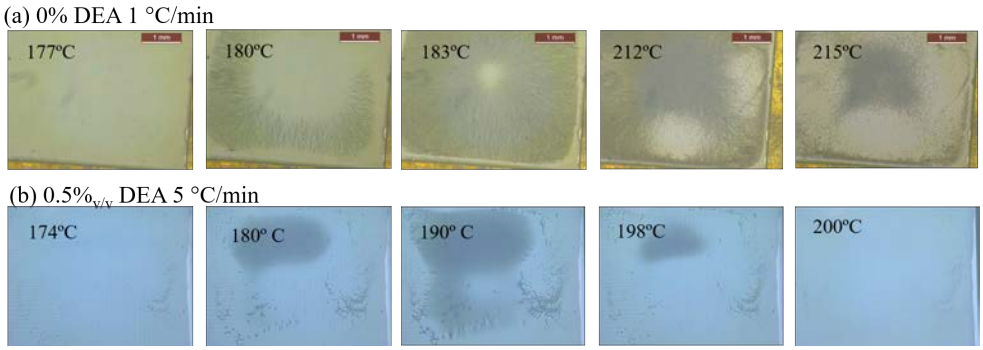

Figure 3.4: *In situ* OM images of film surface during annealing under humid O_2 of IJ printed solutions. Film (a) shows irreversible buckling, while film (b) containing an additional 0.05%$_{v/v}$ DEA shows reversible buckling. Solutions are 0.5M of acetate salts dissolved in propionic acid. Annealing speed is (a) 1°C/min and (b)5°C/min

through the formation of pores [73].

Modulation of porosity is a very interesting tool to modify materials properties. For instance, highly porous MOD derived films are appealing for sensing, optics and microelectronics applications, presenting a higher accessible surface area, low dielectric constant and tuning refractive index [121]. In contrast, residual pores reduce properties of ferroelectric thin films or photovoltaic solar cells [67]. In YBCO films, pores are defects that preclude current percolation [122]. However, very closed porosity may difficult gases release hindering further decomposition reactions.

Thus, control of porosity is an advantage in solution processing, but it still remains a challenge. We show here how solution composition affected film density after calcination.

Cross sections performed by SEM-FIB of multideposited pyrolyzed films (Fig 3.5) reveal distinct microstructure depending on initial precursor solution solvent. The film coated with methanol based solution (Solution E) presents much higher porosity than the coating prepared with full propionic acid solvent (Solution D). Pore densities have been calculated from image analysis and vary

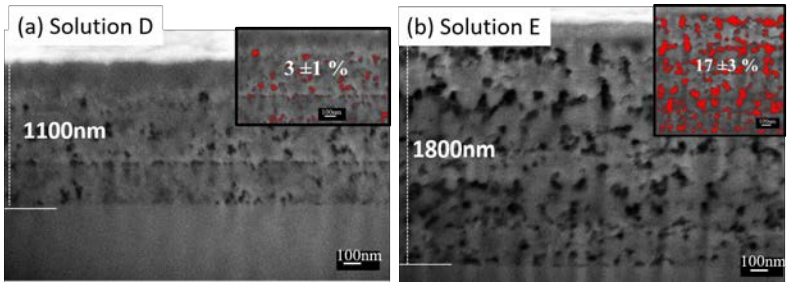

Figure 3.5: SEM of cross sections performed by focused ion beam (FIB) of fired films to 500°C composed by 3 multidepositions of (a) Solution D (100% propionic acid and $5\%_{v/v}$ of TEA) and (b)Solution E (12:88 propionic acid:methanol mixture). Both solution concentrations are 1.5M of total cations. At top of each, pores are coloured in red for quantification analysis

from $3 \pm 1\%$ for the film produced with Solution D (a) to $17 \pm 3\%$ for Solution E (b).

Since pyrolysis have been performed following the same thermal profiles, pores generation has to be triggered already during solvent evaporation. A process that is very fast for methanol, which boiling point is 64.7°C. Quick gas release leaves big void spaces that will be kept along the pyrolysis process. In contrast, the use of higher boiling point solvents (propionic acid, bp. 141.2°C) enables slower evaporation rate, producing smaller and less quantity of pores behind.

As discussed in the previous section, film E is also much thicker than film D. However, this difference can not only be accounted to higher presence of these empty spaces, since for a 1800nm thick film only 306 nm are the 17% accounted to pores. Thus, the amount of material subtracting porosity is still larger for the methanol based solution (1490nm) than the propionic acid (1060nm). The additional difference then lies on the amount of material retained at the deposition step.

Additionally, the fact that every coating is followed by a calcination to 300°C, results in the firsts layers being exposed to multiple thermal treatments in which compaction is produced. This results in a porosity gradient, being the layers close to the interface more dense than the lasts. Also, regions of increased pore

density are those between layers interface. This segregation between layers is another source that produces current blocking and final properties deterioration in TFA films [123]

However, there are no evidences that this is a problematic for liquid growth, since such interfaces are not observed in YBCO film after conversion (see Fig.5.32 in section 5.4.1.1). In this case, the diffusion of the liquid intermediate heals porosity completely.

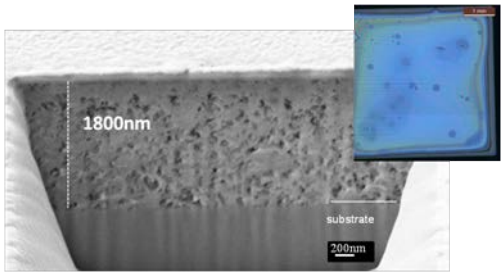

Figure 3.6: SEM-FIB cross section and corresponding surface optical image of a pyrolyzed film of a single deposition by IJP with a solution of propionic acid and $0.5\%_{v/v}$ of DEA. Thermal profile is performed at 5°C/min until 160°C; 3°C /min until 300°, 5°C/min to 500°C under flow of wet oxygen

On the other hand, a single deposition performed by means of IJP about the same thickness (1800 nm after pyrolysis, leading to $\sim 800nm$ after growth), is shown in Figure 3.6. This film was produced with a propionic acid based solution with addition of $0.05\%_{v/v}$ DEA.

The layer presents an homogeneous distribution of small pores. Calculated pore density is 5%±2%, similar to values obtained for the spin coated layers of the same solvent. This fact confirms that low and homogeneous porosity can be kept during decomposition of big volumes if only one annealing process is performed.

3.2 Pyrolysis process of fluorine free solutions

Pyrolysis of the ternary mixture containing Y,Ba,Cu-propionates is investigated in this section. There are some studies reporting on the individual

decomposition of Y, Ba and Cu propionates in powder [67]. However, several differences can exist on thin films and depending on the atmospheric conditions [124]. Additionally, no detailed study exists on the pyrolysis process of this ternary mixture in thin films. In this section we provide insight into this matter.

The final phases of calcined films at 500°C with the standard process are identified by XRD. Figure 3.7 discloses the presence of completely polycrystalline phases, identified as CuO, Y_2O_3 and $BaCO_3$ orthorhombic (natural witherite).

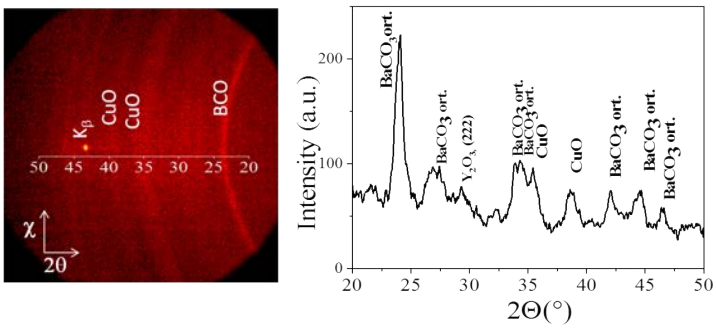

Figure 3.7: At left, two-dimensional XRD pattern of a pyrolyzed film deposited with solution 5B under the standard thermal treatment. At right, grazing incidence XRD of the same film.

CuO is the expected phase formed after the corresponding carboxylate decomposition under wet oxygen, while other processing atmospheres could lead to other copper oxidation states [92, 125].

In contrast, the formation of barium carbonate is preferred over its oxide at atmospheric pressures. The low charge density of this alkaline earth element maintains carbonate polarity low, making it a very stable compound.

Pyrolysis of rare earth propionates may lead to the formation of oxycarbonates (YO_2CO_3) between 300 to 400°C [67, 126]. However, yttrium oxycarbonate in thin films under humid oxygen decomposes to yttrium oxide (Y_2O_3) at around 440°C [124].

3.2.1 *In situ* FTIR analysis on metal propionates decomposition

To disclose the decomposition pathway of the ternary mixture in films, we have performed *in situ* Fourier Transform Infrared spectroscopy measurements during the pyrolysis process. The study has been conducted in collaboration with M. Kreuzer, at MIRAS beamline in Alba synchroton facilities, but working with conventional IR light.

Solutions previously coated on LAO substrates and dried to 70°C are heated to 500°C under gas flow while FTIR spectra is continuously acquired. More details on the methodology and data analysis can be found in section 2.2.6.

The series of spectra during annealing to 500°C at 10 °C/min in wet oxygen are plotted in Figure 3.8.

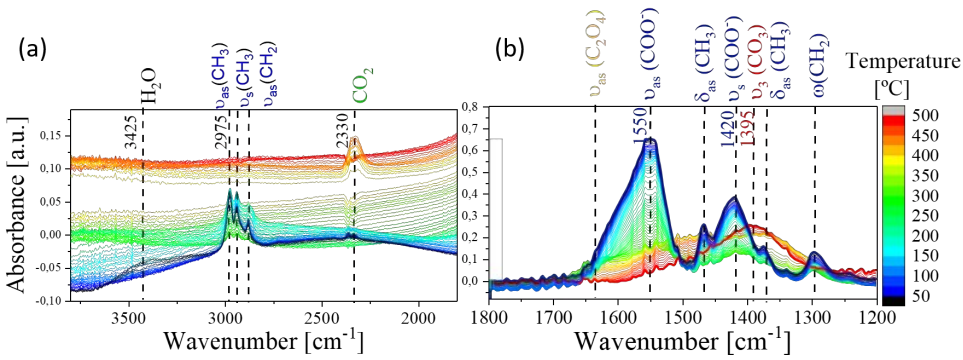

Figure 3.8: *In situ* FTIR for pyrolysis process performed with a heating rate of 10 °C/min to 500°C in wet oxygen ($0.12L \cdot min^{-1}$). Raw data is shown for the high wavenumber range (a), while substrate subtraction has been necessary for low wavenumbers (b) (See section 2.2.6). Precursor solution solvent is composed by propionic acid-methanol (50%).

Chemical composition of as deposited solutions

From the initial FTIR spectrum at 30°C (Fig.3.8, black lines), absorption bands corresponding to propionate groups can be observed. Absorption peaks at 2978, 2944 and 2876 cm^{-1} are accounted to propionate $(C-H)$ vibrations, while the more intense bands at the region $1300-1560cm^{-1}$ are characteristic of the carboxylic group (COO^{-}). Since the starting precursor salts are acetates, this indicates that these have been displaced before annealing. This fact has also been demonstrated with NMR measurements for low fluorine solutions [80].

Additionally, the coordination mode of the ligand can be deduced from carboxylate peaks position. The separation between antisymmetric (ν_{as}) and symmetric (ν_s) stretch absorptions of (COO^{-}) discerns the coordination type within unidentate bridging $(\Delta\nu = 350-500cm^{-1})$, bidentate bridging $(\Delta\nu = 150-180cm^{-1})$ and bidentate chelating $(\Delta\nu = 60-100cm^{-1})$ [127, 128]. In our system, $\nu_{as}(COO^{-})$ absorbs at 1550 cm^{-1} and $\nu_s(COO^{-})$ at 1420 cm^{-1}. Then, a separation of $\Delta\mu = 130cm^{-1}$ denotes that propionate group acts as bidentate, by either as a chelating ligand of one cation or bridging between two. Bidentate structures are advantageous since coordination of water molecules is hindered, making solutions more robust.

Apart from that, no presence of uncoordinated solvents is detected at any temperature. (C=O) band of free carboxylic acid would absorb at 1742 cm^{-1} and ν(C-OH) from methanol would give a broad band at 3500-5640 cm^{-1}. Since the film was previously dried at 70°C after deposition, solvent release would occur below this temperature. Additionally, only a broad band centred at 3433 cm^{-1} is observed and it is related to water, probably absorbed after deposition and drying. This band disappears during thermal treatment before 50°C, indicating that dehydratation occurs at very low temperature and this fact confirms that water molecules are not coordinated.

Decomposition of Y, Ba, Cu propionates mixture

The evolution of FTIR spectra (Fig.3.8) along the thermal treatment shows a progressive diminution of the absorption peaks related to propionate groups, with no changes on wavelengths, indicating that the metallic coordination is not modified.

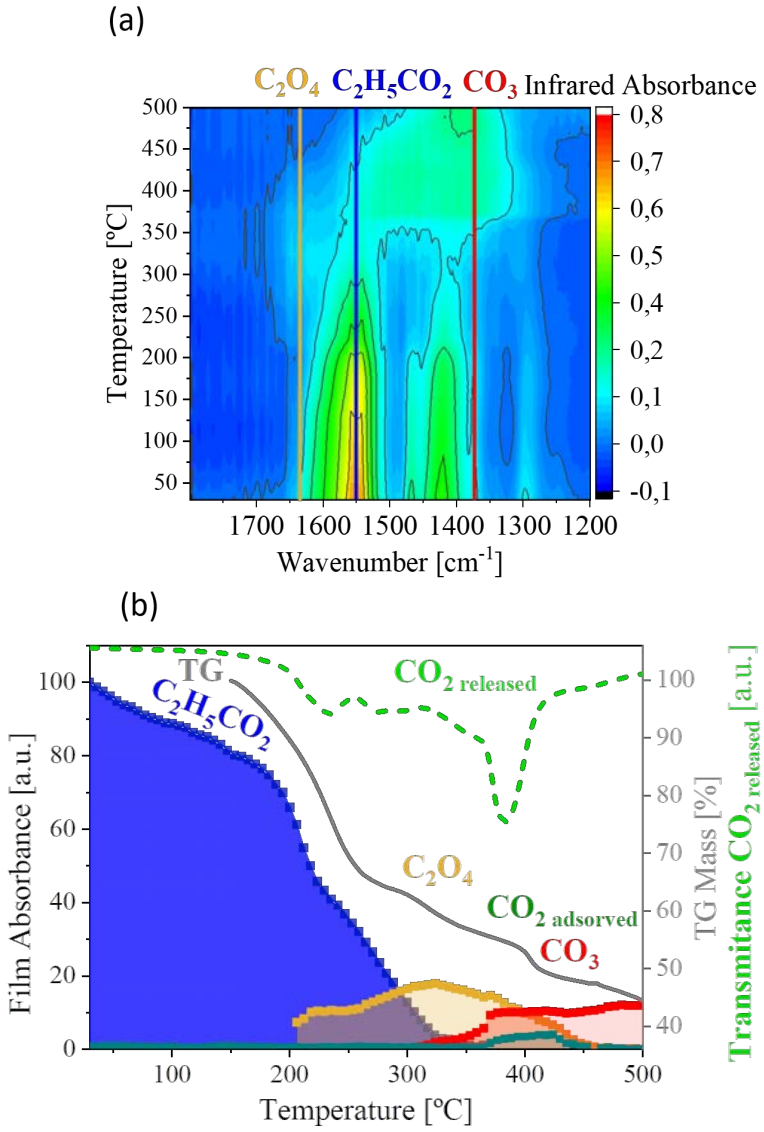

Figure 3.9: (a) Contour map of time resolved FTIR spectra from figure 3.8. Main wavelengths corresponding to propionate (1550 cm^{-1}), oxalate (1635 cm^{-1}) and carbonate (1373 cm^{-1}) groups are indicated and intensities are plotted vs temperature at graph (b). Absorbance has been normalized to theoretical mass of organic matter. Is added for comparison a TG analysis at 5°C/min and TG-FTIR absorbance of CO_2 gas evolved of the same coated solution

Analogous to the propionate groups decomposition, volatile species are evolved and new chemical bonds are formed. The same data is represented in a contour map in Figure 3.9(a). New absorption peaks appearing between 1350-1550 cm^{-1} correspond to carbonate [116]. Additionally, a band shoulder at 1600-1650 cm^{-1} is identified between 200-450°C. This band coincide with asymmetric stretching mode of (C-O) bonds in oxalate groups. These two compounds are linked to the barium propionate decomposition.

A peculiar feature is the significant increase of the CO_2 band centered at 2330cm^{-1} in Figure 3.8(a). It is observed between the range of 374-440°C, accompanied by a change in total absorption baseline for all the samples analysed except for the single substrate. We dismiss atmospheric contamination since evolving gases are rapidly released in continuous flow and no other volatiles are detected. Thus, this band can be attributed to physisorbed CO_2 at the film surface. Physisorbed gases present similar vibrational frequencies to the molecules in gas state since their structure is preserved and the interaction with the material surface is limited to van der Waals forces [129].

No other peaks in the absorbing region of ionic hydroxides (3500-370 cm^{-1}) are detected. While the ones corresponding to oxides are out of measure range due to substrate strong absorption below 1200 cm^{-1}. Oxycarbonate main bands are overlapped with the carbonate, making impossible to discern if yttrium oxycarbonate exists in the ternary mixture as intermediate once barium carbonate is already formed.

The evolution of the organic species along the thermal treatment is depicted in Figure 3.9(b). This data together with TG-FTIR of CO_2 release, disclose the reaction mechanisms during pyrolysis. Different steps can be discerned:

- **100-200°C**
  Up to 200°C no CO_2 is evolved and any new organic molecule is detected in the film. However, propionate signal decreases a $\sim 30\%$. All of which, the hydrolysis to form the corresponding oxides could take place for $Cu(EtCO_2)_2$ and $Y(EtCO_2)_3$:

$$Cu(CH_3CH_2COO)_2 \xrightarrow{H_2O} CuO + 2\,CH_3CH_2COOH\uparrow \tag{3.2}$$

$$2\,Y(CH_3CH_2COO)_3 \xrightarrow{H_2O} Y_2O_3 + 6\,CH_3CH_2COOH\uparrow \tag{3.3}$$

Concerning 1:2:3 cations stoichiometry, complete decomposition of $Cu(EtCO_2)_2$ would correspond to a 46.15% of the total propionates, while $Y(EtCO_2)_3$ represents a 23%. Therefore, it is clear that conversion of these two compounds is not completed by hydrolysis at this stage.

- **200-300°C**
  At this thermal region propionates signal diminish faster until their total decomposition at around 300°C. This process is now accompanied with small quantities of CO_2 gas evolved. It could be accounted to oxidation processes for the remaining $Cu(EtCO_2)_2$ or $Y(EtCO_2)_3$:

$$Cu(CH_3CH_2COO)_2 \longrightarrow CuO + CH_3CH_2COOH\uparrow + CH_3COH\uparrow + CO_2\uparrow \tag{3.4}$$

$$2\,Y(CH_3CH_2COO)_3 \longrightarrow Y_2O_2CO_3 + 3\,CH_3CH_2COOH\uparrow + 3\,CH_3COH\uparrow + 2\,CO_2\uparrow \longrightarrow Y_2O_3 + CO_2\uparrow \tag{3.5}$$

Unfortunately, oxycarbonate IR peaks are overlapped in this experiment with either barium carbonate signal or proportionate groups adsorption bands. So, it is not possible to confirm if yttrium oxycarbonate is formed as intermediate in the ternary mixture. Despite that, it has never been identified by XRD of quenched samples.

On the other hand, at this stage is the formation of barium oxalate and consequently the temperature range that $Ba(EtCO_2)_2$ decomposes. Its formation is completed at 320°C.

$$Ba(CH_3CH_2COO)_2 \xrightarrow{H_2O} 2\,CH_3CH_2COOH\uparrow + Ba(HCO_3)_2 \xrightarrow{H_2O} BaC_2O_4 \tag{3.6}$$

- **300-500°C**
  At higher temperatures barium oxalate is converted to carbonate. In

oxidizing atmosphere, the proposed reaction is shown in Scheme 3.7:

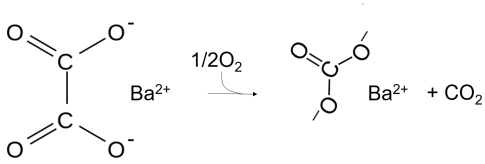

(3.7)

Parallel to carbonate formation, big quantities of CO_2 are evolved and some amount remains physisorbed at the film surface. Physical adsorption of CO_2 on oxide film surfaces is observed frequently on surface catalysis studies at temperatures above 250°C [130, 131].

At higher temperatures, surface carbon dioxide can either be desorbed or oxidated to carbonate, remaining at the film surface. Since no extra gas release coincides with the drop of CO_2 FTIR band in the film, but the CO_3 signal keeps increasing, the second hypothesis is more plausible. Additionally, this reaction is specially favoured with metal oxide layers, which are providers of oxygen atoms.

Studies on the pyrolysis of separated precursor salts are performed by S.Rasi at Universitat de Girona. The thermal behaviour under wet oxygen conditions was revealed of each salt and is summarized in Figure 3.10 for comparison with our data.

The results on separate salts match very well with the mechanisms described for the ternary mixture. It becomes clear that $Cu(EtCO_2)_2$ decomposition takes place first, mainly through hydrolysis until 200°C and completed at 230°C. In the mixture, a reduction on propionate vanishing slope coincides with this temperature.

From the information provided from the individual salts analyses (Fig. 3.10), $Y(EtCO_2)_3$ oxidation is happening above 200°C, yttrium oxycarbonate mass is reached at 350°C and yttrium oxide at 500°C, if completed. Barium oxalate mass is also reach at 350°C, and formation of carbonate proceeds to 500°C. In agreement, we can see at the mixed salts analysis that at 350°C propionate bands have disappeared but there is still a 12% left to decompose.

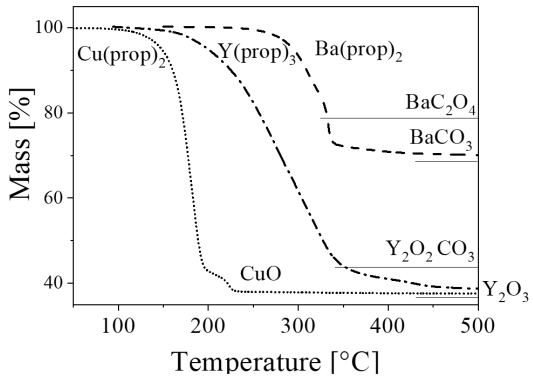

Figure 3.10: TGA performed under flowing humid oxygen of 2μ m thick films of individual Y, Ba and Cu propionates. Heating is performed at 5°C /min

Additionally, at this temperature oxalate absorption is at its maximum intensity and carbonate groups start to rise, also in accordance.

Influence of gas atmosphere

The importance of surrounding gas atmosphere on metal carboxylates decomposition is remarkable since different conditions can lead to distinct final products, reaction paths or microstructure. We have performed the previously shown experiments under wet flow of oxygen, but one could think on tuning it to avoid the formation of barium carbonate.

For instance, it is known that the use of more inert atmospheres (i.e., nitrogen) reduces partially the CuO to Cu_2O, which coarsens and produces phase segregation in the final YBCO film [132]. On the other hand, reported barium oxalate decomposition mechanisms under inert gas involve the formation of elemental carbon [133]:

$$BaC_2O_4 \longrightarrow CO + BaCO_3 \tag{3.8}$$

$$CO \longrightarrow 1/2C + 1/2CO_2 \tag{3.9}$$

The presence of elemental carbon in final YBCO film would be detrimental for superconducting properties, or it can act as reducing agent, modifying metals

oxidation state if it is oxidized to CO or CO_2. As a result, the use of oxidizing atmosphere still seems the most advantageous prospect.

Regarding humidity, one film was heated under dry oxygen in order to investigate its effects. The *in situ* FTIR map (Fig.3.11(a)) shows the same intermediates evolving at similar temperatures as on the coating processed under wet oxygen. XRD performed after film annealing also reveals the same final phases (CuO, $BaCO_3$ and Y_2O_3).

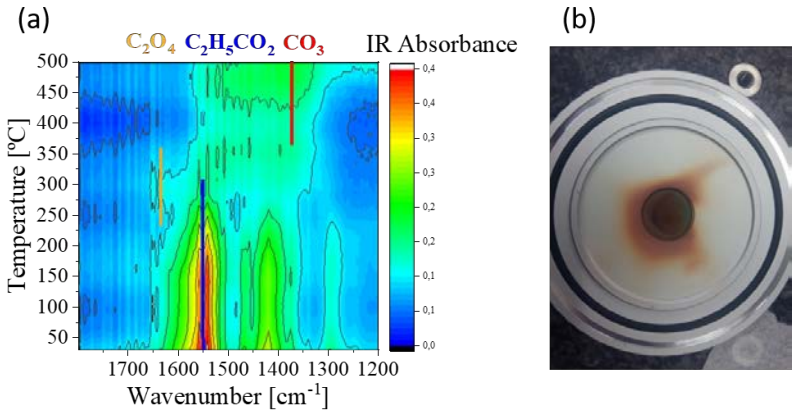

Figure 3.11: (a)Contour map of time resolved FTIR spectra of a film processed under dry oxygen. (b) Image of sublimated copper deposited on heater cover after film processing

Nevertheless, dramatic copper propionate sublimation is happening while heating without the presence of water vapour. Cu was deposited on the heater cover, which can be well observed in Figure 3.11(b). Thus, hydro-stabilization of the salt using humid gas, proposed by McIntryre *et al* for copper trifluoroacetate [104], seems also necessary for copper propionate.

Heating ramp effect

In thermal decompositions, the heating rates can also play an important role on the decomposition temperatures. In Figure 3.12 are compared samples pyrolyzed at rates of 2, 10 and 50°C/min in wet oxygen. Film thickness is

higher for the sample heated at the slowest rate, being 400nm instead of 270nm (thickness after YBCO growth).

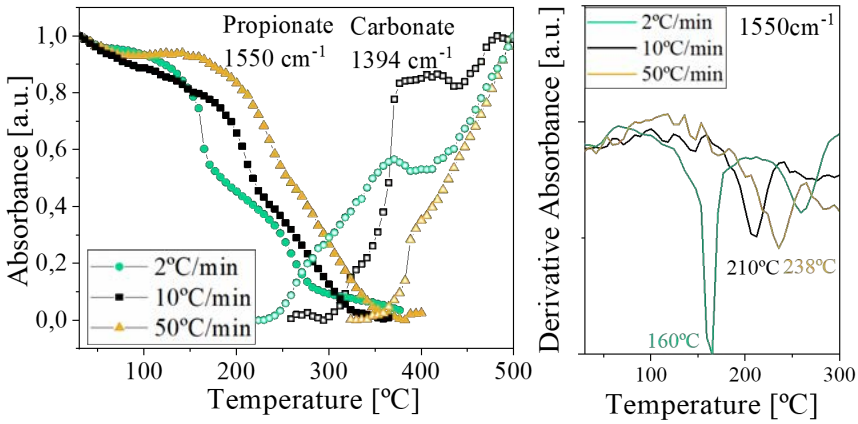

Figure 3.12: At left, evolution of propionate and carbonate normalized absorption bands for heating rates of 2, 10 and 50°C/min. At right, the corresponding dTG help on comparing temperatures. Sample at 2°C/min has been deposited by IJP, while the others by SC with solution 5B

Despite thickness differences, heating rate is shown to have a more important effect on propionates thermal evolution. Propionates decomposition undergoes to lower temperatures as annealing speed is decreased. The main propionate mass loss is taking place at 160°C, 210°C and 238°C for heating rates of 2, 10 and 50°C/min.

The delay on propionates decomposition triggers barium carbonate formation towards higher temperatures. Onset T are 250°C, 310°C and 365°C, respectively. However, complete conversion is not attained until 500°C in all cases.

Consequently, heating speed optimization can be a powerful tool to tune decomposition temperatures with the objective of controlling stress release, specially for thick films pyrolysis very susceptible to buckle or crack.

3.2.2 Nanostructure of calcinated films

Films microstructure is analysed by means of Transmission Electron Microscopy (TEM) analyses. TEM measurements were performed by Dr. R.Guzman. Figure 3.13a presents a cross-section of a pyrolyzed film under wet oxygen using the standard thermal treatment to 500°C, of a spin coated Solution B.

Y, Ba, and Cu EDX maps (Fig. 3.13b) reveal a solid solution composed by nanocrystalline intermediates. Grain sizes for CuO and $BaCO_3$ are around 10-30nm, while Y_2O_3 particles remain as small as 5-7nm.

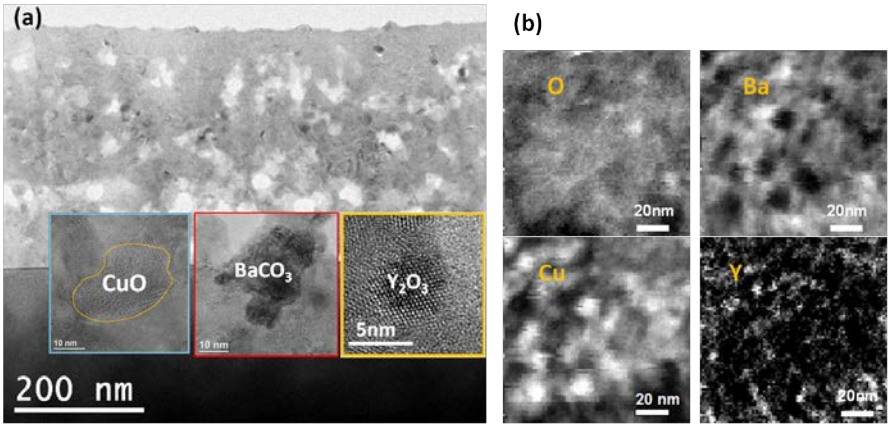

Figure 3.13: Pyrolyzed film with the standard treatment and Solution B. A solid solution composed by the different nanocrystalline phases is observed. (a)BF-HRTEM Bright-field High Resolution TEM The distinct phases are identified in the insets. (b)Energy-dispersive X-ray spectroscopy (EDX) to identify O, Ba, Cu and Y elements

However, EELS elemental mapping along the full film thickness (Fig. 3.14) discloses different concentration gradient perpendicular to the interface for Ba and Cu. Thus, sole phase segregation exists, giving place to Ba-rich and Cu-rich regions on the top and in the middle of the film.

Particularly, Cu map shows larger nanoparticle sizes near the interface. This stronger tendency of CuO to coarsen may preclude a homogeneous distribution of the metals along the layer. As a consequence, local defects in stoichiometry

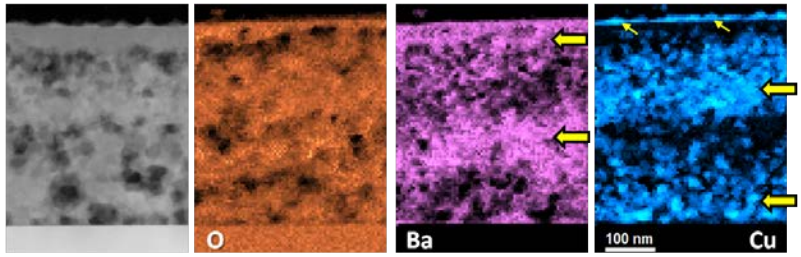

Figure 3.14: EELS elemental maps of Y, Ba and Cu of a pyrolyzed 250nm thick film deposited with solution 5B under standard thermal treatment

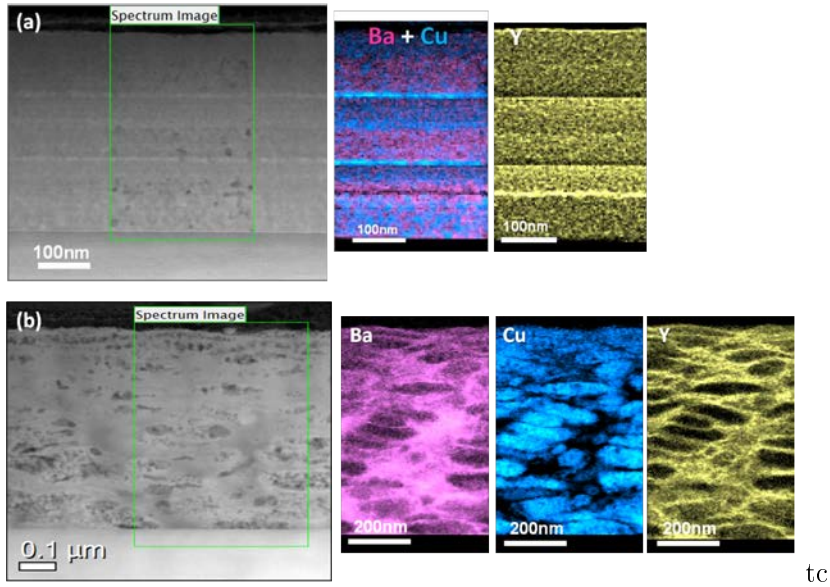

tc

Figure 3.15: Pyrolyzed films produced by (a) 3 layers subsequently spin coated and heated at 5°C/min and (b) single deposition of Ink Jet printed film heated at 0.5°C/min

can affect the reaction pathway. Additionally, bigger particles undergo lower reaction kinetics.

It is well known that coarsening is enhanced when particles are exposed to high temperatures and for long times. This effect is observed in the pyroly-

sis of thick films (∼400nm after growth). Either because multi-spin coatings undergo through several annealings, or because Ink Jet printed films pyrolysis are performed through longer thermal treatments to avoid buckling or cracks derived from compaction stress release of high volumes.

For instance, CuO particles as big as 200 nm are observed in a IJ printed film heated at a rate of 0.5°C/min to 500°C (Fig.3.15). Note that standard pyrolysis is carried out at velocities between 3-5 °C/min.

In contrast, the multideposited film present reasonable particles size, yet the interlayers are composed by strongly segregated CuO phase.

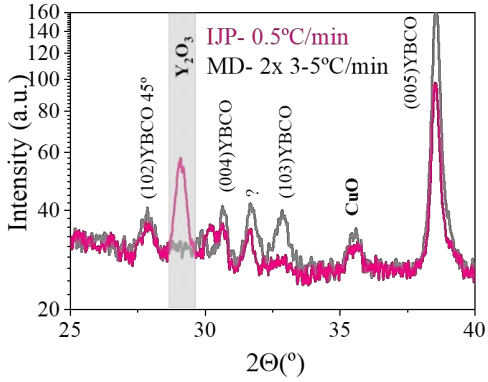

Figure 3.16: Integrated 2D−XRD diffraction patterns show secondary phases in grown YBCO thick films at 840°C by low P_{O_2} route. One has been deposited by IJP and pyrolyzed at 0.5°C/min (purple) and the other is composed by 2 spin coating depositions with standard pyrolysis (grey)

As a result, after YBCO growth, the IJP film presents big amounts of unreacted Y_2O_3 as compared to the multideposited film (Fig.3.16). Still, c-axis YBCO nucleation is not fully achieved in any of the cases.

Thus, it has become clear that the achievement of a fast pyrolysis process is a requirement, not only for time economisation but also for avoiding particles coarsening.

Therefore, one of the main challenges for the growth of thick films with TLAG is the control of the pyrolysis step to obtain homogeneous films at relatively

high rates. Up to now, either a multi-deposition process or one using Ink Jet printing methodology are feasible approaches with distinct advantages and inconveniences. This work is currently continued by group co-workers.

3.3 Water content influence

It is known for trifluoroacetate non-aqueous precursor solutions that water content alters not only homogeneity of pyrolyzed films but it is also detrimental on the final superconducting properties of an epitaxial YBCO layer [134, 107]. For the TLAG process, even more dramatic effects derived from wet solutions have been observed, hindering nucleation of c-axis YBCO and suppressing superconductivity. It seems therefore that although water is evaporated below 100°C, it must modify the reactions pathway to an extent that affects YBCO microstructure.

In this section the influence of water is analysed for fluorine free solutions and the TLAG process.

3.3.1 Solution water content control

Special control is taken during solution preparation and deposition to minimize environmental water contamination and keep initial water content below 2 wt% (see section 2.1). However, since our solutions are composed by carboxylic acid and alcohol, esterification can occur being water a product of the following reaction:

$$CH_3CH_2COOH + CH_3OH \longrightarrow CH_3COOCH_3 + H_2O \tag{3.10}$$

The water content evolution of our stored solutions was measured by means of Karl Fisher titration [107] at different days after preparation (Fig.3.17). The increase on the water content only for the solution having the mixture of both solvents (Solution B), confirms that it is a consequence of esterification reaction between the solvents. Hydratation rate depends on the initial concentration, from 0.07 to 0.16$\%_{wt}$/day.

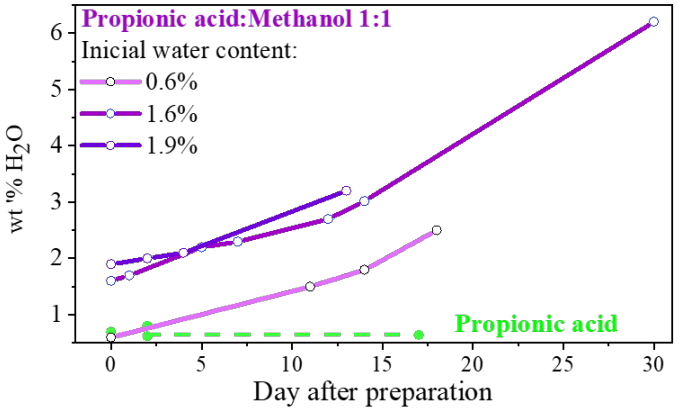

Figure 3.17: Evolution of solution water content measured by means of Karl Fisher titration at different days after solution preparation

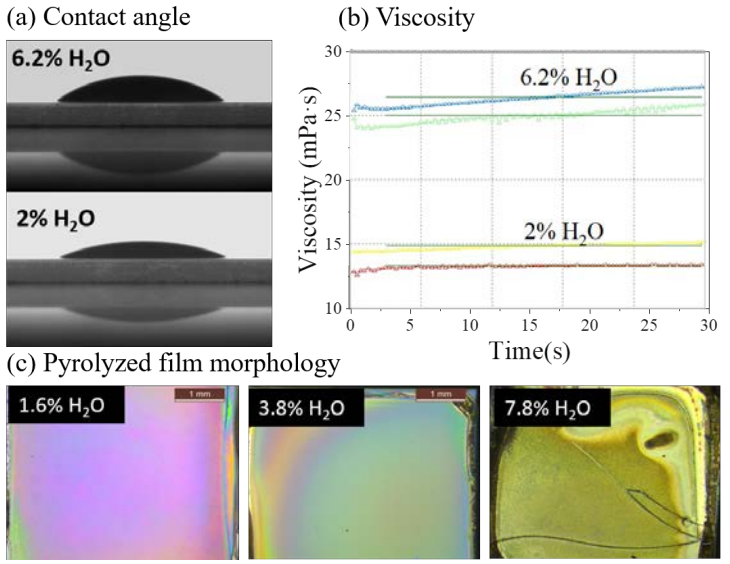

Figure 3.18: Rheological properties depending on solution water content: (a)Drop images for contact angle calculation, (b) Viscosity and (c)MO images of pyrolyzed films

Subsequently, we have observed that solution rheological properties are altered with the increase of water (Fig.3.18). Viscosity increases from 14±1 to 25±1 mPa·s when water content boosts from 2 to 6.2$\%_{wt}$ in Solution B. The same trend is observed for the contact angle, increasing from 27±5°to 34±2°, respectively. The two factors have an influence on film morphology after firing, leading to cracked films when values are high.

Still, film morphology alterations does not explain YBCO properties suppression for solution water contents in the range of 3%, which are still homogeneous.

Hence, a strategy has been used in order to work with solutions composed by the mixed solvents and ensure a robust methodology. A double concentrated "mother solution" is prepared with all the salts dissolved in propionic acid, and methanol is only added before deposition. "Mother solution" is stable up to one month.

In other works, new methodologies were investigated to reduce water content of initial solutions or obtain stable solutions with other solvents, such us butanol [135].

3.3.2 Thermal decomposition of hydrated solutions

To prove insight into the role of water in the decomposition pathway, thermogravimetric analysis have been performed for Solution B, containing a 2.5 and 6.3 $\%_wt$ of initial water (Fig.3.19).

We observe that decomposition of the more hydrated solution undergoes to lower temperatures since completed conversion is attained at 400°C, 100°C before. All of which suggests that water molecules contribute on fastening organic decomposition rate, and thus pyrolysis kinetics. Coordinated water molecules would favour hydrolysis reactions. Since hydrolysis take place at low temperatures, that would explain the bigger mass decrease at this early stage as compared to the dry solution.

Copper propionate is decomposed through hydrolysis already in dry solutions. Thus, being yttium propionate also the most hydrophilic salt, it is reasonable to think that the main difference between humid and dry solutions thermal pathway lies on yttrium propionate decomposition. In the first case, through hydrolysis at low temperatures (Eq.3.3), while in the second case oxidations

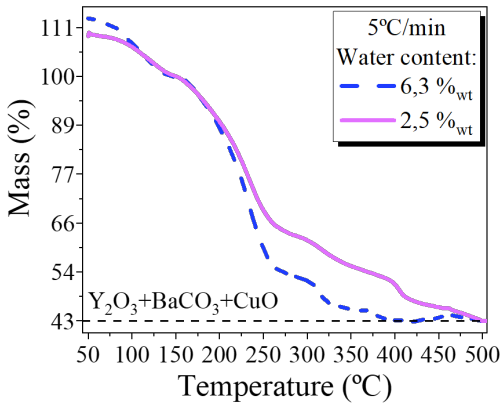

Figure 3.19: TGA of solutions B with 5.4% and 2.5% of water content

are more favourable (Eq.3.5).

A surprising result is the impact on the nature of intermediates formed after pyrolysis. X-ray diffraction patterns of pyrolyzed films at 500°C which solutions contain low and high amounts of water are presented in Figure 3.20(a).

Barium carbonate crystal structure is normally orthorhombic before its transition into the hexagonal phase at 810°C. On the contrary, when using hydrated solutions, the monoclinic form of barium carbonate is produced during pyrolysis. Monoclinic $BaCO_3$ is a metastable phase that at ambient conditions is transformed into orthorhombic within 4 days [136].

This simple structure change has dramatic effects on the formation of YBCO films. $BaCO_3$ decomposition has been observed to be delayed when processing pyrolyzed films containing monoclinic phase rather than orthorhombic. An *in situ* XRD experiment (Fig. 3.20(b)) revealed that before reacting at high temperatures, the monoclinic form is previously converted to the orthorhombic phase. A process that consumes time and some retained barium carbonate can be observed at the YBCO processed films.

Second, TEM images of a pyrolyzed film from a high water content solution is presented in Figure 3.21. It depicts an important presence of copper metallic in some areas of the film, others with CuO or Cu free regions. The presence

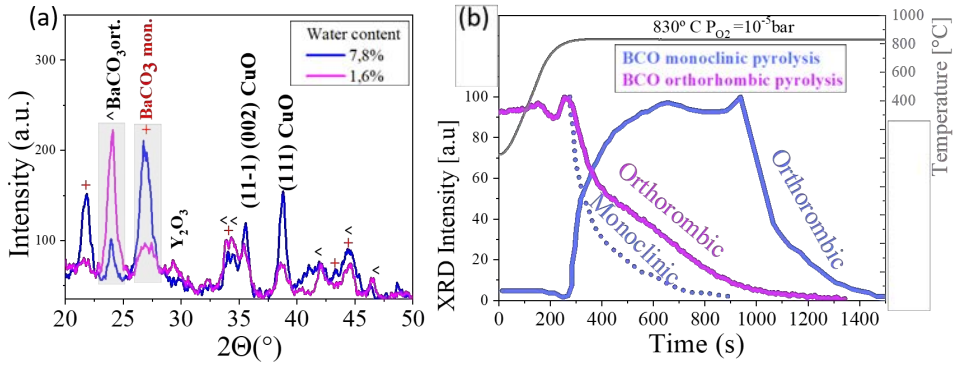

Figure 3.20: (a)Grazing Incidence-XRD of pyrolyzed films at 500°C with Solution B containing 1.6 and 7.8%$_wt$ of H_2O. (b) $BaCO_3$ evolution during film growth by *in situ*XRD. Pyrolyzed films contain monoclinic (blue) or orthorhombic (purple) $BaCO_3$. The transition to orthorhombic is observed from the monoclinic $BaCO_3$ before decomposition

of elementary copper suggests that Cu^{2+} has been reduced during pyrolysis by other oxidative processes.

When a film containing elementary copper is heated to higher temperatures for YBCO synthesis, Cu(0) has to be oxidized to Cu(II) before forming YBCO.

3.3.3 Morphologycal and physical consequences

From TEM analysis, grain sizes have been inferred and are plotted in Figure 3.22 for comparison. The resulting nanoparticles size of Y_2O_3 increases to 20±10nm for a pyrolysis performed from a wet solution. Cu particles size is very inhomogeneous as can be seen in the previous image. Cu particles of wet solution coating can reach 45nm size. This coarsening can be a direct consequence of the metal salts earlier decomposition in wet solutions, leading to a premature formation of crystals that grow along the thermal treatment.

Another effect is illustrated by FIB images in Figure 3.23. A strong decrease of porosity is observed when increasing water content in solutions, specially at

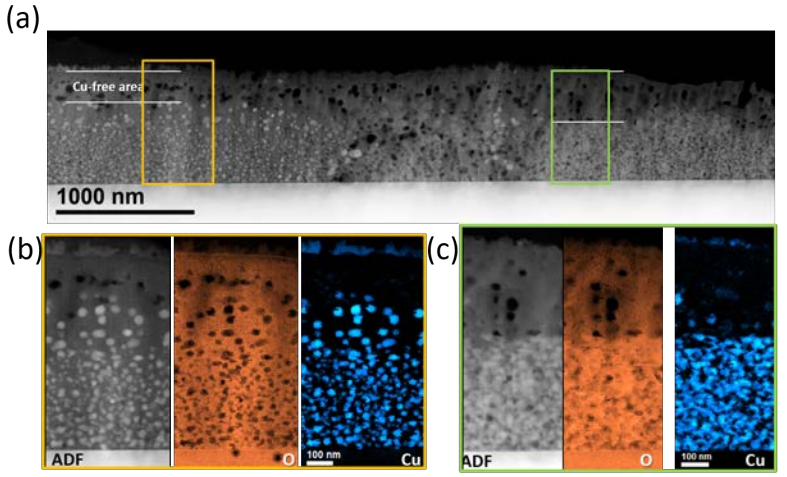

Figure 3.21: (a) STEM of film processed with a solution containing 7.8% of water, showing areas with distinct microstructure: (b) composed by reduced Cu(0) and (c) with CuO

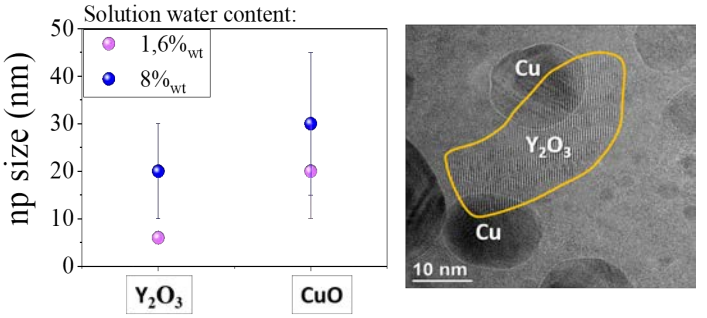

Figure 3.22: At left, plotted grain sizes inferred from TEM images of Y_2O_3 and Cu or CuO nanoparticles for pyrolyzed films from solution B containing 1.6 or 8% of water. At right, TEM image of a big Y_2O_3 particle and elementary Cu

the regions containing elemental copper. Porosity drops form a $\sim$ 5% (a) to $\sim$ 1% (b,c) when water content of solution is increased from 1.6%$_{wt}$ to 3.8%$_{wt}$. Since wet solutions decompose before, compaction can take place during the

remaining thermal profile. Even though low porosity is preferred in the resulting films, extreme density may hinder gas release necessary to eliminate $BaCO_3$.

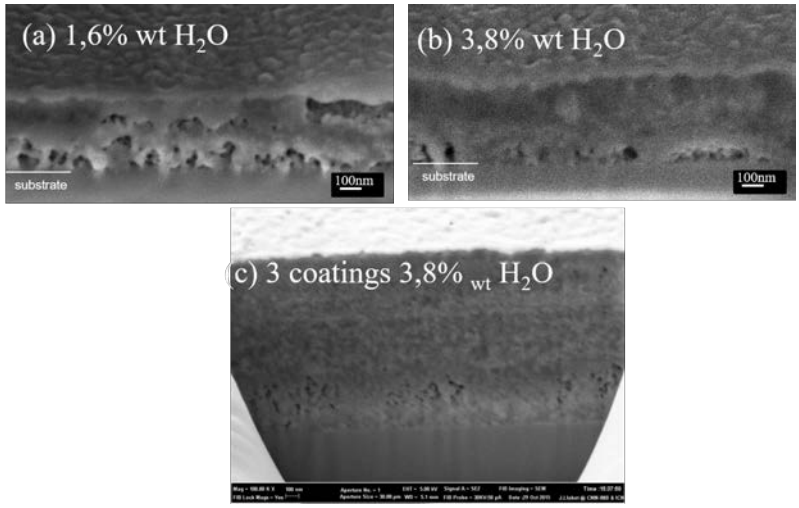

Figure 3.23: SEM-FIB cross sections of (a) films quenched at 670°C which precursor solution contained 1.6 and 3.8% of water and (b) 3 coatings pyrolysis of Solution B with 3.8% of water, shows very low porosity

In Figure 3.24(a) water content is correlated to film performance, in terms of critical current (J_c) of the resulting superconducting YBCO phase. A dramatic suppression of properties is observed when water exceeds $2.3\%_{wt}$. For a 1.5 M (total cation concentration) solution, it corresponds to a 0.85 water to metal cations molar ratio. Thus, for higher water contents, there is more than one water molecule for each cation salt in the precursor solution. Two dimensional XRD results (Fig.3.24(b)) confirm the properties reduction to be a direct consequence of the lost of epitaxy on the resulting YBCO phase.

The cause lies on the combination of all the previously described effects when using wet solutions. $BaCO_3$ transition from monoclinic to orthorhombic and elemental Cu oxidation are extra reactions that drag out the solid reactions pathway. In addition, extreme low porosity and big particles size can hamper reaction kinetics. Altogether alter optimum conditions for c-axis YBCO nucleation, resulting in polycrystalline films.

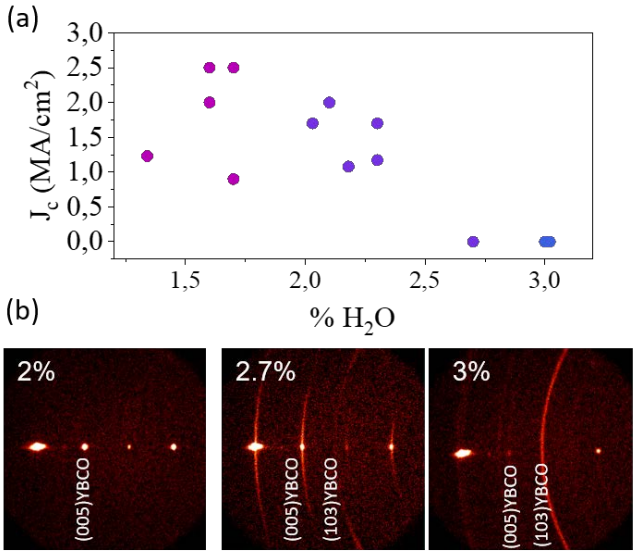

Figure 3.24: (a) Critical current densities (J_c, 77K, self field) of YBCO films diminish with the increase of precursor Solution B water content. In (b), 2D-XRD show polycrystalline YBCO fraction increases for higher solution humidity

3.4 $BaCO_3$ elimination reactions

We have described in the previous section that pyrolysis of the deposited cations carboxylate salts results in a film composed by nanocrystalline $BaCO_3$, CuO and Y_2O_3 phases.

In this section, we study the solid reactions that take place at high temperatures for the pyrolysis phases conversion into to the transient liquid precursor ($BaCuO_2$ + CuO).

This involves the carbonate elimination from $BaCO_3$, a highly stable compound that does not decompose until 1350°C. If carbon is retained in the resulting YBCO film grain boundaries, superconducting critical temperature T_c is decreased [84]. This fact has limited the use of fluorine free solutions for YBCO growth until the present.

Thus, special emphasis has to be taken on the understanding of $BaCO_3$ elimi-

nation, as well as on strategies to enhance this reaction towards the achievement of very fast processing rates.

Typical decomposition for alkaline-earth (A) carbonates is described by the following reaction 3.11:

$$ACO_3(s) \rightleftarrows AO(s) + CO_2(g) \tag{3.11}$$

However, with the presence of a transition metal oxide reagent (M), a mixed oxide can be formed through reaction:

$$xACO_3(s) + yM_zO(s) \rightleftarrows A_xM_{yz}O_{x+y}(s) + xCO_2(g) \tag{3.12}$$

For our pyrolyzed precursor films, being composed by barium carbonate and copper oxide, the formation of the mixed oxide is thermodynamically more stable than the BaO simple oxide, thus reaction 3.12 is more favourable than reaction 3.11 [137]. Therefore, barium carbonate decomposition during thermal treatment at high temperatures towards YBCO formation will be driven by reaction 3.13:

$$BaCO_3(s) + Cu_zO(s) \rightleftarrows BaCu_zO_2(s) + CO_2(g) \tag{3.13}$$

The temperature at which this reaction occurs (T_D) is much lower than the decomposition of single barium carbonate [138, 92]. For instance, Vermier *et al.* performed TGA-DTA measurements in Ar and air which show that $BaCO_3$ powder is stable until 900°C, while the powder binary mixture $2BaCO_3/3CuO$ presents the first mass loss already at 700°C. In other words, CuO can act as a reactant for the $BaCO_3$ elimination.

Furthermore, an additional and very significant drop on decomposition temperatures is occurring at lower P_{O_2} and for thin films as compared to powders, due to grain size effects [139] (T_D= 620°C under N_2 for 500-800 nm, [85] or 640 °C under 200 ppm O_2). Other examples can be found in literature showing a drastic temperature reduction for decarbonatation of $BaCO_3$ nanoparticles in solutions with other metal oxides [140].

These facts reveal the possibility to complete barium carbonate at much lower temperatures than expected in the YBCO ternary system, and specially for thin layers.

However, still many information is missing in order to understand the kinetics and thermodynamics of this intermediate reaction that is also rate limiting for the overall process, as well as avoiding carbonate retention in the thickest films. In this section, we will put insight into this matter.

3.4.1 *In situ* XRD studies of the conversion process

The evolution of pyrolyzed films ($BaCO_3$, CuO, Y_2O_3) to high temperatures, is followed via *in situ*, time-resolved X-ray diffraction performed with synchrotron radiation at SOLEIL synchrotron.

Previously pyrolyzed films on STO substrates were heated inside a chamber under the chosen P_{O_2} conditions. A maximum of 5°C/s heating rate could be used with the provided heater stage at the moment. Films thicknesses are ~400 nm after total conversion.

Intensity was continuously acquired with a 2D detector at acquisition times of 0.2-0.5 s (Fig.3.25a). The detector area covers all the 2θ range where the main species diffract. More details on the methodology and data analysis can be found in section 2.2.5.

The different species can be distinguished by the X-ray diffraction intensity of their main reflections (Fig.3.25b). After data treatment, the main reflections intensities are normalized by their maximum intensity, which we approximate proportional to the phase molar amount. Then, the normalized intensities plotted with temperature or time show the phases evolution along the thermal treatment.

The solid reactions involving $BaCO_3$ and CuO at a heating rate of 0.4°C/s and under different P_{O_2} conditions are disclosed hereunder.

$P_{O_2} = 10^{-3}$ bar

At first, the results at a P_{O_2} of 10^{-3} bar are presented in Figure 3.26.

Two solution compositions have been explored: (i)the YBCO stoichiometric content corresponds to a cations ratio of Y:2Ba:3Cu and (ii)the Y:2Ba:4.66Cu ratio has a Cu excess respect to YBCO. It corresponds to a BaO:CuO relation of 3:7, matching the point of a eutectic reaction in this binary system (see Fig.

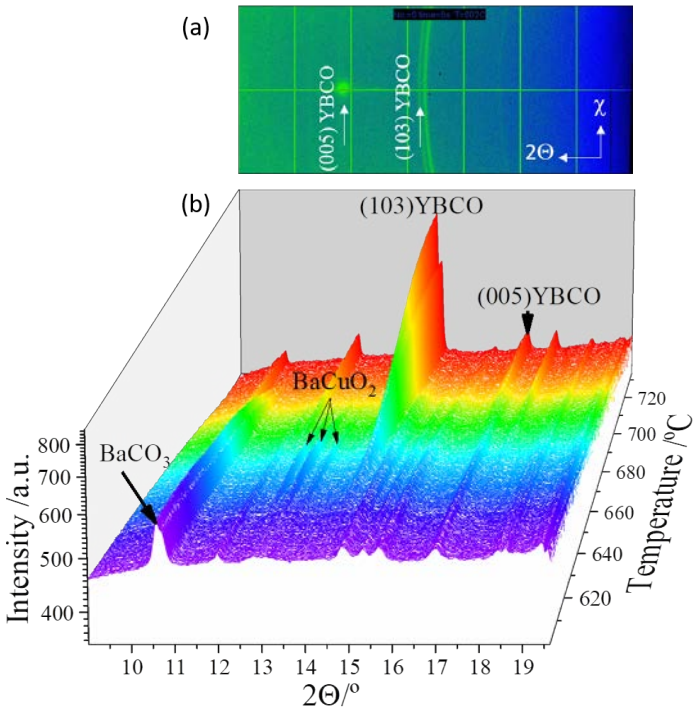

Figure 3.25: Typical data acquired with *in situ* XRD with acquisition points every 0.2 s, during sample growth at 0.4°c/s under 10^{-3} bar O_2 and the 2:3 liquid. (a) 2D detector image (b)Each 2D image acquired along the process is integrated in χ and represented with temperature

3.27).

For the (i) stoichiometric composition, we observe that $BaCO_3$ reacts with CuO to form $BaCuO_2$:

$$2\,BaCO_3(s) + 3\,CuO\,(s) \longrightarrow 2\,BaCuO_2(s) + CuO\,(s) + 2\,CO_2(g) \qquad (3.14)$$

Hence, the solid $BaCuO_2$ XRD intensity evolves in parallel to $BaCO_3$ and CuO decrease, until 650°C. Then, $BaCuO_2$ signal diminishes while YBCO starts growing. When $BaCuO_2$ has completely vanished, YBCO is fully grown.

However, when YBCO starts nucleating, still a 70% of $BaCO_3$ precursor remains and continues decomposing even after $BaCuO_2$ has disappeared. It is

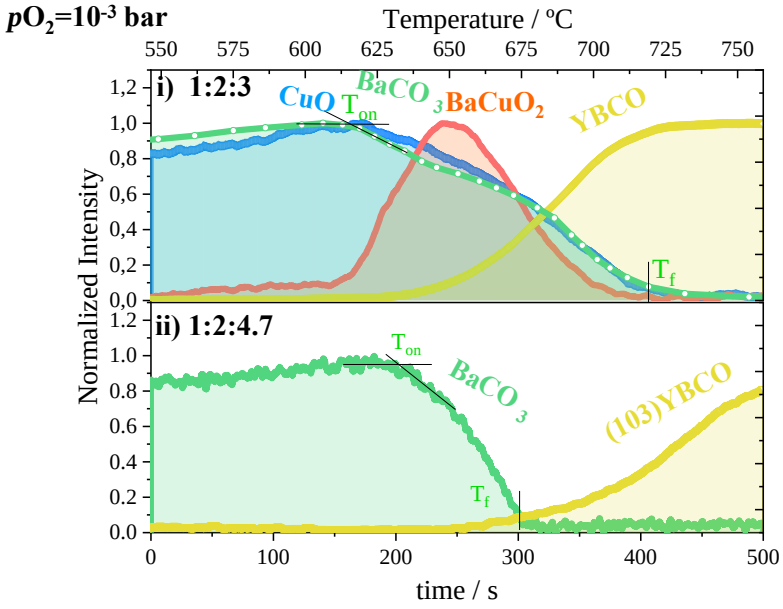

Figure 3.26: Time-resolved evolution of pyrolysis solid species is represented for 400nm films treated at 0.4°C/s under atmosphere of $P_{O_2} = 10^{-3} bar$, $P_{tot} = 1 bar$. Y:Ba:Cu ratios are (i)1:2:3 and (ii)1:2:4.7

evident therefore that reaction 3.14 for the elimination of $BaCO_3$ is the slowest and rate limiting process.

In contrast, during the decomposition path of the (ii) Cu excess composition, the $BaCuO_2$ solid phase is not observed. Additionally, reaction onset temperature is the same for both compositions (630°C±5), but barium carbonate is vanished at (i)720°C and (ii)670°C. For a heating rate of 0.4°C/s, these values correspond to significantly different total reaction times: 220 s and 90 s respectively.

Still, this range of temperatures is very low, which indicates the feasibility of completing decarbonation towards the growth of $YBa_2Cu_3O_{7-\delta}$.

Furthermore, the fact that the crystalline precursor phases have disappeared at the onset of YBCO growth, is a direct poof of the presence of a liquid

intermediate. The existence of a liquid phase under these conditions is not expected in the ternary phase diagram for $YBa_2Cu_3O_{7-\delta}$. However, the binary system of BaO-CuO, without Y_2O_3, presents an eutectic reaction that involves the formation of a melt [85, 141, 142] (Fig.3.27 and section 4.3).

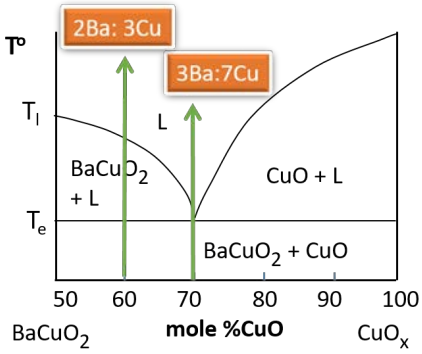

Figure 3.27: Scheme of the $BaCuO_2$-CuO phase diagram [141]. Indicated in arrows the paths followed for each composition

Consequently, the following reaction is proposed, where the intermediate liquid phase subsequently transforms to YBCO by reaction with Y_2O_3:

$$2\,BaCO_3(s) + 4.7\,CuO(s) + \frac{1}{2}\,Y_2O_3(s) \longrightarrow [Ba{-}Cu{-}O](l) + \frac{1}{2}\,Y_2O_3(s) + 2\,CO_2\uparrow \longrightarrow YBa_2Cu_3O_{7-\delta}(s) + 1.7\,CuO(s) \quad (3.15)$$

These reactions, involving the formation of this transient liquid and subsequent fast YBCO growth, are investigated in more detail in section 3.4.2 and in the next chapters.

Hence, the binary diagram represented in Figure 3.27 also explains why the $BaCuO_2$ solid phase is only a solid intermediate when using the stoichiometric composition (2Ba:3Cu). For this composition, $BaCuO_2$ will gradually disappear at expenses of a liquid phase when passing the liquidus line (T_l), at higher temperatures.

This fact also confirms that the 1:2:4.7 composition matches the eutectic point of the binary phase diagram, where no solid species are expected after the

eutectic temperature (T_e). Therefore, the mixed oxide would only be observed if $BaCO_3$ is decomposed before T_e, but it has not been detected so far.

In this case, the $BaCO_3$ elimination reaction leads directly to the liquid phase (equation 3.15), while YBCO is formed with a certain delay due to the induction period for nucleation (See Chapter 4.1.2).

$P_{O_2} = 10^{-5}$ bar

Now, the $BaCO_3$ conversion to high temperatures is observed under reduced P_{O_2}, at 10^{-5} bar and for the 1:2:4.7 composition in Figure 3.28.

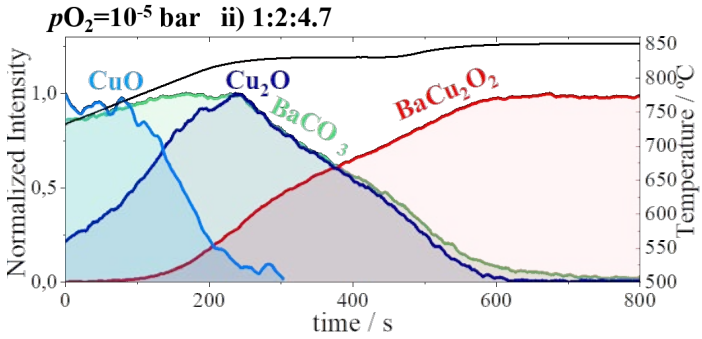

Figure 3.28: Time-resolved evolution of pyrolysis solid species is at 0.4°C/s under $P_{O_2} = 10^{-5}$ bar, $P_{tot} = 5 \cdot 10^{-5} bar$. Solution Y:Ba:Cu ratio is 1:2:4.7.

From *in situ* XRD experiments we observe that $BaCO_3$ removal is driven by its reaction with Cu_2O to form $BaCu_2O_2$, which are the stable phases at this P_{O_2} [143]:

$$2\,CuO \longleftrightarrow Cu_2O \tag{3.16}$$

$$BaCO_3(s) + Cu_2O(s) \longleftrightarrow BaCu_2O_2(s) + CO_2(g) \tag{3.17}$$

First, CuO reduction takes place. It starts around 770°C and proceeds to 820°C, at a rate of 0.5°C/s. Note that equilibrium CuO/Cu_2O should take place at lower temperatures according to the phase diagram (650°C at $P_{O_2} =$

10^{-5}bar) [143] (Fig. 3.30). Once completed, $BaCO_3$ reaction takes place along the thermal treatment dwell at 830°C for, at least, 700 s.

In this case, the formation of $YBa_2Cu_3O_{7-\delta}$ is not observed, as expected in this P_{O_2} range, which is below the phase stability zone [144]. Furthermore, any evidence of a liquid intermediate is found in this case.

Consequently, $BaCO_3$ conversion may be disclosed from YBCO formation and it leads to solid $BaCu_2O_2$ under low enough P_{O_2}.

Thermodynamic considerations

The evolution of barium carbonate from *in situ* XRD experiments is compared in Figure 3.29 for treatments under a wider range of P_{O_2} and heating speed conditions (0.4 and 5°C/s) with the 3Ba:7Cu composition.

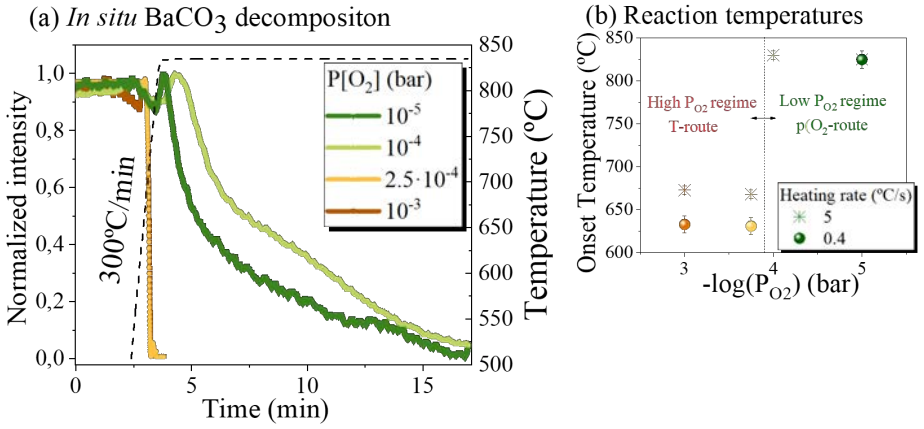

Figure 3.29: (a) $BaCO_3$ evolution along thermal treatment at 5°C/s under different P_{O_2}. (b) Reaction onset temperatures. Cations composition is 1Y:2Ba:4.66Cu and film thickness 400nm. Total pressures are 1 bar for $P_{O_2} \geq 2.510^{-4}$bar and $P_{tot} = P_{O_2} \cdot 5$ for the lower pressures.

Two differentiate regimes can be deduced from $BaCO_3$ elimination reaction rates.

At high P_{O_2}, conversion is as fast as 10s at a heating speed of 5°C/s and starts at low temperatures (~670°C). Such an increased reaction rate could be driven by the presence of the liquid intermediate. The formation of a liquid during the decomposition of solid reactants (e.g. melting, eutectic formation or dissolution), often involves an increased rate as a consequence of the relaxation of the bonding forces responsible for lattice stabilization [145].

In contrast, for P_{O_2} lower than 10^{-4}bar, reactions take more than 10 min and are initiated at higher temperatures (≥820°C). Based on the previous section analysis, $BaCO_3$ elimination at low P_{O_2} originates solid $BaCu_2O_2$. The absence of a liquid phase under these conditions could explain the longer reaction rates to higher temperatures.

We can dismiss the effect of total pressure. First, one would expect that lower total pressure would in any case enhance the reaction by easing CO_2 expel. Second, other experiments performed in the laboratory furnaces at the low P_{O_2} regime, but working at a higher total pressure, ($3 \cdot 10^{-3}$ bar, N_2) show very similar reaction temperatures and speed.

The information concerning these reactions is represented in a T-P_{O_2} phase diagram in Figure 3.30. The crossover for the stability of both mixed oxides (orange line) is reproduced from Lindemer *et al* [143]. It corresponds to equilibrium:

$$BaCuO_2 + CuO \rightleftarrows BaCu_2O_2 + \frac{1}{2}O_2(g) \tag{3.18}$$

Hence, reaction 3.14 to form $BaCuO_2$ and a liquid intermediate takes place when raising temperature at $P_{O_2} \geq 2.5 \cdot 10^{-4}$ bar, above the $BaCuO_2/BaCu_2O_2$ equilibrium. Instead, the reaction 3.17 to form $BaCu_2O_2$ proceeds at $10^{-4} \geq P_{O_2} \geq 10^{-5}$ bar, below the equilibrium line. Thus, $BaCuO_2/BaCu_2O_2$ equilibrium determines the stability zone of each mixed oxide and consequently which reaction for the decomposition of $BaCO_3$ takes place.

This fact can lead to two distinct paths to convert the pyrolysis precursors to the final $YBa_2Cu_3O_{7-\delta}$ phase. One proceeds towards a direct temperature rise at constant $P_{O_2} \geq 2.5 \cdot 10^{-4}$ bar, named Temperature-route (T-route, red arrow in Fig.3.30). For the other, $BaCO_3$ reaction take place while heating at $10^{-4} \geq P_{O_2} \geq 10^{-5}$ bar and under the YBCO stability line conditions, to form solid $BaCu_2O_2$. Then, the growth region for $YBa_2Cu_3O_{7-\delta}$ may be achieved by

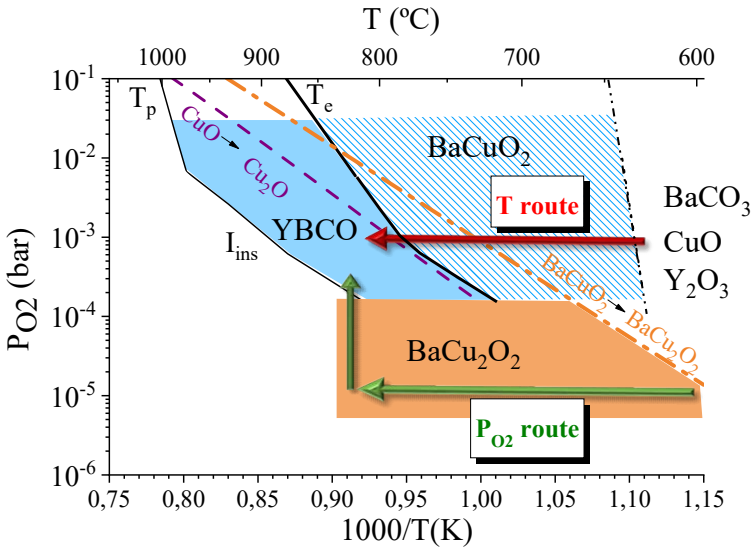

Figure 3.30: Deduced $T - P(O_2)$ phase diagram from the pyrolysis films evolution. The blue regions indicate the area where YBCO is grown from a liquid intermediate. Equilibrium lines are represented for the Ba-Cu-O eutectic reaction (T_e) [115], the YBCO peritectic temperature (T_p) [146, 147], the instability YBCO line (I_{ins}) [148] and the $CuO - Cu_2O$ and $BaCuO_2$-$BaCu_2O_2$ equilibriums [143]. The T-route and P_{O_2}-routes are indicated in arrows

a P_{O_2} step at constant temperature. This approach will be named the oxygen partial pressure route (P_{O_2}-route, green arrow in Fig.3.30).

The heating rate effect is also distinct for the two P_{O_2} ranges. At the high P_{O_2} regime, reaction temperature depends on the annealing speed, being lower for slower heating rates (Fig.3.29b). For instance, reaction onset temperatures are displaced from 620°C to 670 °C for heating speeds of 0.4 and 5°C/s. This is then a thermally activated process following an Arrhenius behaviour.

In contrast, for the explored region at $P_{O_2} \leq 2.5 \cdot 10^{-4}$ bar, a reduction in heating speed showed no decrease of T_{onset}. A constant reaction rate suggests it is controlled by solid interface kinetics.

Lindemer *et al* [144] found the same trend in VTGA analysis of the ternary

mixture, but no explanation was given to the nature of the conversion process at low P_{O_2}.

Therefore, each reaction is controlled by particular kinetic and thermodynamic factors. Metal carbonate decompositions are both endothermic and reversible, which makes it difficult to study kinetics in non isothermal experiments.

The net rate in reversible reactions is the difference between the forward and backward rates. It can be expressed as [149]:

$$\frac{d[P]}{dt} = k^*([R_1][R_2] - \frac{[P]}{K}) \tag{3.19}$$

where k^* is the kinetic constant for the forward reaction and depends on the enthalpy and entropy difference. K is the equilibrium constant, in other words, it implies how far from equilibrium is the system. R_x and P are the reactants and products of the reaction, respectively.

For the studied case, the equilibrium constants are dependent on CO_2(g) since activity of solid and liquid species is constant:

$$K = \frac{[BaCu_zO_2] \cdot P_{CO_2}}{[BaCO_3][Cu_zO]} = P_{CO_2} \tag{3.20}$$

Values reported for the formation of $BaCuO_2$ and $BaCu_2O_2$ were given by Lindemer *et al* [143]:

$BaCuO_2$: K=log(P[CO2][MPa]) = 6.655 - 11144/T

$BaCu_2O_2$: K=log(P[CO2][MPa]) = 6.121 - 10285/T

Equilibrium P[CO_2] is lower for the reaction leading to $BaCu_2O_2$. Looking at equation 3.20, a smaller K results in less quantity of products in equilibrium conditions. In other words, the equilibrium is more displaced to the left in comparison to the other reaction. As a consequence, taking equation 3.19, a lower K results in lower reaction rate for the products formation. This means it is more difficult to decompose the $BaCO_3$ at the low P_{O_2} regime.

3.4.2 Towards ultrafast conversion rates in T-route

We have deduced from previous experiments that reaction kinetics at $P_{O_2} > 2.5 \cdot 10^{-4}$ bar depends on the heating ramp, P_{O_2} and precursor composition.

Additionally, the reactions that follow, including the formation of a liquid, can modify $BaCO_3$ elimination rate as well. In this section, we investigate in more detail these processing parameters with the objective of achieving fast conversion rates.

3.4.2.1 P_{O_2} effect

The experiments shown in the preceding section in Fig. 3.29 with the Y:2Ba:4.7Cu solution are performed only at P_{O_2}=10^{-3} and $2.5{\cdot}10^{-4}$ bar. Thus, the change in P_{O_2} is too small to find relevant differences. In order to disclose the effect of P_{O_2} in the T-route conditions, we performed *in situ* XRD isothermal treatments under P_{O_2} of 10^{-2} bar and $2.5 \cdot 10^{-4}$ bar, using the stoichiometric solution composition. The phases evolution along the thermal profile are depicted in Figure 3.31.

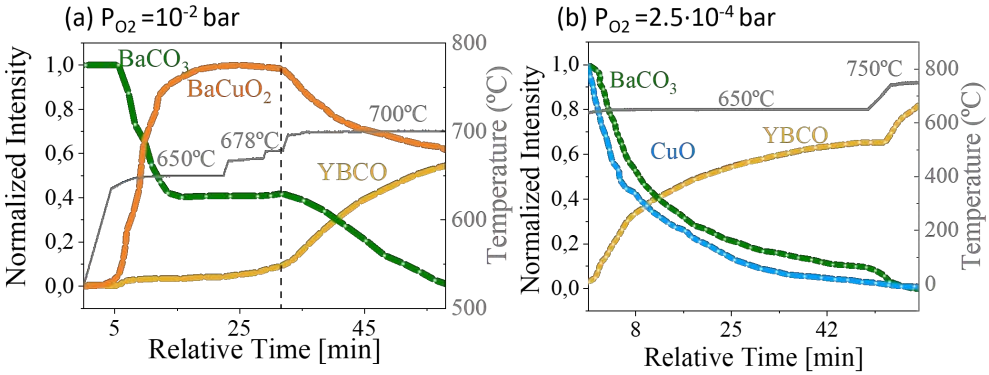

Figure 3.31: Phases evolution on pyrolyzed films of the stoichiometric solution during heat treatment and *in situ* XRD. Multiple thermal isotherms have been applied to study reaction kinetics and are plotted in grey. P_{O_2} conditions are (a)10^{-2} bar, (b)$2.5 \cdot 10^{-4}$ bar

$BaCO_3$ conversion reaction already starts during the isotherm at 650°C, in both cases. Since CO_2 release is limited by the system configuration, equilib-

rium conditions are reached.

At this step, for a P_{O_2}=10^{-2} bar, the equilibrium is achieved at 650°C with a 60% of $BaCO_3$ conversion. The products are $BaCuO_2$ and only 3% of YBCO. Complete carbonate elimination is attained at higher temperatures (678°C), together with the $BaCuO_2$ solid disappearance to form YBCO.

In contrast, when P_{O_2}=$2.5 \cdot 10^{-4}$ bar, the equilibrium entails a 90% $BaCO_3$ conversion at 650°C. The remaining 10% is transformed at 750°C, when equilibrium has been displaced to higher temperatures. YBCO is observed as the only product already at 650°C, without detecting the solid $BaCuO_2$ phase. We deduce that $BaCuO_2$ is not observed because it is in the liquid state and rapidly transforms to YBCO.

These results indicate that for the same temperature, at lower P_{O_2} the system is closer to the liquid and YBCO stability region. This is in agreement with the eutectic temperature downward tendency with the decrease of P_{O_2} (see T_e line in Fig. 3.30).

All of which evince the effects of subsequent liquid reactions on improving the reaction yield, at least when there is low CO_2 expel. Thus, when $BaCO_3$ conversion takes place at the area where product $BaCuO_2$ + CuO becomes liquid, reaction kinetics are enhanced and $BaCO_3$ can undergo complete transformation at lower temperatures.

The same effect explains the sooner $BaCO_3$ transformation previously observed in Fig. 3.26 for the eutectic composition (Y:2Ba:4.7Cu) in comparison to the stoichiometric (Y:2Ba:3Cu), since $BaCuO_2$(s) intermediate is avoided in the first case.

This idea becomes clear once representing the species evolution in the $T-P_{O_2}$ phase diagram in Figure 3.32a for the stoichiometric solution. This diagram has been build using data extracted from *in situ* XRD experiments at heating rates of 0.4°C/s under different P_{O_2}.

First, $BaCO_3$ conversion starts at higher temperatures (T_{on}) at higher P_{O_2}. T_{on} raise from 630°C at $2.5 \cdot 10^{-4}, 10^{-3}$ bar to 660°C at 10^{-2} bar.

Apart from that, at more elevated pressures, reaction proceeds along a larger temperature range due to the presence of intermediate $BaCuO_2$ solid. Consequently, conversion rate is slower. As a result, transformation time drops from

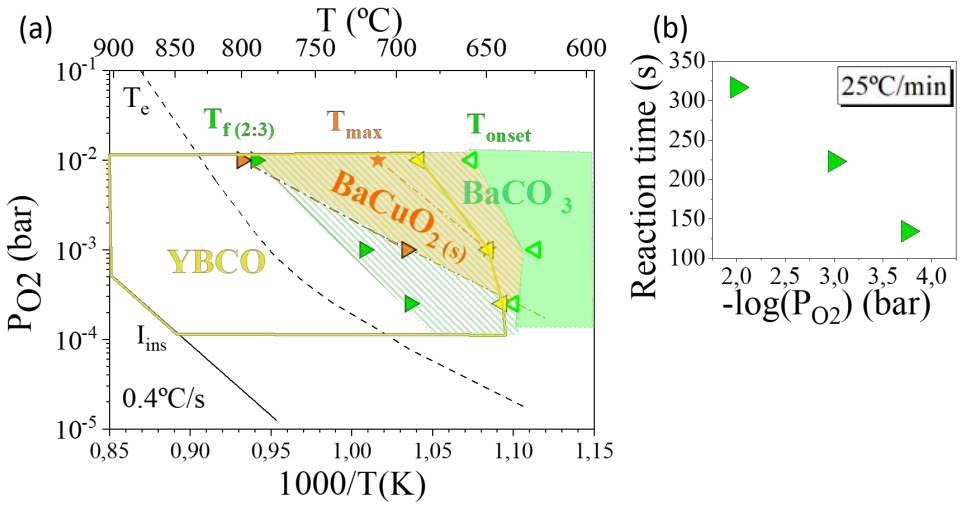

Figure 3.32: (a)$T - P_{O_2}$ phase diagram with phases information from *in situ* XRD heating at 0.4°C/s the YBCO stoichiometric composition. $BaCO_3$ is represented in green and triangles indicate onset and final conversion temperatures. $BaCuO_2$ exists at the orange region and the star symbols depict its maximum intensity. Yellow triangles indicate where YBCO starts nucleating. (b)Barium carbonate decomposition reaction times

315 s to 134 s when pressure is decreased from 10^{-2} to $2.5 \cdot 10^{-4}$ bar, at a speed of 0.4°C/s (Fig. 3.32b).

Note that YBCO starts nucleating below the thermodynamic eutectic line (an issue that will be further discussed in the next chapters).

Knowing this, we deduce that the fastest conversion rates and at lower temperatures will be achieved at the $T - P_{O_2}$ conditions where $BaCuO_2$ solid is avoided and in which subsequent reactions involving the formation of liquid takes place. This is accomplished at the lowest P_{O_2} area for T-route with the stoichiometric composition.

3.4.2.2 Heating rate effect

The effect of heating rate will be widely explored in this section. Various experiments using different annealing rates up to 5°C/s have been performed by means of *in situ* XRD. $BaCO_3$ conversion onset, final temperatures and speeds are represented in Figure 3.33 for both compositions and annealing rates.

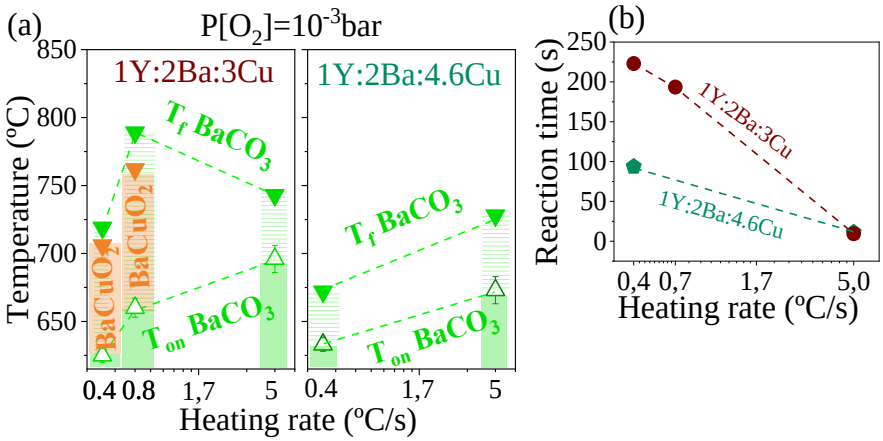

Figure 3.33: (a) $BaCO_3$ and $BaCuO_2$ conversion onset (△) and final (▼) temperatures for both cation ratio during heating rates at $P_{O_2} = 10^{-3}$bar. (b) Reaction times. Values are extracted from corresponding *in situ* time resolved XRD experiments

The increase of heating ramp shifts reactions onset temperature to higher temperatures, as expected for thermally activated processes. T_{on} increases from ~630°C at 0.4°C/s to 690°C (2Ba:3Cu) or 670°C (3Ba:7Cu) at 5°C/s.

Thus, a delay on $BaCO_3$ conversion temperature with fast heating rates may seem a disadvantage towards the objective of avoiding carbon retention. However, reaction kinetics are slow (100-300s) for low T_{onset} (630°C at 0.4°C/s) and very much increased at higher T_{on} (670-690°C, 5°C/s), presenting conversion times as short as 10 s for both compositions.

In the case of the stoichiometric composition, the formation of solid $BaCuO_2$ delays $BaCO_3$ elimination. We observe the mixed oxide at rates until 0.8°C/s, when reaction starts below 660°C. Instead, the use of very fast temperature

rise brings decomposition to higher temperatures, where the solid intermediate formation is hindered in favour of the transient liquid, thus speeding up reaction kinetics. It results on the final decomposition temperature being lower for the fastest annealing, which has higher T_{on}.

Therefore, we can conclude that when conversion starts at temperatures where the reaction product is a liquid (although transient), it enhances the solid reactions rate. Instead, if $BaCO_3$ conversion starts before, the formation of the solid intermediate $BaCuO_2$ will slow down reaction kinetics.

Hence, the use of very fast annealing rates has appeared as a solution for avoiding $BaCuO_2$(s), even at high oxygen partial pressures. Thus, allowing very fast reaction rates in a wide area of processing conditions and for the stoichiometric composition.

Additional advantages from rapid heating are particles coarsening hindering, and more favourable YBCO c-axis nucleation (see Chapter 5).

Ultrafast heating rates

On the light of these findings, we have investigated faster heating rates with quenching experiments. The range of 20 to 100°C/s has been explored using a Rapid Thermal Annealing furnace (RTA).

Pyrolyzed films with final thicknesses off ∼300 nm have been heated up with heating ramps from 20 to 100°C/s and quenched at ∼800°C. The remaining $BaCO_3$ content has been deduced from GI-XRD analysis of the resulting films. Figure 3.34a shows the normalized intensity of the $BaCO_3$ and YBCO main reflections with the time the sample has been exposed to higher temperatures than 650°C during each quench (Fig.3.34b).

We can observe that full conversion has been completed for heating rates slower than 30°C/s. At this speed, the total time that the film been exposed to temperatures > 650°C is $\sim$ 6s (Scheme 3.34(b)). This would be therefore, an approximation of the minimum time needed for a total conversion under these conditions.

Another experiment has been carried out applying a constant heating rate of 80°C/s and different holding times at 800°C, shown in Fig.3.34(c,d). There is no conversion with 0 s of dwell, that corresponds to a time of 2.2s in the

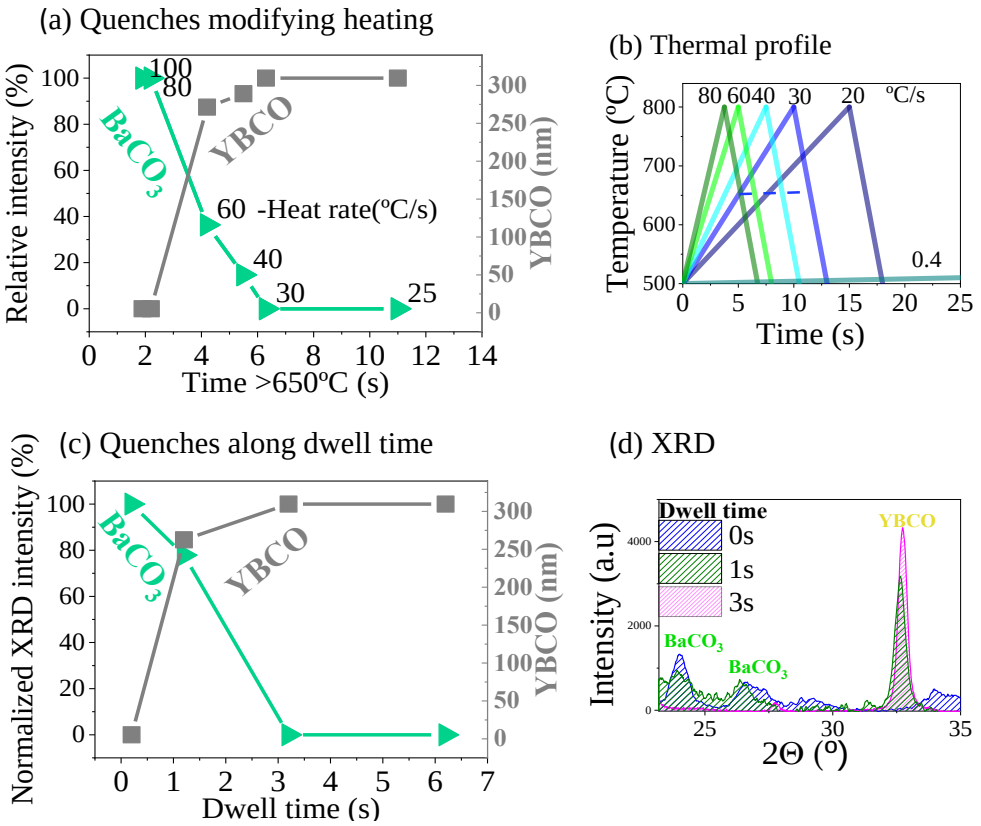

Figure 3.34: Quenched films at 800°C using ultrafast heating ramps from 25 to 100°C/s with the RTA oven. In (a) Intensities corresponding to $BaCO_3$ and YBCO reflections of quenched samples heated at different rates and normalized to a pyolyzed sample. The total time at temperatures above 650°C has been inferred for the real thermal profile, including heating and cooling, is schematised in (b). In (c) quenches performed at 80°C/s with different holding times at 800°C. The corresponding XRD diffraction patterns are plotted in (c). Films thickness are ∼300 nm, produced with solution 5B and atmospheric conditions of P_{O_2}=10^{-2}bar at 1bar

previous experiment. However, by just 1s at high temperature, $BaCO_3$ has

decomposed a 20% of its initial content. Finally, reaction is totally completed with 3 s at 800°C.

Parallel to precursors reaction, is the direct formation of YBCO. No presence of $BaCuO_2$ solid is identified in the XRD (Fig. 3.34(d)). Thus confirming again the use of fast heating speeds to avoid solid intermediates and enhance reaction kinetics.

As a result, we have for the first time proven that the overall process can take place in just 3 s for a final film thickness of ∼300 nm. That would lead to a film conversion rate as fast as ∼100 nm/s. Thus, Rapid Thermal Annealing brings unique opportunities for enhancing the reaction throughput and assure a total fast decarbonation of the films.

3.4.3 CO_2 diffusion

Now, we will focus on the investigation of gasses diffusion effects on reaction kinetics and the influence of film thickness. Note that *in situ* XRD experiments were performed in a semi closed chamber, where gas flow was limited.

3.4.3.1 Thickness dependence

T-route conditions

Carbonate decomposition was followed by Thermogravimetric (TG) and Evolved Gas Analysis (EGA) on deposited precursor solutions resulting in thin films (Fig. 3.35). These experiments were performed by the GRMT group at University of Girona.

A mass loss of 7-12% in weight over the final YBCO mass is observed at high temperatures, depending on film thickness. This step can be accounted to the CO_2 release observed with EGA, corresponding to the gas product of reaction 3.14.

In Figure 3.36, the conversion temperatures (T_D) for films of different thicknesses of stoichiometric composition at 0.4°C/s are depicted for comparison. Temperatures are extracted from the dTG of the mass loss step, corresponding to the maximum slope.

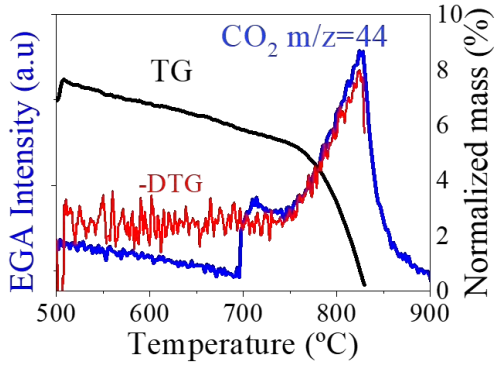

Figure 3.35: EGA and TG analyses at atmospheric pressure showing thermal decomposition of barium carbonate at high temperatures. Heating rate is 0.4°C/s, under atmosphere of wet nitrogen. Nominal film thickness is 2,5μm in order to have signal for the evolved gases. The only volatile detected during this mass loss with m/z=44 is accounted to CO_2

For nominal YBCO final film thickness of 150-300nm, the main decarbonation temperature lies around 690°C, while for films thickness $\sim$ 500 nm it increases to 715°C, for 660 nm to 720°C and $>$ 830°C for a very thick film of 2500 nm.

The $BaCO_3$ reaction in thick films may be hindered by CO_2 retention, either at the film surface or through the thickness. As a result, gradients in carbonate concentration within the layer can also exist. This fact would produce different local reaction rates, thus bringing decomposition to higher temperatures.

Thus, the dependence of reaction T_D on film thickness indicates that the process, in this case, is kinetically limited by the CO_2(g) product out-diffusion.

P_{O_2}-route conditions

Quenching experiments for the P_{O_2}-route conditions (P_{O_2}=10^{-5} bar, P_{tot}=10^{-3} bar) are depicted in Figure 3.37.

XRD patterns of 90 nm thick films, much thinner than *in situ* experiments, show reduction of Cu already at 770°C. However, the formation of $BaCu_2O_2$ and total conversion is only observed after 20 min of dwell at this temperature,

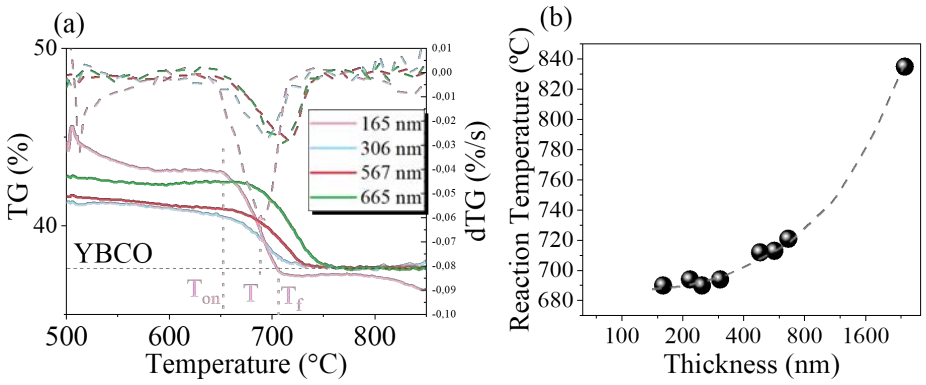

Figure 3.36: (a)TGA and the corresponding derivative curves (dTGA) in dashed lines of the YBCO precursor solution thermal decomposition at high temperatures for different layer thickness. Heating rate is 0.4°C/s, under wet nitrogen and the solution Y:2BA:3Cu. At figure (b) the main decomposition temperatures corresponding to the maximum slope of mass loss extracted from dTG are plotted for different nominal film thickness

or at higher temperature quench (830°C).

For thicker films of 400nm, Cu reduction is observed after 5 min at 830°C, but $BaCu_2O_2$ formation is delayed to higher temperatures. At 840°C is already present, but a big quantity of $BaCO_3$ still remains.

They show similar results. Again, decomposition starts at higher temperatures for thicker films.

Additionally, for thick films, local CO_2 retention within the layer can additionally cause the backward reaction at the already decomposed $BaCu_2O_2$:

$$BaCu_2O_2(s) + CO_2(g) \longrightarrow BaCO_3(s) + Cu_2O(s) \tag{3.21}$$

We have seen the reversible character of this reaction in air at atmospheric temperature. After some days of producing a $BaCuO_2$ film, XRD only showed $BaCO_3$ and Cu_2O precursor phases. The backward reaction has not been observed in $BaCuO_2$ containing films at atmospheric conditions. For this reason, all the analyses involving $BaCu_2O_2$ are carried out right after the sample is

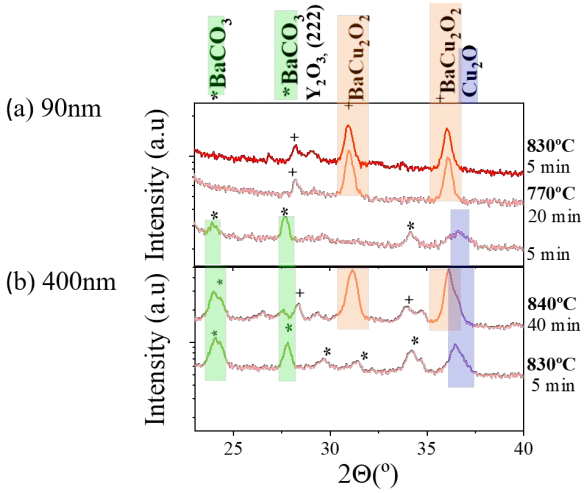

Figure 3.37: Integrated GADDS 2D-XRD diffraction patterns of films heated to 770-840°C and hold for 5 or 20 min. Films thickness are of (a) 90nm (1M5B solution) and (b) 400nm (1.5M5B solution, 2 depositions)

produced.

So, it can be deduced that the barium carbonate reaction to form the mixed oxide that implies CO_2 release is kinetically limiting the process.

Longer annealing times and higher temperatures were probed without success on total decarbonatation due to the limitations of the RTA furnace. Additionally, total pressure is higher ($3 \cdot 10^{-3}$ bar) than with the *in situ* experiments ($5 \cdot 10^{-5}$ bar). Actually, 400nm thick films were totally converted in ~10 min at 830°C during *in situ* experiments at lower total pressure (See Fig.3.26).

3.4.3.2 CO_2 removal towards faster decarbonation

Consequently, knowing that the kinetic behaviour is sensitive to ease of CO_2 removal, different strategies can be developed to enhance this step. Enhancing gas flow and lowering the total pressure are two strategies that will be explored.

On the one hand, the microstrucure and porosity of the starting film can have an influence on the rate of escape of the volatile product by intragranular

diffusion [145]. For this reason, all the comparative studies of this section have been performed with the same precursor solution and maintaining the water content lower than 2%.

On the other hand, we have studied the dependence of atmospheric conditions on carbonate elimination process. Figure 3.38 illustrates the reaction yield under different total pressure and flux conditions. The conversion yield is calculated from carbonate absorption bands before and after quench by means of FTIR spectrometry $((A(COO_3)_{quench}/A(COO_3)_{pyrolysis}) \cdot 100$.

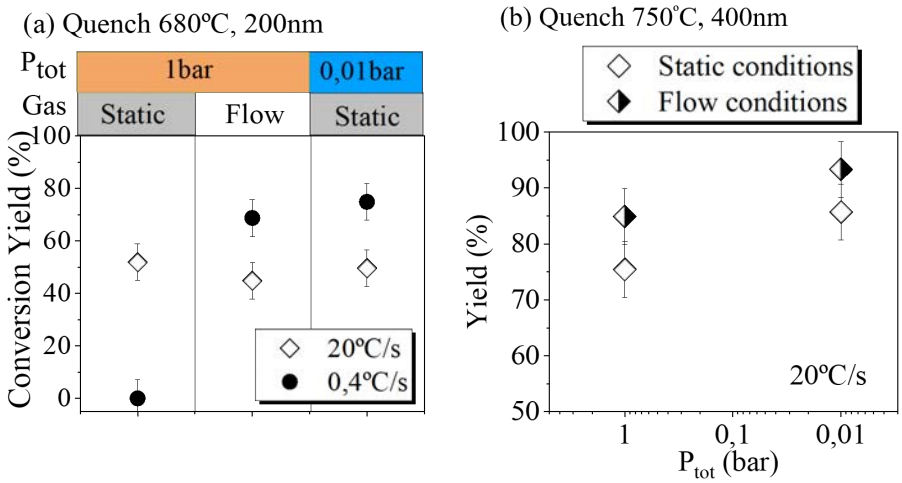

Figure 3.38: Carbonate elimination reaction yield deduced from FTIR measurements of quenched (a)200nm and (b)400nm thick films to 680°C and 750°C, respectively. Depositions have been performed with solution 5D using (a)one or (b)two coating. Annealing has been carried out in a RTA oven with heating rates of 0,4°C/s (●) or 20°C/s (◊). Different atmospheric conditions are plotted: $P_T = 1 - 0.01$bar under static conditions or a flux of 2L/min. P_{O_2} is fixed to 0.01bar in all experiments.

In Figure 3.38a quenches of 200nm thick films are performed at 680°C at 0,4 and 20°C/s rates and different atmospheric conditions:

- Static 1bar: no gas flow at 1 bar of total pressure

- Flow 1bar: maximum gas flow (2L/min) at 1 bar of total pressure
- Static 0.01bar: no gas flow, but total pressure is reduced to 0.01 bar
- Flow 0.01 bar: a gas flow is maintained with a working rotary pump. A stable total pressure of 0.01 bar is obtained

In the film heated with a slow rate of 0.4°C/s (solid symbol in Fig. 3.38a) in absence of gas flow at atmospheric pressure, all the barium carbonate present after pyrolysis is retained after the quench. In other words, the reaction has been blocked.

In contrast, carbonate decomposition does proceed with the same conditions but under gas flow or reduced total pressure to 0.01 bar, giving similar yields of ∼70% conversion.

Both gas flow and reduced pressure are different methods to induce a bigger gradient in the gas phase that drive the gas scape from the film. Consequently, reaction rate for products conversion is increased. This fact is in accordance with equilibrium laws of "Le Chatelier's principle" for reversible reactions. The forced removal of CO_2, since it is the reaction product, generates a disturbance on the equilibrium so that in order to adjust itself, it will reduce the effect by generating more product. In other words, equilibrium reaction is enhanced to the right.

Surprisingly, the blocking effect when working in static conditions is less important when annealing to high temperatures is faster (20°C/s, open symbols in Fig.3.38(a)). The sample treated with no flow at 1 bar presents now a transformation of ∼50%, and it is not dependent on gas conditions.

One explanation is accounted to the formation of a liquid intermediate that enhances the elimination of $BaCO_3$. Somehow, the formation of this liquid, and subsequent YBCO growth, is favoured when heating faster. This issue is addressed in section 3.4.2.2.

In this situation, the fast conversion to the YBCO phase avoids the backward reaction caused by not expelled CO_2.

Quenches of thicker films (400 nm, Fig.3.38(b)) are performed with a fast heating (20°C/s) to 750°C. Being the films thicker, more differences are observed within samples heated with/without flow or atmospheric/reduced total

pressure. The sample treated at 1 bar without flushing presents a transformation of 75%, that working under flow or P_T of 0,01bar is increased to ∼85%. If continuous flow is also present at reduced pressure, reaction yield is the highest, being ∼93%.

Consequently, by using furnace conditions that contribute the most to CO_2 release, a 400nm thick film can be decomposed at temperatures close to 750°C with a very fast ramping speed.

Still, instrumental limitations exist in the RTA furnace to explore a higher range of pressures and gas flow. The big chamber permits a very low effective gas exchange. Yet, total carbon elimination of 400 nm film has been just proved possible under low total pressure (10^{-5} bar) in the synchrotron experiments.

Currently, a new tubular furnace has been installed in our laboratories and allows a high N_2 flux of effective 3L/min. Recent experiments show complete $BaCO_3$ conversion to $BaCu_2O_2$ at $P_{O_2} = 10^{-5}$ bar and 1 bar of total pressure in 400 nm thick films and with only 5 min dwell at 830°C. Therefore, the gas flow effects are remarkable and the use of low total pressure may not be even necessary.

3.5 Conclusions

Pyrolysed thin films up to 1 μm thick can be obtained from deposition with spin coating or Ink Jet Printing. For the first case, combinations of solution solvents with distinct boiling points are used to tune films thickness, morphology and porosity. IJP films are highly homogeneous along film thickness. However, formation of cracks and shrinkage during big solution volumes decomposition requires remarkable efforts and therefore research in this field is still on going. If long thermal treatments are applied, CuO coarsening precludes the reactions during film conversion.

In situ infrared spectroscopy measurements during pyrolysis reveal the decomposition path of the three cations propionate salts mixture. Different thermal regions are identified as heating to 500°C: (1)$Cu(EtCO_2)_2$ and $Y(EtCO_2)_3$ hydrolysis below 200°C, (2)oxidation processes leading to CuO, Y_2O_3 and BaC_2O_4 (3)Barium oxalate oxidation to $BaCO_3$. The decrease of the heat-

ing ramp undergoes these reactions to higher temperatures.

TEM analyses show a resulting nanocrystalline matrix of the three species with very small particles sizes: 10-30 nm for $BaCO_3$ and CuO and 5-7 nm for the Y_2O_3.

A crucial parameter is the control of the water content in the solution. Dramatic effects are derived if it exceeds $2\%_{wt}$. It alters solution rheology and the thermal decomposition path, leading to the formation of monoclinic $BaCO_3$, in contrast to the orthorhombic structure, and metallic Cu. This fact, together with increased particles sizes and reduced porosity modifies drastically the nucleation mechanisms.

Then, the reaction mechanisms for the $BaCO_3$ elimination at higher temperatures are elucidated with *in situ* XRD experiments. Two different reaction paths are evidenced depending on P_{O_2}.

At $P_{O_2} \geq 2.5 \cdot 10^{-4}$ bar, $BaCO_3$ reacts with CuO to give $BaCuO_2$. The $BaCO_3$ is the slowest reaction in the overall conversion process. This mixed oxide becomes a transient liquid at a temperature that depends on the Ba:Cu ratio. Still, with the Y:2Ba:3Cu composition, the formation of the $BaCuO_2$ solid that hinders reaction speed, can be avoided using low P_{O_2} ($2 \cdot 10^{-4}$ bar). Also, the increase of heating ramp undergoes reactions to higher temperatures and faster rates where solid $BaCuO_2$ is avoided. A 300 nm YBCO thick film can be converted with only 3 s at high temperatures when ultrafast heating rates are used (80°C/s).

At $10^{-4} \geq P_{O_2} \geq 10^{-5}$ bar, $BaCO_3$ reacts with Cu_2O, that has been previously reduced from CuO. The resulting phase is the solid $BaCu_2O_2$.

The two reactions have different thermodynamic and kinetic drivers, being the one leading to $BaCu_2O_2$, the slowest one.

We conclude that CO_2 out-diffusion is the kinetic effect that limits the conversion in thick films. Therefore, the enhancement of the gas release with the use of gas flow or reduced total pressures seems to have promising effects on enhancing the reaction yield.

This is specially necessary for the $BaCO_3$ elimination with the P_{O_2}-route, where there is no liquid phase accelerating the reaction at these low P_{O_2}.

Chapter 4

Liquid-assisted nucleation and growth mechanisms

This chapter is devoted to the general description of the transient liquid-assisted growth process, focused on the $YBa_2Cu_3O_{7-\delta}$ material. At first, the general concepts of nucleation and growth from high temperature solutions will be described, and later used as a guidance to address the basic concepts involved in the transient liquid-assisted growth (TLAG).

The nature and factors that drive the kinetically driven formation of the transient liquid will be proposed and the steps for the growth process are described. The processing conditions to do so are also suggested, based on the experiments that will be reported in the next chapters.

A guidance of the supersaturation conditions for nucleation and growth is necessary for the understanding of the future experimental results, as well as for optimizing the process to synthesize the desired structure. $YBa_2Cu_3O_{7-\delta}$ presents an anisotropic cell structure with two matching directions, which makes the task of forming the biaxially textured phase very challenging. The same basic crystal growth concepts will be used to propose the growth rate that can be achieved, together with the corresponding kinetic limiting factors.

Finally, experiments on the $BaCO_3$ and CuO binary mixture will be presented to analyse the liquid formation in different compositions while using the processing conditions for TLAG.

4.1 Fundamental aspects on nucleation and growth from solution

4.1.1 Introduction

Crystallization may be defined as a first-order phase transformation in which a crystalline product is obtained from a liquid. In the case of solution growth, the driving force for crystallization is supersaturation. It is the chemical potential of infinitely large crystal new phase ($\Delta\mu_c$) relative to the chemical potential of the mother phase ($\Delta\mu_l$): $\Delta\mu = \Delta\mu_s - \Delta\mu_c$. In the case of crystallization from solution, the expression can be written as

$$\Delta\mu = kTln\frac{C_\delta}{C_e} = kTln(\sigma + 1) \tag{4.1}$$

where the relative supersaturation σ can be written as:

$$\sigma = \frac{C_\delta - C_e}{C_e} = \frac{C_\delta}{C_e} - 1 \tag{4.2}$$

where C_δ and C_e are respectively the real and equilibrium concentrations of the solute in the liquid solvent. Hence, a supersaturated solution is that in which the solute concentration exceeds the equilibrium solute concentration at given $T - P$ conditions. The solution is therefore out of equilibrium and any disturbance of this metastable state will relax into crystallization of the solute. A supersaturated solution can be produced in different ways depending on the growth technique [45]:

- Temperature gradient or undercooling (LPE)
- Evaporation of solvent
- Addition of solute (HLPE)
- Changing of solvent composition

Figure 4.1 shows a schematic drawing of the metastable zone of supersaturation, so called Ostwald-Meiers regime. The solid line represents the equilibrium solubility C_e curve of the solute in the liquid, while the dashed line is referred

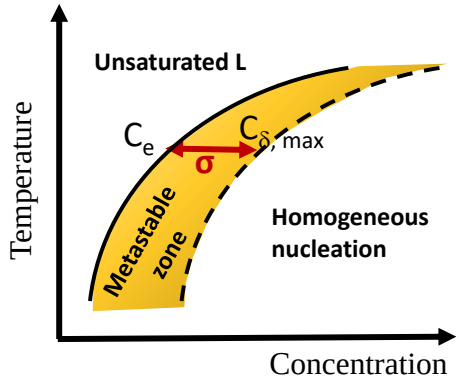

Figure 4.1: Schematic representation of the supersaturated Ostwald-Meiers zone of a liquid with temperature (yellow). The equilibrium concentration C_e is represented in a continuous line, while the boundary of supersaturation is a dashed line where the real concentration C_δ and thus supersaturation reach their maximum

to the boundary of metastability, where maximum supersaturation is achieved. A model to predict the metastable zone width was described by Mersmann and Bartosch and may not have a constant width [150]. Thus, three zones can be distinguished:

- The unsaturated liquid zone where crystallization is impossible
- Supersaturated metastable Ostwald-Miers zone lies between the two lines. In this area spontaneous nucleation is improbable but a crystal can grow in the presence of a seed or substrate that is closely matched to the expected nucleating phase: heterogeneous nucleation
- Spontaneous homogeneous nucleation of the crystal

Overall, crystallization takes place in two differentiated processes. First, nucleation of first new nuclei. Second, growth of these crystals to a larger size to attain macroscopic dimensions.

4.1.2 Nucleation

After reaching the metastable region, nucleation will only take place if forming clusters surpass a critical radius (r^*) and a thermodynamic barrier (ΔG^*). Below r^* clusters are on average dissolving while above r^* they are on average growing to complete the phase transformation [151].

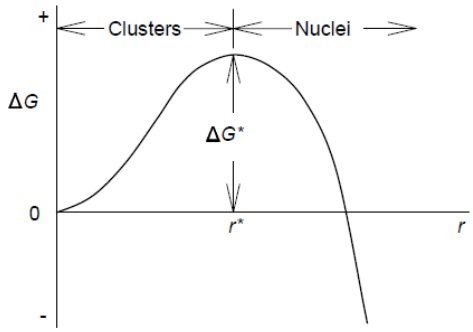

Figure 4.2: Free-energy barrier for nucleation depending on forming clusters radius. Nucleation is possible after a critical radius (r^*) is surpassed

The critical radius may be related to supersaturation ($\Delta\mu$) in the system as:

$$r^* = \frac{2\gamma V_M}{\Delta\mu} \tag{4.3}$$

where V_M is the molar volume of crystal and γ the surface energy of the new phase. Therefore, an increase in supersaturation and decrease of γ will lower r^* and favour nucleation.

The corresponding free energy barrier to overcome (ΔG^*) for homogeneous nucleation (4.4) is usually higher than that for the heterogeneous (4.5) because of a large reduction of surface energy (γ) associated to forming nucleus shape ($f(\theta)$, Fig. 4.3). Note that this factor may depend on the substrate used, solute and melt characteristics. Mathematical derivations and complete analysis can be found elsewhere [45, 152].

$$\Delta G^*_{Homo} = \frac{16\pi\gamma^3 V_M^2}{3\Delta\mu^2} \tag{4.4}$$

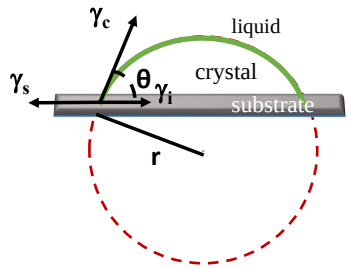

Figure 4.3: Equilibrium forming crystal shape with wetting angle θ. Red dashed line for homogeneously nucleated round crystal and green line denotes heterogeneous nucleation on a foreign substrate. For the latter, equilibrium is attained when γ_s-γ_i=$\gamma_c cos(\theta)$, where γ_s is the substrate surface energy, γ_i the interface energy, and γ_c the crystal surface energy

$$\Delta G^*_{Hetero} = \Delta G^\circ_{Homo} f(\theta) = \Delta G^\circ_{Homo}(\frac{(1-cos\theta)^2(2+cos\theta)}{4}), \qquad (4.5)$$
$$(0 \leq f(\theta) \leq 1 \textbf{ and } 0 \leq \theta \leq \pi)$$

where θ is the contact angle of the growing phase with the substrate, illustrated in Fig.4.3. Thus, a crystal can nucleate heterogeneously with lower supersaturation values than those required for homogeneous nucleation because the nucleation barrier is lower.

Additional complexity is introduced in the case of cuprate oxide superconductors by the close barrier energies of crystallization for different possible epitaxial orientations [153, 114].

The net number of clusters passing the critical size per unit time is the nucleation rate dN/dt. It is defined as the number of critical nuclei generated in a unit volume per second

$$\frac{dN}{dt} = N_0 A^* exp(\frac{-\Delta G^*}{k_B T}) \propto exp(-\frac{\gamma^3}{\Delta\mu^2}) \qquad (4.6)$$

where N_0 is the number of available sites for nucleation and A^* contains kinetic

factors that describe the rate of atoms attachment to the nuclei. k_B is the Boltzmann's constant.

ΔG^* and nucleation rate dependence with supersaturation at a constant temperature are represented in Figure 4.4a,b.

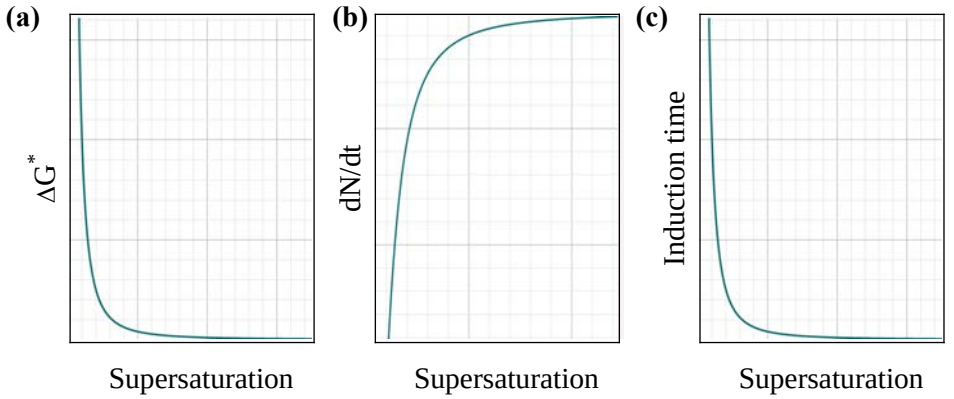

Figure 4.4: Schematic representation at a fixed temperature with supersaturation of (a) nucleation barrier ΔG^* (b) nucleation density dN/dt versus (c)Induction time for nucleation (t_{ind})

According to equation 4.6, nucleation rate changes very rapidly as a consequence of exponential decrease of ΔG^* with supersaturation. At low $\Delta\mu$ nucleation rate is very low and increases very rapidly several orders of magnitude at a certain threshold supersaturation value. For instance, reported values for YBCO nucleation rate with LPE technique may change from $2 \cdot 10^{-54} cm^3/s$ at $\sigma = 0.500$ to $2 \cdot 10^{-3} cm^3/s$ at $\sigma = 0.800$ and to $1 cm^3/s$ at $\sigma = 0.835$ [154].

Yet, the nucleation rate may decrease at low temperatures when the pre-exponential factor A^* is low due to the reduced atomic mobility. Assuming that the atomic mobility scales with the diffusion coefficient D in crystal nucleation from liquids [151, 155]:

$$A^* = \frac{24 D r^{*2/3} N_A}{\lambda^2} \left(\frac{\Delta\mu}{6\pi k_B T r^*}\right) \tag{4.7}$$

where λ is the atomic jump distance and N_A the Avogadro number

Diffusion is in turn related to liquid viscosity η and radius r of the moving particles [156]:

$$D_l = \frac{k_D T}{6\pi r \eta} \tag{4.8}$$

η follows an exponential temperature dependence:

$$\eta = \eta_0 exp(\frac{E}{RT}) \tag{4.9}$$

where E is an activation energy.

As a result, the nucleation rate dependence with temperature is illustrated in Figure 4.5. Its maximum is found at intermediate temperatures and the nucleation rate shows a strong dependence on the interfacial free energy γ [151].

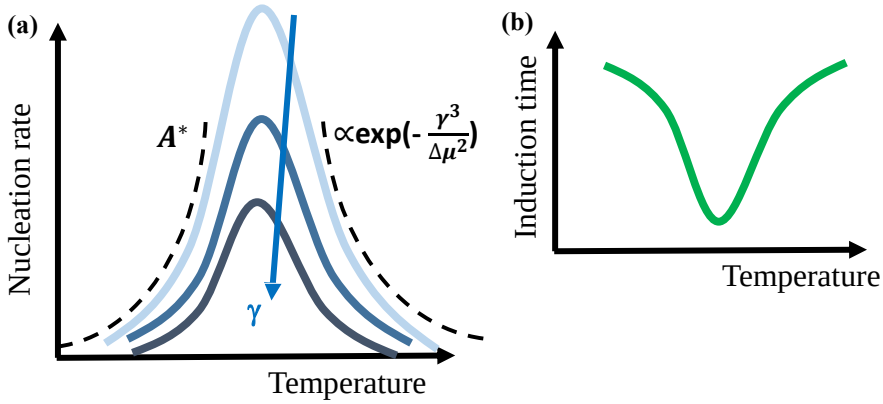

Figure 4.5: (a) Steady-state nucleation rates as a function of temperature when the effect of atomic diffusion is considered and for different γ. At low temperatures atomic mobility limits the rate and at high temperatures the energy barrier increases with the decrease of supersaturation with temperature (b) Induction time for nucleation

The time necessary for reaching the critical nucleus from attainment of supersaturation is called *induction period of nucleation* (t_{ind}) [45]:

$$t_{\text{ind}} = \int_0^{t_{\text{ind}}} \frac{dN}{dt}(T)dt \propto \frac{1}{T, \Delta\mu} \tag{4.10}$$

t_{ind} correlation with supersaturation is plotted in Figure 4.4c; and on temperature in Figure 4.5b.

4.1.3 Epitaxial growth

In general, two main processes for crystal growth were defined by Berthoud (1912): diffusion of solute to the growing interface and surface kinetics processes. The slowest process limits the growth rate of the material and determines the relation between growth rate and supersaturation. Hence, growth rate may become diffusion controlled or interface controlled depending on both mechanisms kinetics in each technique.

In the presence of a liquid layer, steady state growth rate R may be written as [60]

$$R = (1/k + \delta/D)^{-1} \frac{C_\delta - C_e}{C_{xt}} \tag{4.11}$$

where D is the diffusion constant, δ diffusion distance, k the kinetic coefficient and C_{xt} denotes solute concentration in the forming crystal. When $D/\delta >> k$, kinetic surface process are rate limiting and for first order reaction kinetics, R can be approximated to

$$R \sim k \frac{C_\delta - C_e}{C_{xt}} = k\sigma(C_e/C_{xt}) \tag{4.12}$$

Surface kinetics involves three main steps described by the *Kossel model* for layer-by-layer growth:

- (i) Attachment of solute atoms: exchange kinetics of solute molecules between the volume immediately adjacent to the surface and the close-packed terrace where the molecules are adsorbed
- (ii) Surface diffusion of adsorbed molecules on the terraces between steps
- (iii) Integration into the growth steps that involves attachment to a step, diffusion along the step, and integration into the crystal at the kink

Most of the processes mentioned above are difficult to be discerned for their study. However, supersaturation remains the thermodynamic potential that

drives all these mechanisms. There are three classical modes that describe thin films epitaxial growth, which have distinct tendencies with supersaturation: (1) continuous, rough or normal growth, (2) two-dimensional growth and (3) screw dislocations or spiral growth. They are illustrated schematically in Figure 4.6, together with their growth rate dependency on supersaturation.

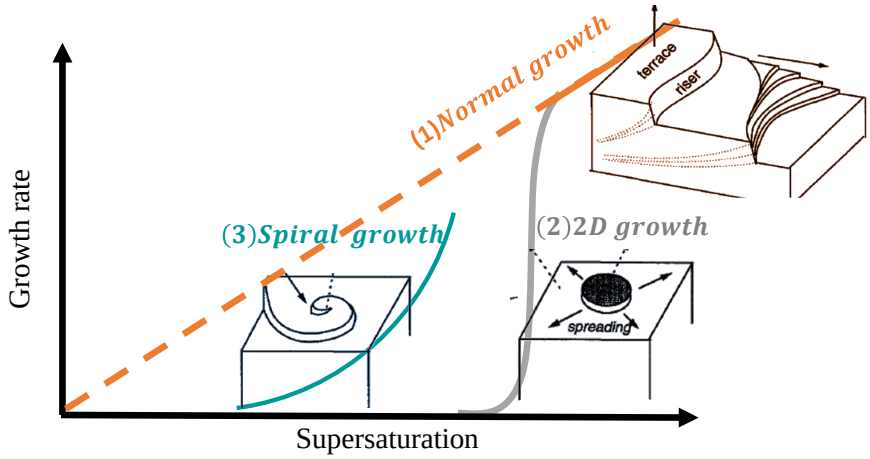

Figure 4.6: Growth modes scheme of crystal growth on their dependence on supersaturation. Adapted from [47]

At very low supersaturation values, the growing film contains screw dislocations that derive from the substrate, or form to relieve substrate misfit stress, these provide a continuous source of growth steps by spiral growth (3). At intermediate supersaturations, 2D nucleation (2) has overcame the activation barrier and it is the dominant mechanism. At higher supersaturations, R dependence with supersaturation is linear ($R_{max} \propto \sigma$). Here, normal growth (1) is possible.

Finally for much higher $\Delta\mu$, homogeneous nucleation can occur leading to growth instabilities and roughening. Supersaturation boundary for the latter would correspond to the limit of supersaturation (Ostwald-Miers line).

4.2 Transient Liquid Assisted Growth general characteristics

4.2.1 Transient liquid growth principles

Liquid Assisted growth requires a system composed of a melt as a vehicle where a given atomic element must dissolve in supersaturated conditions to crystallize a new solid phase. Transient liquid is referred to a liquid phase that is formed and subsequently disappears to transform into a new crystallized phase.

The formation of the liquid component is usually driven by a change in temperature (melting), but it can also happen following a change in composition or pressure. Phase diagrams are used to represent phases transformations with the various conditions of temperature, pressure and composition. Consequently, they show which phase or mixture of phases is thermodynamically stable under certain conditions.

However, TLAG is based on the kinetic preference to form transient liquids at the equilibrium conditions of the crystal product, where it is not thermodynamically expected. Yet, the liquid formation is the more kinetically accessible path because of the energy barrier for nucleation of the equilibrium crystalline phase (which delays its formation through an incubation time). Solid state direct crystallization entails very slow rates, but when a transient liquid assists this process, it can serve as a vehicle for enhancing growth rate or lowering growth temperatures due to the faster diffusion in liquid state than in solid phases. A similar case was only reported for the growth of germanium nanowires [157].

To do so, the system should start with mixed particles that, during processing, some form a liquid while others remain as solute. A scheme is drawn in Figure 4.7 for the transient liquid-assisted synthesis of $YBa_2Cu_3O_{7-\delta}$.

When placing a mixture of $BaCuO_2$, CuO and Y_2O_3 solid phases in the $YBa_2Cu_3O_{7-\delta}$ stability region, the system forms the eutectic BaO-CuO liquid although this phase is not expected in the ternary phase diagram [144]. Y_2O_3 nanoparticles remain solid and will be dissolved to supersaturate the melt due to particles small size. Then, heterogeneous nucleation takes place upon Y diffusion to the lattice matching substrate interface where free energy for nu-

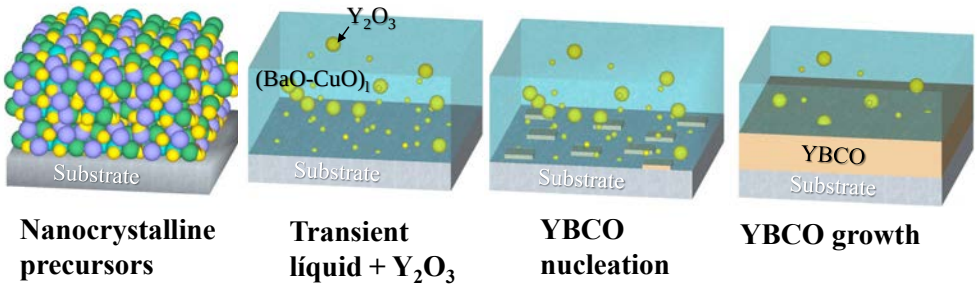

Figure 4.7: Draw of the transient liquid-assisted growth process for epitaxial $YBa_2Cu_3O_{7-\delta}$ from a nanocrystal solid solution

cleation is lower. Crystal growth proceeds through the same mechanism from bottom to the top of the film. Experimental evidences of this process will be given in the next two chapters.

A melt of Ba-Cu-O composition exists at high temperatures after an eutectic reaction in the $BaCuO_2$-CuO binary system [115, 141, 143, 158] (see section 4.3). Then, solubility of RE elements in such melts have also been reported and widely used as driving force for YBCO crystallization in the liquid growth based techniques for REBCO (see section 1.5.1). Though, none of them use transient liquids and they are limited to other regions of the phase diagram where a stable melt persists, neither through low cost solution processing approaches.

To generate the precursor phases, we use Chemical Solution Deposition methodology (CSD). $BaCuO_2$, CuO and Y_2O_3 are precursor phases formed after fluorine-free solutions decomposition and $BaCO_3$ elimination. The processes and requirements from solution design to the formation of such phases are described in chapter 3.

Benefits for CSD methodology are the low cost and easily scalable methodology. No special requirement of atmosphere control and no F would be generated in contrast to CSD using trifluoroacetate solutions. This fact facilitates enormously the implementation of parallel tape fabrication and so much higher production throughput could be envisaged. Additionally, introduction of preformed nanoparticles in precursor solution that can generate nanocomposites

would provide particles size control and enhanced vortex pinning similarly to that demonstrated for TFA-CSD [159].

We expect the combination of TLAG ultrafast growth with chemical solution deposition (CSD) to be a breakthrough to achieve high throughput manufacturing of long length coated conductors for energy and large magnet applications.

4.2.2 Working window for YBCO TLAG growth

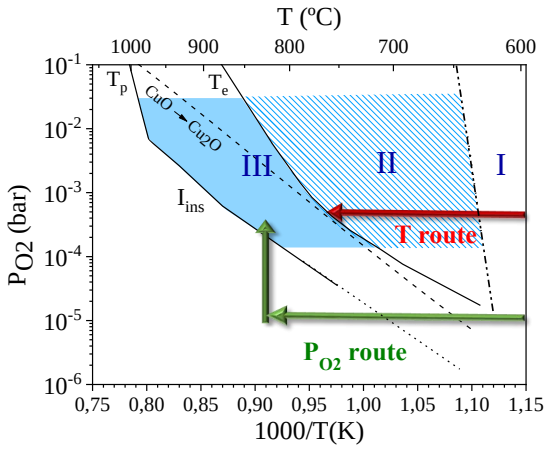

Figure 4.8: T-P_{O_2} diagram for YBCO TLAG growth. The $BaCuO_2$-CuO eutectic temperature (T_e) [143, 115], the YBCO peritectic temperature (T_P) [146, 147], the instability YBCO line (T_{ins}) [148] and CuO/Cu_2O reaction [143, 158] are shown. The T-route and P_{O_2}-route are indicated in arrows. Conditions where fast YBCO growth is possible are pointed in white triangles

A schematic phase diagram for TLAG is constructed on the basis of thermodynamic lines that will be used only as a guideline , because the conversion process is not undertaken at equilibrium. Transient liquid growth should occur in the T-P_{O_2} region (blue region, zone III) between three lines: eutectic line from $BaCuO_2$-CuO system (T_e), peritectic $YBa_2Cu_3O_{7-\delta}$ decomposition to Y_2BaCuO_5 (T_P) and phase boundary instability line at low P_{O_2} (T_{ins}).

T_e line was reproduced from [115]. The line was determined for pyrolyzed

thin films containing $3BaCO_3$-7CuO eutectic composition and analysed by thermogravimetry (TG), differential thermal analysis (DTA), and in-situ and ex-situ X-ray diffraction (XRD) experiments. Very advantageously, the eutectic reaction takes place at lower temperatures as P_{O_2} is decreased. Below $P_{O_2} = 10^{-4}$ bar, CuO reduction to Cu_2O and crystallization of $BaCu_2O_2$ precludes formation of the eutectic liquid phase, as we observed in chapter 3.

Yet, the extent of formed liquid is sensitive to the Ba-Cu molar ratio due to the existence of a liquidus line for compositions different from (3Ba-7CuO) eutectic point [141]. Section 4.3 will be devoted to further study liquid formation in the binary system depending on molar composition and temperature ramps, very relevant parameters in TLAG.

However, transient liquid mediated growth below T_e is also observed, at temperatures as low as 650°C (dashed blue region, zone II). One possibility is that a Y supersaturated liquid is generated much below the expected binary $BaCuO_2$-CuO equilibrium eutectic temperature T_e. Other systems exist in which nanometric dimensions liquid growth is achieved the below bulk eutectic temperature [157, 160, 161].

Yet, the fundamental processes that govern this behaviour are not completely understood. There are also references in literature regarding the existence of a quasi-liquid layer (QLL) below thermodynamic line for thin films ($< 50\,nm$) [60]. There is no accepted quantitative description for QLL. It is proposed that such layers form by surface melting, or as a quasi-liquid adsorption layer.

Peritectic decomposition line, the upper temperature limit, may depend on RE element [147] and substrate misfit. Temperature is shifted to lower values with the increase of lattice substrate mismatch with YBCO [162].

The path followed for the conversion process through the transient liquid mediated YBCO formation can be accomplished in two different ways. We name them Temperature-route (red arrow Fig. 4.8) and P_{O_2}-route (green arrows ig. 4.8), depending if transient liquid formation proceeds with the increase of temperature or P_{O_2}, respectively.

Temperature-route consists on a single processing step in which the film is heated at a constant P_{O_2} to the YBCO stability region. Hence, transient liquid is formed after crossing T_e line. All conversion reactions take place consecutively and consequently kinetics on precursors reaction ($BaCO_3$ elimination to form

$BaCuO_2$) may play a key role.

In contrast, for P_{O_2}-route the transient liquid is formed after crossing T_{ins} line from a rise on P_{O_2} atmospheric conditions at a constant temperature. In this case, total film conversion proceeds in two processing steps. The first stage in which the film is led to a temperature below T_{ins} can be advantageously used to decouple $BaCO_3$ elimination reactions from YBCO nucleation and growth.

Since there is very few bibliography about YBCO nucleation in different regions using fluorine free routes, we should explore the optimal parameters for c-oriented YBCO nucleation in the possible transient liquid zone and for the different conversion paths. This task will be extensively reported in the next chapters. For next sections studies, we will consider both routes and different Ba-Cu molar ratio compositions to disclose the reactions mechanisms.

4.2.3 Supersaturation in TLAG as driving force

Nucleation and growth mechanisms for TLAG can be described within the general theoretical framework of crystal growth from solution. Yet, the understanding of crystallization mechanisms from a transient liquid process exposes extra difficulties.

The basis on crystallization in TLAG will be adapted from considerations from classic Liquid Phase Epitaxy (LPE) and closer related Hybrid Liquid Phase Epitaxy (HLPE) processes. However, such expressions will only be used as a guidance, since a more exhaustive theoretical basis has still to be developed. A quantitative treatment would require molecular dynamics modelling. Additionally, there is a lack of essential data and reliable measurements on the [BaO-CuO] liquid properties due to the highly corrosive character of this melt.

In TLAG, growth occurs by Y dissolution and transport through the melt to the growing crystal interface. To achieve a full control of the nucleation and growth conditions, the degree of supersaturation needs to be carefully controlled. The driving force for crystallization is the difference between the supersaturated concentration (C_δ) and the equilibrium concentration (C_e) of the yttrium in the liquid, as previously described in equations 4.1 and 4.2.

Solubility C_e tuning by melt composition

C_e is an intrinsic parameter depending on temperature and the nature of the solute and melt. Solubility of RE in Ba-Cu solution increases with increasing RE size [163, 58]. Additionally, Nakamura *et al* showed that the Y solubility increases with P_{O_2} (from 10^{-2} bar to 1 bar) [164].

$C_e(T)$ values also depend on BaO:CuO ratio of the liquid. There are a few estimations for Y solubility in BaO-CuO melt with various compositions. However, an additional complication on determining it is the highly corrosive character of the liquid, thus dissolving the crucible. Furthermore, most of them are measured at high values of temperature and P_{O_2} (>0.01 bar).

Yao *et al* reported the Y solubility increase with the Cu content ratio of the melt composition [163]. In this thesis, we compare the 3Ba:7Cu and 2Ba:3Cu liquid compositions. Figure 4.9a shows the extrapolated Y equilibrium concentration $C_e(T)$ in both melt compositions.

$C_e(T)$ values for the 3:7 flux are extracted from [165] in air. We have found no data for the stoichiometric 2:3 composition so far. As an approximation, we have used extrapolated $C_e(T)$ data for 3BaO-5CuO melt from references [63, 164].

Once having C_e(T), to prove guidance into the variation of supersaturation, we fix C_δ to 10%. Now, a correlation of supersaturation with the processing temperature for a fixed $C_\delta = 10\%$ can be depicted (Fig. 4.9b). Values of C_e ~0.01 were estimated near the eutectic point at low P_{O_2} with the 3BaO-5CuO melt [60]. For this reason, lower values than this have not been considered.

Supersaturation increases exponentially as C_e approaches very low values at low temperatures. Consequently, very high $\sigma \sim 1000$ is achieved close to T_e and rapidly drops as temperature increases.

Very significant is also the effect produced by the distinct $C_e(T)$ when changing the Ba:Cu ratio. The same supersaturation levels may be achieved in a temperature difference of 100°C, depending on the molar stoichiometry. This fact may be relevant on the search for lower processing temperatures and epitaxial nucleation control.

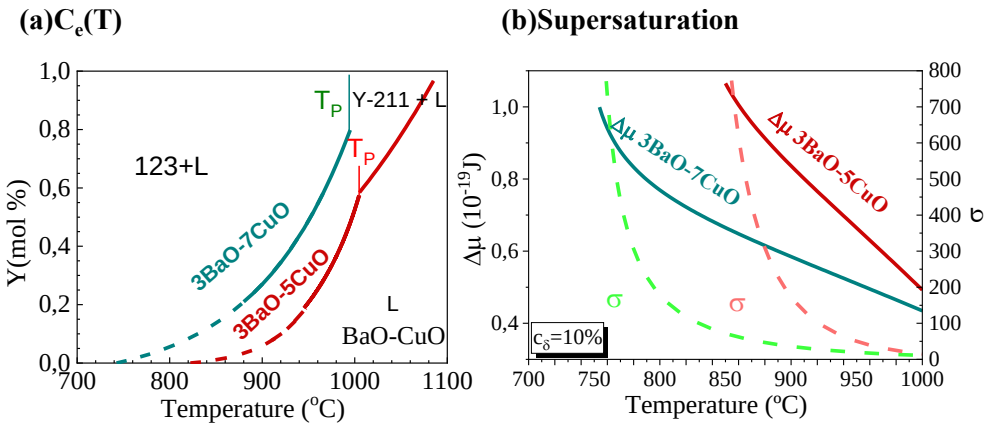

Figure 4.9: (a)Equilibrium concentration C_e with temperature for Y in the BaO-CuO melt for the Ba:Cu ratios 3:7 (turquoise) and 3:5 (red) in air. The data is extrapolated to lower temperatures from references [165, 63, 164]. (b) Computed supersaturation values $\Delta\mu$ (continuous line) and σ (dashed line) assuming constant $C_\delta = 10\%$

Y concentration C_δ

In HLPE technique, the Y concentration in the flux C_δ is controlled by external Y feeding with physical methods during growth, which rate can be adjusted to the crystal growth rate. In TLAG, a supersaturated solution is achieved upon formation of a kinetically favoured liquid around a nano crystalline matrix of Y_2O_3. Thus, all the Y necessary for the $YBa_2Cu_3O_{6+\delta}$ stoichiometric ratio, which is a 17%, is already in the layer when the liquid is formed. Then, if all Y contained in the Y_2O_3 nanoparticles dissolves in the forming liquid, σ can become very high (> 1000).

An estimation of the Y dissolution C_δ can be drawn in the phase diagram by extending the liquidus line from the region containing thermodynamically stable L+ Y_2O_3 phases at higher temperatures. It is represented in Figure 4.10a. From this assumption, it could be in the order of C_δ=10%.

Consequently, TLAG could operate at very high σ. This fact may be bene-

ficial for the achievement of very fast growth rates, but more effort is required to limit nucleation to epitaxial c-axis orientation, as we will expose in the next section 4.2.4.

Possible relative supersaturation changes owing to variations of C_δ are shown in Figure 4.10b. We assume $C_e(T)$ to be in the order of 0.01-0.6 mol% Y, in our temperature range and studied melt compositions.

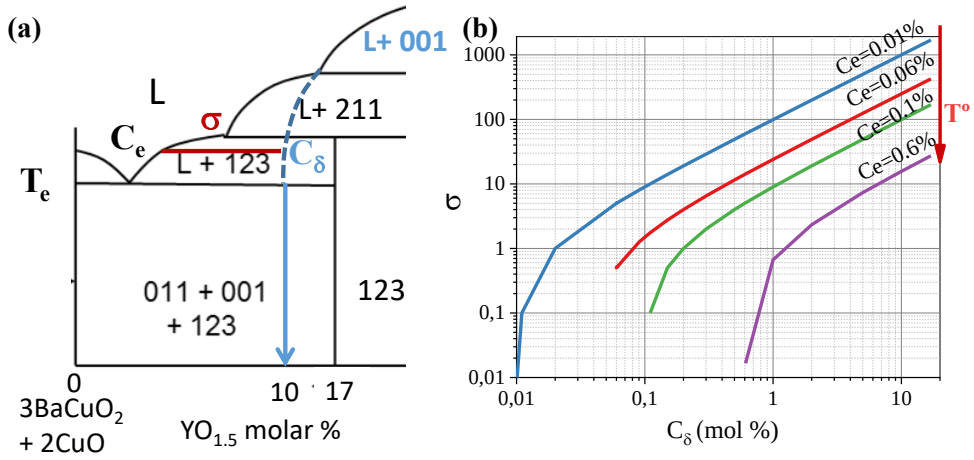

Figure 4.10: (a) $BaCuO_2$-Y_2O_3 temperature phase diagram reproduced from [48], where the liquidus line from the high temperature L+Y_2O_3 region is extended. Numbers are accounted to Y:Ba:Cu phases composition ratio. 17mol% Y is the $YBa_2Cu_3O_{7-\delta}$ composition (b)Computed relative supersaturation σ variation with C_δ at different C_e values. Note that C_e increases with temperature and Cu mol%

For instance, if C_δ is 10%, σ can vary 2 orders of magnitude (from 1000 to 10) by C_e changes when tuning temperature or melt composition. For an 1% of dissolved Y, σ range would be between 1 and 100; and very low Y solubility (0.1%) would give σ between 0.1-10.

Supersaturation can be compared experimentally in relation to the synthesis conditions upon analysis of the growing phases. In the following sections of this Thesis, the tuning of C_e and C_δ will be elucidated for both processing TLAG

routes (T-route and P_{O_2}-route).

Y dissolution C_δ may depend on several factors. It can be tuned by indirect parameters (see section 5.1.2), or by the solution molar ratio. For instance, different Y concentrations for nucleation and growth could be obtained using multi layered structures of different composition. An example is reported in section 5.3.1.4.

4.2.4 Nucleation competition between $YBa_2Cu_3O_{7-\delta}$ orientations

For YBCO integration in a CC architecture, the crystal cell has to lay biaxially aligned in c-direction perpendicular to substrate or buffer layer surface ([001] orientation). However, the close lattice parameters for different orientations (Fig. 4.11) adds additional complexity and entail a fine control to discern supersaturation conditions for epitaxial nucleation.

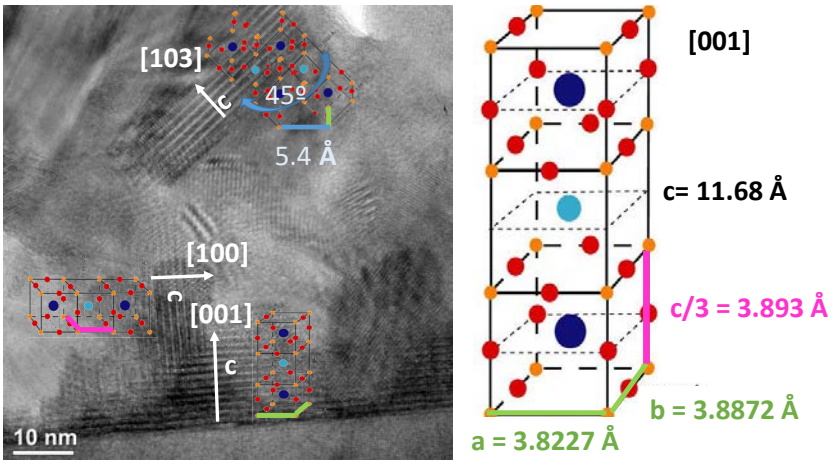

Figure 4.11: TEM image where three different $YBa_2Cu_3O_{7-\delta}$ orientations can be observed with the c-axis of the crystal oriented parallel, perpendicular, or at 45°with the substrate surface. At right, the YBCO cell structure with the lattice parameters. The values for a, b and c/3 are very similar

We name a/b-oriented grains to crystals that grow with c-axis parallel to

substrate surface ([100] orientation). If present, a/b-grains are always observed on c-axis layer nucleated at the substrate interface (Fig. 4.11). They usually grow to the film surface in form of elongated rods.

Occasionally, we have detected a preferential [103] orientation, with c-axis at 45°respect to the substrate surface and also 45°rotated in plane to match the cell diagonal inter-distances.

The crossover behaviour between c-nucleation ([001]) and a/b-nucleation ([100]) is depicted in Figure 4.12 on the basis of the previous described theory applied to a cylindrical shaped nucleus of certain interfacial energies γ [166, 114].

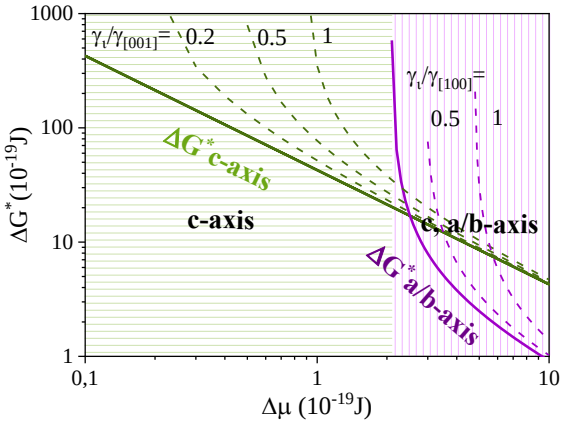

Figure 4.12: Free energies for nucleation of c and a/b-oriented YBCO nucleation versus supersaturation [166]. Calculations for enhanced interfacial surface energies corresponding to different levels of $\gamma_i/\gamma_{[001]}$ exemplifies the effect of substrates with increased lattice mismatch

Free energies (ΔG^*) for nucleation of both orientations are plotted versus supersaturation values. Surface energy of [001] plane is smaller ($0.59 : J/m^2$) than that of [100] plane ($0.82 : J/m^2$) [153]. For this reason, c-axis orientation presents smoother and lower barrier energy than ab-oriented nucleation. However, above a certain $\Delta\mu$ threshold value, ΔG^* for a/b nucleation gets in

the order of c-nucleation and consequently a mixture of both orientations can nucleate.

The choice of an adequate substrate has also a close influence on the early stages of crystal nucleation. The misfit, misorientation, surface morphology and defect structure of the substrate are critical to modify the free energy required for each nucleation type. The effect of increased interfacial energy due to modified strains when the lattice mismatch with YBCO is changed, is also represented in Figure 4.12.

Supersaturation values differ within growth processes and thus each technique requires a particular tuning through processing parameters for controlling nucleation. Hence, thermodynamic considerations will differ from well known TFA-CSD routes and have to be completely new developed.

Consequently, the correlation between supersaturation with T-P_{O_2} processing conditions is essential for the achievement of biaxially textured YBCO. Figure 4.13 represents nucleation free energy barriers (ΔG^*) for both epitaxial orientations respect to processing temperature owing to $C_e(T)$ for two melt compositions and the maximum supersaturation $C_\delta = 10\%$.

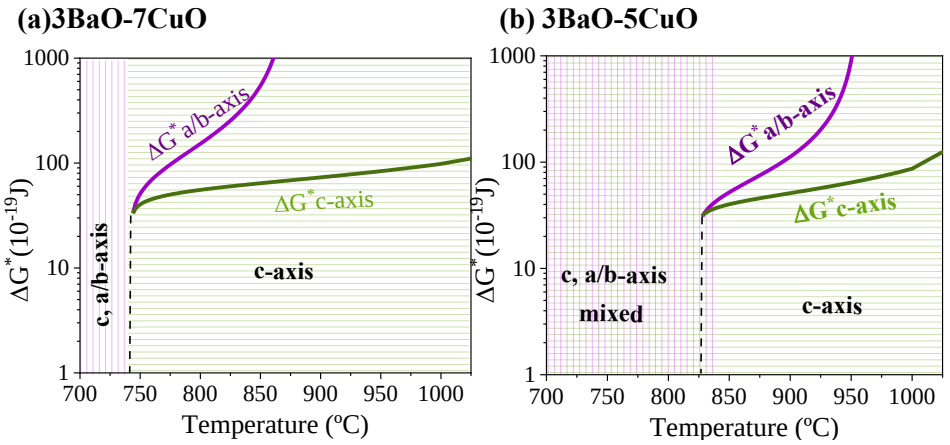

Figure 4.13: Estimation of free energies for nucleation of c and a/b-oriented YBCO nucleation versus temperature in TLAG, owing to a C_δ =10%. C_e(T) are taken from (a)the 3BaO-7CuO melt and (b)3BaO-5CuO

ΔG^* of the two orientations crossover happens at the lowest temperatures, when supersaturation is higher. Below this crossover temperature, a mixed film with heterogeneous ab and c-axis oriented grains will be obtained.

We can observe the temperature for the formation of only c-axis nucleation is ∼100°C lower for the melt matching the eutectic composition, with larger Cu excess respect to stoichiometric $YBa_2Cu_3O_{6+\delta}$ molar ratio.

4.2.5 Rate controlling factors for growth

On the basis of a fully formed transient liquid, then three processes operate in series for film growth:

1. Yttrium dissolution in the melt
2. Yttrium diffusion to the growing interface
3. YBCO nucleation and growth (surface kinetics)

The crystallization process is illustrated in Figure 4.14. At right, schematic representation of yttrium atoms concentration in the three environments: in the Y_2O_3 nanoparticles (C_Y^{YO}), dissolved in the $BaCuO_2{-}CuO_{(l)}$ transient liquid at supersaturated conditions (C_Y^L) and finally in the YBCO solid crystal (C_{xl}^{YBCO}). For reference, the Y equilibrium concentration (C_e) and supersaturation (σ) are also pointed out in the diagram. Composition differences are the driving force for providing the necessary solute for growth.

Only upon understanding kinetics of the three mechanisms, one can clarify what limits growth rate. Hence, growth rate will be adjusted to the slowest step.

Dissolution of Y particles in the melt from Y_2O_3 nanoparticles is determined by $\Delta C = C_Y^{YO} - C_{Y,\delta}^L$, where $C_{Y,\delta}^L \propto \frac{2\gamma_{YO}}{\Delta S_f r}$ and γ_{YO} is the Y_2O_3-Liquid interfacial energy, ΔS_f the volumetric entropy of fusion and r the radius of Y_2O_3 particle [49].

Therefore, Y solubility from the NPs is enhanced by their small size. Since smaller particles have a higher surface energy per unit volume than the larger ones, they tend to dissolve faster.

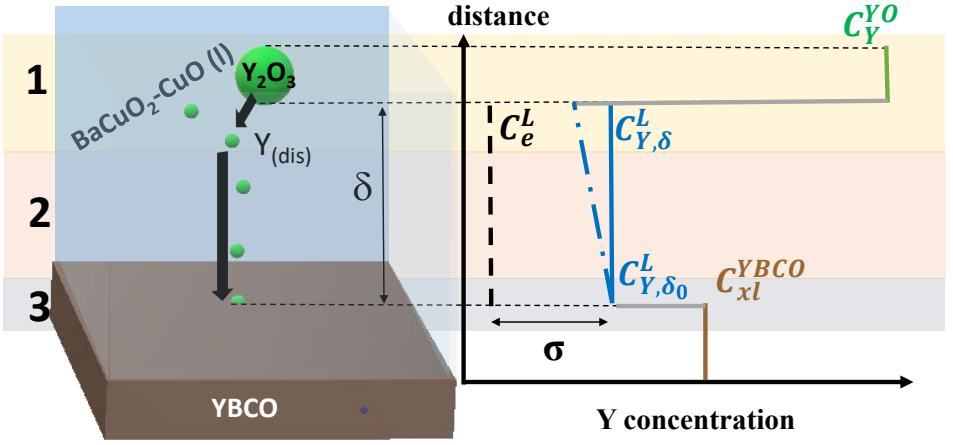

Figure 4.14: Scheme of the steps in the TLAG crystallization process. At right, C_δ depending on the distance δ to the growing interface. C_Y^{YO} is the Y concentration in the Y_2O_3 nanoparticles, C_Y^L, the concentration in the $BaCuO_2{-}CuO_{(l)}$ liquid and C_{xl}^{YBCO} in the forming YBCO crystal phase

Diffusion coefficient D_l for Y in the molten flux (3BaO-5CuO) was estimated to be $4 \cdot 10^{-10} m^2 s^{-1}$ at 870°C [53], but it decreases with temperature as $D_l = \frac{k_D T}{6\pi r \eta}$.

The surface kinetic coefficient was calculated by Kursumovic *et al*, and it is in the range of $k \sim 10^{-5} - 10^{-6} ms^{-1}$ [63]. It slightly depends on temperature as $k \propto \sqrt{T}$ [167], and P_{O_2} conditions. A value for $k = 2 \cdot 10^{-6} ms^{-1}$ will be considered as an approximation for our calculations.

Owing to very small δ distance from the dispersed Y_2O_3 nanoparticles to the growing interface in TLAG and $D > k$, we can consider diffusion to be much faster than interface kinetics in an ideal situation of our system. This fact implies $C_{Y,\delta} \leq C_{Y,\delta_0}$, as drawn in scheme 4.14. Of course, at lower temperatures or when solid species coexist with the transient liquid, diffusion could still be a limiting factor.

Consequently growth rate R is dependent on surface kinetics mechanisms. According to the previous theoretical discussion, R is proportional to the level

of supersaturation and C_e (Fig. 4.15a): $R \sim k\frac{C_\delta - C_e}{C_{xt}} = k\sigma(C_e/C_{xl})$. Where C_{xl} is 17 mol% Y. C_e range from 0.01 to 0.6 for the considered temperatures and melts, and different C_δ are computed.

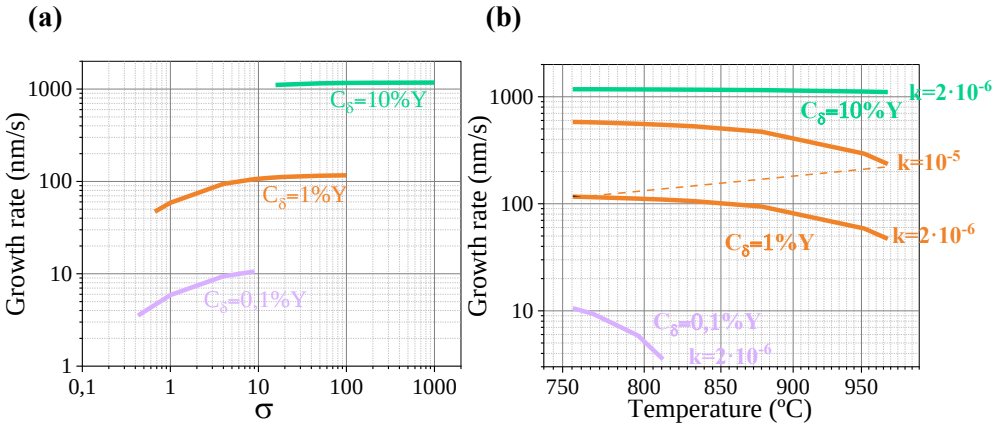

Figure 4.15: Growth rate R in liquid growth limited by surface kinetics at different levels of solubility (C_δ), depending on (a) relative supersaturation and (b) temperature with the 3Ba-7Cu melt. C_e varies from 0.01 mol%Y to 0.6 mol%Y $k = 2 \cdot 10^{-6} ms^{-1}$ is considered in (a) and also $k = 10^{-5} ms^{-1}$ in (b) for $C_\delta = 1\%$. The dashed line suggests the real dependence

We can observe that the major influence on growth rate depends on the order of Y concentration in the liquid C_δ. For the estimated 10% Y, σ varies between 10 and 1000 depending on temperature and melt composition and growth rate around 1000nm/s is calculated. 40-100nm/s would be achieved for 1% of dissolved Y and around 3-10nm/s for 0.1% of dissolved Y.

In Figure 4.15b, an approximated tendency respect to temperature is inferred for Y $C_e(T)$ in the 3Ba-7Cu melt. Growth rate presents a trivial downward tendency with the increase of temperature since supersaturation diminish with it. However, the kinetic coefficient increase with temperature may affect R in a larger extent, as suggested with the dashed line in Fig.4.15b. As a result, growth rate could increase with temperature.

Yet, it is possible that diffusion is hindered for situations which the extent of

liquid is limited, not fully formed or not homogeneously distributed along the thickness. Note that present correlations imply the assumption of an already formed full liquid ($T > T_e$). However, in practical terms apart from growth rate, transient liquid formation is also temperature dependent.

Experimentally, we have proven with *in situ* XRD growth rates up to 100 nm/s at high temperatures for both conversion procedures (T-route and P_{O_2}-route), that will be reported in the corresponding chapters.

4.2.6 Supersaturation and morphology in REBCO techniques

Relative supersaturation σ can vary by several orders of magnitude for different deposition techniques [165]. For instance, Liquid phase epitaxy (LPE)[57, 58] is regarded as a very low supersaturation ($\sigma \sim 0.02 - 0.1$), near-equilibrium with layer-by-layer growth processes. As consequence, very flat surfaces with high degree of perfection are obtained [168].

Tri-phase epitaxy (TPE)[61, 169] or also called Hybrid Liquid Phase Epitaxy (HLPE)[60, 170] techniques overcome mass transport limitations by deposition from a thin flux layer (10-100nm). This fact allows the use of higher relative supersaturation values, typically σ ~0.1-10. The resulting increase leads to faster growth rates (10-35 nm/s) and more induced defects in the films [63].

Among non liquid growth mediated techniques, physical vapour deposition (PVD) and chemical vapour deposition (MOCVD) are commonly treated as high supersaturation growth processes (σ = 10-100). They generally grow through Volmer-Weber mode and tend to present higher density of defects such as growth dislocations, stacking faults and antiphase boundaries. Overall, it leads to increased vortex pinning and higher J_c values.

However, growth rates are limited to 10 nm/s [41, 42] due to the lower atoms concentration on the surface ($10^{-9} - 10^{-6}$) in the vapour as compared to the liquid in LPE ($\sim 10^{-1}$) [44].

Finally, TFA-chemical solution deposition (CSD) also presents Volmer-Weber growth and growth rate is limited to 3 nm/s due to slow solid-gas state diffusion reaction [43].

For TLAG, having very high supersaturation values, Volmer-Weber growth or even normal growth could be expected. Therefore, the resulting micro-

and nano-structure does not necessarily have to reassemble liquid mediated techniques, but it could be more similar to those using highly supersaturated growth processes, as the just mentioned.

4.3 $BaCuO_2$-CuO eutectic reaction

The binary phase diagram for $BaCuO_2$-CuO was measured by several authors for sintered powders [85, 141, 142]. It is represented in Figure 4.16. At high temperatures, above T_l line, any combination of $BaCuO_2$ and CuO leads to a homogeneous liquid. On the other hand, the lowest temperature region is a heterogeneous solid system where $BaCuO_2$ and CuO coexist as separate entities.

At intermediate temperatures, above the system eutectic temperature (T_e), there are two separate regions of partial melting. The formed phases are [$BaCuO_2$ + Liquid] for 50-70 mol% CuO and [CuO + Liquid] for molar percentage between 70-100 mol% CuO.

The solid phases proportion diminish as temperature is raised. The eutectic point in which $T_e = T_l$ corresponds to the molar ratio composition 3Ba-7Cu.

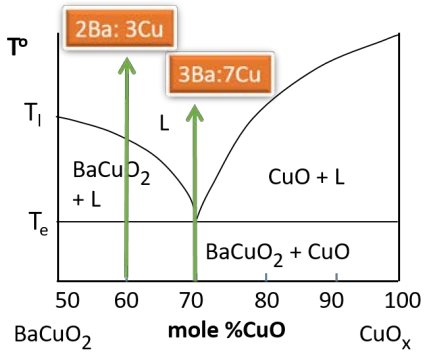

Figure 4.16: Scheme of the eutectic system $BaCuO_2$-CuO phase diagram. Temperatures are dependent on P_{O_2}

In this section, liquid formation temperatures will be explored for pyrolyzed films containing a mixture of $BaCO_3$ and CuO, the TLAG-CSD precursor phases with the exception of Y_2O_3. Two molar compositions will be proven.

The one corresponding to $YBa_2Cu_3O_{7-\delta}$ molar ratio (2BaO-3CuO, 2-3) and the one matching the eutectic point composition (3BaO-7CuO, 3-7).

The films are brought to the same T-P_{O_2} conditions where TLAG growth is performed. Heating rates of 20°C/s using a Rapid Thermal Annealing (RTA) furnace are used to reach the different final temperatures. The samples are held for 2 min before quenching to room temperature. Atmosphere is kept under gas flow at $P_{O_2} = 10^{-3}$ bar. Figure 4.17 reports Grazing incidence X-ray diffraction patterns obtained after the experiment for samples composed of (a) 3-7 and (b) 2-3 compositions. Film thickness is constant and estimated to be around 300 nm before annealing.

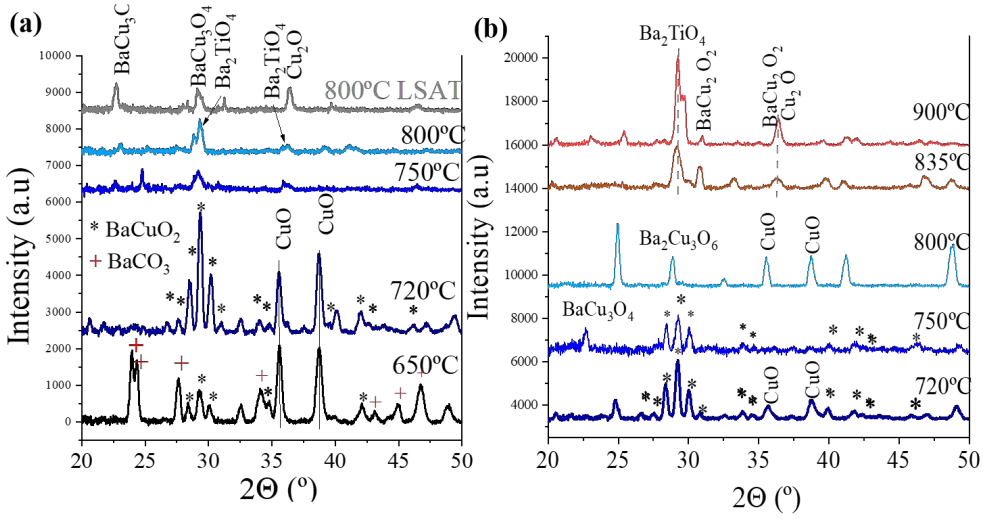

Figure 4.17: Grazing incidence X-ray diffraction patterns after 2 min annealing at high temperatures (dT/dt=20°C/s, $P_{O_2} = 10^{-3}$ bar). Solutions Ba:Cu ratio are (a)3:7 and (b)2:3. All samples are on STO substrate, except for one with 3-7 flux at 800°C, marked in grey

The pyrolysis phases $BaCO_3$ and CuO first react to give solid $BaCuO_2$, the phase in equilibrium according to the BaO-CuO binary phase diagram at this P_{O_2} [158]. The reaction has reached completion at 720°C, in both solutions. We observe that at 650°C with the 3-7 composition, the reaction has already

started but not finished. Since $BaCuO_2$ is a crystalline solid, these would be the conditions below the eutectic line.

XRD patterns change drastically for the experiments above 750°C. On the one hand, 3-7 solution patterns indicate very poor crystallinity. The main peaks that are resolved correspond to Ba_2TiO_4 on STO, indicating that the film has reacted with the STO substrate. At 800°C, their intensity has increased. At the same temperature but on a film deposited on LSAT substrate, reactivity is avoided and the forming phases after quench are $BaCu_3O_4$ and Cu_2O.

Thus, the transformation detected at 750°C is consistent with melting. First, the absence of equilibrium phases (barium cuprate and copper oxide) means that crystallization from the liquid has been impeded by rapid quenching; i.e. most of the film has remained amorphous. Second, enhanced reactivity with the substrate is expected when a liquid is formed. In the LSAT case, the melt would have partially crystallized in form of $BaCu_3O_4$ during cooling.

On the other hand, crystalline $BaCuO_2$ is still present at 750°C, but peak intensity have diminished respect to the initial amount, and CuO has completely disappeared. In parallel, a peak accounted to $BaCu_3O_4$ has appeared. At this point, we can deduce that the eutectic line has been crossed and the results match the expected $BaCuO_2$ + L phases below the liquidus line T_l.

At 800°C the equilibrium phase $BaCuO_2$ has completely vanished. This is an indication that liquidus line has been crossed at this temperature and melt has crystallized in form of other barium cuprate phases while cooling. In accordance, Ba_2TiO_4 appears above 835°C as consequence of melt reaction with the substrate, which intensity increases with temperature rise. CuO has reduced to Cu_2O, as expected at these temperatures.

Corresponding films images by optical microscopy are presented in Figure 4.18. Films annealed between 650-720°C, which contain the $BaCuO_2$ and CuO solid phases, are dense and continuous. At higher temperatures, melt formation is evidenced from the micron size drops leaving a large uncovered substrate surface as a consequence from liquid dewetting. The poor wetting behaviour of this melt is well known [171]. Hence, liquid like morphologies are observed above 750°C and 800°C for compositions 3BaO-7CuO and 2BaO-3CuO, respectively. Thus, the eutectic and liquidus reactions are confirmed from the solidification microstructure and they agree with the XRD results.

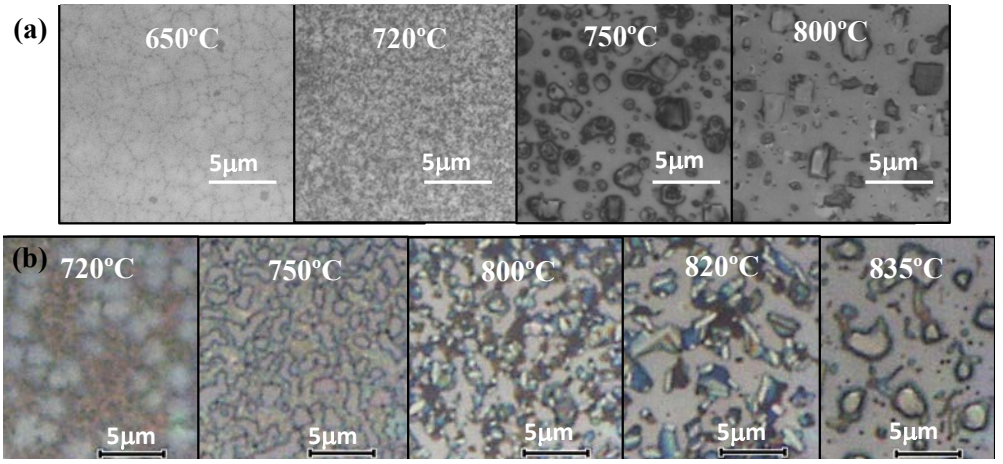

Figure 4.18: Optical images at 100x magnification of the films in Fig.4.17. Solutions Ba:Cu ratio are (a)3:7 and (b)2:3

Higher resolution surface images are obtained by means of Scanning electron microscope (SEM) and are shown in Figure 4.19. Film (a) at 720°C is composed of $BaCuO_2$ and CuO nanometer size grains conforming a dense film. The same 3-7 composition annealed above 750°C shows characteristic liquid drops on a dewetted substrate surface. Some of these crystallized drops are up to $5\mu m$ in diameter size and both rounded and squared shape grains can be observed. Electron dispersive x-ray spectroscopy (EDX) analyses on several grains indicate different Ba-Cu-O ratios with some smaller Ti and Sr signals (not shown here).

Film (b), corresponding to stoichiometric 2Ba-3CuO ratio, doesn't show the same microstructure until 820°C. At 750°C, the remaining solid $BaCuO_2$ between eutectic and liquidus line has coarsened joining several grains that compose larger structures. Completely different crystals are revealed from the films annealed to 800°C. The new phases could be produced after crystallization of the melt during cooling. Still, liquid dewetting is not widely observed. This fact points out that atomic diffusion is still limited in this case.

Consequently, we could deduce eutectic and liquidus temperatures for the two

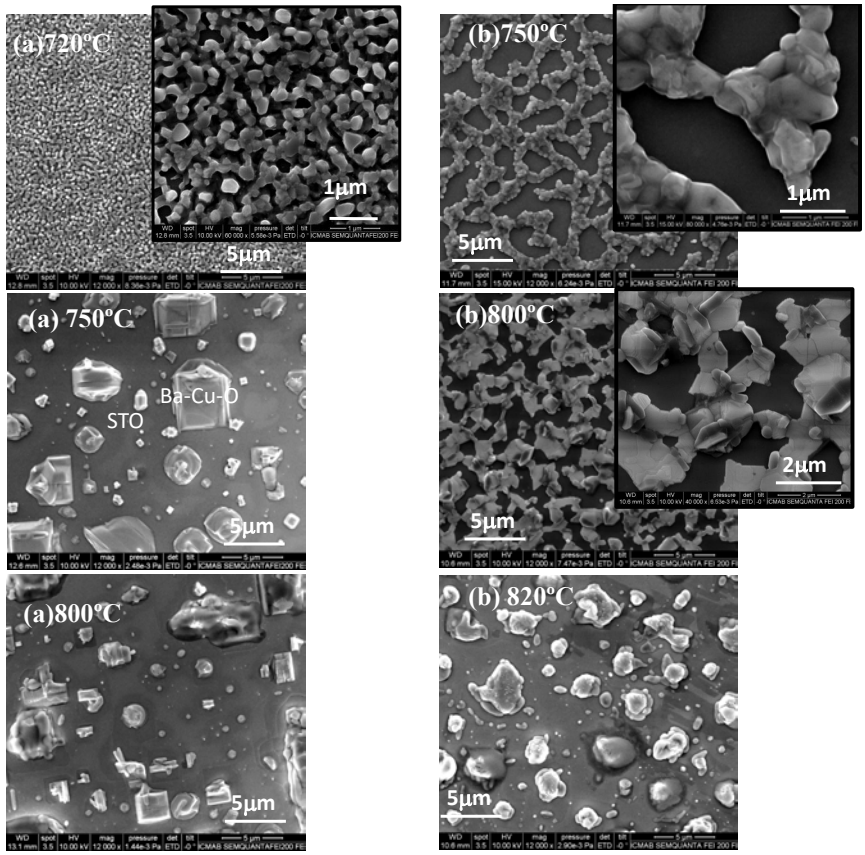

Figure 4.19: SEM images of the films in Fig.4.17. Solutions Ba:Cu ratio are (a)3:7 and (b)2:3

compositions that will be studied along this thesis, and for similar processing conditions (i.e. heating rates of 20°C/s).

Heating rate seems to be an important parameter. The binary system was analysed by *in situ* XRD at rates of 5°C/s, and onset melting for the 3-7 eutectic composition at 10^{-3} bar was 765°C [115]. Our results on fast heating experiments have pointed out complete liquid formation already between 730-750°C. Therefore, temperature has decreased by about 20°C by increasing the heating rate a factor 4.

This fact could be related to influence of grain sizes as found in other systems [172] and could also explain the temperature shifts between thin films and bulk. However, more experiments should be performed at different rates to confirm if T_e and grain sizes significantly change with heating rate.

4.4 Conclusions

Transient liquid assisted growth (TLAG) is based on the formation of the [$BaCuO_2$-xCuO] transient liquid in the region of the phase diagram where solid YBCO is the equilibrium phase. The kinetic hindrances in YBCO crystallization from these solid precursor phases are advantageously used to generate the eutectic liquid from the binary system instead. Then, upon dissolution of the Y_2O_3 nanoparticles in the Ba-Cu-O transient liquid and Y diffusion towards the substrate interface, the fast epitaxial growth of YBCO occurs.

Therefore, in contrast to other existing methodologies, the working window of processing conditions is the stability zone of $YBa_2Cu_3O_{7-\delta}$, at relatively low temperatures, even below the eutectic temperature of the binary system composting the liquid, and atmospheric pressure. Two paths are proposed to reach the growth region: through heating at a constant P_{O_2} (T-route) or by a P_{O_2} jump at constant temperature (P_{O_2}-route).

The existence of this liquid with the used compositions and processing conditions of TLAG has been proven with experiments using the binary mixture ($BaCO_3$+CuO). The eutectic composition 3Ba:7Cu leads to 100% liquid at lower temperatures than the stoichiometric 2Ba:3Cu ratio. The latter has the $BaCuO_2$ phase as solid intermediate until the liquidus line is surpassed at higher temperatures.

TLAG can be understood as a type of high temperature solutions growth technique. The relation between Y concentration in the transient liquid (C_δ) and the equilibrium solubility (C_e(T)) is the driving force for nucleation. Hence, the values of these two factors are the key parameters to understand the resulting nucleation processes and the growth rate of the forming crystal.

C_e basically depends on temperature and the Ba:Cu ratio composition of the melt. While C_δ can not be directly controlled or measured. The dissolution

process takes place *in situ* from the big quantities of Y in the Y_2O_3 nanoparticles when the melt is formed. Yet, very high values of relative supersaturation $\sigma = (C_\delta/C_e) - 1$ are foreseen $(100 - 1000)$. Hence, the supersaturation conditions in TLAG would be much higher than those in the other solution growth techniques for REBCO.

On the one hand, this fact entails a fine control of nucleation, since the different $YBa_2Cu_3O_{7-\delta}$ crystal orientations are favourable at high supersaturation values. Conditions for epitaxial growth are more likely to be reached as temperature increases and with a Cu excess composition.

On the other hand, owing to the low diffusion distance of Y from the close Y_2O_3 particles to the growing interface, and the high diffusivity in the liquid, the limiting step for growth rate is thought to be interface surface kinetics. High growth rates (R) are expected since $R \propto \sigma$.

Chapter 5

TLAG Temperature-route

In TLAG Temperature-route, YBCO crystallization takes place upon Y dissolution in the transient liquid formed while heating at a constant pressure. These conditions are achieved at P_{O_2} higher than $2.4 \cdot 10^{-4}$ bar, the region where $BaCO_3$ and CuO precursors decomposition lead to solid $BaCuO_2$, and to transient liquid in subsequent reactions during heating.

Epitaxial growth is achieved through tuning of supersaturation conditions. Liquid composition and RE element solubility in the melt are the relevant parameters influencing nucleation. Two different liquid stoichiometries are compared: 2BaO-3CuO ($YBa_2Cu_3O_x$) and 3BaO-7CuO ($YBa_2Cu_{4.66}O_x$). It is of interest to correlate experimentally supersaturation values with processing conditions to promote c-axis growth.

Then, YBCO growth is studied by means of *in situ* XRD from synchrotron radiation together with TEM images. Very high growth rates up to ~100 nm/s will be demonstrated.

Liquid assisted growth, however, exposes new challenges that need to be properly overcome. Liquid reactivity with the substrates or buffer due to its highly corrosive nature, improper substrates wettability with the viscous liquid, remaining liquid at grain boundaries giving rise to percolative currents, are some of them. We report an investigation of the cause of this phenomena as well as possible solutions to minimize their effect.

Finally, resulting epitaxial films microstructure and nanosize defects will be correlated to processing conditions and superconducting performances. Films up to 3 MA/cm^2 at 77K, self-field could be achieved with T-route, while in-field behaviour is enhanced by small ab grains acting as pinning sites in pristine films.

5.1 Supersaturation tuning for epitaxial $YBa_2Cu_3O_{7-\delta}$ nucleation

In Chapter 4 we have stated the basic crystallization rules for TLAG. The type of $YBa_2Cu_3O_{7-\delta}$ predominant nucleating orientation depends on relative supersaturation of yttrium in the liquid which is defined as

$$\sigma = \frac{C_\delta - C_e(T)}{Ce(T)} = \frac{C_\delta}{C_e(T)} - 1 \tag{5.1}$$

where $C_e(T)$ is the equilibrium concentration at a particular temperature and C_δ is the real concentration of yttrium in the liquid.

Now, both C_δ and $C_e(T)$ have to be inferred for the particular conditions of T-route and correlated to resulting forms of crystallization. The possible observed orientations are: randomly oriented grains, textured with the ab plane perpendicular to the substrate (ab-axis nucleation) or biaxially textured with the c-axis oriented perpendicular to the substrate (c-axis nucleation).

The latter is the desired one because it permits the highest current flow within the ab plane of the material due to its anisotropy.

5.1.1 Nucleation control with temperature and melt composition at ultrafast heating rates

With the aim of studying YBCO nucleation in isothermal conditions with the temperature path, we performed these experiments using very fast heating rates (60°C/s) with a Rapid Thermal Annealing (RTA) furnace.

Under ultrafast ramps, we expect that all conversion reactions, and so YBCO nucleation and growth processes, proceed in isothermal conditions at the defined final temperature while nucleation at lower temperatures during the heating step is avoided. We can now disclose the temperature dependence of YBCO nucleation processes.

Several samples were processed with TLAG T-route path to different final environments. Two solution compositions are compared corresponding to the YBCO stoichiometric composition (Y:2Ba:3Cu) and the (3Ba:7Cu) eutectic

liquid (Y:2Ba:4.66Cu), with Cu excess. The resulting crystal structures were characterized with X-ray diffraction using a 2D GADDS detector.

200 nm pyrolyzed films of the two studied melt compositions were heated to several T-P_{O_2} conditions and hold for 2 min before fast cooling. Atmosphere was controlled by N_2:O_2 gas flow at 1 bar of the desired P_{O_2}.

$YBa_2Cu_3O_{7-\delta}$ nucleation

In Figure 5.1a, the fraction of biaxially textured YBCO with c-axis perpendicular to the substrate surface is depicted with respect to other possible orientations (homogeneous nucleation and a/b-oriented grains). These values are displayed for the different processing temperatures, P_{O_2} and compared for both liquids.

Epitaxial fractions were inferred from X-ray diffraction analyses, which procedures are detailed in section 2.2.4.3. The corresponding integrated patterns are displayed at appendix Figure 7.1.

XRD diffraction patterns show no remains of $BaCO_3$ and CuO precursors or $BaCuO_2$ intermediate, thus indicating that the prior reactions have attained full completion.

The two liquid compositions show different dependence of YBCO nucleation processes with temperature. It can be observed in Fig.5.1c that for the same annealing conditions at 650°C, composition corresponding to the eutectic point (Y:2Ba:4.66Cu) leads to >95% epitaxial YBCO nucleation and growth, which is maintained in all the temperature range explored.

With the stoichiometric solution (Y:2Ba:3Cu) homogeneous and a/b-oriented nucleations are also present. Competition between crystallization orientations diminishes when raising temperature, achieving only c-axis YBCO at temperatures above 750°C for both P_{O_2} explored.

All YBCO orientation relative quantities for 2:3 liquid and 60°C/s heating rate are disclosed in Figure 5.2. For temperatures below 700°C, a/b oriented grains represent a ∼50% of total YBCO at $P_{O_2} = 10^{-2}$ bar and ∼30% at $P_{O_2} = 10^{-3}$ bar, while random grains fractions are much lower, 12% at 615°C and 1.7% at 700°C.

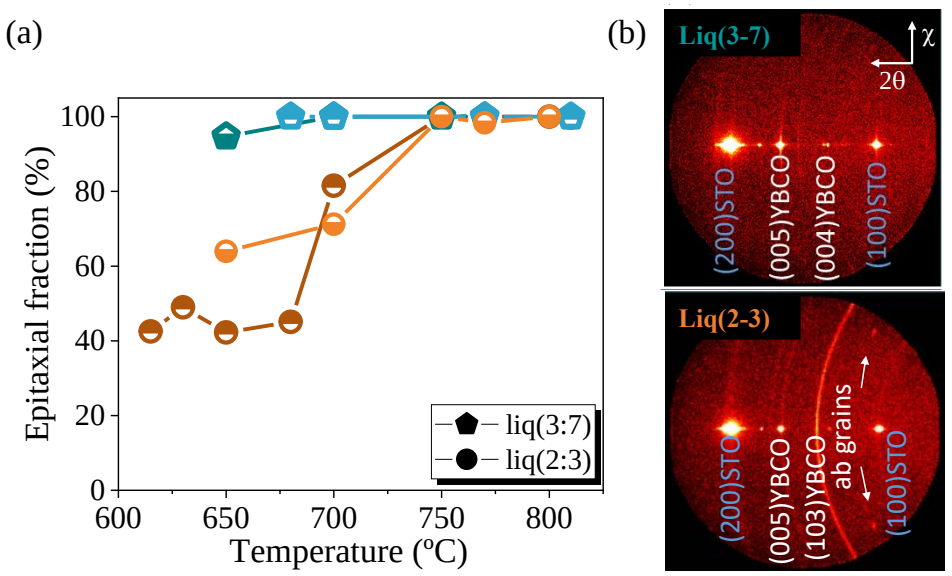

Figure 5.1: (a) $YBa_2Cu_3O_{7-\delta}$ epitaxial fraction respect to ab grains and polycrystalline nucleation for samples grown at 60°C/s. Liquid composition is indicated with different symbols and colours ((3:7)melt bluish ⬠and 2:3 melt orange ○) while P_{O_2} is shown with open symbol at the upper part (10^{-3} bar) or at the lower part (10^{-2} bar) of the symbols. (b)2D XRD frames corresponding to samples grown at 650°C and 10^{-3} bar O_2

Supersaturation conditions: C_e tuning

The differences on the resulting crystal orientation depending on melt and growth temperature can be assigned to different supersaturation σ values. As an approximation, this is proportional to the C_δ/C_e ratio.

Homogeneous and a/b-axis orientation require of a larger supersaturation to nucleate than c-axis orientation due to interfacial energies of the resulting configurations (see Chapter 4.2.4). Hence, completely c-axis epitaxial $YBa_2Cu_3O_{7-\delta}$ will only be achieved at small enough σ values.

If C_δ is assumed similar for both liquids, since $C_e(T)$ increases with Cu content in the liquid [163], σ will indeed be lower for the (3:7) melt [170]. An

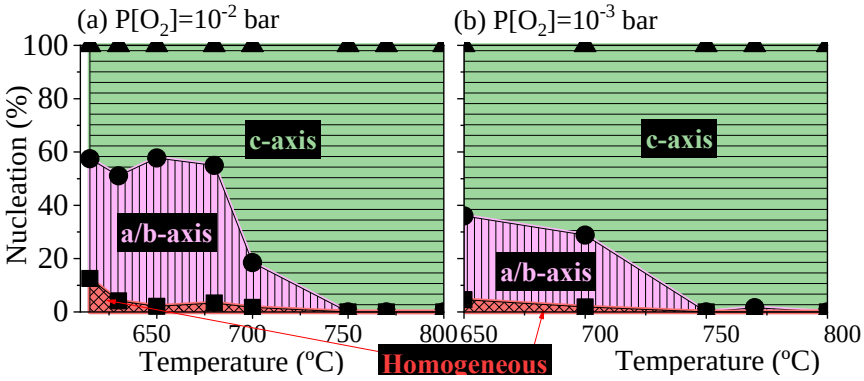

Figure 5.2: Relative quantities of resulting YBCO orientation (c, a/b-axis or homogeneous nucleation) for 2:3 liquid and 60°C/s heating rate under P_{O_2} of (a) 10^{-2} bar and (b) 10^{-3} bar

extended theoretical discussion is given in section 4.2.3.

A lower supersaturation for (3:7) melt is confirmed with the experimental results by the formation of only c-axis epitaxial YBCO in all the temperature range explored.

Instead, with the stoichiometric (2:3) liquid below 750°C, the lower C_e increases σ greatly enough to allow higher energetic homogeneous nucleation and a/b grains formation.

Then, intrinsic C_e increase with growth temperature is reflected on the drop of other orientations above this temperature due to σ reduction.

As a consequence, the temperature window for epitaxial growth is larger with the Cu excess composition, permitting the formation of fully c-axis oriented film at temperatures as low as 650°C. For the stoichiometric composition, it is achieved above 750°C.

Secondary phases

However, phases other than YBCO are present at high temperatures when ultrafast growth rates are used. In Figure 5.3a we display the total intensity of c-axis YBCO as function of the processing final temperature. Although solution

(3:7) presents a higher amount of epitaxial YBCO at lower temperatures, it drops above 700°C. In contrast, composition (2:3) c-axis keeps increasing in accordance to a higher epitaxial fraction. XRD of films grown at 770°C for 2 min (Fig. 5.3b,c) indicate that secondary phases are different for the two compositions.

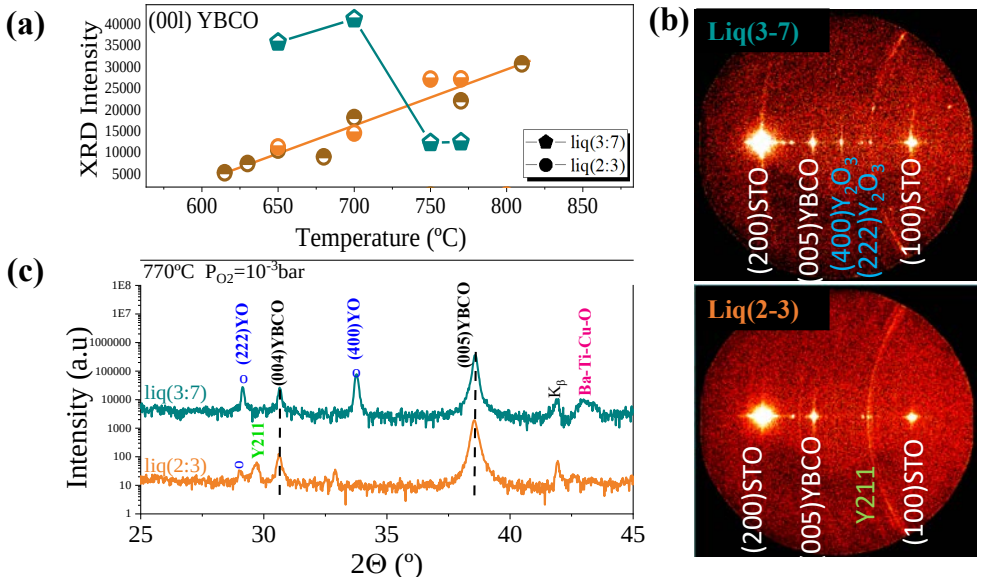

Figure 5.3: Samples grown at 60°C/s. Liquid composition is indicated with different symbols and colours ((3:7)melt turquoise ⬠and (2:3)melt orange ○) while P_{O_2} is shown with open symbol at the upper part (10^{-3} bar) or at the lower part (10^{-2} bar) of the symbols. (a)XRD intensity of (005)YBCO epitaxial reflection depending on final temperature. (b)2D-XRD frame at 770°C and 10^{-3} bar O_2. (c) Corresponding χ-integrated diffraction patterns

On the one hand, for Cu excess composition, intense peaks at 2θ 29.1°and 33.7°correspond to (222) and (400)Y_2O_3 orientations, respectively. Then, a peak at 43°is accounted to phases containing Ba, Cu and some amount of Ti, as a consequence of reactivity with STO substrate. These phases have been identified in several occasions by means of EDX in TEM and SEM observations.

On the other hand, the stoichiometric composition shows some amount of Y_2BaCuO_5 (Y211), the so called "green phase", instead of yttria. A phase that is actually the Y-rich secondary phase coexisting with YBCO or a product of YBCO decomposition [143, 173].

Kinetic processes are enhanced with rapid heating, giving access to formation of higher energy metastable phases, as for example the 211 phase.

Precipitation of either Y211 or Y_2O_3 preference was shown to be influenced by lattice matching and supersaturation, that can modify the relative importance of surface (favouring Y_2O_3) and volume (favouring Y211) energy terms in nuclei formation [174].

The 211 phase can be observed with SEM images of stoichiometric solution samples as incoherent inclusions within c-axis YBCO (Fig. 5.4). The length of grains increases with temperature, from 5 μm to 20 μm and 50 μm at 700, 750 and 770°C, respectively. Above 800°C, 211 phase diminishes while other secondary phases products from reactivity with the substrate rise.

Partial conclusions

As a result, we identify different events occurring depending on solution composition at ultrafast rates: non reacted Y_2O_3, reactivity with the substrate cations and formation of Y_2BaCuO_5 metastable phase. The nature of these processes and the influence on heating speed are elucidated in the next sections.

Still, this fact does not affect previous conclusions where $C_e(T)$ is the main reason for lower supersaturation and preferred c-axis nucleation in the Cu rich composition, since those phases are not observed at the lowest temperatures.

Overall, this section demonstrates that complete fast liquid mediated growth of epitaxial YBCO is possible at temperatures as low as 650°C, much below the $BaCuO_2$-CuO eutectic temperature. This fact brings unique opportunities to film manufacturing by employing rapid thermal annealing furnaces.

5.1.2 Nucleation control with heating rate

In this section, the effects of heating rate on YBCO crystallization related to supersaturation will be disclosed for the TLAG temperature path.

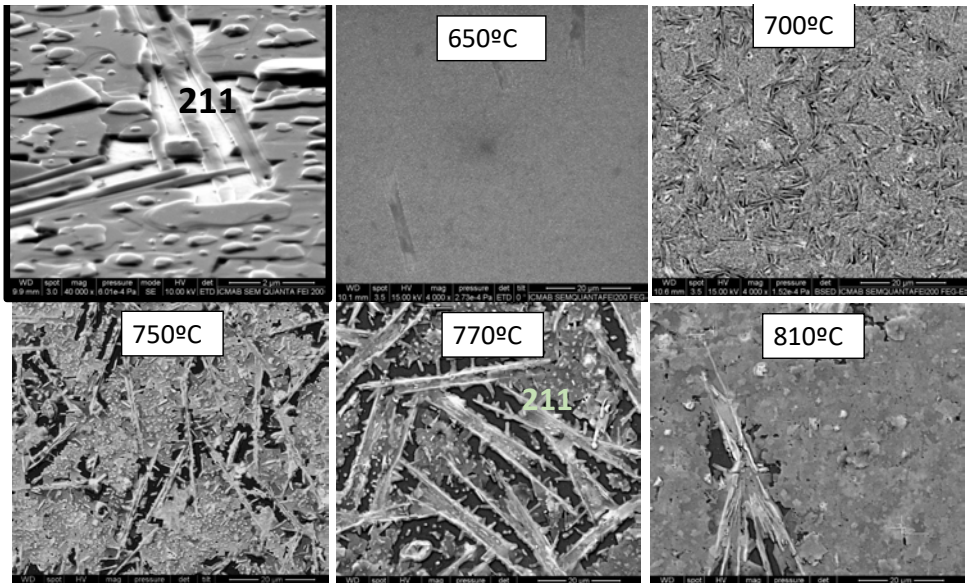

Figure 5.4: Surface SEM images where Y_2BaCuO_5 elongated grains inclusions within YBCO matrix can be observed at different annealing temperatures for (2:3)liquid films reached at 60°C/s under 10^{-3} bar O_2

We have demonstrated that epitaxial growth can be achieved by tuning thermodynamic supersaturation with processing temperature and liquid composition. Now, the use of lower heating speeds seems necessary to restrict the occurrence of undesired kinetically favoured events described above when annealing at 60°C/s.

Pyrolyzed films were heated up to several temperatures using different heating rates: slow (0.4-2°C/s, brown), fast (20°C/s, blue) and ultrafast (60°C/s, pink) rates. P_{O_2} was fixed at 10^{-3} bar. A tubular furnace was used for 0.4°C/s rates and a Rapid Thermal Annealing (RTA) for faster heating speeds.

All presented samples have attained full precursors conversion and orientations percentage is not altered if longer dwells at final temperature are carried out. However, long holding times at high temperature have been shown to produce film dewetting [175]. Possible secondary phases are not considered in

this section, a matter that will be discussed separately in the next sections.

The resulting YBCO orientations percentage have been deduced from 2D-XRD measurements using random fraction and a/b-axis fraction calculations. This methodology is described in section 2.2.4.3. The results are displayed in Figure 5.5 for the two studied liquid compositions. Representative integrated 2θ spectra are at the Appendix in Figure 7.2.

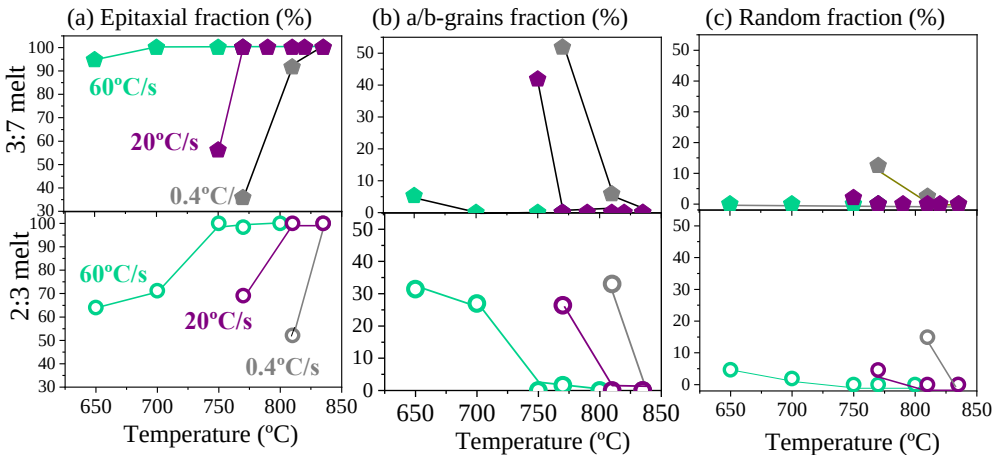

Figure 5.5: Relative percentages for obtained YBCO orientations depending on processing temperature for different heating ramps and the two melt compositions. 3:7 at left and 2:3 at right columns. Line (a)c-axis epitaxial growth, (b) a/b-axis oriented grains and (c) polycrystalline grains. Heating ramps are coloured in pink (60°C/s), blue (20°C/s) and brown (0.4°C/s). Samples were hold for 2-5min before cooling and $P_{O_2} = 10^{-3}$ bar

For the same final temperatures, films processed at slower heating rates have higher presence of homogeneous nucleation and ab grains. The occurrence of both non desired crystallization types decreases when rising the final temperature, the heating ramp or Cu in the liquid composition.

Random YBCO nucleation is found in small amounts (Fig.5.5c). A maximum of 15% random fraction explored so far has been calculated to be formed at 800°C with a rate of 0.4°C/s with the stoichiometric composition. 12% is the

maximum calculated for the eutectic composition at 770°C.

The a/b-axis grains (Fig. 5.5b) can represent a 50% of total YBCO using the slowest rates.

Figure 5.6a summarizes the crossover temperatures for the achievement of fully epitaxial YBCO layers at each heating rate and for both compositions. Additionally, the degree of epitaxial fraction is indicated in contour maps in Fig.5.6b.

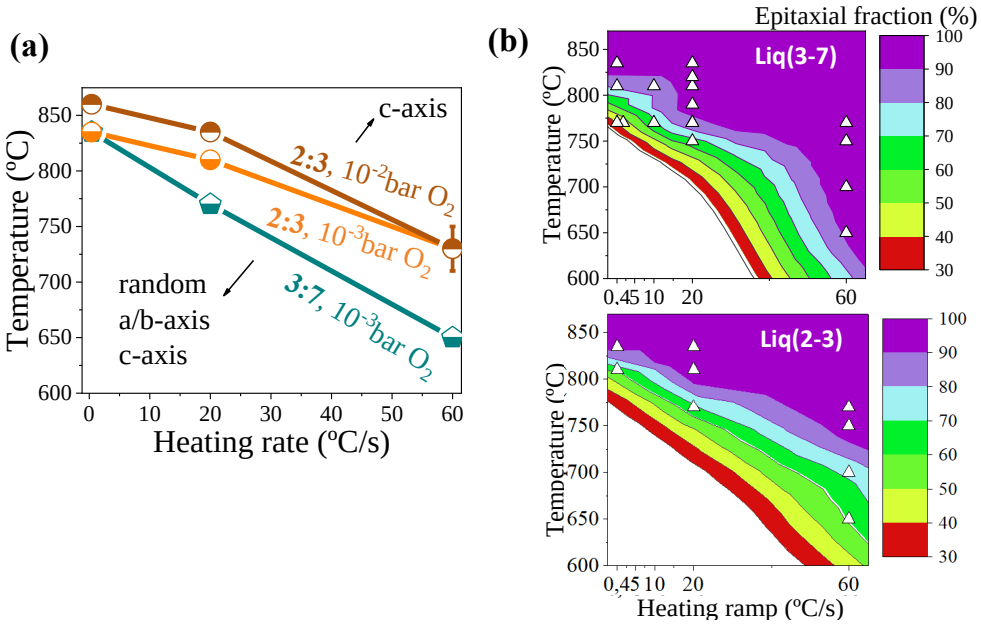

Figure 5.6: (a) growth temperature crossover for YBCO crystallization with >95% of biaxial texture (c-axis) depending on heating rate and for the two studied melt compositions and P_{O_2}, indicated in the graph. (b) Contour maps of YBCO epitaxial fraction obtained depending on temperature-heating ramp conditions for both liquids at 10^{-3} bar O_2

For instance, at $P_{O_2} = 10^{-3}$ bar with the Cu excess solution, fully epitaxial layer is achieved at 650°C at 60°C/s, 770°C at 20°C/s and 835°C at 0.4°C/s. Instead, with stoichiometric composition c-axis is obtained at higher temper-

atures; at 750°C, 810°C and 835°C , by the above mentioned heating rates respectively. Even higher temperatures (+20°C) are needed if P_{O_2} is increased to 10^{-2} bar.

Discussion

The previous discussed tendency regarding promotion of epitaxial nucleation at higher temperatures and with the increase of Cu in the melt composition is maintained for the other heating rates (Fig. 5.5a). These changes are a consequence of C_e behaviour, inversely proportional to supersaturation.

However, the dependence on nucleation and supersaturation with heating rate can not be explained by changes in C_e. This fact points out the influence of kinetic factors in this process. Different facts have to be considered from several steps during TLAG growth:

Liquid formation Transient liquid is formed as soon as precursors react during the thermal profile, and so YBCO nucleation can occur before the final processing temperature, specially with slow heating rates (see section 3.4.2.2).

Solid phases The presence of solid secondary phases in the liquid can contribute to induce an undesired homogeneous growth at these sites [154].

Supersaturation Y dissolution and diffusion kinetics may influence the resulting C_δ, and so supersaturation.

Nucleation rate An induction period of nucleation (t_{ind}) is needed to start YBCO nucleation after formation of the supersaturated liquid, which is inversely proportional to σ.

The first evidence explains partially the higher degree of random and a/b-oriented nucleation achieved with the decrease of heating ramp. Both require highly supersaturated solutions to surpass larger free energy barriers for nucleation (ΔG^*). First, slower conversion reactions are produced with slower heating rates. In this situation (0.4°C/s), precursor phases and solid $BaCuO_2$ with the 2:3 melt are still present during YBCO formation, which can be a source for disoriented nucleation.

Second, slow heating rates produce conversion reactions at lower temperatures, and so YBCO nucleation. Consequently, crystallization is attained before the final processing temperature, where σ values are higher due to $C_e(T)$ tendency.

This is unlikely to happen with the faster heating rates (>20°C/s), when there is not time enough to overcome the induction period of nucleation during the heating ramp.

Still, C_e change within the possible nucleation temperature discrepancies is not large enough to induce the colossal nucleation differences observed. Hence, C_δ must vary in a larger extent with heating rate, thus altering the C_δ/C_e ratio proportional to supersaturation.

Differently from high temperature liquid techniques such as HLPE, in transient liquid the amount of dissolved Y can not be directly controlled since the Y_2O_3 nanoparticles are already present in the film, and we don't have any way to measure these values at present. The C_δ values can only be deduced from the results on crystallization. Lower σ, and thus lower C_δ, are obtained at faster heating rates since the YBCO epitaxial fraction increases.

One would expect the opposite, since fast heating rates are known to hinder coarsening of precursor phases. This fact would result on smaller particles size, fastened precursors intermediate reactions and enhanced Y dissolution in the melt from Y_2O_3 nanoparticles (see section 4.2.5).

More studies on YBCO growth mechanisms are necessary to provide more insight on determining which is the rate limiting factor for Y supersaturation in the liquid. We have been able to perform so far *in situ* experiments at slow heating rates, up to 5°C/s, which are discussed in the following section.

Partial conclusions

The epitaxial samples of each composition and heating rate are represented in the T-P_{O_2} phase diagram in Figure 5.7.

The temperature window for epitaxial growth is very wide, as compared to classic CSD or vacuum deposition techniques [59]. Obviously, this is because supersaturation has a particular T-P_{O_2} dependence in each technique.

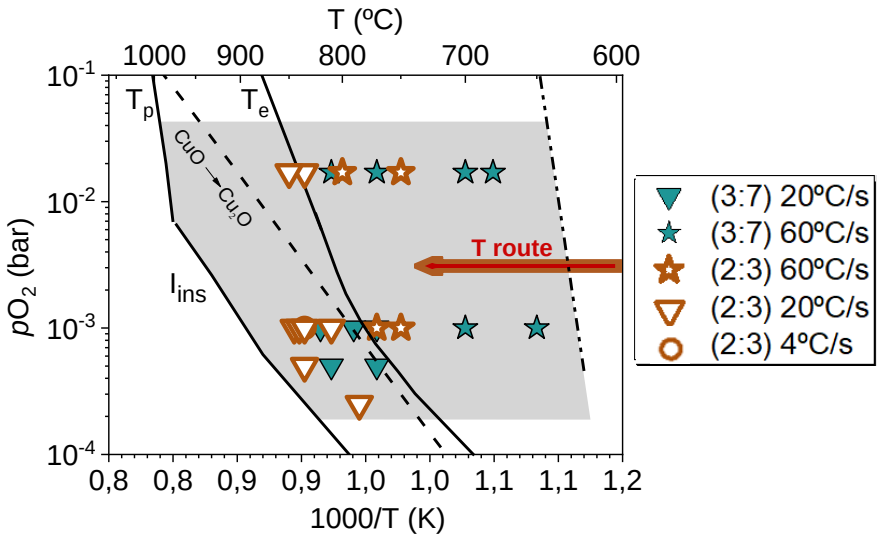

Figure 5.7: T-P_{O_2} phase diagram where symbols are epitaxial samples: open brown symbols (2:3 composition) or closed turquoise symbols (3:7 composition). Heating rates are 60°C/s ($\star$), 20°C/s ($\triangledown$) and 0.4°C/s ($\bigcirc$)

In TLAG, the growth of epitaxial YBCO thin films can be performed at all heating rates, but the final temperature depends on the heating ramp. Since it is a kinetically driven process, when high heating rates are used, the Y ions dissolution from the Y_2O_3 nanoparticles into the melt might be compromised, and the Y concentration in the liquid, C_δ, will decrease. As a consequence, the relative supersaturation of the liquid σ will drop, leading to the enhanced c-axis nucleation and growth window observed.

Additionally, our results point out that in all cases epitaxial nucleation is favoured at higher temperatures and using the liquid Cu excess composition, while lower P_{O_2} is preferred.

5.2 YBCO growth

In the temperature route, all precursor reactions and YBCO formation from liquid take place consecutively while heating. *In situ* XRD analysis with synchroton light and high resolution scanning transmission electron microscopy (STEM) have enabled us to disentangle YBCO growth mechanisms, growth rates and their link to processing conditions and precursors transformations.

5.2.1 *In situ* XRD studies of YBCO growth

Only with fast acquisition *in situ* XRD during synthesis, YBCO nucleation temperatures and growth rates can be directly inferred. Two stays at DiffAbs beamline in Soleil synchrotron allowed us to follow the transient liquid assisted growth of YBCO with from acquisition times every 100 ms with good resolution.

Previously pyrolyzed films on STO substrates were annealed inside a chamber under the chosen gas conditions. A maximum of 5°C/s heating rate could be used with the provided heater stage. Films thicknesses were around 400 nm after growth. More details on the methodology and data analysis can be found in section 2.2.5.

The different forms of YBCO crystallization are distinguished by the X-ray diffraction intensity of their main reflections: (103) for the homogeneous and (005) for c-axis heterogeneous nucleation, acquired in the same 2θ-χ frame. Unfortunately diffraction peaks corresponding to the ab-axis heterogeneous nucleation could not be observed in the same range.

After data treatment, the main reflections intensities are normalized by their maximum intensity, which we approximate proportional to the phase molar amount. Then, the normalized intensities plotted with temperature or time show the phases evolution.

Samples composed by the two studied compositions, (Y:2Ba:3Cu) and (Y:2Ba:4.66Cu), were heated to high temperatures using different heating ramps at $P_{O_2} = 10^{-3}$ bar.

5.2.1.1 Ultrafast growth of epitaxial $YBa_2Cu_3O_{7-\delta}$

As deduced in the last section, the use of fast heating rates favours epitaxial nucleation. Figure 5.8 shows time-resolved YBCO growth, together with all solid phases evolution when heating at a velocity of 5°C/s for (a) stoichiometric and (b) Cu excess compositions.

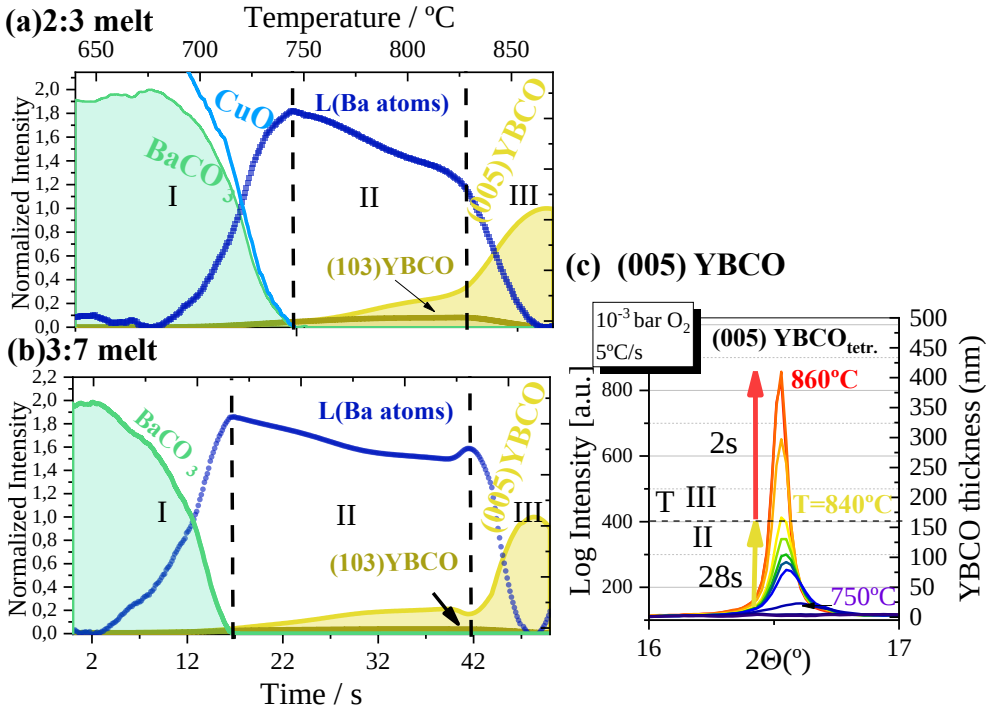

Figure 5.8: Time-resolved solid species evolution at a heating rate of 5°C/s for (a)2Ba:3Cu and (b)3Ba:7Cu liquid composition under $P_{O_2} = 10^{-3} bar$, $P_{tot} = 1 bar$. XRD intensities have been normalized to their respective molar amounts, while random YBCO nucleation has been normalized to the epitaxial YBCO intensity. Blue circles indicate predicted evolution of the liquid. (c)Evolution with temperature of (005)YBCO reflection from (b)

One can observe that there is a delay between precursors decomposition and $YBa_2Cu_3O_{7-\delta}$ formation, as well as thermal zones with distinct growth rates:

- I Precursors are decomposing and metastable liquid is formed in parallel
- II Slow YBCO growth from metastable liquid, below T_e
- III Fast YBCO growth from liquid, above T_e

No other significant solid phase are observed in zone II. The corresponding full scans for (2:3) liquid at 5°C/s are represented in Figure 5.9.

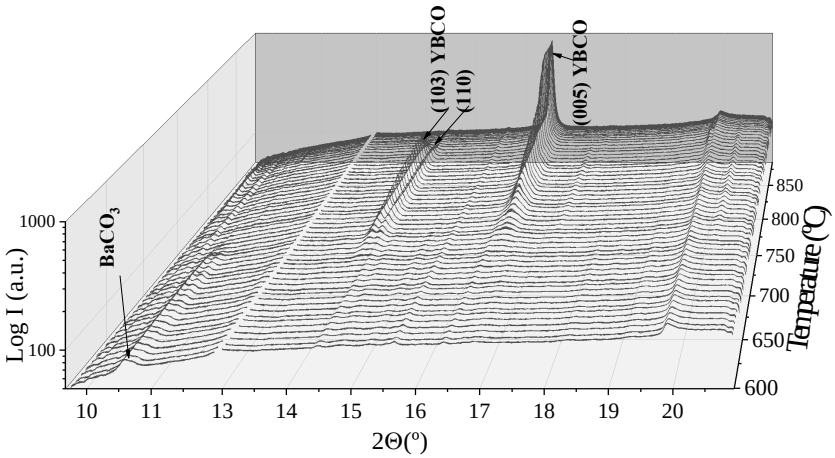

Figure 5.9: χ-integrated X-ray diffraction spectra during heating at 5°C/s the stoichiometric composition pyrolysis under 10^{-3} bar O_2. An intense peak from the heater at 2θ =12°has been eliminated for better visibility of the other phases

Only a small peak at 2Θ 20.3°(X-ray energy=18 keV) can be accounted to Ba_2CuO_3(s) secondary phase evolving and decomposing in parallel to liquid, but in very small extent. This phase will not be taken into account in this study due to low quantity that represents.

As a consequence, the absence of other solid phases at the onset of YBCO crystallization directly demonstrates the existence of the transient liquid phase.

The amount of liquid (blue circles in Fig. 5.8) can be predicted using the atoms conservation method. The overall solid species relation can be described

as:

$$2\,BaCO_3 + (3+z)CuO + \frac{1}{2}\,Y_2O_3 \longrightarrow YBa_2Cu_3O_{7-\delta} + zCuO \tag{5.2}$$

where z is 0 for the stoichiometric composition and 1.7 of Cu excess for (3:7) melt.

Since no other intermediate phases are detected by XRD, Ba atoms must be shared between $BaCO_3$, YBCO and the liquid.

$$M_{Ba\,(l)} = 2 - 2\,M_{YBCO} - M_{BaCO_3} \tag{5.3}$$

where M_i is the molar amount and 2 is accounted to the initial molar content of Ba atoms.

Peak intensities have been scaled to their molar amount in the film at the beginning and at the end of the transformation, as represented in Figure 5.9. After that, the liquid phase evolution has been predicted using equation 5.3.

As a result, we can observe that $BaCO_3$ elimination directly leads to liquid, but subsequent $YBa_2Cu_3O_{7-\delta}$ formation is much delayed in continuous fast heating experiments. The reason can be found on the induction time needed for nucleation(t_{ind}), after reaching supersaturated conditions. This depends on the nucleation density (dN/dt), proportional to supersaturation (σ) and it is temperature dependent:

$$t_{ind} = \int_0^{t_{ind}} \frac{dN}{dt}(T)dt \propto \frac{1}{T,\sigma} \tag{5.4}$$

Hence, specially at conditions of low σ when using fast heating rates, t_{ind} may be high enough to avoid nucleation during a certain time while heating.

Once the first nuclei have been formed, we observe two growth rate regimes depending on temperature. The crossover temperature is similar for both compositions under the same processing conditions, despite the fact that precursor conversion happens earlier in the Cu excess sample. Another interesting event starting at this crossover is the disappearance of the random $YBa_2Cu_3O_{7-\delta}$ grains (brown lines in Fig. 5.9 and subsection 5.2.1.3).

Fast growth rate region

Very fast growth rates are achieved above 835°C in both melts, in zone III above T_e. YBCO thickness evolution can be approximated from the maximum intensity of the epitaxial (005)YBCO reflection (Fig.5.8c), while total final thickness of 400 nm has been proven with TEM. YBCO growth rate may be calculated from the time between 30-80% of the phase intensity, or by the YBCO derivative, which maximum is reached at 840°C for both compositions.

Growth rates above T_e with TLAG T-route are 36nm/s (200nm/5.5s) and 90nm/s (200nm/2.2s) for the (2:3) and (3:7) melts, respectively. The differences between compositions are uncertain, may be related to interfacial kinetics (e.g. Y mobility), which is thought to be the rate limiting step.

Maximum growth rates calculated from the slope are 40 nm/s for the (2:3) and 110 nm/s for the (3:7) melt. The latter is about a factor 100 higher than the growth rate of conventional CSD using TFA solutions [77] and most of the non liquid mediated growth techniques [5].

Additionally, physical properties could be measured for the 400 nm (2:3) film. Critical temperature is 91 K and $J_c^{sf} = 0.85\ MA/cm^2$ at 77 K, despite the fact that conditions are not optimized. Calculated ab-grains fraction after film growth is only 1.3%. As a result, this demonstrates that very fast growth rates do not compromise texture quality and very good physical performances can be obtained, in the order of those achieved with HLPE technique at only 10 nm/s for similar thicknesses [170].

Low growth rate region

The lower temperature zone II, ranging from precursors consumption to 835°C, is a T-P_{O_2} zone where liquid is metastable, below the thermodynamic eutectic point (see Fig. 4.8)

Inferred maximum growth rates in this region are 6 nm/s for the stoichiometric (2:3) composition and 5 nm/s for the eutectic (3:7) composition, respectively. In this case, the slightly faster growth rates and higher random fraction with the (2:3) liquid in comparison to the (3:7), are a directly consequence of the increased supersaturation in the stoichiometric liquid $R \sim k\sigma(C_e/C_{xl})$

The growth velocity in this region may be limited by one of the following processes: (1) poor dissolution of Y particles (C_δ) in the metastable liquid, (2) hindered diffusion to the interface due to metastable liquid viscosity or (3) interface kinetics (see section 4.2.5). More effort is needed in order to determine which is the slowest rate step and underpin the nucleation mechanisms in this zone.

When heating slow enough or in isothermal conditions, all YBCO growth may be completed at the slow growth rate region II. Figure 5.10 shows YBCO crystallization and phases evolution at heating rates of 0.4°C/s from the two studied liquids.

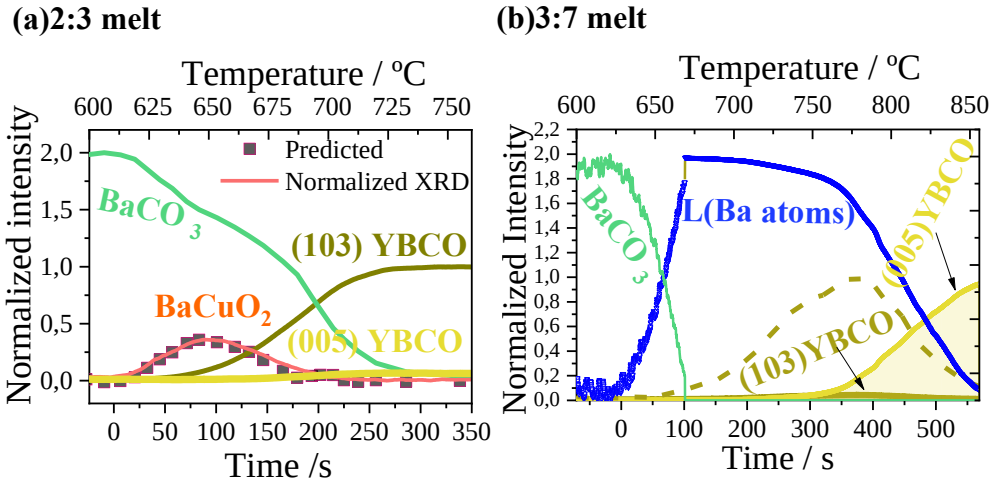

Figure 5.10: Time-resolved solid species evolution at a heating rate of 0.4°C/s for (a)2Ba:3Cu and (b)3Ba:7Cu liquids under $P_{O_2} = 10^{-3} bar$, $P_{tot} = 1 bar$. XRD intensities have been normalized to their respective molar amounts (continuous lines). Dashed brown line in (b) corresponds to random (103)YBCO reflection normalized to 1, for better visibility. Symbols indicate predicted evolution for (a) $BaCuO_2$ and (b)liquid. Full spectra corresponding to (a) can be observed in Figure 3.25

The epitaxial YBCO growth rate calculated for the eutectic composition

from 5.10b is 2 nm/s from its derivative and 1.5 nm/s from the time between its 30-80% of XRD intensity. So, with a rate of 0.4°C/s, the growth of YBCO was almost completed before reaching the higher temperature fast growth rate region III.

Hence, the use of rapid heating is mandatory for producing epitaxial YBCO at ultrafast growth rates. This is further confirmed in section 3.4.2.2, where the fast growth of TLAG is obtained from rapid thermal annealing samples quenched at 800°C demonstrating that 3 seconds are enough to grow a ∼300 nm YBCO film (i.e. 100 nm/s) with a heating ramp of 80°C/s.

Another alternative to reach region III directly is through the P_{O_2} change approach, which will be described in Chapter 6.

5.2.1.2 Growth of randomly oriented $YBa_2Cu_3O_{7-\delta}$

As observed, the amount of random nucleation is only outstanding for the stoichiometric solution (Fig. 5.10a). The (2:3) melt composition at low temperatures is the only combination that may lead to high enough supersaturation. As a result, the induction period for nucleation (t_{ind}) is short and the driving force for nucleation, is big enough to nucleate polycrystalline grains. Additionally to the possible nucleation at the sites of $BaCuO_2$ solid intermediate particles, only formed in this case.

For the other cases, (103)YBCO random main reflection intensity represents less than 8% of final (005)YBCO epitaxial diffraction ($I_{(103)}/I_{(005)}$*100), although intensities comparison is cumbersome due to the slightly different ω values used that can modify the epitaxial peak intensity.

The overall solid species relation from Fig. 5.10a can be simplified as:

$$(2\text{-x})BaCO_3 + (3\text{-x})CuO + xBaCuO_2 + \frac{1}{2}Y_2O_3 \longrightarrow YBa_2Cu_3O_{7-\delta} \quad (5.5)$$

where x depends on temperature.

From the proposed above reaction, we can state that Ba atoms must be shared between the liquid, $BaCuO_2$, $BaCO_3$ and $YBa_2Cu_3O_{7-\delta}$. Peak intensities for $BaCO_3$ and $YBa_2Cu_3O_{7-\delta}$ can be scaled to their molar amount, but $BaCuO_2$ quantity is unknown. For this reason, the calculated remaining Ba atoms will

be shared between the liquid and this intermediate phase. Then, conservation leads to:

$$M_{Ba\,(l)} + M_{BaCuO_2} = 2 - 2\,M_{YBCO} - M_{BaCO_3} \tag{5.6}$$

where M_i is the molar amount and 2 is accounted to the initial content of Ba atoms for 2Ba:3Cu composition.

In this case, the calculated $M_{Ba\,(l)} + M_{BaCuO_2}$ (square symbols) evolution with temperature fits completely the one corresponding to solid $BaCuO_2$ XRD peak intensity. Hence, we can conclude that YBCO growth from liquid is faster than solid species transformation to liquid and so, transient liquid can not be detected.

Indeed, maximum growth rate for random YBCO, matching precursors decay, is 4 nm/s. The rate calculated from 30 to 80% of its XRD intensity is 2.6 nm/s. In this case, the rate limiting step for YBCO growth is the $BaCO_3$ elimination reaction.

5.2.1.3 Polycrystalline YBCO grains elimination

A surprising result is the reduction of randomly oriented YBCO grains when the fast growth regime for epitaxial YBCO starts. 2D-XRD acquired *in situ* at temperatures before and after the growth rate shifts are represented in Fig. 5.11. Image at 835°C shows diffraction of (103) and (110) reflections homogeneously distributed along χ in form of a ring, attributed to YBCO grown randomly oriented. The ring can also be observed at the (005) reflection, but this has an intense peak in the Bragg conditions with the epitaxial part. It can be observed that at 870°C, the polycrystalline contributions have completely disappeared. Peaks evolution with temperature is illustrated in the 3D image to the right. (103) reflection decay corresponds to the highest slope for the (005) peak increase.

Thus, misoriented grains are either reoriented or dissolved when liquid changes its properties in zone III (above C_e) and recrystallized towards c-axis grains. The driving force towards recrystallization from random to epitaxial grains is the decrease of the total energy of the system. Therefore, if random grains are small, their associated energy will be high, thus enhancing the driving force towards recrystallization or reorientation. Size and distribution of these grains is

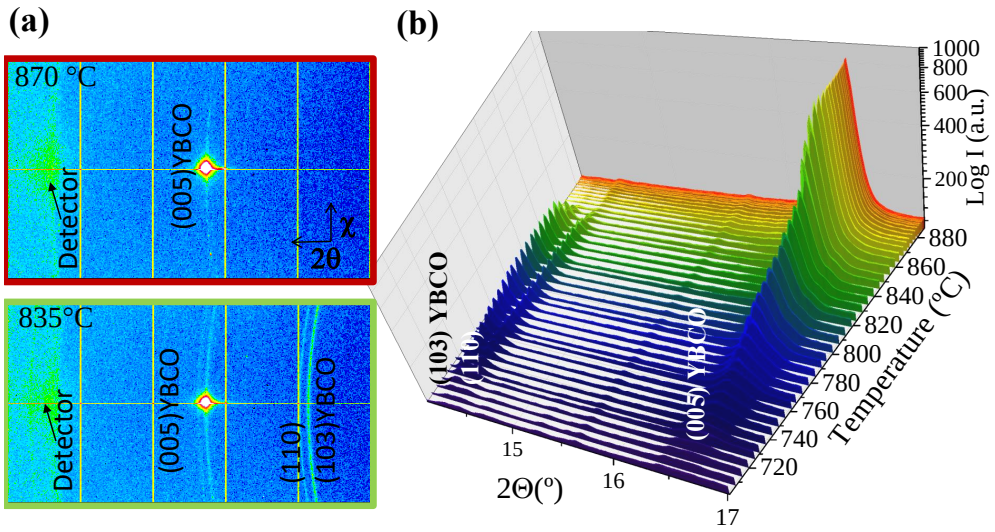

Figure 5.11: Evolution of random and epitaxial YBCO reflections for the stoichiometric composition heated at 5°C/s under 10^{-3} bar O_2. (a)Frames acquired with the 2D detector at 835°C and 870°C (b) χ-integrated X-ray diffraction spectra during heating

illustrated in the next subsection 5.2.2 by means of TEM images from quenched samples at different stages.

This fact explains how fully epitaxial YBCO films of good quality can be obtained at relatively low heating rates and opens a very wide window of processing conditions. Still, a limit on the amount of random phase that can be dissolved or reoriented may exist and should be further investigated.

5.2.2 Microstructural evolution

Films microstructure at the different stages is observed by means of transmission electron microscope imaging. Samples have been quenched at a certain temperature after a very fast heating rate of 20°C/s under oxygen partial pressure of 10^{-2} bar with the 2:3 composition. Corresponding XRD and TEM images are presented in Figure 5.12.

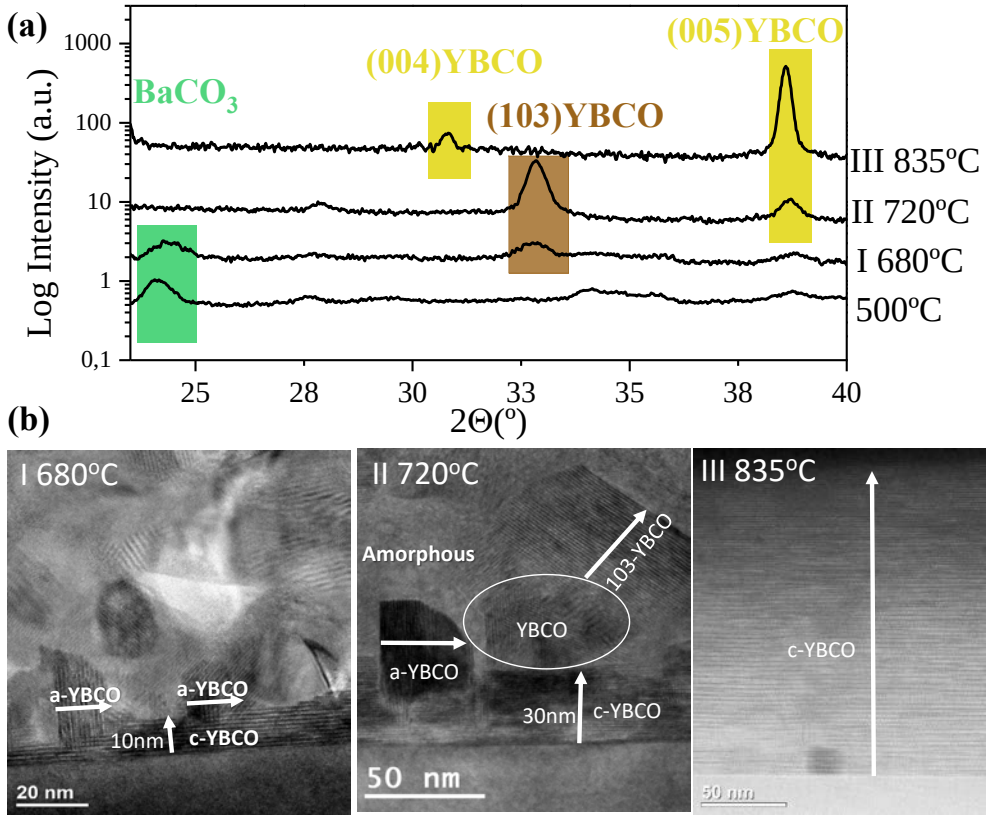

Figure 5.12: Quenched films with the stoichiometric composition after pyrolysis at 500°C, and to zones I (680°C), II (720°C) and III (835°C) after 20°C/s heating rate under $P_{O_2} = 10^{-2}$ bar. (a)χ-integrated GADDS XRD patterns (b)I, II bright-field TEM and III scanning transmission electron microscopy (STEM) cross section analysis

In stage I, pyrolysis precursors $BaCO_3$ and CuO reaction takes place in parallel to the growth of first YBCO nuclei (reaction 5.5). XRD reveals that a quench at 670°C which is composed by mainly pyrolysis precursors $BaCO_3$, CuO, Y_2O_3 and (103) YBCO reflection.

As temperature increases, precursors disappear and YBCO grows. Conver-

sion reactions are completed at 720°C but temperature is below thermodynamic eutectic point. We call this stage II, a zone where liquid is metastable. XRD at this temperature exhibits polycrystalline YBCO.

If the quench is performed at higher temperatures, above the eutectic temperature in stage III, YBCO (005) reflection from epitaxial YBCO prevails instead. TEM image confirms full c-axis oriented YBCO along all film thickness.

TEM and STEM images at intermediate stages depicts that YBCO nucleates heterogeneously at the substrate interface. As reaction proceeds, epitaxial YBCO grows in c-direction and non decomposed precursors are kept on the top of the film. Thicknesses corresponding to the heterogeneous nuclei are 10 nm at 670°C and 30 nm at 720°C, with a 2.5s difference when heating at a rate of 20°C/s. This would correspond to a growth rate of 8 nm/s, in the order of rates determined in zone II by *in situ* XRD.

At the film in stage II, precursors have attained complete conversion to the liquid state while the epitaxial layer represents just a 10% of the full thickness. Amorphous zones are observed together with dispersed misoriented grains on top of the c-oriented YBCO. Calculated random fraction for the YBCO grains, as compared to those that are epitaxial, was calculated from 2D-XRD analysis, and it represents a 12%. Homogeneously nucleated grains are of similar thickness along their c-axis as the epitaxial layer, indicating they have been formed during similar times.

Occasionally, a/b-YBCO grains are formed on a c-YBCO epitaxial layer.

Figure 5.13 illustrates the distribution of unreacted solid precursors at stage I. STEM-HAADF image (a) shows YBCO nucleation, presenting a brighter contrast, which can be found continuously along all substrate interface. On top, a porous film is still preserved with a morphology similar to that generated after pyrolysis. EDX (b) confirms that Ba and Cu remain separated as $BaCO_3$ and CuO nanoparticles in a nanocrystalline matrix. CuO and Y_2O_3 particles can be observed with BF-HRTEM High Resolution image (c). Also some homogenous YBCO grains have nucleated in the bulk. Indicating that liquid has been formed in punctual areas of the film and led to randomly oriented YBCO grains with a typical platelet size of 10x20 nm.

Inferred particles sizes are around 20-40 nm for CuO, being larger those closer to substrate interface, while Y_2O_3 remains smaller than 10 nm. Thus, confirm-

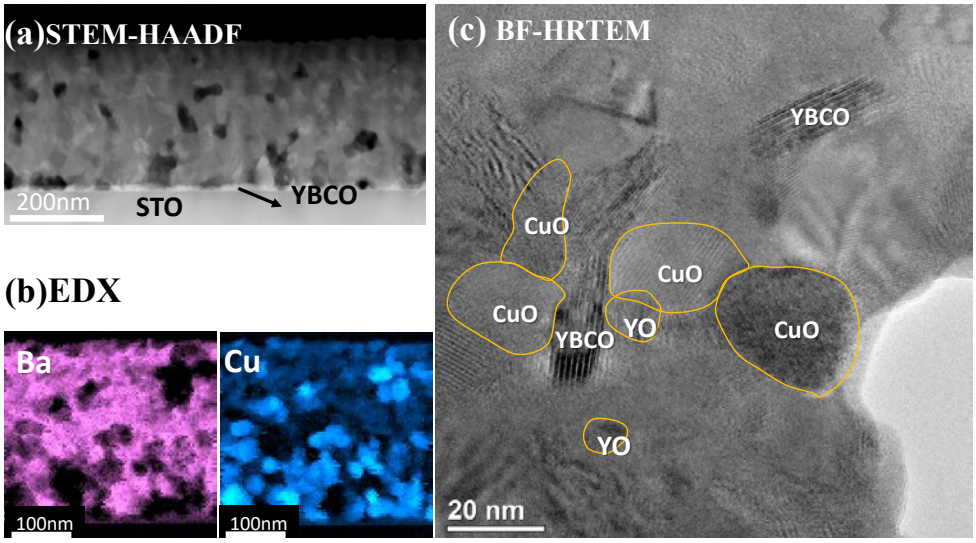

Figure 5.13: TEM analysis of the quench at 680°C ($P_{O_2} = 10^{-3}$ bar, dT/dt=20°C/s). (a)High angular dark field-STEM (b)EDX maps for Ba and Cu (c) bright field-High resolution TEM

ing that coarsening of the precursors is precluded when heating at a fast rate of 20°C/s.

The nanocrystalline size of the homogeneously nucleated YBCO grains supports the previously mentioned result (section 5.2.1.3) that these grains can be either reoriented or redissolved in the liquid to recrystallize as c-axis oriented epitaxial film.

5.3 Processes derived from the liquid properties

The formation of a large extent of melt has implications on film morphology and nucleation processes. The main concerns are liquid wettability leading to phases segregation when it is too poor and reactivity at the substrate interface due to the highly corrosive character. These features have already been noticed in other liquid-assisted processes [170, 64] and special care was necessary to

overcome them.

Thus, liquid assisted growth exposes new challenges that need to be properly overcome. The main issues related to these topics are studied in this section.

5.3.1 Liquid diffusion

Figure 5.14 illustrates the effect on final film microstructure of a film fired at an ultrafast rate of 60°C/s with the Y:2Ba:4.7Cu solution composition (3:7) liquid.

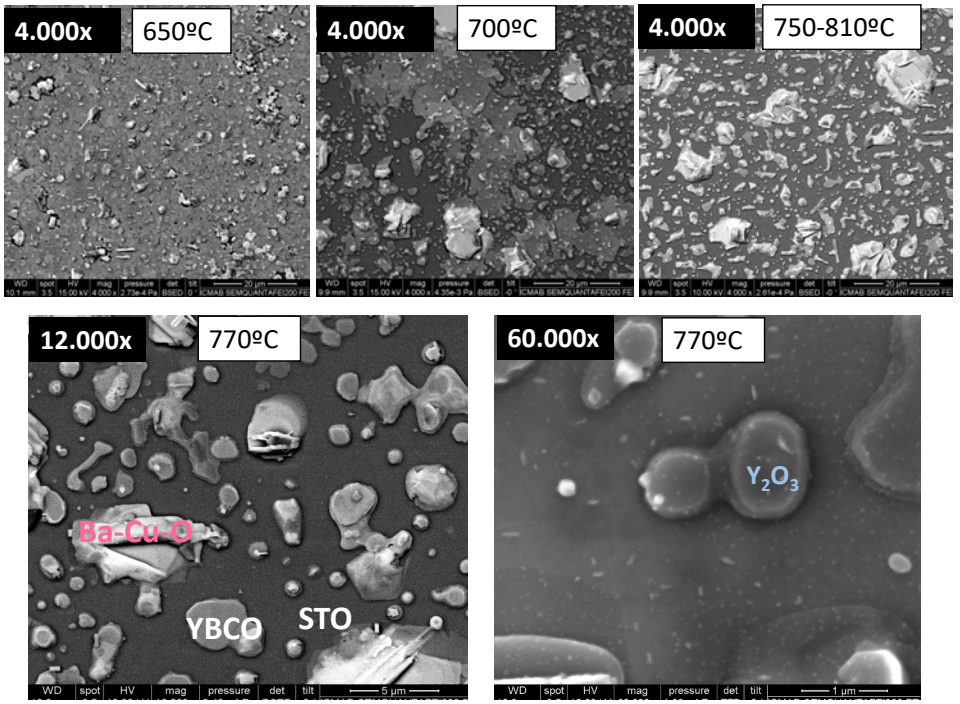

Figure 5.14: SEM images with backscattered electrons (BSE) detector illustrating phase segregation in the eutectic composition Y:Ba:Cu 1:2:4.7 films grown at 60°C/s under $P_{O_2} = 10^{-3}$ for 2 min. Final films thickness of the samples shown here is 90 nm. Higher magnifications are shown for the sample grown at 770°C

While the coating grown at 650°C is a continuous YBCO film, above 700°C rounded grains presenting different composition and size are rather dispersed, leaving large areas of uncovered STO substrate (darker areas).

X-ray energy dispersive analyses (EDX) and image contrast reveal the presence of some regions with flat YBCO growth, nanometric size particles containing mainly Y_2O_3 and larger, brighter grains with enhanced Cu and Ba signal with some amounts of Ti. The stoichiometric composition varies for each individual grain.

Such a microstructure giving round dispersed phases resembles solidification of melts with poor wetting behaviour due to a large surface tension. Liquid spreading on the solid depends on the contact angle, which is defined by the balance of three interfacial energies (γ) as follows:

$$\gamma_{SV} = \gamma_{SL} + \gamma_{LV} + cos(\theta) \tag{5.7}$$

where the subscripts S, L, and V represent solid, liquid, and vapour, respectively.

Figure 5.15 contrasts good and poor wetting based on the contact angle θ. The wetting angle depends on solubility or solid surface chemistry [176].

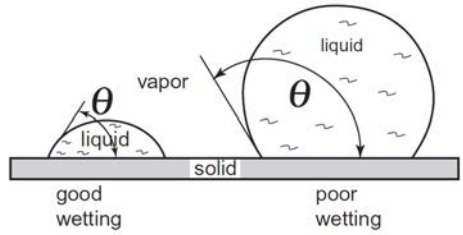

Figure 5.15: Wetting behaviour for a liquid. Low contact angle supports wetting while a high contact angle shows poor wettability. Reproduced from [176]

Actually, very similar images are obtained when films containing only Ba and Cu, the elements composing the liquid, are grown above the eutectic point (See Chapter 4.3).

The poor wettability of the Ba-Cu-O liquid was one of the main concerns in melt textured growth of bulk YBCO [171]. Also, strong mass transport on

a millimetre scale was demonstrated for fluorine free solutions processing by Wesolowski *et al* [177]. An indication of the very high diffusion coefficient (D_l) of the species forming this melt. According to the Stokes-Einstein equation:

$$D_l = \frac{kT}{6\pi r\eta} \tag{5.8}$$

where D_l is temperature dependent and related to liquid viscosity η and radius r of the moving particles [156]. At the same time, η follows an exponential temperature dependence:

$$\eta = \eta_0 exp(\frac{E}{RT}) \tag{5.9}$$

where E is an activation energy.

Hence, diffusivity and consequently phases segregation is enhanced at high temperatures.

Several authors demonstrated that D_l can be decreased by tuning physico-chemical parameters of the melt, such as viscosity [178], using doping at low concentrations (<5%) with Pt [179] or CeO_2 [180]. However, preliminary studies on CeO_2 doping in TLAG did not show any improvement towards reducing liquid movement.

Wetting behaviour also depends on the substrate [171]. Yet, (100)STO is already one of the reported substrates presenting better wettability for Ba-Cu-O melt.

2D-XRD image in Fig. 5.16a shows big quantities of remaining yttria particles. Those are either textured following the (l00) plane of the substrate, but also discontinuous spots in χ for (222) diffraction indicate particular favourable directions instead of polycrystallinity. Then, the small intensity of the only peak accounted to Ba-Cu-O grains indicates that most of them can be amorphous as a product from melt solidification. The YBCO and Y_2O_3 XRD intensities are plotted with temperature (Fig. 5.16b). C-axis oriented YBCO quantity presents its maximum at 700°C. Then, intensity strongly decreases in parallel to the increase of Y_2O_3 amount and particle size (Fig. 5.16c) .

This correlates with phases discontinuity observed in film morphology. Hence, XRD together with the corresponding SEM images point out that strong spacial segregation of cations occurs at high temperatures as a consequence of extensive melt formation and dewetting.

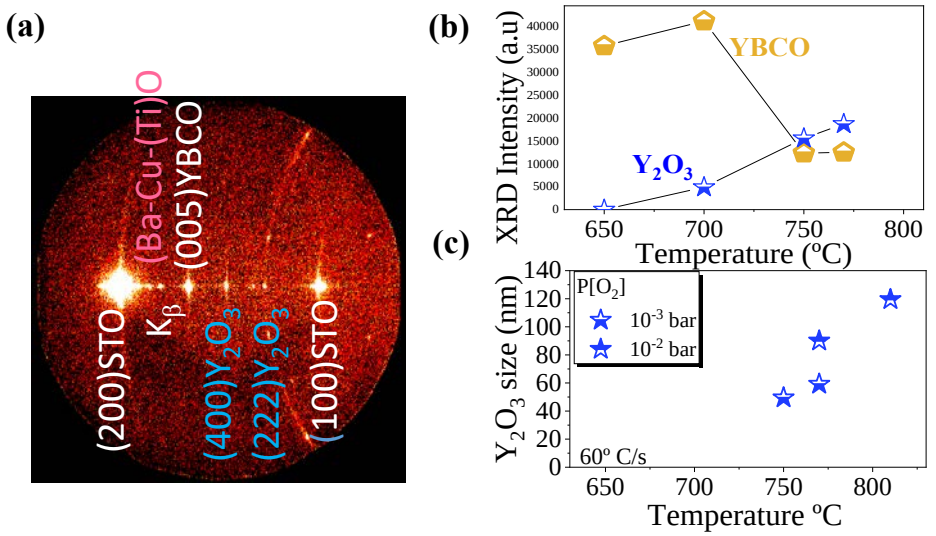

Figure 5.16: (a)2D-XRD frame of a sample grown from the eutectic liquid composition (3:7) at 770°C and 10^{-3} bar O_2. (b) $YBa_2Cu_3O_{7-\delta}$ and Y_2O_3 quantities evolution with temperature. XRD intensities are integrated from the diffraction poles of (104)YBCO and (222)Y_2O_3 reflections. (c) Y_2O_3 out of plane particles sizes calculated with Debye Scherrer equation from the (l00) reflections from HR-XRD measurements

As a result, we observe, on the one hand, grains formed by the solidified Ba and Cu phases composing the melt, while Y has contributed to Y_2O_3 particle coarsening. Thus, the YBCO formation has been hindered. The induction period for YBCO nucleation (t_{ind}) at conditions of small supersaturation (e.g high temperatures with (3:7) liquid) is longer, which may contribute on leaving time for cations diffusion to form the Ba-Cu-O and Y_2O_3 phases instead.

Y_2O_3 out of plane size has been inferred from HR-XRD using Debye Scherrer equation from (l00) reflections (Fig. 5.16c). Particles size increases from 50 nm to 120 nm with the increase of temperature and P_{O_2}.

Particle coarsening in Ba-Cu-O liquids was studied by Izumi *et al* [179]. In that case 211 grain size in the L was found to be proportional to the time that particles are in the melt (t) and liquid properties $D_l\Gamma$, where Γ

is the Gibbs-Thompson coefficient. The average 211 radius (R) was defined as: $R=\alpha(D_l \Gamma t)^{1/3}$.

We can conclude that, the Y_2O_3 coarsening behaviour, linked to dewetting, is closely related to diffusivity and YBCO t_{ind}.

Thus, it is crucial to limit the proportion of liquid in order to limit diffusion of cations. Some strategies which could help are:

- Slower conversion rate
- Liquid composition out of eutectic point
- Increase Yttrium content

We should take into account that these strategies go against favouring heterogeneous nucleation since they imply an increase of supersaturation. Therefore, it is clear that a compromise will be required to mantain epitaxy and fast growth of YBCO, while also mantaining micro-structural homogeneity in each case.

5.3.1.1 Control by heating rate

As stated before, conversion rate in T-route is controlled by the processing heating ramp. Lower velocities undergo melt formation to start at lower temperatures, where liquid cations diffusivity is lower; and t_{ind} for YBCO nucleation, shorter. These two factors should benefit on preventing cations segregation before YBCO nucleation, as deduced in the previous subsection.

Several samples of eutectic composition (Y:2Ba:4.7Cu) and 90 nm thick were grown during 2 min at different final temperatures using heating rates from 0.4°C/s to 60°C/s with the RTA oven.

Films presenting cation segregation, and consequently Y_2O_3 coarsening (see XRD in Fig.5.17a), are plotted in blue in Figure 5.17b, in contrast to continuous films represented in grey. SEM images corresponding to samples grown at 20°C/s (Fig.5.17c) confirm that a continuous YBCO film is formed below this crossover temperature while uncovered substrate with dispersed grains are seen, above.

Note that at these crossover temperatures YBCO is already 100% c-axis oriented. The green line in the plot (Fig.5.17b) marks the limits for c-axis

YBCO nucleation, which is slightly below the segregation crossover, leaving an area where c-axis and homogeneous YBCO could be obtained.

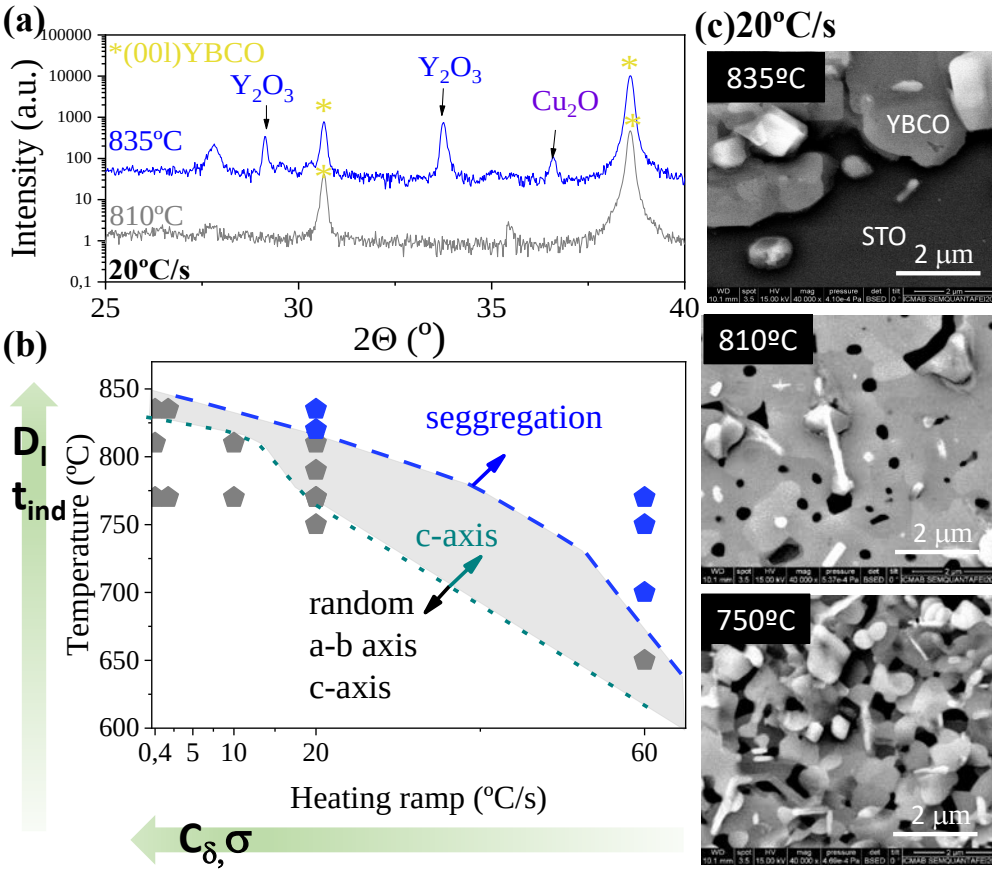

Figure 5.17: Cation segregation depending on T-dT/dt conditions for eutectic composition (a)HR-XRD of films grown at 20°C/s to 835°C and 810°C. The first presents Y_2O_3 coarsening. (b) T-dT/dt plot where blue symbols represent samples with strong dewetting and remaining Y_2O_3, while grey symbols depict continuous films. Dashed line limits the area where only c-axis epitaxial YBCO is favoured. The arrows parallel to the x and y axes indicate the trends followed by several film parameters D_l and t_{ind} are enhanced at high temperature while C_δ and σ are enhanced at low heating ramps. (c) SEM images of samples grown at 20°C/s. At 835°C, large substrate areas (black) are uncovered. $P_{O_2} = 10^{-3}$bar and films thicknesses 90 nm on STO

For instance, at 835°C with a rate of 20°C/s (Fig.5.17a, blue), Y_2O_3 intensity respect to (005)YBCO is 39.5%. This represents a smaller amount than the Y_2O_3 left at 750°C at a rate of 60°C/s (55.8%) (fig. 5.16b). Therefore, the temperature in which these phenomena start is lower as heating rate is increased. Above 700°C at 60°C/s, 820°C at 20°C/s and never observed until the explored range (<835°C) at 0.4°C/s.

Hence, the experimental results confirm that the spatial segregation of cations depends on heating speed. This may suggest a correlation with changes in yttrium concentration (C_δ) with the heating ramp, thus modifying supersaturation (σ) in the liquid. Therefore, lower C_δ achieved with fast heating rates, induces longer t_{ind} and consequently dewetting.

Clever designs will be needed to maximize superconducting properties. For instance, standard conditions for epitaxial YBCO growth with the (3:7) melt lie between 770°C and 810°C heating at 20°C/s.

Within this region, despite the fact that no secondary phases are observed by HR-XRD, still a certain degree of voids and unreacted regions that hinder current percolation may be observed with more detailed microscopy analyses.

Image 5.18a corresponds to a TEM cross-section of the sample grown at 810°C, 20°C/s. Still, intergrain areas totally uncovered are observed, leaving the substrate exposed, in agreement with the "holes"observed by SEM in Fig.5.17.

Other cases show secondary phase particles are left between the two growing YBCO islands: CuO, Y_2O_3 or Ba-Cu-O. In thick enough films with a good wetting we should expect that these secondary 'hases should remain at the film surface.

Distances between non merged grains are around 600 nm and YBCO islands size in a/b direction are 1-5 μm long. It can be deduced that distances between a first formed YBCO nuclei may be in the order of several microns as a result of small nucleation density (long t_{ind}).

5.3.1.2 Film thickness and substrate

Surprisingly, this effect is even enhanced with film thickness increase. Fig.5.18b images are taken from a 400 nm thick film. Tilted SEM images show larger film

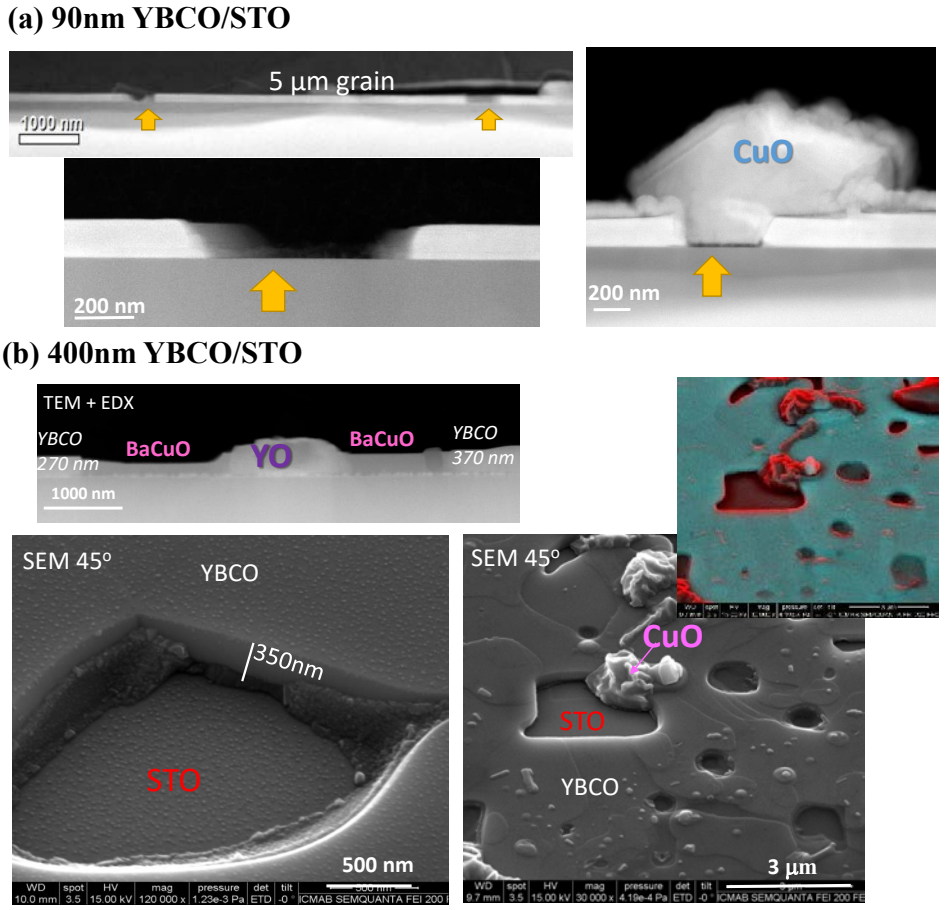

Figure 5.18: (a) 90 nm (3:7) sample grown at 810°C, where dewetting is observed between YBCO islands. (b) 400 nm (3:7) thick film grown at 770°C. Cross-section TEM and 45°tilted SEM images evidence the presence of film free areas. Phase identification has been performed with EDX analyses. Colours in inset image represents different chemical composition, from BSE detector. Both are produced on STO substrate, 20°C/s and 10^{-3} bar O_2

free areas of irregular shape are left between the growing islands. Some left remaining material can be observed at grains boundaries, while the voids may

be of several microns of diameter. In many cases, the bigger empty spaces are close to CuO grains.

Several sources of residual porosity in YBCO films are described in literature: incomplete healing of pyrolyzed film porosity, formation of voids associated to a/b-axis oriented grains or secondary phase impurities [181, 182, 183, 184].

Film free larger areas can occur due to film dewetting during long post-annealing processes, that can be caused as a result of interfacial stress generated by the lattice mismatch of YBCO with the substrate [175]. This phenomena is enhanced with long thermal treatments, at high temperatures and for thinner films.

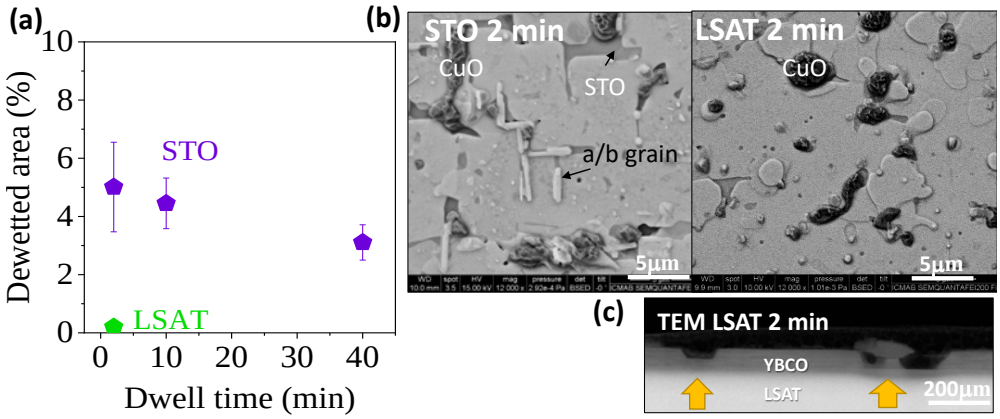

Figure 5.19: (a)Film free area (%) inferred from optical microscopy images and imaging treatment for 400 nm thick films grown at 770°C on STO and LSAT substrates depending on annealing time (dT/dt=20°C/s, $P_{O_2} = 10^{-3}$ bar). (b) Corresponding SEM images for 2 min dwell and (c)Cross-section TEM for the LSAT substrate sample where still some holes not reaching the substrate are observed

In order to identify if this is the case of those films, we have grown 400 nm thick films with increased dwell times: 2, 10 and 40 min. YBCO uncovered area was inferred from SEM surface images and imaging treatment (Fig. 5.19a).

Voids percentage on STO drops from 5% to 3% with the increase of annealing time. This fact rules out the possibility that it is a spontaneous dewetting post-growth phenomena. In contrast, longer annealing would favour grains coalescence, as we observe.

Therefore, the voids in TLAG are distinguished from typical porosity or dewetting in TFA-CSD films. Instead, it is confirmed that in TLAG-CSD pores can be accounted to liquid movement (D_l) and low nucleation density (high t_{ind}) when supersaturation is small.

More differences are observed depending on the substrate used. SEM image reveal that when YBCO growth is performed on LSAT, the dewetted area is considerably reduced (Fig.5.19). TEM cross-section of 90 nm YBCO film grown at 770°C (dT/dt=20°C/s) on LSAT demonstrates that porosity does not reach the substrate in this case, producing just steps on film thickness. These have been the more favourable conditions found so far to achieve continuous film covering of epitaxially grown YBCO from the eutectic liquid composition.

5.3.1.3 Cation composition effects

Strong segregation of phases has not been observed so far when using the stoichiometric liquid composition (1:2:3). Differences between the two melts relay on supersaturation and the quantity of liquid formed, being the 2:3 melt limited by the coexisting solid $BaCuO_2$ phase in the region between eutectic and liquidus temperatures. Images on the melt dewetting for both compositions are shown in section 4.3.

Apart from that, the molar Y content in relation to atoms forming the liquid is 17% for 1:2:3 (γ) and 13% for the 1:2:4.66 (α) composition that has been used. Thus, since yttria remains solid until Y dissolution in the liquid, its amount may also contribute to increasing the solid/liquid ratio.

Preliminary results are presented with the 3:7 melt but with an increased Y molar content to 17% instead of 13% molar. The total Y:Ba:Cu cations ratio is now 1.35:2:4.66 (β). A film has been processed to 835°C at 20°C/s and $P_{O_2} = 10^{-3}$ bar, conditions where a strong phase separation was observed with the 1:2:4.66 (α) ratio. Both structural and morphology characterizations of the films are compared in Figure 5.20, also with the 1:2:3 (γ) solution.

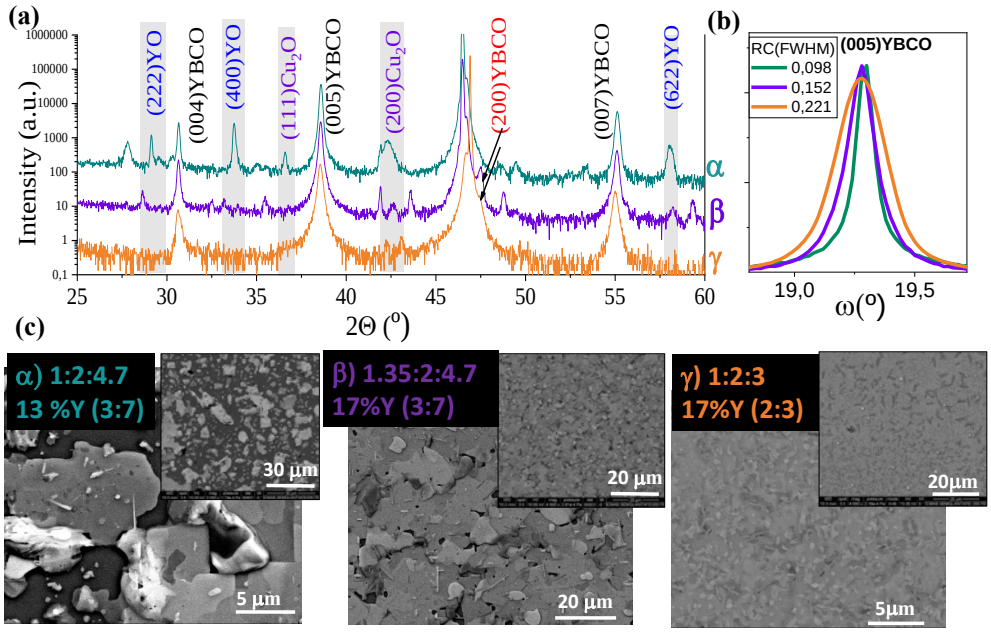

Figure 5.20: Dewetting comparison of samples on STO with Y:Ba:Cu ratios (α)1:2:4.66 in turquoise, (β)1.35:2:4.66 in purple and (γ)1:2:3 in orange. Growth temperature 835°C, dT/dt=20°C/s, 2 min dwell, P_{O_2} 10^{-3}bar. At (a)HR-XRD, (b) (005) YBCO rocking curve and (c) SEM images with the BSE detector show strong dewetting only in solution α. Film thicknesses are 90 nm

Paradoxically but in accordance with the hypothesis, films with increased Y to 17% (β, γ) in both melt compositions show by XRD (Fig. 5.20a) no Y_2O_3 remaining in the final film, while a 13% of Y in the solution (α) leads to a very high percentage of unreacted Y_2O_3 after YBCO growth (39.5%=I(Y_2O_3)/I(YBCO)).

As stated before, and observed with SEM images, unreacted and dispersed phases are formed due to melt dewetting. Thus, solid Y_2O_3 remains only when it is segregated. In contrast, continuous YBCO films can be formed without remaining Y_2O_3, when a larger amount of solid Y_2O_3 in the initial solution limits diffusion of liquid cations before Y dissolution.

We can also deduce that Y_2O_3 excess in the (3:7) melt results in an increase of C_δ as evidenced from the formation of a/b grains. This demonstrates that Y dissolution and phase segregation are correlated phenomena. Yet, it is still not clear if the increased C_δ is the consequence or the cause of preventing dewetting.

The width of rocking curves of (005)YBCO Bragg peaks also increase with Y content, and even more with the 2:3 melt. This is a consequence of the higher supersaturation.

The samples shown here have been grown under the same conditions for comparison, but the optimum growth parameters are different in each composition, and has to still be optimized for composition β. Films β and γ present rather low critical currents of 0.24 and 0.003 MA/cm^2 at 77K and critical temperatures of 86K and 79.5K, respectively. This can be explained by the presence of ab-grains, some voids still observed between the grain boundaries in sample β, or structural inhomogeneities in film γ, observed in the SEM images.

To sum up, the increase of Y_2O_3 content and higher C_δ can be a very effective tool to limit liquid movement. These results open the path to explore also other possibilities of solid phases such us the introduction of nanoparticles that at the same time are used for vortex pinning in the resulting nanocomposite.

5.3.1.4 Multilayered structures

Solution processing is a versatile methodology that allows deposition and pyrolysis of multilayered structures that can be grown together. With this idea, several strategies can be designed in order to decouple nucleation from growth conditions with the use of layers with different composition.

For instance, the combination of the two liquid compositions can join the advantages of (3-7) composition in terms of low supersaturation to promote c-axis nucleation, while (2-3) melt on top can preclude cations movement.

Preliminary experiments demonstrate that phase segregation is avoided with a 200 nm (2-3) solution layer on top of a 90 nm (3-7) layer (Fig. 5.21). Additionally, very small rocking curve values of the (005) YBCO of 0.11°and ab-grains percentage of only 4%, point out to a higher texture quality than the stoichiometric (2-3) solution without seed layer (see Fig. 5.30 for comparison).

On the other hand, SEM and TEM images show a totally pore free contin-

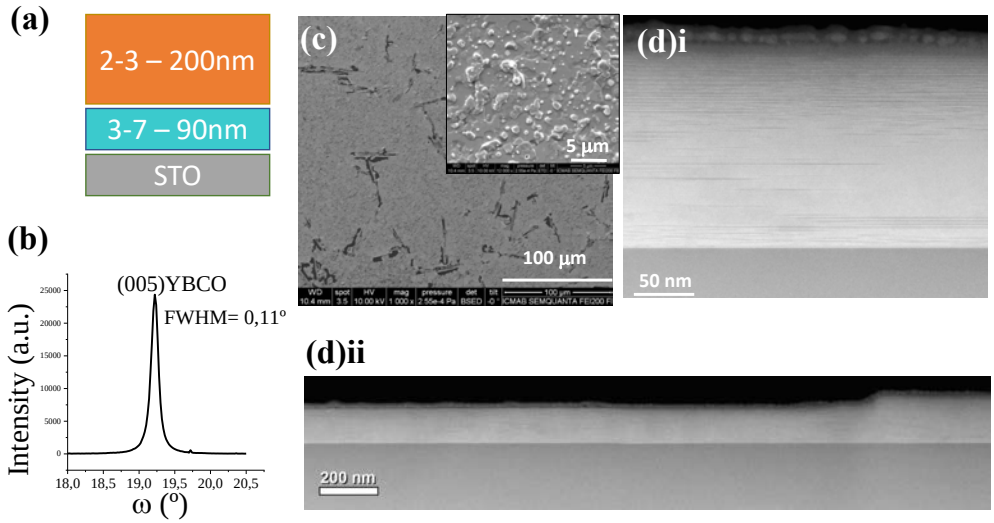

Figure 5.21: Bilayered film composed of Y:Ba:Cu ratios: 1:2:4.7 (α) 90 nm in the first layer and 1:2:3 (γ) 200 nm on top. Film was grown at 810°C, 10^{-3} bar O_2, 20°C/s. (a)Scheme (b)(005)YBCO rocking curve width is small (c)SEM and (d)cross-section STEM images

uous layer, except from some spare structural inhomogeneities accounted to reactivity. Therefore, cations diffusion have been effectively precluded by the (2-3) layer on top. No noticeable interface between the two layers is observed and remaining Cu from the first solution is also not trapped in between, but dissolved by the next layer liquid.

Still, a certain local reactivity and barium cuprate phases exist (see XRD at the Appendix in Fig.7.3), which limit the percolative critical current density in this sample (J_c=0.1 MA/cm^2 at 77 K). However, there is still much room for optimizing growth conditions and this strategy results are very promising for future work.

Overall, this is a “proof-of-principle”experiment showing that understanding the optimal conditions of nucleation and growth can allow a "design" of optimal thick films and CCs.

5.3.2 Interfacial chemical reactivity

One of the major problems of YBCO synthesis from melts was the high reactivity of the barium cuprate solution. Most substrates react strongly or are dissolved in the liquid at high growth temperatures (900°C) [171, 154]. One of the consequences is substrate cations dissolution in the liquid to nucleate new secondary phases that compete with YBCO.

Many examples of these phases have been found with a different extent depending on substrate and processing conditions. Here we report investigations on (l00)$(LaAlO_3)_{0.3}(Sr_2AlTaO_6)_{0.7}$ (LSAT), (l00)$SrTiO_3$ STO monocrystals and 50 nm YBCO buffer layer on STO. These substrates have been proven to be suitable for YBCO c-axis nucleation with TLAG. They were chosen for the close lattice parameters to YBCO, thermal expansion, polished surface quality, stability and robustness.

The resulting phases on $SrTiO_3$ substrate can be very diverse, making it very harsh to identify the exact composition by means of X-ray diffraction. Usually epitaxial peaks at 42-43°in 2θ arise when reactivity with the substrate is observed (See Fig.5.3). EDX and TEM in Figure 5.22a reveal dissolution and diffusion of mainly titanium to form Ba-Ti-(Cu)-O phases. The competing new phases are nucleated along all film thickness.

On LSAT substrates, tantalum is dissolved in the melt to form epitaxial tetragonal Ba_2YTaO_6 (BYTO) that grows on the substrate surface and below YBCO (Fig. 5.22c). Without the presence of Y, no reactivity derived phase nucleates on LSAT (see Chapter 4.3, Fig.4.17).

Sample c was synthesized on already grown 50 nm YBCO on STO. TEM shows 1 μm long step on STO surface, an indication that liquid has reached the substrate, completely dissolving the buffer layer as well. This example illustrates the highly corrosive character of the liquid, which should be avoided either by a blocking unreactive buffer layer or substrate, or by tuning the processing conditions.

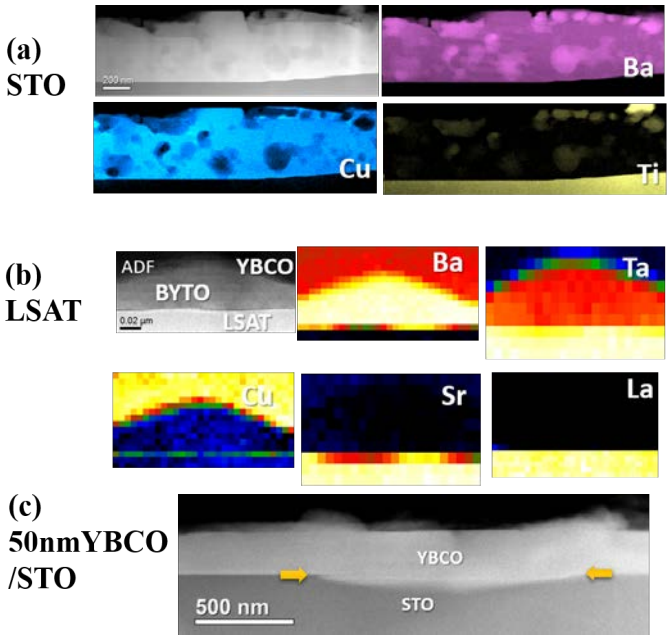

Figure 5.22: Examples of TEM and STEM analyses combined with EDX showing transient liquid extensive reactivity and the forming secondary phases on substrates of (a)STO, (b)LSAT and (c)50 nm YBCO deposited with PLD on STO

5.3.2.1 T-P_{O_2} dependence

Quantitative studies on reactivity under different conditions have been carried out for stoichiometric composition Y:Ba:Cu 1:2:3 (γ) on LSAT, since cations segregation is avoided with this composition and the (200)BYTO orientation diffracts at $2\theta = 45°$(Fig.5.23a), which can be easily identified. Although the extent of competing phases depends on each substrate, similar trends depending on processing conditions were observed.

In Figure 5.23b the relative quantity of BYTO is represented in the T-P_{O_2} phase diagram of quenched samples after heating at 20°C/s. The XRD peak area of the (200)Ba_2YTaO_6 reflection is normalized with the (005)$YBa_2Cu_3O_{7-\delta}$. The integrated XRD diffraction patterns are displayed at the Appendix in Fig.7.4.

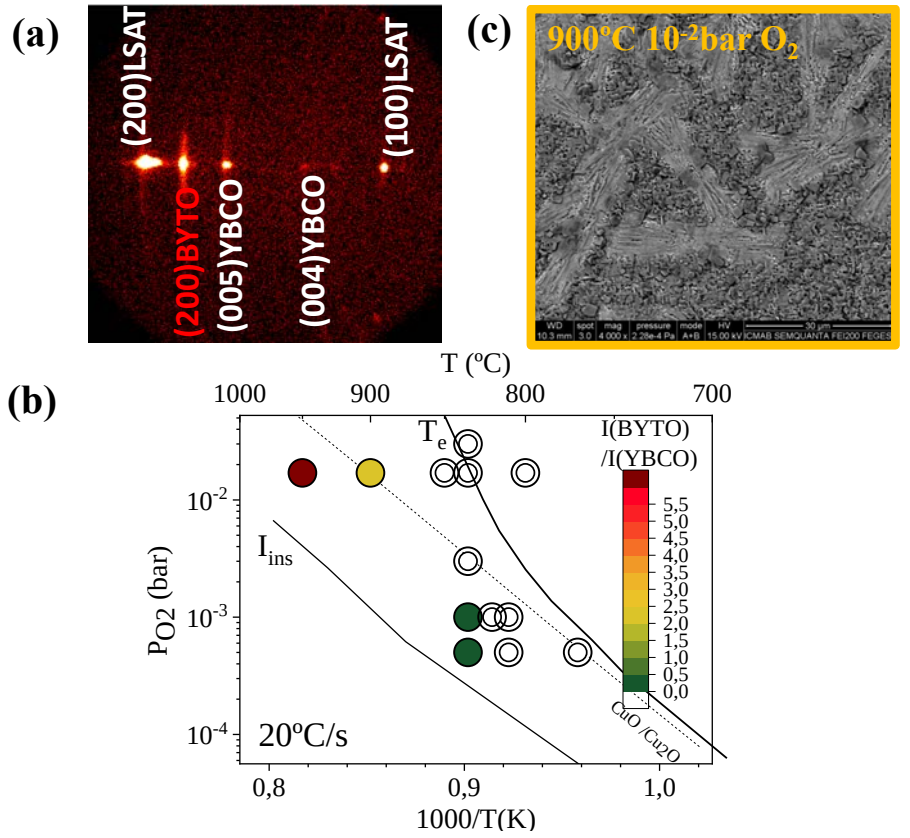

Figure 5.23: Reactivity of samples grown on LSAT substrate during 2 min at a rate of 20°C/s with stoichiometric composition and are 200-300 nm thick (b)T-P_{O_2} processing conditions. Colours indicate XRD peaks are of the reactivity product (200)BYTO reflection normalized to the (005)YBCO. (a)2D-XRD GADDS image and (c)SEM image of a sample grown at 900°C and 10^{-2} bar O_2

The formation of Ba_2YTaO_6 is highly enhanced in samples treated at high temperatures and at low oxygen partial pressures. For instance, XRD intensity for BYTO can be 6 times bigger than YBCO at temperatures higher than 900°C. BYTO phase in form of elongated grains can be observed on the corre-

sponding SEM image at Fig.5.23c.

The reacted fraction (β) in diffusion controlled reactions is linked to the reaction time t and diffusion parameter Γ as follows [176]:

$$1-(1-\beta)^{1/3}=\Gamma t^{1/2} \tag{5.10}$$

At higher temperatures, atomic diffusion is enhanced and YBCO t_{ind} is longer due to the smaller supersaturation. This results in longer exposure time of the melt to the substrate and can explain the higher amount of reactivity derived phases.

The increase of reactivity when lowering P_{O_2} is less clear, but it could be related to changes in the liquid properties, such as viscosity and diffusivity.

5.3.2.2 Heating ramp dependence

One could think on reducing the time t that the melt is exposed to the substrate by fast annealing.

Several samples of stoichiometric composition (Y:2Ba:3Cu) were grown during 2-5 min to different final temperatures using heating rates from 0.4°C/s to 60°C/s with the RTA oven.

Films presenting the reactivity derived Ba_2YTaO_6 phase, identified with XRD, are plotted in red at the T-dT/dt plot in Figure 5.24. Those films in which no reactivity has been observed are coloured in grey, and green depicts the presence of the Y_2BaCuO_5 (Y211) phase, for reference (see section 5.1.1). Some integrated XRD diffraction patterns are presented in the Appendix figures 7.4 and 7.5.

The results show an unexpected increase of substrate derived secondary phases as heating becomes faster (Appendix Fig. 7.5). Thus, reactive phases are observed beginning from lower temperatures. Also, reactivity starts at lower temperatures under lower P_{O_2} conditions, in accordance to Fig.5.23 results.

Again, diffusivity D_l and induction time for YBCO nucleation t_{ind} tendencies (represented in arrows in Fig.5.24), explain this behaviour. On the one hand, dissolution of substrate elements is enhanced when they are in contact with an unsaturated liquid (C_δ is lower at higher heating rates). On the other hand, this results in a longer YBCO t_{ind}, giving time for other phases to nucleate.

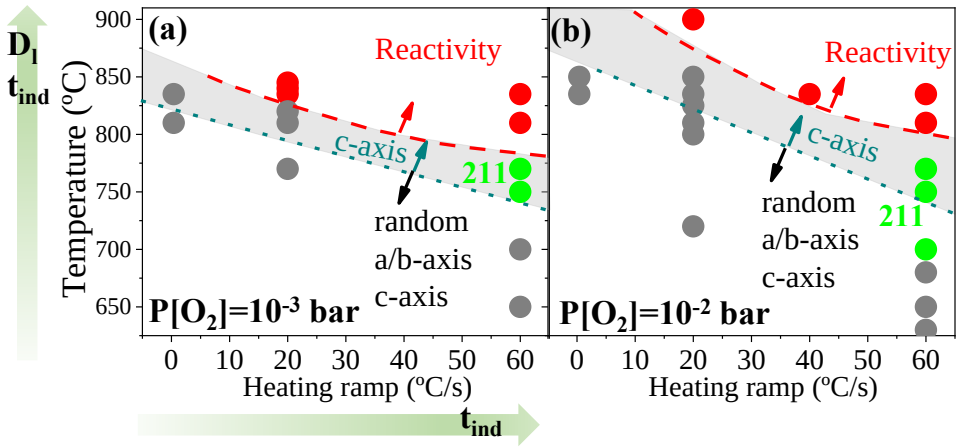

Figure 5.24: Reactivity on LSAT depending on T-dT/dt conditions for the stoichiometric composition (200-300nm thick) where samples are coloured in red if BYTO is detected by XRD, grey if not detected and green if the Y_2BaCuO_5 (Y211) phase appears (see section 5.1.1). P_{O_2} are (a)10^{-3} bar and (b)10^{-2} bar. Green dashed line limits the area where only epitaxial YBCO is favoured

The crossover temperature for epitaxial growth, plotted in a dark green dashed line, lies slightly below the reactivity line for both P_{O_2}. It seems necessary to either reduce growth temperatures or encounter non reactive buffer layers. More experiments are being performed by group co-workers in both directions. Other authors using liquid mediated growth techniques for YBCO have already succeeded on limiting reactivity with the use of buffer layers such as $LaMnO_3$, $Sr_{0.5}Ba_{0.5}TiO_3$ or YBCO [170, 64].

5.3.2.3 Local reactivity

More cases of interfacial reactivity has been observed by means of microscopy techniques when the phase is not detected with XRD. For instance, films morphology of two samples grown at 835°C under 10^{-2} bar of oxygen are presented in Figure 5.25.

In film *a*, rod-shaped grains of about 15 μm long are dispersed in the film.

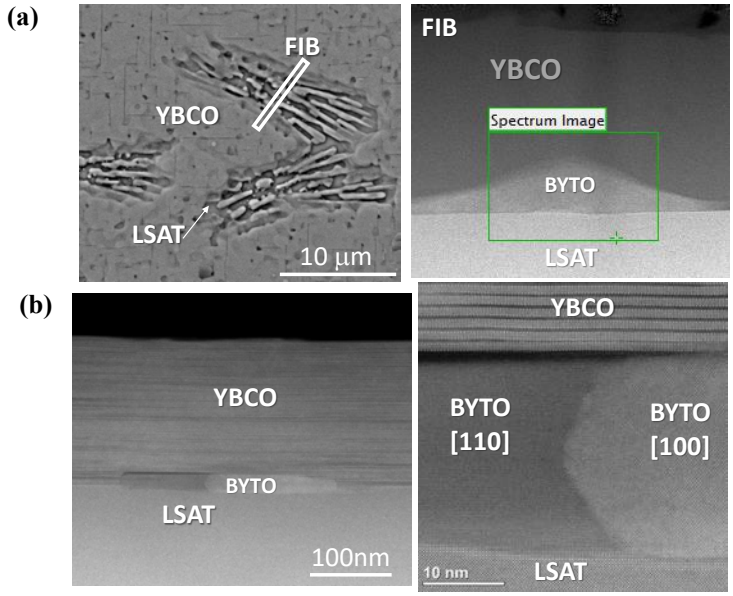

Figure 5.25: Microscopy analyses on samples grown with the 2:3 liquid at 835°C, 20°C/s, $P_{O_2} = 10^{-2}$ bar and of 200 nm thickness (a) SEM image, DF-TEM and EELS performed at a FIB cross-section where the film inhomogeneity is observed by SEM. BYTO growing at the interface distorts YBCO growth on top (corresponding EELS shown in Fig. 5.22). In case (b), TEM images show a continuous and epitaxial YBCO layer on top of BYTO

Composition was elucidated with TEM analysis on a particular grain cut by means of the FIB technique (Fig. 5.25a). The brighter contrast phase at the interface observed with dark field imaging points out to the presence of Ta, which is confirmed by EELS analysis. Ba_2YTaO_6 particles are rounded and 50 nm thick, while YBCO grows around following this shape. Consequently, it results on a structural inhomogeneity that breaks the the YBCO layer continuity.

Another example is illustrated in film *b*. Ba_2YTaO_6 can be found at the interface, oriented along [100] and [110] directions with a thickness of 35 nm. In this case, YBCO growth remains undisturbed along the c-direction, perpendicular to the plane, maintaining epitaxy in a continuous film.

These cases evidence the existence of local and inhomogeneous reactivity, probably starting at substrate defects. As a consequence, it is a source of irreproducibility and more robust buffer layers are required.

YBCO superconducting performances depend on the amount of secondary phase and the effects it produces on YBCO matrix. For all samples grown at these conditions (20°C/s, 845°C, 10^{-3} bar O_2), critical temperature is 90±1 K. An indication that Ta cations are not introduced in the YBCO crystal cell. However, self-field critical currents depend on film morphology. Sample *a* and similar present self-field J_c around 0.2 MA/cm^2, while J_c in sample *b* is 1.2 MA/cm^2.

5.4 Microstructure and physical characterizations of epitaxial YBCO films with T-route

A thorough study has been carried out in order to define the optimal processing parameters for synthesizing fully c-oriented YBCO thin films with TLAG. Different combinations of heating rate, melt composition and T-P_{O_2} conditions lead to fully epitaxial layers. Now, we correlate the resulting microstructure with the superconducting performances of those films.

Critical current density (J_c) and critical temperature (T_c) are the main parameters to be evaluated. J_c is an extrinsic property that depends on macroscopic defects influencing current percolation (J_c self-field, no applied magnetic field) and nanoscale distortions controlling vortex pinning, those increasing J_c in-field.

Hence, aiming at superior superconducting performance, it is necessary to have high homogeneity at the macroscale but with desirable defect landscape at the nanoscale. Inhomogeneities larger than coherence length ξ order parameter have been found to hinder percolating critical current [40].

Necessary microstructural characteristics for high J_c in HTSC materials are [49]:

- Good texture
- Homogeneity

- High density, low porosity [185]
- Low-angle grain boundaries [186]
- Pinning sites
- Optimum oxygen content (T_c)

Typically, films derived from melt growth techniques are of very low porosity and high texture quality. However, J_c in-field enhancement is limited by the difficulties to introduce artificial pinning defects in a melt.

On the other hand, solution processing techniques allow the introduction of secondary phases that act as pinning centres, such as preformed nanoparticles stabilized in the precursor solution [187, 159]. However, current percolation can be affected by the higher degree of porosity or defects in YBCO from CSD methodology [185, 122, 181]. Several types of structural inhomogeneities were identified for YBCO thin films affecting properties in different degree [188, 183, 189].

TLAG presents an opportunity to join the advantages of high quality liquid derived microstructure with the possible introduction of artificial pinning centres by chemical solution processing techniques. Hence, both J_c self-field and in-field can be maximized.

5.4.1 Growth regimes and texture quality

SQUID and transport measurements have shown good performances of films processed with T-route (Fig. 5.26). Critical current densities up to $3\,MA/cm^2$ at self-field and 77 K have been achieved. Critical temperatures 90-92K point out a good oxygenation level and no carbon contamination.

It has been observed that performances and reproducibility strongly depends on processing conditions. In Figure 5.27a, the amount of epitaxial samples that could be reproduced at the optimum zone for c-axis oriented heterogeneous YBCO growth for each composition, depending on the heating ramp.

The uncontrolled nucleation happening during slow heating entails limited reproducibility on YBCO crystallization. For instance, among all processed samples at the most optimum conditions for (2:3) liquid at 0.4°C/s ramp (835°C,

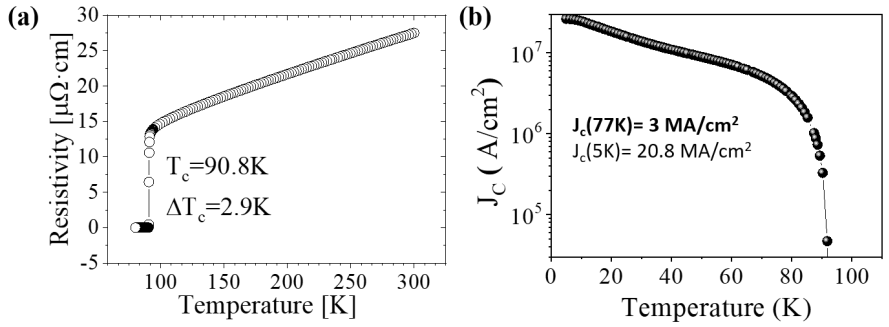

Figure 5.26: (a) Resistivity with temperature from transport measurements. T_c=90.8 K. (b)Self-field J_c with temperature for 300 nm YBCO film grown from the stoichiometric solution at 835°C, 0.4°C/s, 10^{-3} bar O_2

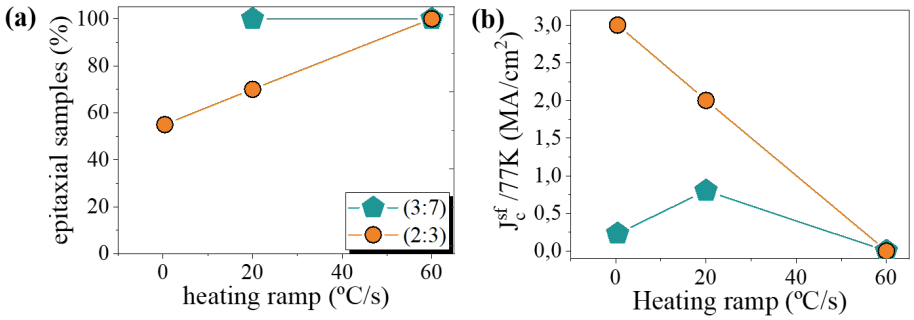

Figure 5.27: (a)Reproducibility represented by the number of epitaxial samples obtained after growth at the optimum conditions for each heating ramp and Ba:Cu ratio: (2:3), in orange and (3:7), in turquoise. (b) Maximum self-field J_c at 77 K achieved in each case

10^{-3} bar O_2), a 50% lead to some polycrystalline or a/b-oriented YBCO grains. Instead, with the increase of heating rate, nucleation conditions are better controlled by the defined final processing temperature.

Differently, liquid (3:7) gives rise to 100% reproducibility on $YBa_2Cu_3O_{7-\delta}$ crystallization due its lower supersaturation as compared to the (2:3) melt,

favouring in all cases epitaxial nucleation.

However, maximum self-field J_c values with the TLAG T-route were achieved with the slowest heating rates and the stoichiometric composition (Fig. 5.26). In Figure 5.27b, maximum self-field J_c obtained so far for each composition and heating rate explored, are presented.

Yet, superconductivity is vanished when using ultrafast rates. The upper limit is ascribed to enhanced reactivity, metastable secondary phases or cations segregation affecting current percolation, described in last section.

Thus, a trade-off between reproducibility and performances is achieved at intermediate fast rates ($\sim 20°C/s$), for both solutions.

There is a very close relationship between processing conditions, microstructure and performances. Maximum critical currents achieved in the possible T-P_{O_2} conditions for TLAG growth are also illustrated in Figure 5.28a for rates of 20°C/s and both melt compositions.

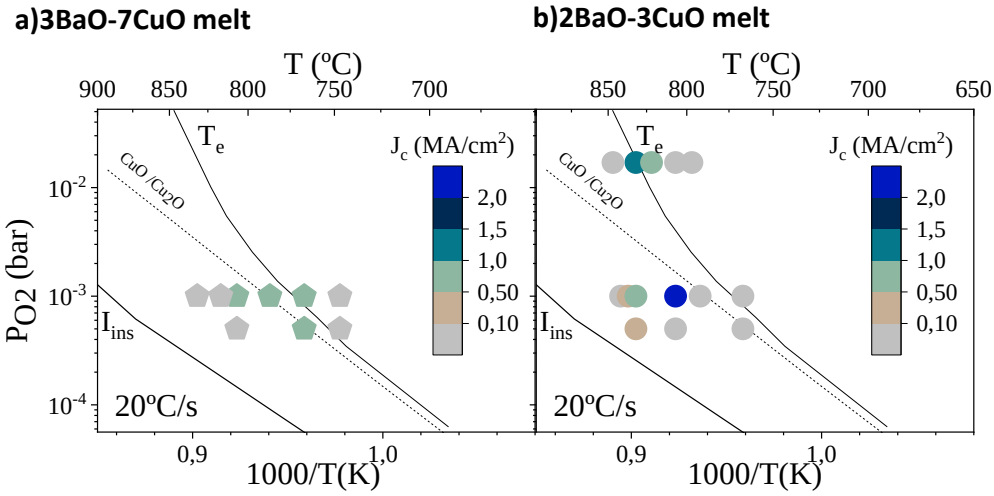

Figure 5.28: Maximum self-field J_c at 77 K (coloured scale) after growth at 20°C/s on T-P_{O_2} different conditions. For liquids (a)(3:7) and (b)2:3

It can be observed how the processing window for the (2:3) melt is quite narrow (Fig.5.28b), restricted to high temperatures (>810°C) and low P_{O_2} for epitaxial nucleation; and limited by melt reactivity with the substrate, as demonstrated in the last section 5.3.2.

In contrast, (3:7) melt allows fully c-axis nucleation at lower temperatures (770°C) and a wider temperature range (Fig.5.28a). As a consequence, reactivity is hindered in these conditions and both factors benefit achieving higher reproducibility.

Maximum J_c values for rates of 20°C/s are also plotted in Figure 5.29a depending on growth temperature. For 3-7 melt, maximum J_c at 77 K is up to 1 MA/cm^2, and to 2 MA/cm^2 for the 2-3 melt. Critical temperatures (Fig. 5.29b) are maintained above 90K in all cases and ΔT_c around 1 K, suggesting optimal doping and no contamination of C or other elements.

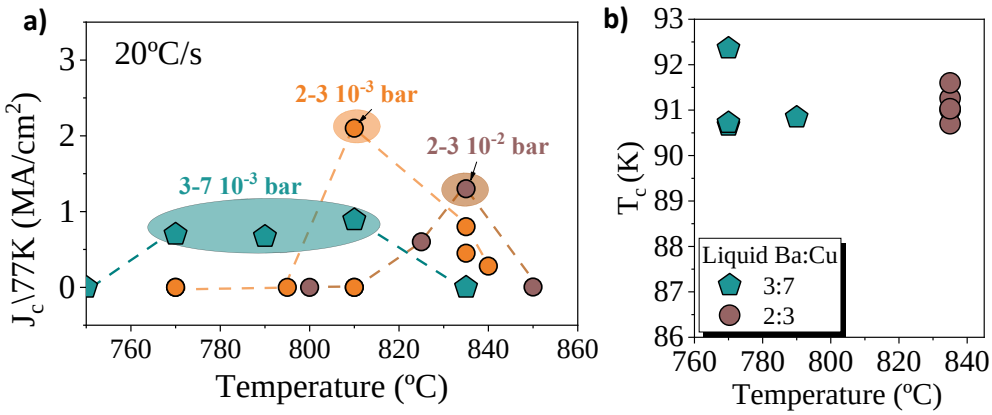

Figure 5.29: (a)Maximum self-field J_c at 77 K at 20°C/s depending on growth temperatures and solution composition, P_{O_2}, indicated in the graph (b) Critical temperatures measured by the Van der Pauw method [190]

The reason for the limited critical currents at self-field, specially for solution

with Cu excess, requires of a deep analysis to correlate microstructure with superconducting physical properties.

At first, texture quality is evaluated for maximized J_c samples. Due to the anisotropic character of superconductivity in cuprate superconductors, a good texture is a requirement for the achievement of high J_c values. Misoriented grains will affect current percolation, controlling J_c at self-field.

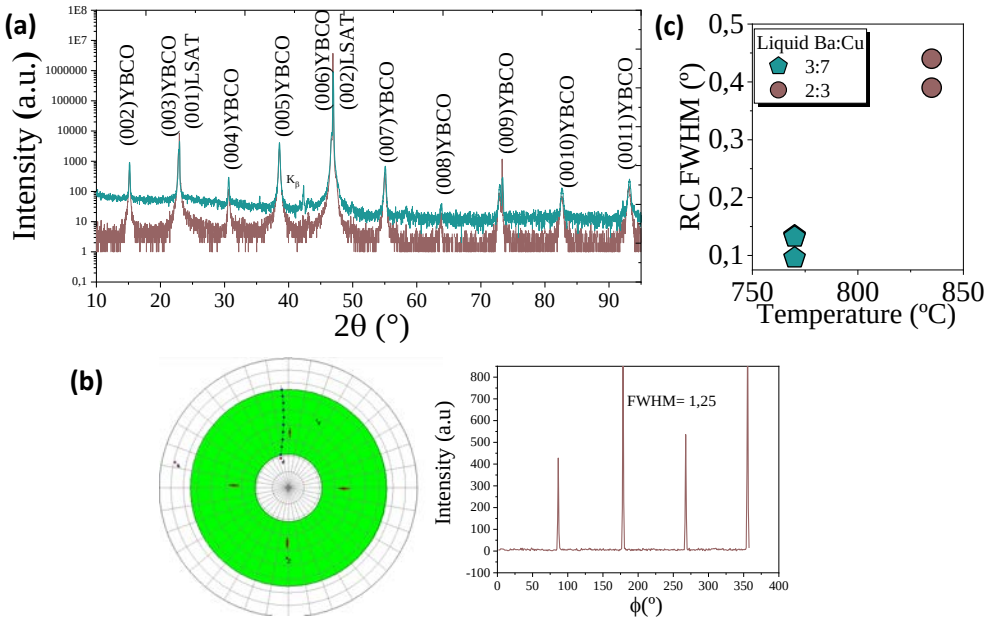

Figure 5.30: Standard YBCO films grown from (2:3) liquid at 835°C (orange), and (3:7) liquid at 770°C (turquoise), at 20°C/s. (a)HR-XRD, only epitaxial YBCO is observed (b) YBCO (103) pole figure and φ scans (c) FWHM values corresponding to YBCO (005) ω scans

Figure 5.30 shows HR-XRD with (00l)YBCO diffraction planes, with no presence of other secondary phases. (103) φ-scan exemplifies a standard sample with four-fold symmetry and low misorientation angle (1.2°). Out-of-plane ω rocking curves are documented in Fig(5.30c). Extracted FWHM values for both melt compositions indicate a high degree of out-of-plane texture, specially for

(3-7) solution (0.12±1°), with nearly single crystal quality.

Hence, the high degree of texture quality has been found to be comparable to that from liquid mediating growth, specially when using 3-7 melt composition that allows larger melt extent. Therefore, the limitation on self-field J_c can not be explained by crystal misorientations.

5.4.1.1 Growth of thick films

One of the technology requirements in CCs is the growth of large thickness layers for enhancing total critical current I_c [31]. The results presented above are for layers around 200 nm thick, deposited with one spin coated deposition.

We have identified that most of the steps are influenced by film thickness. First, pyrolysis process of large solution volumes is more difficult and there is still room for improvement in order to achieve completely homogeneous thick pyrolyzed films with a proper nanocrystalline distribution.

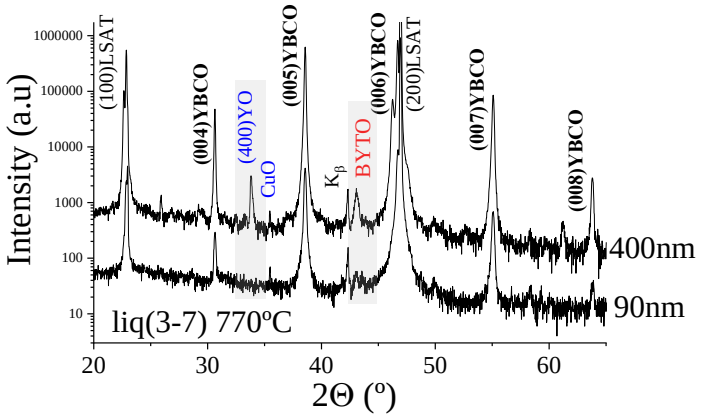

Figure 5.31: HR-XRD of 90 nm (1M solution) and 400 nm (2depositionx1.5M solution) thick films grown at the standard conditions for the (3:7) liquid (770°C, 20°C/s and 10^{-3} bar O_2 on LSAT) Reactivity phase BYTO is only observed in the thickest film

Then, barium decarbonation is delayed with the film thickness increase, thus altering conditions for YBCO nucleation and growth during heating. For in-

stance, HR-XRD in Fig.5.31 demonstrate that dissolution of substrate elements to produce competing phases (BYTO in this case) is enhanced when annealing thicker films in the same conditions. This is a consequence of the precluded barium carbonate reactions, triggering YBCO nucleation to happen at higher temperatures while heating, when melt becomes more corrosive. As a consequence, we observe an increase of reactivity with the film thickness at the same processing conditions. Changes on film thickness require new optimization of processing parameters.

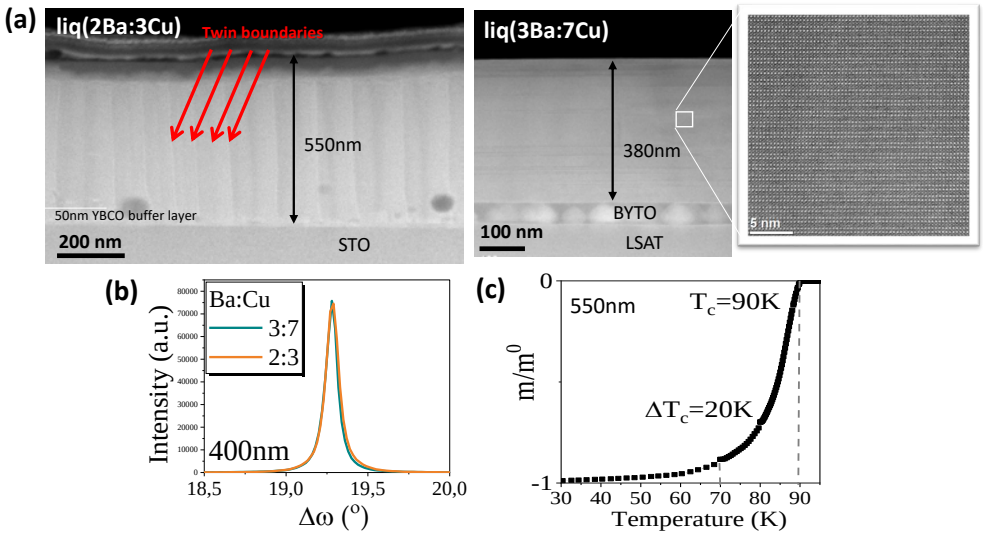

Figure 5.32: (a)STEM images for YBCO thick films deposited by the multideposition approach with the two liquid compositions. The 2:3, at left has been deposited on a 50nm PLD YBCO buffer layer and grown at 820°C/, 20°C/s, 10^{-2} bar O_2. The 3:7 liquid, at right, at 770°C and 10^{-3} bar O_2 and on LSAT, instead (b) YBCO (005) ω scans (c) T_c measured by SQUID for the 550 nm thick film from (2:3)liquid

Still, feasibility of growing epitaxial thicker layers up to 500 nm has been demonstrated. STEM images displayed in Figure 5.32a show homogeneous, pore free and epitaxial layers for both studied liquid compositions. The 3-7 liquid composition presents reactivity on LSAT substrate interface, but without

altering YBCO matrix on top. Higher magnification with atomic resolution STEM confirms the highly crystalline quality of the epitaxial growth. Additionally, no boundaries are observed between multi-coated layers or the buffer layer. For the 2:3 composition, straight twin boundaries crossing the total film thickness can additionally be identified.

Rocking curves (Fig 5.32b) on the (005)YBCO reflection are extremely low (0.09°and 0.08°using 2-3 and 3-7 melt, respectively), confirming that a high degree of epitaxy is maintained along film thickness.

Critical temperatures for 550 nm thick films remains as high as 90.1K, an indication that no carbon is retained at the grain boundaries also for thick films. However, a large $\Delta T_C \sim 20$K points out a certain degree of macroscale inhomogeneities or unreacted phases that also limit J_c self field to 0.2 MA/cm^2. Thus more effort is needed to maximize properties of thick films with processing optimization.

5.4.2 Films morphology and granularity

Films homogeneity and density can be analysed by means of Scanning Electron Microscopy (SEM) of films surfaces.

Low magnification images (Fig. 5.33) reveal homogeneous surfaces with some precipitates on top attributed to remaining CuO or $BaCuO_2$. The amount of surface grains is higher for the films that have been grown in fast heating rates. The biggest ($> 1\mu m^2$) and darker grains are CuO, which are present in higher amount on Cu excess film. Hence, remaining CuO in the latter case is pushed up to the surface as YBCO grows. A positive fact that indicates exceeding Cu is not trapped inside YBCO matrix and does not affect final physical properties.

Surface morphology is compared with CSD-TFA route in Figure 5.34, in which YBCO growth is driven by solid-gas reactions. It leads to porous films with small grains (Film *a*). In contrast, CSD-TLAG films surfaces show a very low degree of porosity and much smoother grains. Such topographic differences evidence the different growth mechanisms and the existence of an intermediate liquid phase for the latter.

Within TLAG films, significant morphological differences at the micrometer

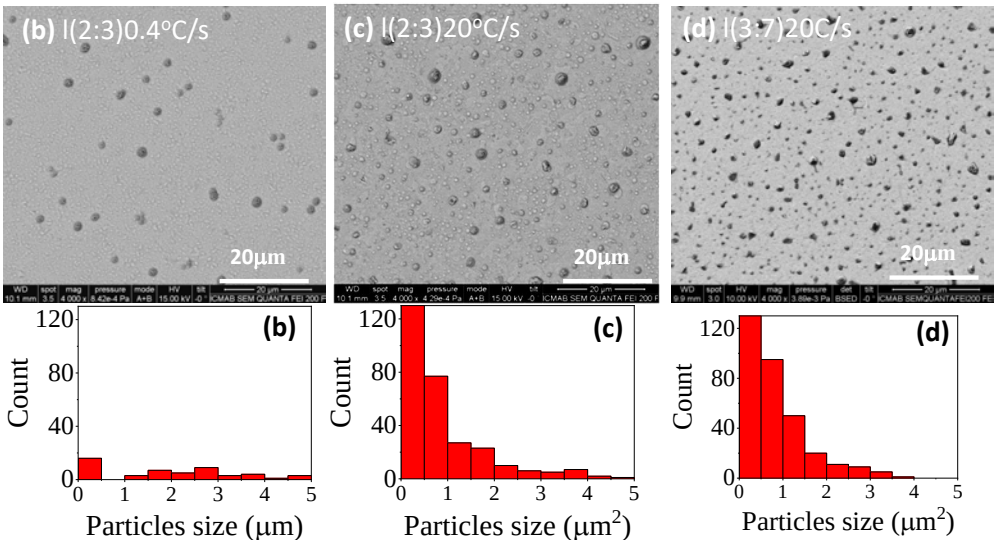

Figure 5.33: Surface SEM images at 4000x with SE detector of standard samples which annealing rates and Y:Ba:Cu compositions are: *b* 0.4°C/s, 1:2:3; *c* 20°C/s, 1:2:3; *d* at 20°C/s, 1:2:4.7.

scale can be observed depending on annealing rate or flux composition. A film grown at a slow heating velocity (Film *b*, 0.4°C/s, 1:2:3) presents smaller and more density of grains. In contrast, fast heating ramps (20°C/s) lead to plate-like grains of large in-plane grain sizes and meandering grain boundaries. In this case, some voids of uncovered substrate with irregular shape are present between grain boundaries.

Films processed with distinct conditions entail nucleation and growth at different supersaturation σ levels. As reported in section 5.1, σ degree gets smaller for increased heating rates and Cu excess: *b*(2-3,0.4)> *c*(2-3,20)> *d*(3-7,20).

Since nucleation rate and growth modes depend on supersaturation, we can ascribe a relationship between morphology and grain sizes with σ for the distinct growth conditions in TLAG.

Figure 5.35 illustrates the process of nuclei ripen into larger grains. After first nuclei has reached a critical size r^* to nucleate (t_{ind}), continuous films arise

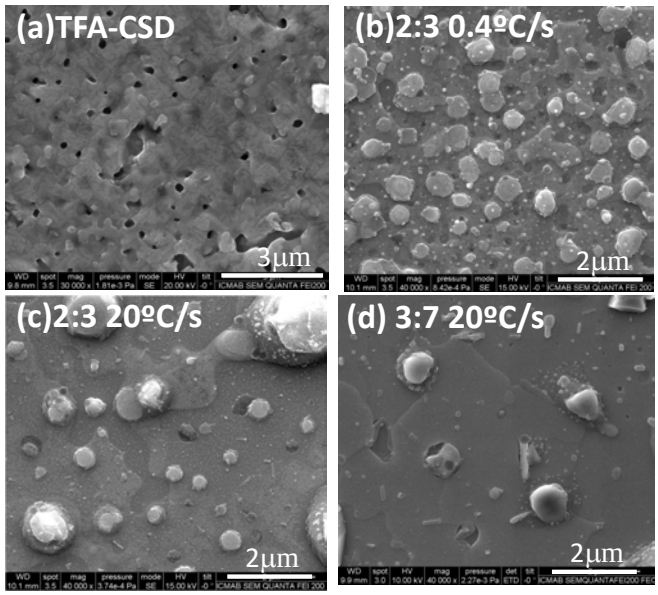

Figure 5.34: SEM of films surface at 40.000x of *a* CSD-TFA, *b* 0.4°C/s, 1:2:3; *c* 20°C/s, 1:2:3; *d*, *e* 20°C/s, 1:2:4.7.

as a result of individual grain merging.

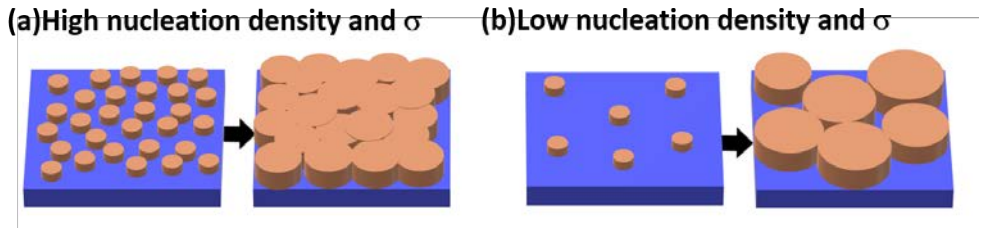

Figure 5.35: Schematic representation of nuclei ripen process, when nucleation density and supersaturation σ is (a)large and (b)small

Nucleation rate is exponentially enhanced as supersaturation increases (see

section 4.1). As a result, large σ will produce higher density of nuclei, leading to smaller final grain sizes, matching SEM observations of sample T(2-3)0.4.

With the supersaturation decrease, nucleation density may become very small. Then, dispersed nuclei are produced. Due to long intergrain distances between nuclei, larger grains are produced and coalescence may not be completed, leaving some film free areas. That would be the case for T(2-3)20 and T(3-7)20, the latter in a larger extent.

Magnetic granularity

Local current density in grains (J_c^G) can be discerned from percolative J_c^{sf} with a non-destructive inductive technique (Palau's model) [191, 192, 193]. J_c^{sf} exhibits a clear correlation with film morphology, while J_c^G is not modified by the presence of macro inhomogeneities. A decrease of percolative J_c can be related to magnetic granularity [122, 194].

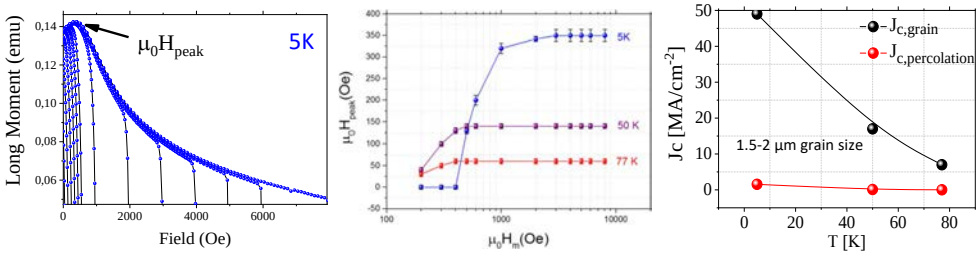

Figure 5.36: Magnetic granularity analysis by Palau's method on a sample grown at 20°C/s, 810°C 10^{-3} bar O_2 with 2:3 liquid. (a)Magnetization at different applied fields (b)Maximum magnetization peak ($\mu_0 H_{peak}$) versus applied field at different temperatures (c)Calculated grain J_c (black) as compared to percolative J_c (red)

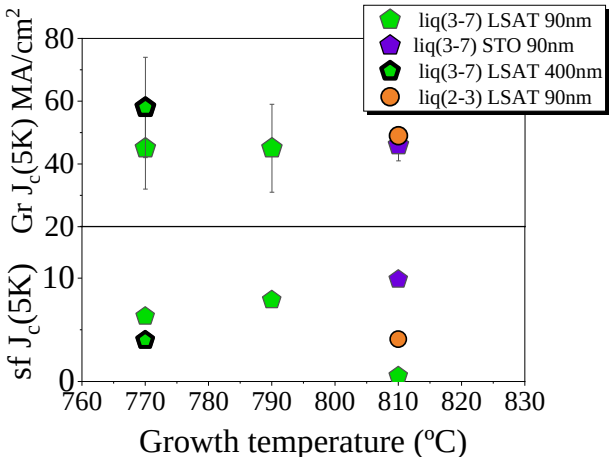

Figure 5.37: Self-field J_c measured with SQUID at bottom and grain J_c calculated with Palau's method, at top; for different samples

Studies on granularity have been performed by group co-worker J. Banchewski. Palau's method is exemplified in Figure 5.36 for a film grown on STO at 810°C with stoichiometric composition. As a result, inferred magnetic grain sizes are 1.5-3 μm and J_c grain highly increased respect to percolating current density up to 7 MA/cm^2 at 77K and 49 ± 15 MA/cm^2 at 5K.

A similar increase is observed for the rest of samples grown to different final growth temperature, leading to J_c^G at 5K around 45 MA/cm^2, also independently from solution composition, annealing conditions or percolative J_c. The thickest sample presents the highest J_c^G=58 MA/cm^2 at 5 K, while its self-field critical current density is the lowest (3.6 MA/cm^2).

Thus, YBCO has been demonstrated to give excellent superconducting properties. These experiments point out that the main difficulty triggering J_c self-field is magnetic granularity, most probably caused by low supersaturation levels that hinders nucleation density. This situation results on poor grains coalescence and residual voids left within grain boundaries that block current percolation.

5.4.3 Nanoscale defects landscape in T-route

Several nanometric size defects of different dimensionality have been identified to act as pinning centres in YBCO films. For example, twin boundaries, intergrowhts, anti-phase boundaries, point defects, edge dislocations or secondary phases. Those serve as pinning sites that enhance J_c performances at different regions of the H-T phase diagram, necessary for the use in a broad number of power applications [183, 195].

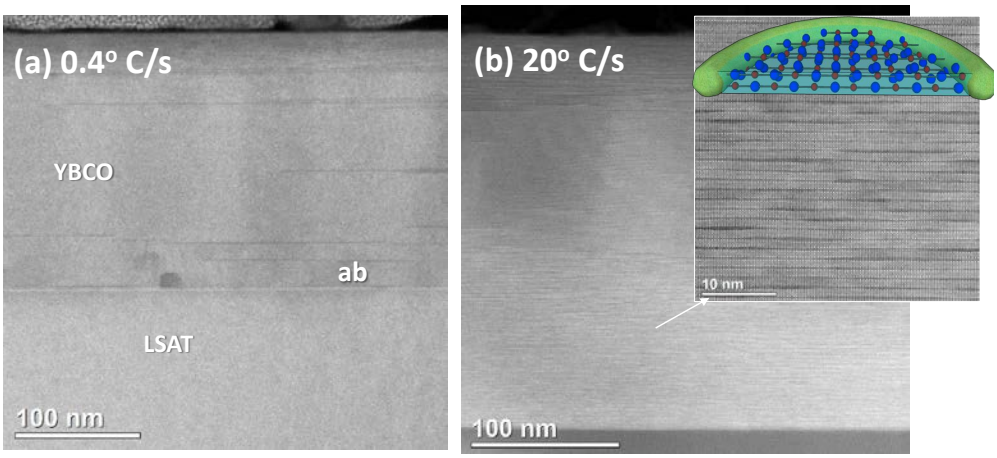

Figure 5.38: TEM images of YBCO films grown with the 2:3 liquid at heating rates of (a)0.4°C/s and (b)20°C/s to 835°C

In TLAG, each route may lead to distinguished microstructural characteristics in the final products. TEM images in Figure 5.38 illustrate the microstructure for films grown with the stoichiometric composition at different rates. Using a processing slow heating rate (Fig.5.38a), most of the film grows during heating at the YBCO slow growth rate region, around 2-5nm/s (see section 5.2.1). A defect-free microstructure is observed in agreement.

At a heating rate of 20°C/s to 835°C (Fig.5.38b), we have shown that YBCO grows at the fast growth rate region, at 40-100 nm/s. Therefore, the fast growth induce a highly defective YBCO matrix. The main defects appearing are the

$Y_2Ba_4Cu_8Ox$ (Y248) intergrowths (double CuO chains or stacking faults), similarly to the TFA-CSD process [196]. It is known that the Y248 intergrowth is one of the lowest energy defects able to accommodate large distortions in YBCO. This is in agreement with the ultrafast growth in TLAG-CSD process.

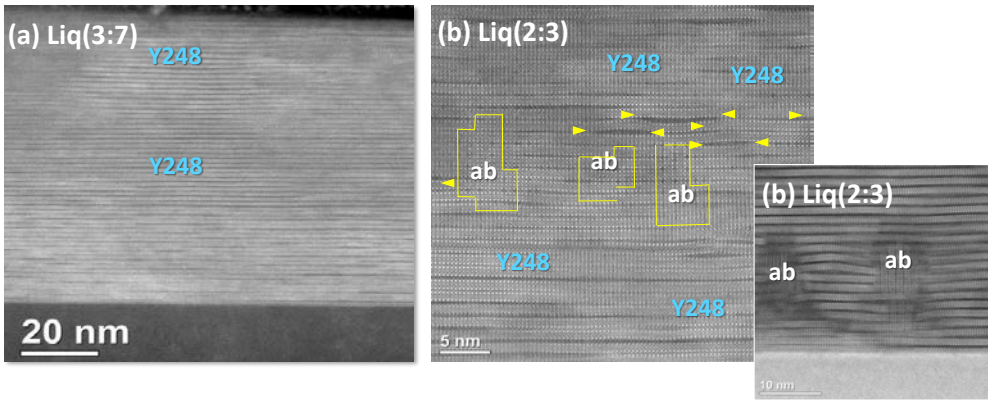

Figure 5.39: TEM images of YBCO films grown at 20°C/s with the (a) 3:7 liquid to 770°C and (b)2:3 liquid to 835°C

Now we compare the most characteristic defects in both studied liquid compositions at fast growth rates. Stacking faults (SFs) in solution (3:7) are larger than in the solution (2:3), for the same heating rate. Additionally, the film is free from ab-grains, in agreement to lower supersaturation for growth.

In contrast, nanoscale ab-grains in the range of 5-10 nm contribute on causing short lattice distortions in the (2:3)melt (Fig. 5.39b).

Figure 5.40 illustrates the magnetic field dependence of the critical current density, J_c. Both applied magnetic field in parallel to ab plane ($H^* \| ab$) or c-axis ($H^* \| c$) are shown, affected in different degree by the distinct defects. TLAG sample processed from stoichiometric (2:3) melt is compared to pristine TFA-CSD film and BZO TFA-CSD nanocomposite.

Pristine TLAG samples display a much smoother in-field J_c dependence and a large single vortex pinning plateau (identified by the H^* parameter) in both applied magnetic field directions respect to pristine TFA films. H^* can even

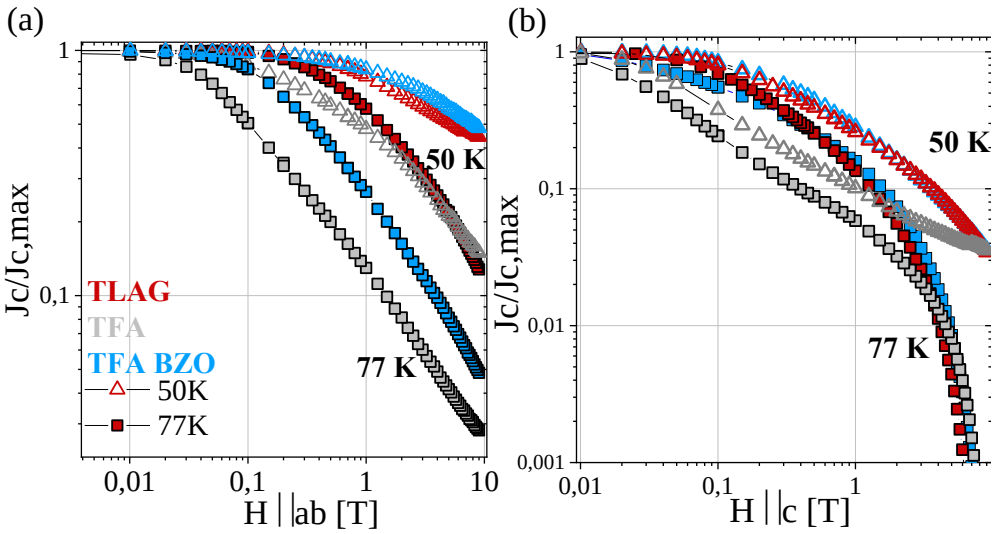

Figure 5.40: Normalized critical current density, J_c, dependence on the magnetic field at 50 K (open symbols) and 77 K (solid symbols) for a pristine TLAG YBCO with (2:3) solution (red), pristine TFA-CSD (grey) and BZO TFA-CSD nanocomposite (blue). At applied magnetic field in parallel to (a) ab plane ($H^*\|ab$) and (b) c-axis ($H^*\|c$). Films thickness is 200-300 nm

reach values 10 times higher than TFA pristine samples and 4 times BZO-TFA nanocomposites with pristine TLAG (2-3) solution, containing short SFs and nanosize ab grains, at 77K and $H^*\|ab$. At lower temperatures and $H^*\|c$, pristine TLAG magnetic field dependence performs like nanocomposite-TFA.

To conclude, we demostrate that TLAG technique nanostructure can be modulated by the growth process and solution composition. We have observed a very rich defect landscape in fast growth processed TLAG films leading to an increase of J_c in field. More extensive studies regarding physical properties are currently being performed by group co-workers, as well as the introduction of artificial pinning centres in TLAG. The influence of ab grains is more deeply studied in chapter 6.

5.5 Conclusions

The conditions for $YBa_2Cu_3O_{7-\delta}$ epitaxial nucleation and growth with a transient liquid were explored using the Temperature-route path; direct heating to the liquid and YBCO growth zone at a constant P_{O_2}.

Several strategies to reduce supersaturation ($\sigma \propto \frac{C_\delta}{C_e(T)} - 1$) of Y in the liquid and induce biaxially textured $YBa_2Cu_3O_{7-\delta}$ films were explored. On the one hand, σ can be tuned controlling the equilibrium concentration C_e with processing temperature and liquid composition. It was demonstrated that a melt with Cu excess favours epitaxial nucleation at lower temperatures, down to 650°C at a rate of 60°C/s.

On the other hand, heating rate is a crucial parameter in T-route, since we found that the amount of Y dissolved in the melt C_δ is compromised when fast heating rates are used. As a result, epitaxial films can be produced at all rates, but final temperature can be decreased if fast heating rates are used. Overall, there are many combinations and a wide processing conditions window that lead to epitaxial YBCO nucleation.

In situ XRD with synchrotron radiation of the transient liquid mediated growth process revealed two distinct T-P_{O_2} processing zones that could be accounted to distinct properties of the liquid. High temperatures induce very high growth rates of the epitaxial phase, up to 100 nm/s. At lower temperatures, YBCO growth velocity is in the order of 2-5 nm/s and polycrystalline grains are also formed. A surprising result is the disappearance of those misoriented grains in favour of c-axis heterogeneous growth when the crossover between the two zones is passed.

TEM analyses of quenched samples showed that the first heterogeneous nuclei of YBCO grow at the substrate interface whereas $BaCO_3$ grains (size around 40-50 nm) remain in the bulk of the film. This confirms that the slowest reaction is the $BaCO_3$ elimination. At the low temperature zone, ab-oriented $YBa_2Cu_3O_{7-\delta}$ grains nucleate on the epitaxial layer, and small random grains within the material bulk. At the final stage, at high temperature, a full YBCO epitaxial layer is observed and $BaCO_3$ has completely disappeared.

Some challenges had to be addressed to overcome the liquid reactivity with the substrates, due to its highly corrosive nature and improper substrates wet-

tability with the viscous liquid. High diffusivity and long induction time for YBCO nucleation ($t_{\text{ind}} \propto \frac{1}{T,\sigma}$) are the crucial parameters inducing liquid movement, resulting on phase segregation or formation of voids with the Cu excess composition; and interfacial reactivity with the substrate elements, in both solutions. Both are enhanced at high temperatures and fast heating rates, unfortunately the same conditions that favour epitaxial growth.

Several solutions are proposed for limiting liquid movement based on increasing the fraction of solid respect to the liquid. (i) A higher amount of Y_2O_3 has a huge effect on preventing liquid dewetting. Other solid phases could be tried, such as additives, nanoparticles or other RE elements with higher C_e to limit supersaturation. (ii) Clever designs using multilayered structures have a lot of potential to control liquid properties by the use of different combined compositions. The chemistry of the substrate is also important on liquid wettability. Reduced movement was found on LSAT substrates as compared to STO monocrystals.

The most straightforward strategy to avoid reactivity with the substrate would be the finding of an adequate buffer layer or the reduction of growth temperature with the already described strategies.

The understanding of the processing-structure-properties relationship is crucial to obtain good superconducting performances. The lower Y supersaturation in the eutectic liquid composition (3:7) gives rise to a very good reproducibility, excellent texture quality and a larger processing window for epitaxial growth without secondary phases. However, self-field critical currents (J_c) are limited by the presence of magnetic granularity. This is related to the resulting grain sizes, which depend on nucleation density, proportional to σ. High density and small grains seems to favour currents percolation and avoid film free areas.

In contrast, nanoscale defects are beneficial for J_c in field behaviour. Fast YBCO growth or small ab-grains induce a high density of defects, mainly in form of $Y_2Ba_4Cu_8Ox$ intergrowths. Overall, different microstructures are reached depending on the process route and parameters, making TLAG-CSD a very tunable process also for vortex pinning.

Chapter 6

TLAG-P_{O_2} route

This Chapter is devoted to TLAG films processing with the P_{O_2} approach. In this case, transient liquid assisted growth is achieved towards a switch on P_{O_2} conditions from below YBCO stability line at high temperatures.

Reaction paths during all steps, as well as YBCO growth rate, are studied by means of *in situ* XRD with synchrotron radiation. Then, supersaturation conditions are elucidated under this route characteristics. From these results, processing conditions for obtaining the epitaxial phase are optimized.

Finally, structural characterizations reveal texture quality, films morphology, the presence of reactivity derived secondary phases or a/b grains. All these factors influence final superconducting properties.

Overall, it will be demonstrated which are the growth requirements for achieving very high J_c values, up to 5.3 MA/cm^2 at 77K, self-field.

6.1 Reaction mechanisms in P_{O_2} route

In P_{O_2} route, transient liquid zone and YBCO growth are achieved from the region below YBCO stability upon a P_{O_2} change at constant temperature.

To do so, two processing steps are differentiated. During a first stage, the film is led to T-P_{O_2} conditions below YBCO stability ($T < T_{ins}, P_{O_2} \sim 10^{-5} - 10^{-4}$ bar. Under this environment, $BaCO_3$ elimination to form the binary oxide is expected without subsequent YBCO crystallization (see Fig.3.28 in Chapter 3).

Depending on the base oxygen partial pressure, precursor phases and conversion reactions may be different. This study is devoted to a low P_{O_2} range between $10^{-5} < P_{O_2} < 10^{-4}$ bar.

A second step is used to generate the transient liquid and crystallize YBCO by placing the sample to YBCO stability zone in the phase diagram. This process is carried out by increasing atmospheric P_{O_2} to $2 \cdot 10^{-4} - 10^{-2}$ bar at a constant temperature ($T > T_e$).

Thermodynamic species below YBCO stability line and 850°C reported by Driscoll *et al* are Y_2BaCuO_5 (Y211), $YBa_3Cu_2O_{6.5}$ (Y132) and $BaCu_2O_2$. The latter becomes liquid at higher temperatures [148]. On the other hand, Seok *et al* identified liquid already below 850°C and Y_2O_3 instead of Y211, coming from amorphous precursors [197].

Our synthesis takes place in short times and thermodynamic equilibrium conditions are not achieved. For this reason, it is necessary to elucidate reaction mechanisms with *in situ* techniques. To do so, we performed X-ray diffraction with a two dimensional detector during the synthesis process at very fast acquisition times using synchrotron radiation.

As precursors, we used pyrolyzed thin films composed by $BaCO_3$, CuO and Y_2O_3 nanocrystals.

For this study, a 800 nm pyrolyzed film of Y:2Ba:4.66Cu cations molar ratio (3-7 melt), was annealed under $P_{O_2} = P_{tot} = 10^{-5}$ bar at a rate of 5°C/s to 850°C and hold until $BaCO_3$ total decomposition reaction was attained (200 s).

Then, without modifying sample temperature, a fast change on P_{O_2} to $2 \cdot 10^{-2}$ bar was achieved by switching gas inlet to a line provided by a rotary pump and air flow under 0.1 bar.

In such experimental configuration, the entrance of cold gas diminished eventually sample temperature from 850°C to 770°C. In an optimized experiment, the gas should be preheated to avoid a temperature decrease.

Meanwhile, XRD data acquisition with a two dimensional detector was performed every 500ms and 100ms for steps 1 and 2, respectively (see section for more experimental details 2.2.5).

The corresponding XRD diffractograms are displayed in Appendix 7.6. After data treatment, the main reflections intensities evolution from all identified phases were normalized by their maximum intensity. As a result, species evolution along the two processing steps are depicted in Figure 6.1.

The reactions observed to synthesize YBCO are summarized hereunder:

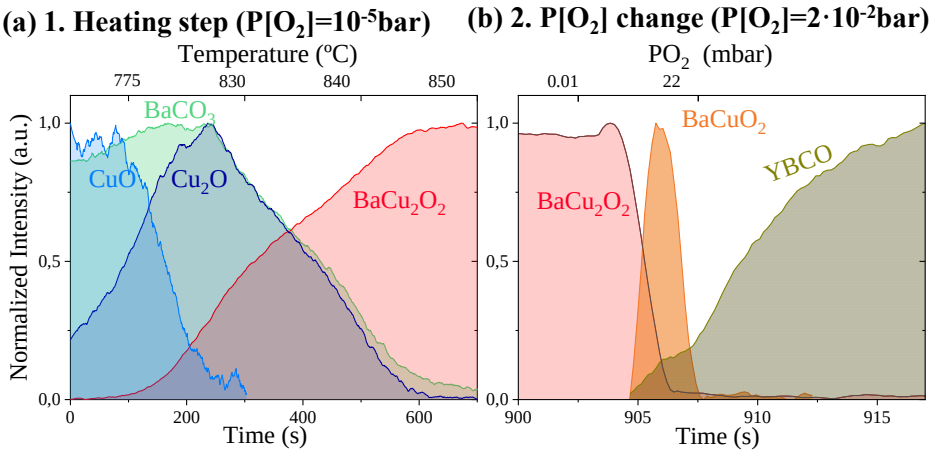

Figure 6.1: Phases evolution inferred from peak intensities *in situ* XRD by synchroton radiation (a) Step 1 temperature increase to 850°C at $P[O_2]_i = 10^{-5}$ bar; (b) Step 2 accounts to P_{O_2} switch to $P[O_2]_f = 2 \cdot 10^{-2}$ bar. Temperature was unstable between 850-780°C. $P[tot]_i = 10^{-5}$ bar and $P[tot]_f = 10^{-1}$ bar.

- **Step 1: Heating at low P_{O_2}**

$$4\,\mathrm{CuO} \longleftrightarrow 2\,\mathrm{Cu_2O} \tag{6.1}$$

$$2\,\mathrm{BaCO_3(s)} + 2\,\mathrm{Cu_2O\,(s)} \longleftrightarrow 2\,\mathrm{BaCu_2O_2(s)} + 2\,\mathrm{CO_2(g)} \tag{6.2}$$

- **Step 2: P_{O_2} change**

$$2\,\mathrm{BaCu_2O_2} + \mathrm{O_2} \longrightarrow 2\,\mathrm{BaCuO_2} + 2\,\mathrm{CuO} \tag{6.3}$$

$$2\,\mathrm{BaCuO_2} + 2\,\mathrm{CuO} + \frac{1}{2}\,\mathrm{Y_2O_3} \longrightarrow 2\,[\mathrm{BaCuO_2} + \mathrm{CuO}]\,(\mathrm{l})$$
$$+ \frac{1}{2}\,\mathrm{Y_2O_3(s)} \longrightarrow \mathrm{YBa_2Cu_3O_{7-\delta}} + \mathrm{CuO} \tag{6.4}$$

Step 1: Temperature rise at low P_{O_2}

Along a temperature rise at 10^{-5} bar, CuO is first reduced to Cu_2O after surpassing the corresponding thermodynamic line [198].

Then, $BaCO_3$ reaction with Cu_2O leads to $BaCu_2O_2$ between 800-850°C, the stable mixed oxide at these conditions. No other of the thermodynamic predicted species or melting were observed after 5 min dwell at 850°C (see XRD A7.6).

Hence, differently from T-route, in this case $BaCO_3$ elimination may be disentangled from the YBCO growth if it is completed at low P_{O_2} regime, below YBCO stability region.

Kinetic considerations regarding this reaction, focused on $BaCO_3$ elimination are presented in Chapter 3.4. $BaCO_3$ reaction with Cu_2O to form $BaCu_2O_2$ at $P_{O_2} < 10^{-4}$ bar is slower than the one with CuO to form $BaCuO_2$ at higher oxygen pressures. Additionally, the absence of a liquid in this step, which benefit very fast decarbonataion rates in the Temperature-route, is here not present.

Still, applicable to this route, $BaCO_3$ elimination can be enhanced by promoting CO_2 outdiffusion. As we demonstrated, the lower P_{total} or higher flux rate, the faster the decomposition of $BaCO_3$.

Notice that in this process only oxygen partial pressure is the crucial parameter and not total pressure.

Yet, total carbon elimination of 400 nm film has been just proven possible under low total pressure (10^{-5} bar) in the synchrotron experiments.

Currently, a new tubular furnace has been installed in our laboratories and allows a high N_2 flux of 3L/min with $P_{O_2} = 10^{-5}$ bar. Recent experiments show complete $BaCO_3$ elimination in 400 nm thick films during step 1 at 1 bar of total pressure. Therefore, the possibility to work at atmospheric pressures makes this route even more cost effective.

Step 2: P_{O_2} change

Then, during step 2, a P_{O_2} jump from 10^{-5} to $2 \cdot 10^{-2}$ bar brings first the barium copper oxide to its oxidized solid form $BaCuO_2$. Yet, the X-ray intensity of the latter diminishes immediately. This fact implies therefore the formation of the liquid [$BaCuO_2$-xCuO] that can not be detected with XRD.

Finally, YBCO crystallization can be followed by a gradual intensity increase

that continues after any other signal for solid phases is present. Hence, we can deduce that $YBa_2Cu_3O_{7-\delta}$ is formed by subsequent Y dissolution from Y_2O_3 nanoparticles into the melt, diffusion and reaction at the substrate interface.

In the light of these findings, we confirm the occurrence of a transient liquid at the same final crystal stability zone in the phase diagram. For this reason, TLAG-P_{O_2} route can be distinguished from other methods such us co-evaporation and direct reaction (RCE-CDR) [64] or high-rate molecular beam epitaxy (MBE) [59]. Both techniques are based on thermodynamically stable liquids at other regions in the phase diagram.

As a consequence, TLAG could allow a wide room for conditions processing at lower temperatures and higher total pressures, thus requiring less complex processing systems and without the need of high vacuum.

6.2 YBCO crystallization decoupled from $BaCO_3$ elimination

We have proven that in P_{O_2} route YBCO nucleation and growth takes place in isothermal conditions and it is decoupled from $BaCO_3$ rate limiting reaction. Hence, crystallization temperature can now be directly defined before the P_{O_2} jump.

Consequently, nucleation temperature is in this case independent from precursors reaction kinetics, in contrast to T-route, in which all reactions take place consecutively. This fact represents a huge advantage for controlling supersaturation conditions for epitaxial nucleation and growth rate.

6.2.1 *In situ* YBCO growth rate

In this section $YBa_2Cu_3O_{7-\delta}$ growth rate is estimated from *in situ* XRD experiments. Two different final P_{O_2} are compared.

Additional to the *in situ* XRD experiment described in the last section (i) ($P[O_2]_{final} = 2 \cdot 10^{-2}$ bar), another experiment was carried out with the same step 1 conditions but to lower final oxygen pressure (ii) $P[O_2]_{final} = 2.5 \cdot 10^{-4}$ bar). In this case, atmospheric conditions were achieved by switching gas

inlet to N_2 flow at 1 bar. The real P_{O_2} was measured with a P_{O_2} -meter. Total pressure jump was therefore one order of magnitude higher than in the other experiment ($P_{tot,i} = 0.1$ bar and $P_{tot,ii} = 1$ bar).

Temperatures before P_{O_2} switch were 850 and 830°C respectively although unfortunately after pressure jump those were fluctuating down to 780°C and 750°C as the cold gas was introduced. Hence, the gas should be previously heated for future more precise experiments. For this reason, with our present results, we can disentangle growth rate dependence on P_{O_2} but not on temperature.

Other parameters are films thicknesses, being 400 nm and 200 nm after growth, respectively.

The corresponding time resolved XRD patterns during P_{O_2} increase for YBCO synthesis can be observed in Figure 6.2a.

In Figure 6.2b, the precursors evolution and YBCO main reflections intensities are plotted along the P_{O_2} change. The first observation is related to the growth rate. Significant differences on YBCO formation speed exist when comparing both samples.

First, c-axis $YBa_2Cu_3O_{7-\delta}$ growth rate is analysed for sample (ii) ($P[O_2]_{final} = 2 \cdot 10^{-4}$ bar) in Fig.6.2, which processing conditions result on the formation of a fully epitaxial layer.

(005) YBCO intensity reflection is assumed proportional to the YBCO c-axis oriented film thickness. Conversion of this film up to 70% based on the XRD intensity, is attained with only 2s, which gives a growth rate of ∼100 nm/s. Maximum speed inferred from the maximum slope implies 130nm/s.

In contrast, sample (i) ($P[O_2]_{final} = 2 \cdot 10^{-2}$ bar) attains much slower growth rate. After all solid phases have reacted, ∼ 160 s are needed to reach 70% of total (005)YBCO reflection intensity. This results on a growth rate of 2.5 nm/s.

The reasons for growth rate differences between these *in situ* experiments are still unclear since several parameters were not fully optimized and they differ in more than one parameter (films thickness, final P_{tot}, P_{O_2} jump speed). Still, the $BaCu_2O_2$ oxidation to $BaCuO_2$ observed in sample (i) in Fig.6.2 demonstrates that the final P_{O_2} has been reached and the transient liquid is formed when the slow YBCO growth rate is observed.

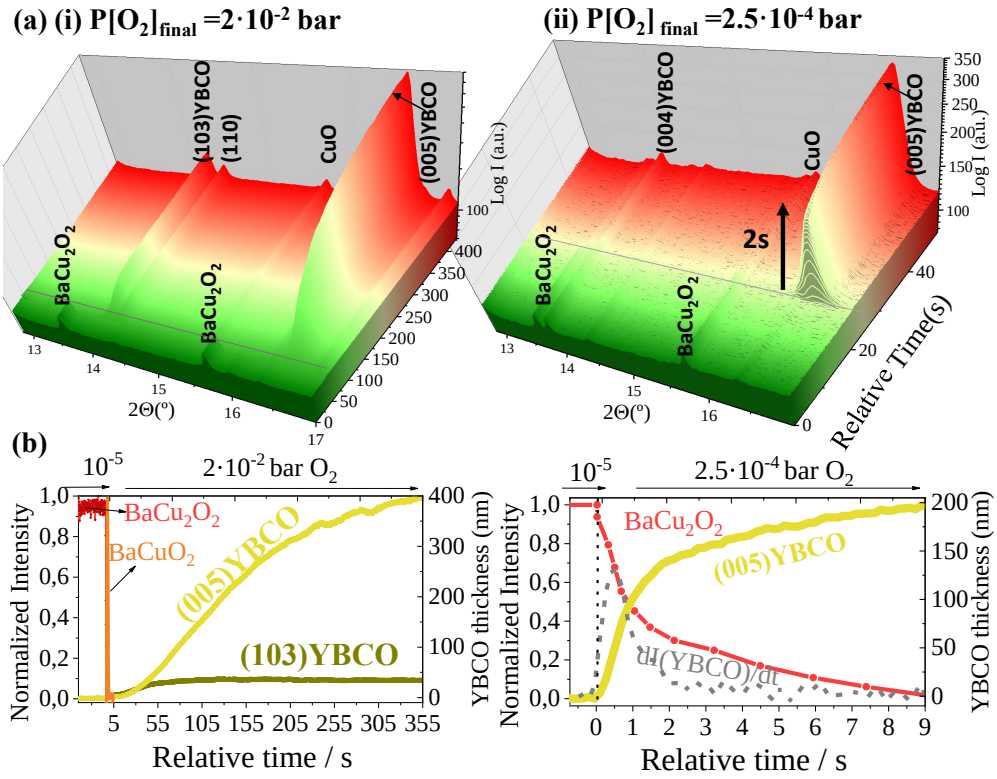

Figure 6.2: *In situ* XRD patterns for YBCO synthesis along P_{O_2} switch represented in (a) three dimensional plot and (b) normalized main peak intensities evolution. Atmospheric conditions are (i)$P[O_2]_{final} = 2 \cdot 10^{-2}$ bar and (ii)$P[O_2]_{final} = 2.5 \cdot 10^{-4}$ bar, while $P[O_2]_i = 10^{-5}$ bar in both cases. Initial temperatures are 850°C and 830°C with 70 and 80°C drop

The main parameter determining growth rate may be related to the growth T-P_{O_2} conditions. A TLAG schematic phase diagram is represented in Figure 6.3a, where the two *in situ* experiments conditions are indicated among *ex situ* samples that will be discussed in the next section 6.2.2.

For instance, the eutectic temperature diminishes with the decrease of P_{O_2}. For sample (i) processed at $2 \cdot 10^{-2}$ bar O_2, growth conditions lay at $T < T_e$

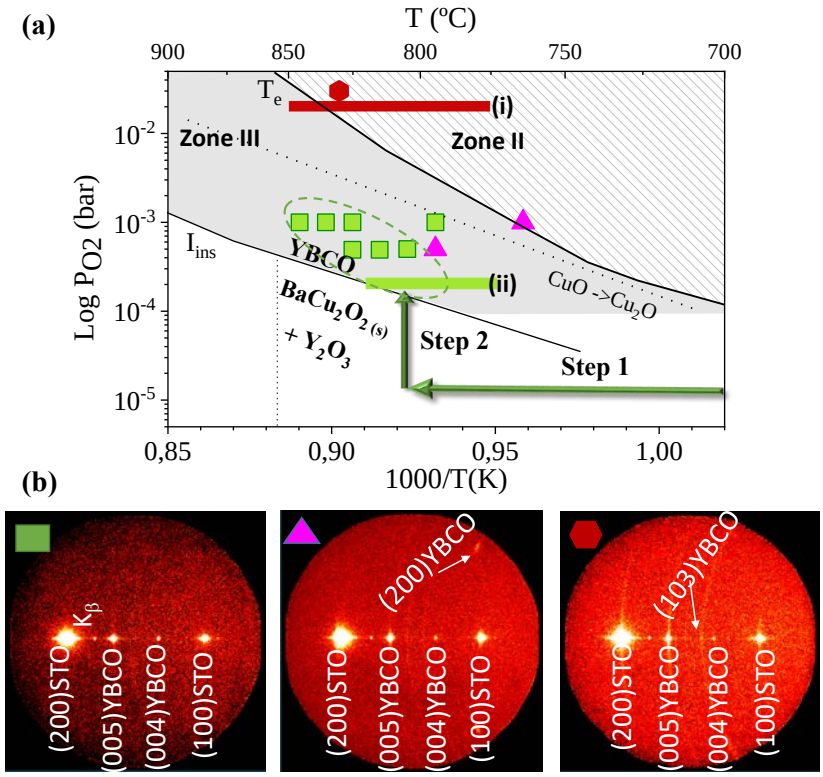

Figure 6.3: (a) YBCO orientation depending on T-P_{O_2} processing conditions from P-route path. Green denotes c-axis growth, pink c-axis with $> 10\%$ ab grains and red the presence of polycrystalline grains. The symbols along a wide temperature range represent the *in situ* experiments (b) Examples of 2D GADDS-XRD for each case.

in zone II at the phase diagram (see Fig. 6.3). In contrast, sample (ii) at $2.5 \cdot 10^{-4}$ bar O_2 is grown in zone III where $T > T_e$.

TLAG Temperature-route experiments showed a similar difference on growth rate for the two zones in the phase diagram. YBCO growth rates are about 100 nm/s at high temperatures (zone III) and ~5 nm/s at lower temperatures (zone II). The differences were mainly accounted to changes in liquid properties

that may affect Yttrium dissolution or diffusion.

Additionally, the (103)YBCO reflection observed in film (i) corresponds to homogeneous nucleation that occurs during the first 35 s seconds of YBCO growth. It represents a 10% in peak intensity respect to the epitaxial phase. Homogeneous nucleation is also observed in T-route at zone II.

Instead, the film (ii) processed in zone III, attains completely epitaxial growth, also in accordance with T-route results.

In the next section, *ex situ* experiments are presented in order to discuss in more detail nucleation mechanisms in different T-P_{O_2} conditions.

To sum up, very fast YBCO formation velocity (100 nm/s) and completely epitaxial growth can also be achieved with the P_{O_2} approach. Growth rates are comparable to those obtained through directly heating to the same final processing zones.

In this perspective, TLAG becomes a very versatile technique, since very fast epitaxial growth takes place independently from the reaction path.

6.2.2 Nucleation control with the processing conditions

Several samples have been processed with the P_{O_2}-route path to different final environments with the RTA furnace. The resulting crystal structures have been characterized *ex situ* with X-ray diffraction and a 2D GADDS detector.

The symbols in the TLAG schematic phase diagram in Figure 6.3 indicate crystallization type achieved after processing at each condition.

Green squares represent epitaxial c-axis orientation, pink triangles depict c-axis with $> 10\%$ ab grains and red hexagon the presence of polycrystalline grains. Examples of the corresponding characteristic 2D-XRD images are shown hereunder for each mixture.

The results on YBCO nucleation type are similar to the *ix situ* films in spite of the experimental processing differences.

The *ex situ* experiments have been performed in a Rapid Thermal Annealing (RTA) oven allowing very fast P_{O_2} change (2ms). All samples have been processed using eutectic melt composition 3-7 (Y:2Ba:4.66Cu). Final films thicknesses are 90 nm.

Step 1 conditions are 0.4°C/s to 830°C and 5 min of holding time at $P_{O_2} = 10^{-5}$ bar, $P_{tot} = 3 \cdot 10^{-3}$ bar. The use of longer dwells produces $BaCuO_2$ coarsening, leaving afterwards unreacted Ba-Cu-O phases within the grown film. 5 min is enough to decarbonate thin films, but $BaCO_3$ elimination is not completed for thicker films than 200 nm due to the poor flow conditions performance of this furnace. These results are shown in Chapter 3.4.

The step 2 switch to YBCO stability zone is carried out by introducing gas while the rotatory pump is still working. The resulting final pressure is $P_{tot} = 2 \cdot 10^{-2}$ bar while P_{O_2} is modified with $N_2 : O_2$ gas ratio. Temperature is fixed from the low P_{O_2} conditions and 2 min temperature dwell is kept after the step. (more experimental details are given in section 2.1.4.1).

Supersaturation for $YBa_2Cu_3O_{7-\delta}$ nucleation depends on final T-P_{O_2} processing conditions.

With the P_{O_2} change approach and differently from the heating route, nucleation can be directly performed at zone III ($T > T_e$), avoiding nucleation at zone II area ($T < T_e$) where growth rate is limited and supersaturation is higher.

A small amount of homogeneous nucleation is only observed at the highest P_{O_2} conditions explored so far and in zone II of the phase diagram. The results are in accordance with the *in situ* experiment (i) described in section 6.2.1.

At $P_{O_2} < 10^{-3}$ bar in zone III, all films are epitaxial with variable amount of a/b grains, particularly higher at the lowest temperatures.

The best zone for epitaxial growth found so far with the P_{O_2} approach is marked with a circle in Figure 6.3. This is above 810°C and P_{O_2} between $2.5 \cdot 10^{-4}$ bar to 10^{-3} bar, the region that lies just above the low stability line (T_{ins}). Samples with excellent superconducting properties, up to 5 MA/cm^2, could be obtained.

Supersaturation conditions for nucleation

The obtained nucleation orientations and texture quality can be correlated to supersaturation levels for nucleation. a/b-orientation requires of a larger supersaturation to nucleate than c-axis-orientation (see Chapter 4.2.4).

The relative supersaturation can be expressed as $\sigma = (C_\delta - C_e(T))/Ce(T) = (C_\delta/C_e) - 1$, which equilibrium concentration C_e is temperature dependent (increasing with T) and particular for each liquid composition.

Then, the actual Y concentration C_δ may depend on the growth technique. In TLAG, the different paths to reach the transient liquid zone may lead to distinct C_δ.

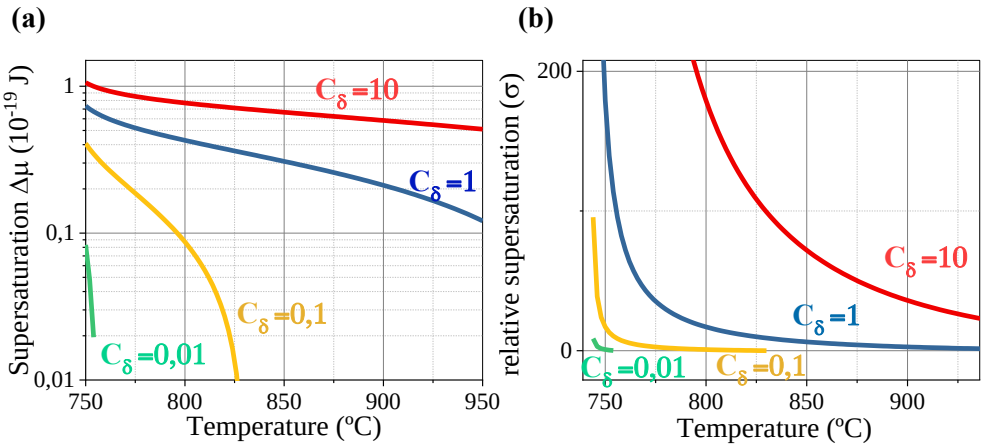

Figure 6.4: Estimations of the tendencies for (a)Supersaturation $\Delta\mu$ and (b) relative supersaturation σ with temperature at different C_δ values and $C_e(T)$ corresponding to 3-7 melt extrapolated from [165].

For a better comprehension, we display supersaturation evolution with temperature at different C_δ values in Figure 6.4. We have estimated $C_e(T)$ for the 3-7 melt composition from reference [165].

Now, a/b grains fraction respect to the c-axis phase are extracted experimentally from XRD measurements as a function of temperature (Fig. 6.5a) and for two different P_{O_2} .

Films processed with TLAG P_{O_2}-route are indicated in green symbols and are compared with the results from the Temperature-route path with a heating rate of 20°C/s. All samples are processed from the (3-7) melt composition.

One can realize that the fraction of a/b nuclei diminish in all cases with the

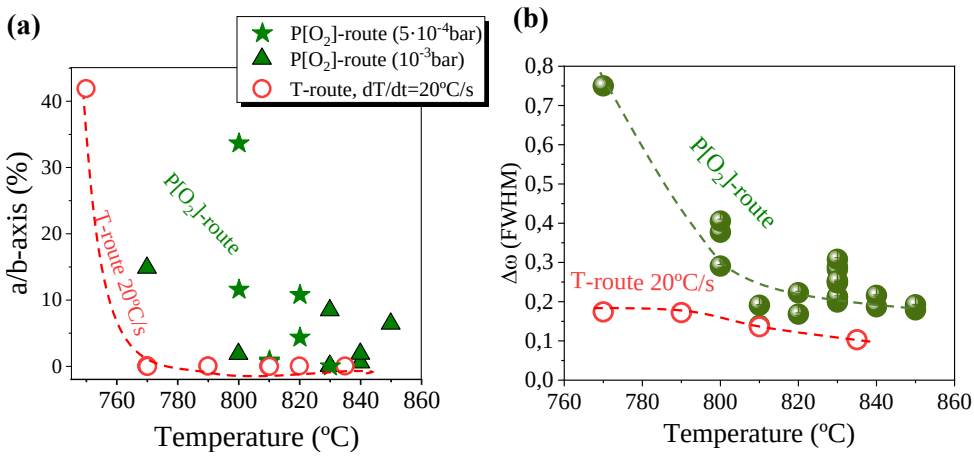

Figure 6.5: (a)a/b-grains fraction for (Y:2Ba:3.7Cu) films processed to different temperatures and P_{O_2} of 10^{-3} bar ($\triangledown$) and $5{\cdot}10^{-4}$ bar ($\star$). (b) Rocking curve for (005)YBCO reflection. Green solid symbols indicate P-route processed samples, while open red circles are T-route films heated at 20°C/s and 10^{-3} bar O_2.

increase of temperature. Accordingly, as observed in Fig. 6.4, supersaturation tends to lower values due to C_e increase at high temperatures. At low $\Delta\mu$, free energy barrier for a/b-orientation is too high to allow nucleation of a/b-grains with higher interfacial energies.

Yet, samples processed with P-route present higher a/b grains percentage than with T-route. Aiming to the theoretical estimations, we can deduce that enhanced supersaturation has been attained and so C_δ is significantly larger in the P-route as compared to the T-route most standard heating rate (20°C/s).

Note that in T-route, C_δ decreases with heating rate increase (Chapter 5.1). Thus, supersaturation conditions and optimal epitaxial zone in the P_{O_2}-route samples are more comparable to those for T-route slowest heating rates, which also attain completely epitaxial growth above 810°C at 0.4°C/s (see Fig.5.5 in section 5.1.2).

The influence on P_{O_2} is less certain. Nakamura *et al* showed C_e increases at higher P_{O_2} [164]. However, we do not have enough evidences to state real differ-

ences between 10^{-3} bar and $4{\cdot}10^{-4}$ bar. Additionally, P_{O_2} in TLAG determines the liquid formation temperature that modify other parameters influencing supersaturation and crystallization.

Overall, optimum processing temperatures for c-axis nucleation lay above 810°C for the P_{O_2}-route, and above 770°C for the Temperature approach. Still, a dispersion up to 10% of ab nucleation exists in all P-route range, while T-route samples with 3-7 solutions are a/b grains free.

Rocking curves on (005)YBCO reflection are a measurement of texture quality (Fig.6.5b). FWHM values (<0.3°) become lower as temperature increases, above 810°C in P-route. Again and according to previous results, texture quality is better for T-route samples at the same temperatures. The lower supersaturation is, lower FWHM values are obtained, which is probably related to the growth rate, also proportional to supersaturation.

In conclusion, it seems that the P_{O_2} route proceeds, as a general trend, under a higher supersaturation, similar to the slow heating process (0.4°C/s) in the T-route.

Supersaturation levels in the P_{O_2} route could be lowered by modifying the solution towards an increase of C_e ($\sigma \propto 1/C_e$). For instance, it can be done with more relative amount of Cu [163], or by adding other RE elements with higher C_e, such as Y-Nd, Y-Sm mixtures [165].

6.3 Reactivity in P_{O_2} route: $BaTiO_3$

High Resolution-XRD patterns and GADDS 2D-XRD images of some samples (Fig 6.6) show a significant presence of an epitaxial secondary phase diffracting at 2θ 31.6°and 66 °. These peaks can be attributed to (002) and (004) reflections of pseudocubic $BaTiO_3$ perovskite.

Phase structure and morphology was observed by means of TEM. $BaTiO_3$ can be encountered close to substrate interface (Fig. 6.7a) in the form of nanoparticles. EDX analyses confirmed the phase composition, containing only Ba and Ti atoms (Fig. 6.7b).

The presence of such particles does not seem to disturb the YBCO matrix around in this example. $BaTiO_3$ pseudocubic lattice parameters are close to

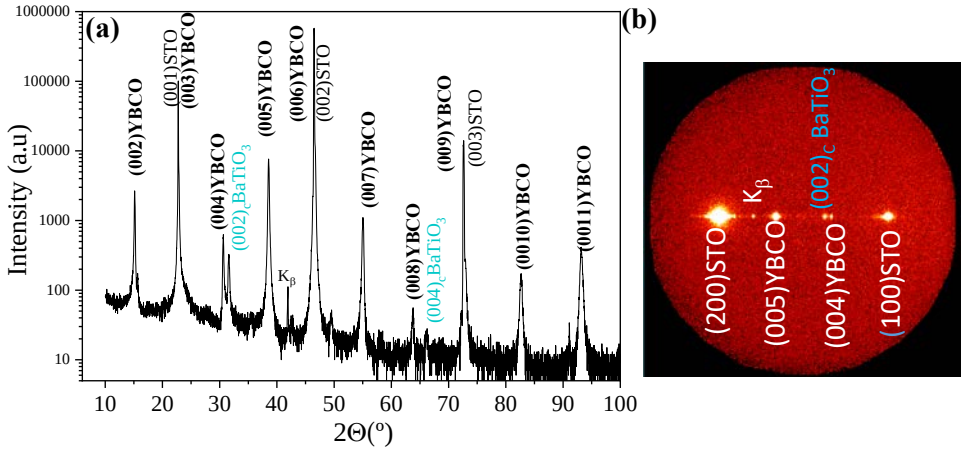

Figure 6.6: (a) High Resolutioin X-ray diffraction and (b) 2D-XRD with GADDS detector corresponding to a 90 nm film annealed to 830°C at $5{\cdot}10^{-4}$ bar O_2 with the P-route path

those of YBCO and STO. Lattice mismatch is 4.1% and 4.8% with YBCO and STO, respectively (Fig. 6.7c).

This can only be a reactivity product of Ti atoms from STO substrate dissolution in the melt. It is noticeable that with the P_{O_2} route the resulting reactivity phase on STO is always the same epitaxial $BaTiO_3$. Instead, with the temperature approach, many different derived phases containing Ti can nucleate, or even Ti substitution in the $YBa_2Cu_3O_{7-\delta}$ matrix occurs with the highest heating ramps.

Hence, reactivity derived phases on STO are different depending on the processing approach, even at the same final conditions. Additionally, straight comparisons within the two reaction paths are cumbersome since in T-route the degree and type of reactivity strongly depends on heating ramp.

$BaTiO_3$ appears in different extent depending on chosen final T-P_{O_2} . In Figure 6.8a, HR-XRD peaks corresponding to the phase main reflection and (004)YBCO are plotted together for different processing conditions. YBCO reflection slightly decreases at expenses of $BaTiO_3$ phase formation.

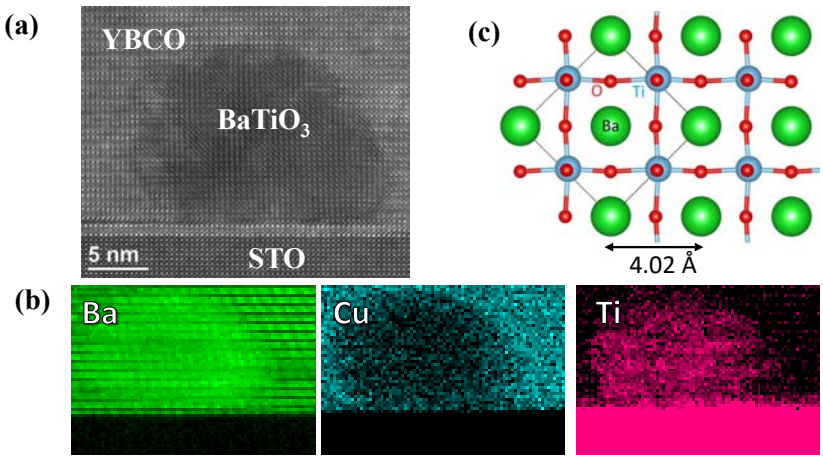

Figure 6.7: TEM image of a $BaTiO_3$ particle spontaneously formed from reaction with Ti substrate atoms during YBCO growth with P-route

Additionally, grains thickness perpendicular to the substrate have been inferred applying the Debye-Scherrer equation [199] with the two visible XRD diffraction peaks (Fig. 6.8b). Particles sizes are between 30 and 60 nm for the films processed at $5 \cdot 10^{-4}$ bar. 25 nm has been calculated for the film at 840°C at 10^{-3} bar.

Hence, reactivity increases with annealing temperature. Yet, P_{O_2} also has a strong influence. Big amounts of $BaTiO_3$ are formed with a small decrease of the final P_{O_2}, from 10^{-3} bar to $5 \cdot 10^{-4}$ bar.

This trend is similar for the Ba_2YTaO_6 formation on LSAT with the T-route (Fig.5.23 in section 5.3.2). We deduced that reactivity is closely related to the atoms diffusion and the time the liquid is exposed to the substrate without nucleating YBCO (t_{ind}).

Therefore, diffusion is enhanced at higher temperatures and t_{ind} is longer due to a decrease of supersaturation. The effect of P_{O_2} is not straightforward. From the conclusions on supersaturation from the last section, t_{ind} should be shorter at lower P_{O_2}. Therefore, we can only account the higher reactivity at low P_{O_2} to changes on the liquid properties. For instance, diffusion depends on

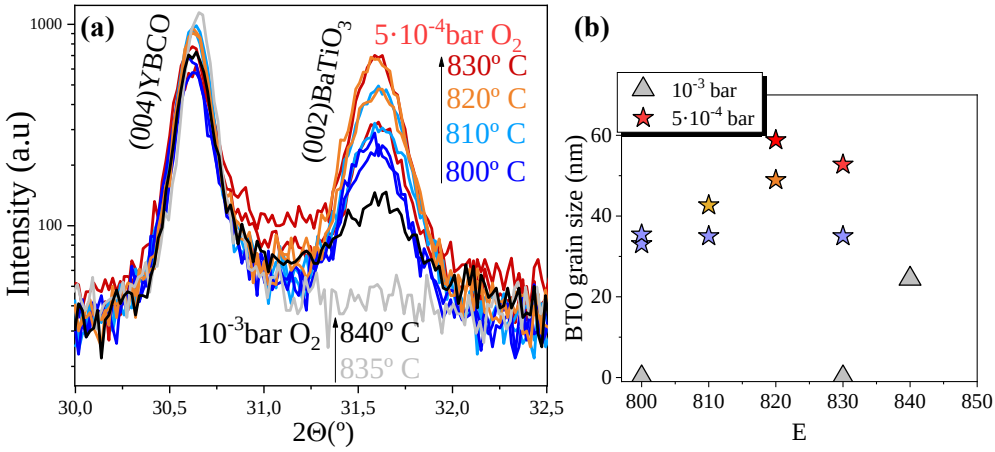

Figure 6.8: (a) HR-XRD (004) and $(002)_c$ $BaTiO_3$ reflection for films grown to different processing temperatures under 10^{-3} bar (red-grey) and $5 \cdot 10^{-4}$ bar (blue to red) O_2 on STO. In (b) calculated $BaTiO_3$ out of plane size with Debye-Scherrer equation

liquid viscosity (η) as $D_l = \frac{k_D T}{6\pi r \eta}$.

From these results it can also be deduced that transient liquid formation only occurs at the high P_{O_2} regime, since reactivity is only dependent on the final conditions in step 2.

If any other melt phase would dissolve substrate atoms at 10^{-5} bar during step 1, all samples would have shown some reactivity deriving in secondary phases or incorporating Ti in the $YBa_2Cu_3O_{7-\delta}$ matrix, independently from the final T-P_{O_2} conditions.

Consequently, reactivity can be minimized performing the P_{O_2} jump for growth to higher oxygen pressures.

For samples containing epitaxial $BaTiO_3$ ($P_{O_2} = 5 \cdot 10^{-4}$ bar), no decrease of YBCO texture has been observed, as well as no apparent detriment on J_c self-field values as compared to those without reactivity ($P_{O_2} = 10^{-3}$ bar) (see fig.6.13 in section 6.5).

Hence, the presence of these $BaTiO_3$ particles does not seem to diminish the

YBCO films properties. This is also different from BYTO secondary phases, which in some cases appeared very long grains disturbing YBCO homogeneity and being detrimental to the film properties.

6.4 Structural characterizations

6.4.1 Grains morphology

The resulting microstructure is closely related to supersaturation ($\Delta\mu$) from which YBCO has crystallized. $\Delta\mu$ determines grain orientations, nucleation rate and growth rate.

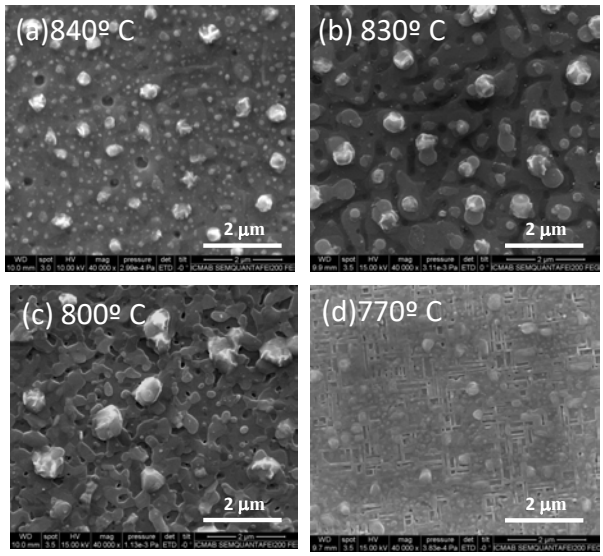

Figure 6.9: SEM images of YBCO films showing the surface produced at different temperatures (a)840°C, (b)830°C, (c)800°C and (d)770°C under P_{O_2} 10^{-3} bar.

We first analyse the superficial microstructure of films heated up to different processing temperatures at a fixed P_{O_2} at 10^{-3} bar (Figure 6.9). No meaningful differences have been observed with the surface of films annealed at $5 \cdot 10^{-4}$ bar

for $T > 820°C$ (see Fig.6.5).

Overall, all films treated above 820°C present a typical morphology of epitaxial YBCO, while CuO excess remains at the film surface.

At high processing temperatures, such as film (a) at 840°C, the formation of pores is observed from the corresponding SEM image.

At 830°C the film is rather dense and porous-free. Flat small gains with meandering grain steps can be discerned.

At 800°C, YBCO is epitaxial but with high rocking curve values (>0.35°). Grains misorientation is evidenced from SEM image (c).

The a/b grains formed at lower temperatures (770°C) can be observed in SEM image (d) in form of $\sim 500nm$ long rods in two directions. Those grow within the epitaxial matrix, leaving big voids around.

Grain sizes with P-route are smaller than in those samples processed at fast heating rates (20°C/s) and more similar to those produced at a slow heating rate (0.4°C/s) with the T-route.

These results are in accordance with nucleation studies from which we deduced higher $\Delta\mu$ in P-route than in T-route 20°C/s, for the same temperature and melt composition. The larger $\Delta\mu$ is, the higher YBCO nucleation rate and smaller grains are produced. An increased nucleation density is very beneficial from the structural point of view to avoid film free areas between grain boundaries.

6.4.2 Nanoscale defects

Typical cross section TEM images are exemplified in Figure 6.10 for YBCO films produced with the P-route at final conditions of $P_{O_2} = 5 \cdot 10^{-4}$ and 830°C. Both films shown here are ab grains free.

Film (a) shows a completely defect-free microstructure of pure YBCO phase and very good c-axis texture. It resembles the microstructure obtained with the slowest heating rates (0.4°C/s) with TLAG T-route for the low density of defects. This particular film presents a self-field critical current density of 3.8 MA/cm^2 at 77 K.

Although processed at the same conditions, film (b) presents higher amount

of defects. Mainly $Y_2Ba_4Cu_8O_x$ (Y248) intergrowths (double CuO chains or stacking faults) are present, specially at the top of the film, similarly to TLAG T-route fast heating rates and TFA-CSD process [200].

There is therefore a certain variability on the amount of stacking faults in seemingly equal films, or even in different regions within the same sample.

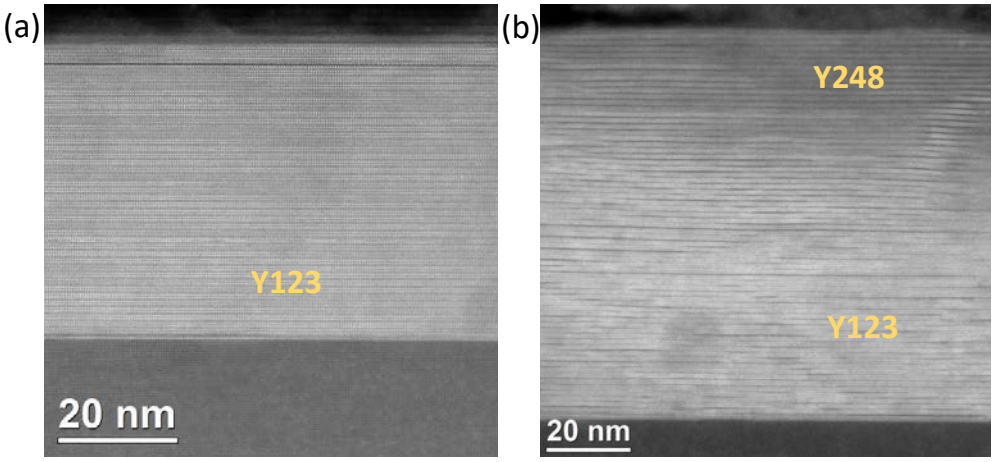

Figure 6.10: TEM cross-sections for a samples grown at $P_{O_2} = 5 \cdot 10^{-4}$ and 830°C and not having a/b oriented grains

The most typical macroscopic defects in P-route films, apart from $BaTiO_3$ phase derived from reactivity, are $YBa_2Cu_3O_{7-\delta}$ a/b-oriented grains. Those are also present until a certain extent in films grown at the most optimum conditions for c-axis orientation, as observed in the last section.

TEM images corresponding to (a) large and (b) small a/b grains can be observed in Figure 6.11.

On the one hand, we can find typical large ab grains, growing along the full layer thickness in the fastest a/b direction from their nucleation. They are interposed within the c-axis epitaxial phase, leaving material free areas at the grain boundaries that can be observed from SEM images (Fig.6.9 770°C). Those pores were proved to reduce percolative superconducting currents [201].

On the other hand, nanosized grains are encapsulated within YBCO c-axis

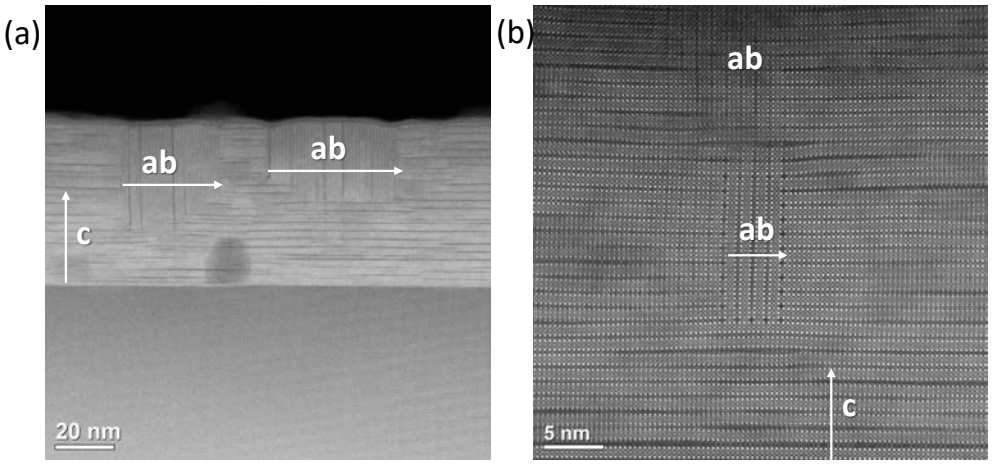

Figure 6.11: TEM showing YBCO a/b oriented grains grown in the c-axis matrix. (a) large grains and (b) small grains in a film with 8% a/b percentage grown at 830°C at 10^{-3} bar O_2

matrix. This can only be produced due to small composition fluctuations, while the c-axis YBCO continues growing around without leaving any void. Lattice distortions in form of stacking faults are produced in the epitaxial matrix around them.

Such small encapsulated grains of a/b grains have also been observed in T-route, but are for the first time reported in YBCO films.

Lattice distortions in the YBCO c-axis epitaxial film can be quantified by XRD Williamson-Hall analysis in terms of nanostrain.

Figure 6.12 displays strain values for P-route samples as a function of critical current density J_c. a/b grains percentage is indicated next to symbols and samples processed to either 10^{-3} bar or $5 \cdot 10^{-4}$ bar at 830°C are painted in dark pink or yellow, respectively.

The most noticeable increase of strain is for all those films annealed at $P_{O_2} = 5 \cdot 10^{-4}$ bar respect to those grown at $P_{O_2} = 10^{-3}$ bar. We should notice that, J_c self-field values are maintained high in both cases. Hence, some structural differences exist between the two processing conditions that do not affect critical

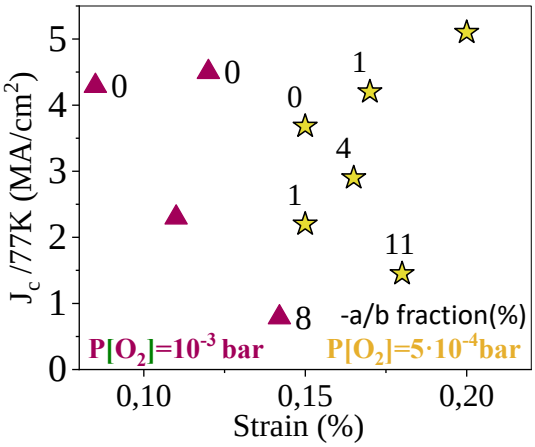

Figure 6.12: Strain values inferred from XRD Williamson-Hall analysis as function of critical current density (J_c) of films grown with the P-route at 830°C. a/b grains percentage is indicated next to symbols and films processing final P_{O_2}: 10^{-3} bar or $5 \cdot 10^{-4}$ bar are dark pink or yellow, respectively

current percolation.

One possible cause that needs to be further studied is the effect that reactivity derived $BaTiO_3$ particles may have on the YBCO lattice. BTO is only produced in films grown at the lowest P_{O_2} in form of epitaxial particles on the substrate interface. Such inclusions and so their effects could be similar to previously studied self-assembled interfacial nanodots [202, 203, 204].

Then, c-$YBa_2Cu_3O_{7-\delta}$ strain also increases gradually with a/b-oriented grains content. However, the presence of a/b nucleation has a detrimental effect on percolating J_c that will be later discussed.

6.5 Physical characterizations

For the YBCO films processed with the P_{O_2} route, phase segregation seem not to be an issue, as well as reproducibility in terms of epitaxial growth, in contrast to the temperature approach.

Now we can underpin straighter correlations between growth conditions and physical properties in order to maximize superconducting performances.

Figure 6.13a shows the relationship between T-P_{O_2} YBCO growth conditions and J_c self field values at 77.3K.

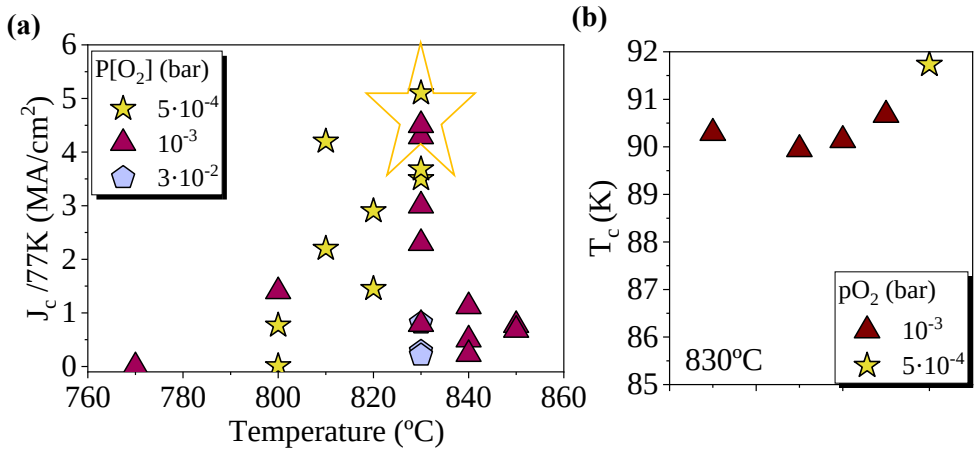

Figure 6.13: (a) Critical current density (J_c) self-field at 77.3 K of resulting $YBa_2Cu_3O_{7-\delta}$ 90 nm films grown with P-route at different T-P_{O_2} conditions of step 2. (b) the corresponding critical temperatures T_c measured by Van der Pauw method [190]

All samples processed so far between 800°-830°C and P_{O_2} $5\cdot10^{-4}$ to 10^{-3} bar present J_c values higher than $1\,MA/cm^2$. $5.3\,MA/cm^2$ was the maximum achieved, at 835°C and $5\cdot10^{-4}$ bar, while at 10^{-3} bar the maximum was $4.5\,MA/cm^2$.

These conditions correspond to the optimal window for epitaxial growth deduced in section 6.2.2 (Fig.6.3).

At higher temperatures ($T \geq 840$°C), the presence of pores may be the reason to a detriment on current percolation, although further nanostructural studies are necessary to clarify this issue.

At lower temperatures ($T \leq 800$°C), the high supersaturation levels enhance the nucleation of a/b-oriented $YBa_2Cu_3O_{7-\delta}$ grains and might produce grains

misalignment. Both factors may contribute on decreasing significantly J_c.

Critical temperatures (T_c), evaluated by means of Van der Pauw method, [190] are plotted in Figure 6.13b. Standard P-route samples present excellent critical temperatures, above 92-93.5 K and sharp transitions. An indication that samples are well oxygenated and no contaminated.

Consequently, P_{O_2} route presents a wide processing window, giving higher J_c values than the Temperature approach, which the maximum J_c was 3 MA/cm^2.

The reason for J_c values dispersion (1 to 5 MA/cm^2) within optimum conditions will require a very fine understanding of all structural details related to superconducting properties. For instance, the variability of secondary a/b grains quantity, which effects will be investigated in the next section.

Transport measurements of a pristine sample processed with P-route without $BaTiO_3$ and a/b grains are presented in Figure 6.14. Absolute J_c values are measured under a magnetic field applied parallel to c direction and for different temperatures. A pristine sample synthesized with the BaF_2 TFA-CSD technique is also represented at 77 and 5K for comparison.

As a result, very high critical current densities of 5.3 MA/cm^2 at 77K and 35 MA/cm^2 at 5K are demonstrated for TLAG films. Those values are even higher than TFA-CSD pristine samples and also present a slightly improved in-field performance .

Therefore, TLAG-P_{O_2} route is able to produce very high critical current densities at 100 nm/s rates, hence equalizing performances for pristine samples processed with much longer thermal treatments (> 100 times) with the TFA-CSD technique [40].

6.5.1 a/b-oriented grains effects

The presence of YBCO crystals oriented in a/b direction within the c-axis epitaxial YBCO is the most common defect in films grown with the P_{O_2} approach. As we have discussed before, it is very likely that this phenomenon is associated to the high supersaturated conditions used in the nucleation and growth steps. In this section we study the influence that these inclusions have on the physical properties.

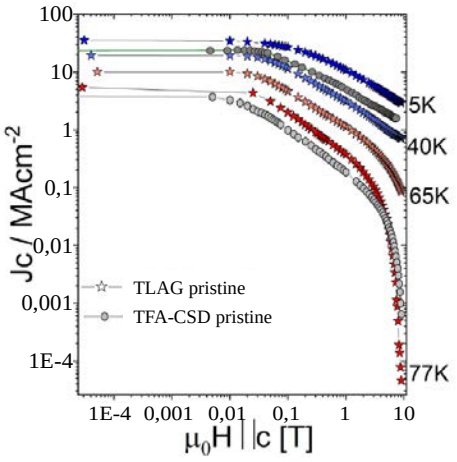

Figure 6.14: Critical current density (J_c) dependence on the magnetic field at 5 K, 65 K, 40 K and 5 K for 90 nm YBCO film processed with P-route at 830°C and $5 \cdot 10^{-4}$ bar (coloured star symbol), as compared with a 200 nm standard TFA-CSD film (grey circles)

Percolative current

The a/b percentage respect to the c-axis phase has been inferred for many samples processed with the P_{O_2}-route with a quantification method from 2D-XRD measurements, detailed in section 2.2.4.3.

In Figure 6.15, the maximum critical current (J_c, at self-field and 77 K) ever obtained is displayed depending on a/b-oriented grains percentage.

Maximum performances at 77 K and self-field ($> 4\ MA/cm^2$) are achieved when a/b grains percentage is close to 0. Then, maximum J_c values decrease as a/b fraction increases. Amounts below 4% give J_c until $3\ MA/cm^2$, below 15% gives $1\ MA/cm^2$ and more than 20% J_c is less than $0.1\ MA/cm^2$.

It is clear then the strong relevance on minimizing a/b grains nucleation in order to achieve the maximum superconducting performances. It is, therefore, important to achieve some control on the supersaturation degree in the P_{O_2} route to TLAG.

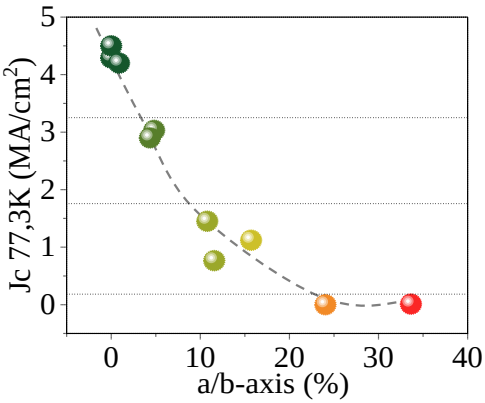

Figure 6.15: Maximum self-field J_c at 77 K vs a/b-grains percentage in c-axis YBCO films processed with P-route

As mention before, the presence of ab grains was proved to induce magnetic granularity that reduces percolative superconducting currents [201]. Granularity correlates with the shift in the hysteresis loop of the maximum magnetization to positive applied magnetic fields due to the existence of a reverse return field at the grain boundaries [191, 122].

The peak shift to higher field values (Fig.6.16a) with the increase of ab grains indicates increased magnetic granularity. In Figure 6.16b, the H_{sat} increase with ab grains percentage can be observed with a larger number of samples with the same thickness and processed with P-route.

Hence, these results confirm that the presence of ab grains correlates with an increase of magnetic granularity that diminishes J_c percolation.

We can conclude that, while in the T-route magnetic granularity is related to grain size and nucleation density, depending on processing conditions, in P_{O_2} route these two factors are optimum for achieving good current percolation. Instead, a/b grains are the main source for percolative current detriment in P_{O_2} route, but in a lower extent.

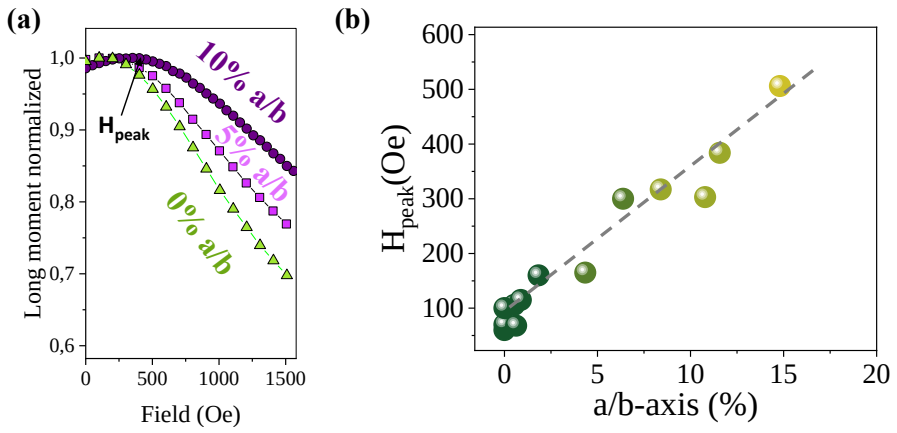

Figure 6.16: (a) Magnetic field with the magnetization peak (H_{peak}) at 5 K (b) Magnetization peak (H_{sat}) versus a/b grains fraction for standard P-route samples

Magnetic field behaviour

Now we would like to correlate magnetic field dependence of J_c with the ab grains content (Fig 6.17a). A smoother in-field J_c dependence can be observed with the increase of ab grains concentration for normalized maximum J_c. Most probably the reason lies on a highly distorted matrix evidenced from TEM and nanostrain observations. Local nanoscale lattice distortions is suggested to determine the vortex pinning efficiency [82, 83].

However, J_c absolute values (Fig 6.17b) are lower, due to the granularity effect mentioned in the previous discussion.

These results suggest that ab grains can indeed produce some sort of vortex pinning, most likely when size is kept small, in the range of the coherence length ($\sim$ few nm). A more detailed study would be necessary in order to control the generated a/b grains size that could be used to produce vortex pinning without creating at the same time magnetic granularity.

Still, with CSD methodology, preformed nanoparticles introduction in the

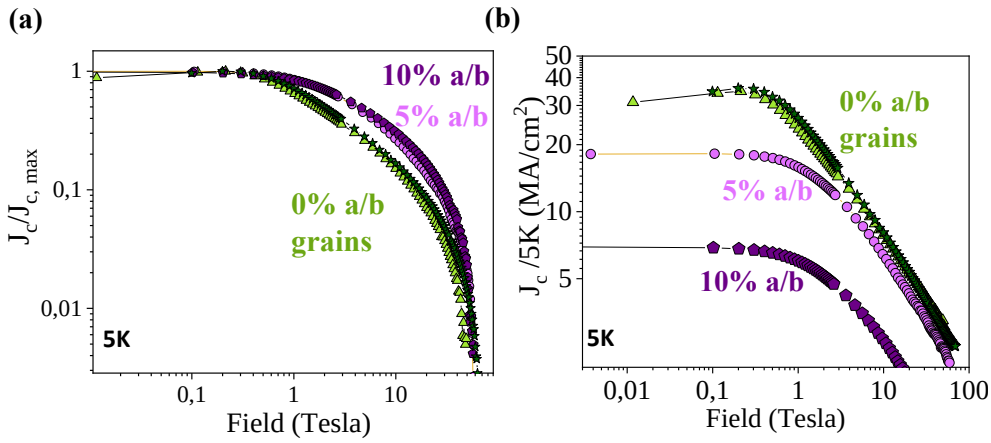

Figure 6.17: J_c(H) curves at 5K measured by SQUID for films with different ab contents (0, 5 and 10%). In (a) values are normalized to maximum J_c and absolute values plotted in (b)

solution is the most effective strategy to pin vortices at high magnetic fields [159, 187]. The latter approach has already been proved to further boost superconducting performance also in TLAG grown films [205].

6.6 Conclusions

In situ XRD synchrotron experiments elucidate the reaction mechanisms towards YBCO formation by two processing steps. During a heating step at low P_{O_2}, pyrolysis phases are transformed to solid $BaCu_2O_2$ and Y_2O_3. Either low total pressure or high gas flow can be used to promote CO_2 outdiffusion and attain full reaction complementation for thick films. $BaCO_3$ elimination up to 400 nm final film thickness was proved.

In a second step, a P_{O_2} raise to the $YBa_2Cu_3O_{7-\delta}$ stability zone promotes liquid assisted growth. Very fast c-axis $YBa_2Cu_3O_{7-\delta}$ growth rate, up to 100 nm/s is demonstrated with this approach. Hence, transient liquid assisted growth is revealed to be feasible independently from the path used.

C-axis YBCO epitaxial nucleation is possible along a wide range of final $T - P_{O_2}$ processing conditions with very good reproducibility, specially at the region that lies just above the instability line.

Supersaturation conditions ($\sigma \approx C_\delta/C_e$, if $\sigma >> 1$) for nucleation are deduced to be higher (increased C_δ) than those obtained with TLAG by direct ultrafast heating at a constant pressure. Instead, C_δ levels are closer to those achieved at slow heating rates (0.4°C/s).

As a consequence, a/b-oriented YBCO nuclei are characteristic defects in P-route films that should be limited. Furthermore, epitaxial $BaTiO_3$ particles nucleate from reaction with the substrate when final P_{O_2} is low ($\sim 10^{-4}$ bar).

At present, ab grains inclusions are the main source of percolative current decrease, but their influence can be minimized by further reducing supersaturation. Since C_δ is high (the Y is well dissolved), strategies to change supersaturation are restricted to tune C_e. Some ideas that could work are to increase the relative amount of Cu, or to add other RE elements (Y-Nd, Y-Sm mixtures).

The opportunities that a decoupled reaction path offers on choosing the processing conditions for crystallization has enormous benefits. Overall, nucleation and growth conditions lead to highly homogeneous, low granular morphology that presents excellent superconducting current percolation. J_c up to 5.3 MA/cm^2 at 77K and T_c higher than 90 K has been reported.

For this reason, TLAG P_{O_2} route is revealed as a very promising approach to obtain high quality and reproducible $YBa_2Cu_3O_{7-\delta}$ films with the low cost, fast throughput TLAG method.

Furthermore, in contrast to other liquid-based techniques restricted to regions in the phase diagram where the liquid is a stable phase [64, 59], TLAG-CSD requires less complex processing systems and no high vacuum is needed.

Chapter 7

General conclusions

In this thesis we have reported the development and first elucidations of the novel Transient Liquid-Assisted Growth (TLAG) technique derived from carboxylate solutions.

It is for the first time reported, a method that takes advantage of the kinetic hindrances on crystallization to reach the equilibrium phases in the phase diagram, as a vehicle to induce ultrafast growth. Overall, a fine combination of kinetic and thermodynamic features.

The "proof-of-principle"of this new approximation viability has been achieved with the use of rapid thermal annealing furnaces, allowing heating rates up to 80°C/s.

We have demonstrated through these pages that this methodology is valid to obtain epitaxial $YBa_2Cu_3O_{7-\delta}$ films up to 500 nm at very fast growth rates (100 nm/s). Additionally, it has been proved that the films can present excellent superconducting properties (up to J_c=5 MA/cm^2 at 77 K, self-field and T_c=90-92 K). Overall, the material growth rates overpass the present throughput of conventional Chemical Solution Deposition (CSD) by a factor 100, while performances equalise the maximum of the present "state of the art"concerning YBCO pristine films on single crystalline substrates.

Along the 4 results chapters, we have reported a broad spectrum of experimental results and we have provided insight into all the processes involved in TLAG-CSD, with the help of *in situ* techniques and microscopy analyses, among others. The main transformations are listed below:

- **Solution deposition**. TLAG is compatible with multideposition of pyrolyzed layers and scalable Ink Jet printing patterning techniques. Up to 1 μm thick films have been demonstrated to be homogeneous along thickness.

- **Solution decomposition**. Y,Ba,Cu-propionates pyrolysis results in an homogeneous nanoporous layer of Y_2O_3, $BaCO_3$ and CuO nanocrystalline phases, through hydrolysis and oxidation processes

- **$BaCO_3$ elimination**. $BaCO_3$ reacts with Cu-phases to form $BaCu_zO_2$ + Cu_zO at much lower temperatures than its decomposition, where z and reaction rate depends on P_{O_2}.

- **Ultrafast growth of $YBa_2Cu_3O_{7-\delta}$**. The formation of the [$BaCuO_2$ + CuO] transient liquid from the respective solid phases eutectic reaction is kinetically driven at the T-P_{O_2} conditions where YBCO(s) is the stable phase. The oxide nucleation and growth occurs upon the liquid supersaturation with Y from the solid Y_2O_3 nanoparticles.

- **Film characteristics** the resulting phase structure, film morphology, nanostructure and superconducting properties are closely linked to the supersaturation conditions for crystallization.

A key point on the design of TLAG derived from chemical solutions is the prevention of $BaCO_3$ retention. Two different conversion paths give rise to TLAG of epitaxial films:

- **Temperature-route** precursors reactions and TLAG take place consecutively while heating at $P_{O_2} > 2.5 \cdot 10^{-4}$ bar. The use of a rapid thermal annealing furnace brings unique opportunities for film processing at ultrafast heating rates.

- **Oxygen partial pressure-route** $BaCO_3$ elimination is completed at $P_{O_2} = 10^{-5}$ bar upon the formation of solid $BaCu_2O_2$, while TLAG occurs after a jump to higher P_{O_2}.

CO_2 out-diffusion is the kinetic effect that limits the conversion in the thickest films. Therefore, the use of high gas flow or reduced total pressures seems to have promising effects on the reaction yield. We additionally found that $BaCO_3$ decomposition reaction is enhanced by the formation of the liquid phase with the T-route. Thus, conversion rates for the total decarbonation as high as $\sim$100 nm/s were achieved by increasing the heating ramp.

Epitaxial film growth is ensured at low supersaturation conditions of the liquid by the dissolved Y. However, at very low levels, the deficient nuclei density produces a film with voids. If, additionally, diffusivity is high, then the main limitations rely on the liquid dewetting or corrosive character with the substrate.

Therefore, intermediate supersaturation values seem to be the optimum. The cations composition and processing conditions (temperature, heating ramp oxygen partial pressure, reactions path) have to be optimized for this purpose. The best J_c at self-field were obtained with the P_{O_2}-route and the Y:Ba:Cu composition 1:2:4.7. Furthermore, this approach entails better control of the reaction temperatures and therefore, good reproducibility.

Since TLAG is not restricted to the use of an equilibrium liquid phase, there is a very wide window of possibilities. Epitaxial growth can even be performed at very low temperatures, such as 650°C.

To sum up, TLAG-CSD of been proved to be a successful and versatile technique for the growth of YBCO films at very high growth rates.

Future work and outlook

The results suggest that the approach based on a P_{O_2} change gives rise to better performances and robustness. Still, further concepts related to the growth mechanisms in this route should be further investigated to make a clear statement.

The Temperature-route is still very attractive for its versatility and faster decarbonation. Yet, since all reactions are linked, its study and control involves a higher complexity. Therefore, it is still not clear which of the two methodologies would be easier to implement in continuous reel-to-reel production.

Further strategies are required to ensure epitaxial growth while preventing the above mentioned difficulties, in a reproducible way.

Some directions that may give light to this matter would be:

- The finding of non-reactive buffer layers.
- Increase the solid/liquid ratio while maintaining low supersaturation can be made using out of stoichiometry compositions (more Y and Cu) or other RE elements with improved equilibrium solubility.
- Use of optimized multi-layered structures

We have observed very different microstructures depending on the process route and parameters. This fact provides unique opportunities to tune the material defects landscape for vortex pinning or other requirements. This is an interesting field to be more deeply studied.

Additionally, deposition from chemical solutions allows the controlled introduction of secondary phases or preformed nanoparticles for the synthesis of nanocomposites. This fact overcomes one of the main limitations of the liquid-assisted techniques based on vacuum deposition.

Consequently, we believe that the features of the new TLAG growth approach makes this technique very promising in view of a scaling process for industrial manufacturing. Besides the interest in enhancing the throughput of manufacturing due to a higher growth rate, we anticipate that the instrumentation required for a reel-to-reel continuous production of TLAG coated conductors

could be greatly simplified, as compared to the present existing manufacturing systems.

Overall, therefore, we are convinced that TLAG has the potential of becoming a very competitive approach to CC production. For this purpose, some requirements to be demonstrated are the TLAG compatibility with buffer layers and the growth of thicker layers ($\sim$3 μm) at also high throughputs.

For single pyrolysis of thick films, much efforts are needed in order to prevent the formation of cracks and inhomogeneities while reducing the thermal treatment time to avoid CuO coarsening.

Then, decarbonation is also more critical for large thicknesses, and specially for the P_{O_2}-route. Currently, decomposition of thick films is being tested at much increased flow rates, with very promising results.

If not possible, owing to the ultrafast growth rates of TLAG, a process including several deposition-growth steps of multi-layers could still be a feasible solution.

Last but not least, TLAG-CSD opens the horizon towards preparation of other complex oxide epitaxial films. On the one hand, to fulfil manufacturing requirements. On the other hand, since material microstructure and defects landscape depend on the growth technique, materials with new characteristics could be prepared with TLAG-CSD, leading to distinct functional properties.

Glossary

List of acronyms

TLAG	Transient Liquid Assisted Growth
MOD	Metal Organic Deposition
TFA	Trifluoroacetate
LF	Low Fluorine
IJP	Ink Jet printing
SC	Spin Coating
MD	Matching Distance
PLD	Pulsed Laser Deposition
CSD	Chemical Solution Deposition
TGA	Thermogravimetric analysis
DTA	Differential thermal analysis
EGA	Evolved Gas Analysis
MS	Mass Spectroscopy
SEM	Scanning Electron Microscopy
HR	High Resolution
TEM	Transmission Electron Microscopy
HAADF	High-angle Annular Dark-field
STEM	Scanning Transmission Electron Microscope
EDX	Energy-dispersive X-ray spectroscopy
AFM	Atomic Force Microscopy
XRD	X-Ray Diffraction
GI	Grazing Incidence
GADDS	General Area Detector Diffraction System
FWHM	Full Width at Half Maximum
FIB	Focused Ion Beam
FTIR	Fourier Transform Infrared Spectroscopy
SQUID	superconducting quantum interference device
RTA	Rapid Thermal Annealing
T-route	Temperature route
P-route	Oxygen partial pressure route

List of abbreviations

YBCO	$YBa_2Cu_3O_{7-\delta}$
$EtCO_2$	$CH_3CH_2COO^-$
TEA	Triethanolamine
DEA	Diethanolamine
Y211	Y_2BaCuO_5
Y225	$Y_2Cu_2O_5$
LAO	$LaAlO_3$
STO	$SrTiO_3$
LSAT	$(LaAlO_3)_{0.3}(Sr_2AlTaO_6)_{0.7}$
BYTO	Ba_2YTaO_6
BTO	$BaTiO_3$

List of symbols

T_D	Decomposition temperature
P_{O_2}	Oxigen partial pressure
C_δ	Yttrium concentration
C_e	Equilibrium concentration
C_{xt}	Solute concentration in the forming crystal
σ	Relative supersaturation
$\Delta\mu$	Thermodynamic supersaturation
t_{ind}	Induction period of nucleation
T_e	Eutectic temperature
γ	Interfacial energy
Γ	volume fraction
k_B	Boltzmann's constant
k	Kinetic coefficient
D	Diffusion coefficient
δ	Diffusion distance
R	Growth rate

Appendix

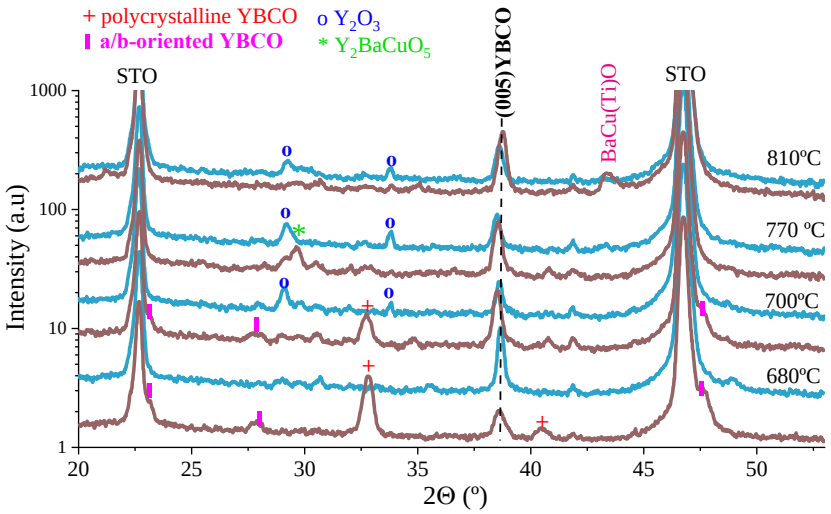

Figure 7.1: 2θ diffraction patterns after χ integration of 2D GADDS XRD frames. They correspond to T-route processed samples at different temperatures at 60°C/s and 10^{-2} bar of O_2. Liquid compositions (2-3) and (3-7) are indicated in brown and blue, respectively

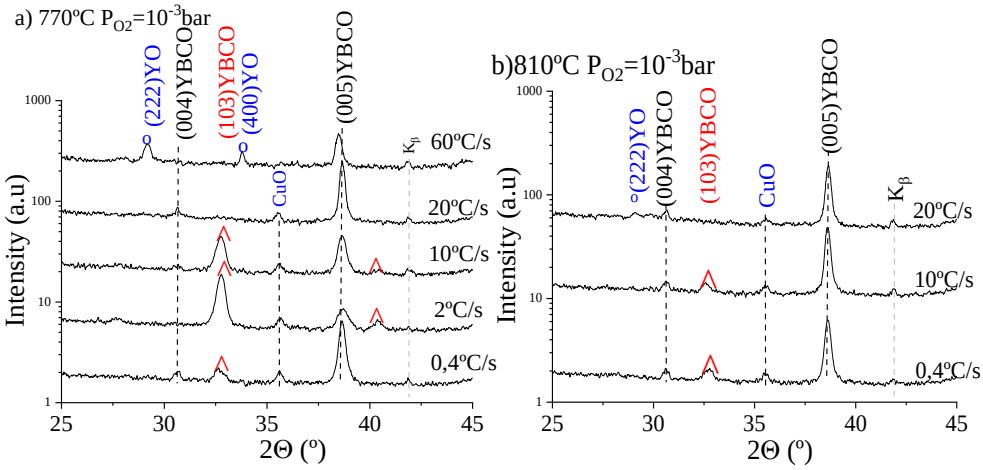

Figure 7.2: χ Integrated 2D GADDS XRD diffraction patterns corresponding to samples annealed at different rates at (a) 770°C and (b)810°C with the 3:7 melt at 10^{-3} bar O_2

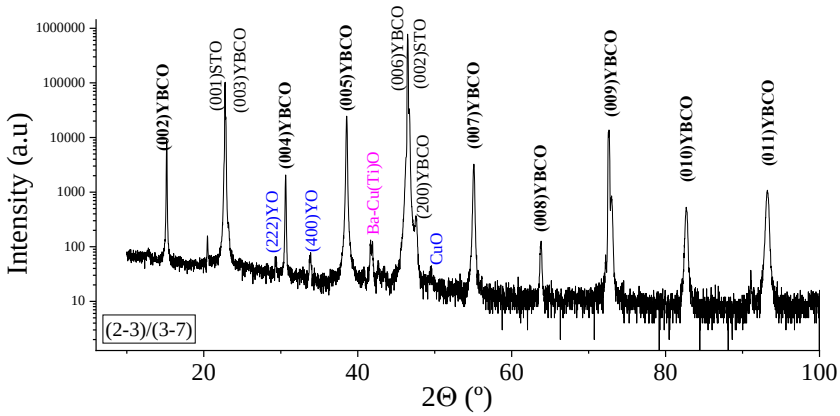

Figure 7.3: HR-XRD of a bilayered film composed of Y:Ba:Cu ratios: 1:2:4.7 (α) 90 nm in the first layer and 1:2:3 (γ) 200 nm on top. IT shows some secondary phases accounted to reactivity from the STO substrate. Film was grown at 810°C, 10^{-3} bar O_2, 20°C/s.

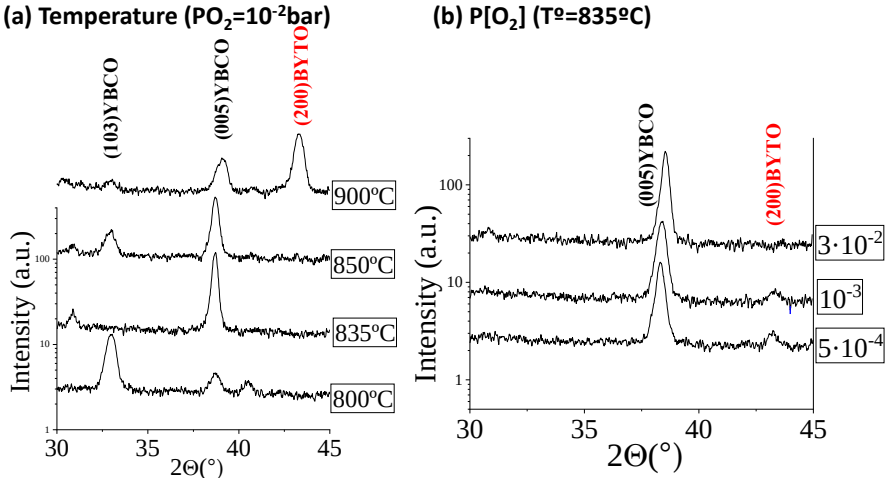

Figure 7.4: χ-integrated XRD diffraction patterns showing reactivity on LSAT at different conditions with the stoichiometric composition and at 20°C/s. At (a)fixed P_{O_2} at 10^{-2} bar and (b)temperature at 835°C.

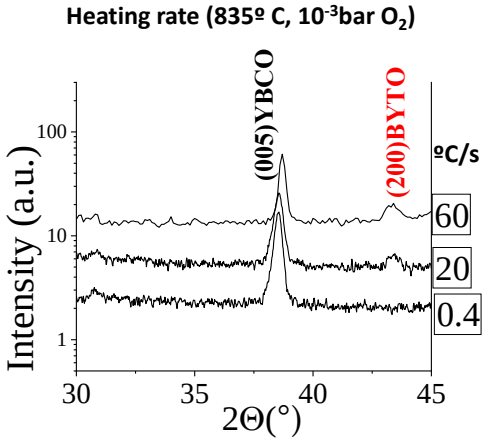

Figure 7.5: χ-integrated XRD diffraction patterns showing reactivity on LSAT at different heating ramps with the stoichiometric composition at P_{O_2} at 10^{-3} bar and 835°C.

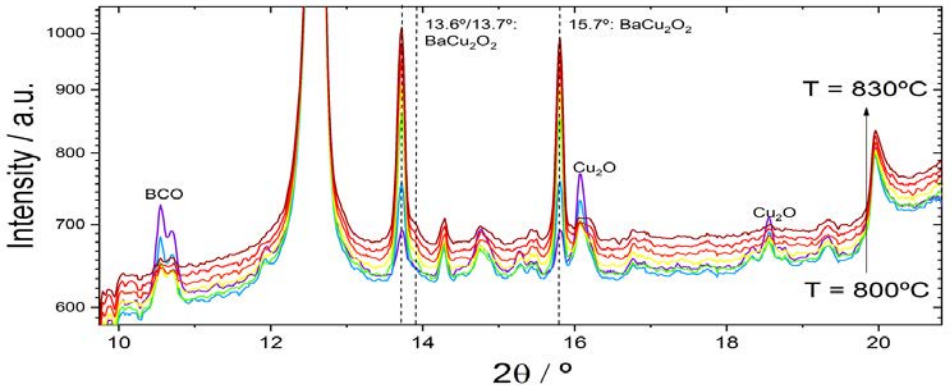

Figure 7.6: time resolved diffraction patterns during the $BaCO_3$ elimination step in the P_{O_2} route at $P_{O_2} = 10^{-5}$ bar heating to 850°C at 5°C/s.

Bibliography

[1] J. Ebenezar, "Recent trends in materials science and applications," 2017. 1

[2] V. Dusastre, *Materials for sustainable energy: a collection of peer-reviewed research and review articles from Nature Publishing Group*. World Scientific, 2011. 1

[3] I. E. Agency, *World Energy Outlook 2018*. 2018. 1

[4] D. Larbalestier, A. Gurevich, D. M. Feldmann, and A. Polyanskii, "High-t c superconducting materials for electric power applications," *Nature*, vol. 414, no. 6861, p. 368, 2001. 2, 3

[5] Y. Shiohara, T. Taneda, and M. Yoshizumi, "Overview of materials and power applications of coated conductors project," *Japanese Journal of Applied Physics*, vol. 51, no. 1R, p. 010007, 2012. 2, 3, 8, 154

[6] A. Malozemoff, "Second-generation high-temperature superconductor wires for the electric power grid," *Annual review of materials research*, vol. 42, pp. 373–397, 2012. 2, 7

[7] X. Obradors and T. Puig, "Coated conductors for power applications: materials challenges," *Superconductor Science and Technology*, vol. 27, no. 4, p. 044003, 2014. 2, 3, 7, 8

[8] B. G. Marchionini, Y. Yamada, L. Martini, and H. Ohsaki, "High-temperature superconductivity: A roadmap for electric power sector applications 2015-2030," *IEEE Transactions on Applied Superconductivity*, vol. 27, pp. 1–7, 2017. 2, 3, 7

[9] P. Capper and M. Mauk, *Liquid phase epitaxy of electronic, optical and optoelectronic materials*, vol. 21. John Wiley & Sons, 2007. 2

[10] H. Rogalla and P. H. Kes, *100 years of superconductivity*. Taylor & Francis, 2011. 2

[11] H. Kamerlingh Onnes, "Further experiments with Liquid Helium. D. On the change of Electrical Resistance of Pure Metals at very low Temperatures, etc. V. The Disappearance of the resistance of mercury," *Koninklijke Nederlandse Akademie van Wetenschappen Proceedings Series B Physical Sciences*, vol. 14, pp. 113–115, 1911. 2

[12] W. Meissner and R. Ochsenfeld, "Ein neuer effekt bei eintritt der supraleitfähigkeit," *Naturwissenschaften*, vol. 21, no. 44, pp. 787–788, 1933. 2, 4

[13] J. Bardeen, L. N. Cooper, and J. R. Schrieffer, "Theory of superconductivity," *Phys. Rev.*, vol. 108, pp. 1175–1204, Dec 1957. 2

[14] V. Ginzburg, "On the theory of superconductivity," *Zh. eksper. teor. Fiz.*, vol. 20, pp. 1064–1082, 1950. 2

[15] B. Josephson, "Possible new effects in superconductive tunnelling," *Physics Letters*, vol. 1, no. 7, pp. 251 – 253, 1962. 2

[16] J. G. Bednorz and K. A. Müller, "Possible high T_c superconductivity in the Ba-La-Cu-O system," *Zeitschrift fur Physik B Condensed Matter*, vol. 64, pp. 189–193, June 1986. 3

[17] J. Nagamatsu, N. Nakagawa, T. Muranaka, Y. Zenitani, and J. Akimitsu, "Superconductivity at 39 k in magnesium diboride," *nature*, vol. 410, no. 6824, p. 63, 2001. 3

[18] Y. Kamihara, T. Watanabe, M. Hirano, and H. Hosono, "Iron-based layered superconductor La [O1-x F x] FeAs (x= 0.05- 0.12) with tc= 26 k," *Journal of the American Chemical Society*, vol. 130, no. 11, pp. 3296–3297, 2008. 3

[19] A. Gurevich, "To use or not to use cool superconductors?," *Nature materials*, vol. 10, no. 4, p. 255, 2011. 4, 8

[20] M. P. Fisher, "Vortex-glass superconductivity: a possible new phase in bulk high-t c oxides," *Physical review letters*, vol. 62, no. 12, p. 1415, 1989. 4

[21] R. Koch, V. Foglietti, W. J. Gallagher, G. Koren, A. Gupta, and M. Fisher, "Experimental evidence for vortex-glass superconductivity in y-ba-cu-o," *Physical review letters*, vol. 63, no. 14, p. 1511, 1989. 4

[22] M.-K. Wu, J. R. Ashburn, *et al.*, "Superconductivity at 93 k in a new mixed-phase Y-Ba-Cu-O compound system at ambient pressure," *Physical review letters*, vol. 58, no. 9, p. 908, 1987. 5

[23] J. MacManus-Driscoll, S. Foltyn, *et al.*, "Strongly enhanced current densities in superconducting coated conductors of YBa2Cu3O7–x+ BaZrO3," *Nature materials*, vol. 3, no. 7, p. 439, 2004. 5

[24] J. Gutierrez, A. Llordes, J. Gazquez, M. Gibert, N. Roma, S. Ricart, A. Pomar, F. Sandiumenge, N. Mestres, T. Puig, *et al.*, "Strong isotropic flux pinning in solution-derived YBa2Cu3O7-x nanocomposite superconductor films," *Nature materials*, vol. 6, no. 5, p. 367, 2007. 5, 37

[25] V. Breit, P. Schweiss, *et al.*, "Evidence for chain superconductivity in near-stoichiometric YBa 2Cu3Ox single crystals," *Physical Review B*, vol. 52, no. 22, p. R15727, 1995. 5

[26] S. Graser, P. J. Hirschfeld, T. Kopp, R. Gutser, B. M. Andersen, and J. Mannhart, "How grain boundaries limit supercurrents in high-temperature superconductors," *Nature Physics*, vol. 6, no. 8, p. 609, 2010. 5

[27] D. Dimos, P. Chaudhari, J. Mannhart, and F. LeGoues, "Orientation dependence of grain-boundary critical currents in YBa2Cu3O7- δ bicrystals," *Physical Review Letters*, vol. 61, no. 2, p. 219, 1988. 6

[28] N. F. Heinig, R. D. Redwing, I. F. Tsu, A. Gurevich, J. E. Nordman, S. E. Babcock, and D. C. Larbalestier, "Evidence for channel conduction in low misorientation angle [001] tilt YBa2Cu3O7- x bicrystal films," *Applied physics letters*, vol. 69, no. 4, pp. 577–579, 1996. 6

[29] D. M. Feldmann, J. L. Reeves, *et al.*, "Influence of nickel substrate grain structure on YBa2Cu3O7-x supercurrent connectivity in deformation-textured coated conductors," *Applied Physics Letters*, vol. 77, no. 18, pp. 2906–2908, 2000. 6

[30] Y. Iijima, N. Tanabe, Y. Ikeno, and O. Kohno, "Biaxially aligned YBa2Cu3O7- x thin film tapes," *Physica C: Superconductivity*, vol. 185, pp. 1959–1960, 1991. 6

[31] M. P. Paranthaman and T. Izumi, "High-performance YBCO-coated superconductor wires," *MRS bulletin*, vol. 29, no. 8, pp. 533–541, 2004. 7, 188

[32] C. M. Bayer, *Characterization of High Temperature Superconductor Cables for Magnet Toroidal Field Coils of the DEMO Fusion Power Plant*, vol. 18. KIT Scientific Publishing, 2017. 7

[33] F. Rizzo, A. Augieri, A. Kursumovic, *et al.*, "Pushing the limits of applicability of REBCO coated conductor films through fine chemical tuning and nanoengineering of inclusions," *Nanoscale*, vol. 10, no. 17, pp. 8187–8195, 2018. 8

[34] S. Foltyn, L. Civale, J. MacManus-Driscoll, Q. Jia, B. Maiorov, H. Wang, and M. Maley, "Materials science challenges for high-temperature superconducting wire," in *Materials For Sustainable Energy: A Collection of Peer-Reviewed Research and Review Articles from Nature Publishing Group*, pp. 299–310, World Scientific, 2011. 8

[35] M. G. Blamire, J. L. MacManus-Driscoll, N. D. Mathur, and Z. H. Barber, "The materials science of functional oxide thin films," *Advanced Materials*, vol. 21, no. 38-39, pp. 3827–3839, 2009. 8

[36] L. Martin, Y.-H. Chu, and R. Ramesh, "Advances in the growth and characterization of magnetic, ferroelectric, and multiferroic oxide thin films," *Materials Science and Engineering: R: Reports*, vol. 68, no. 4-6, pp. 89–133, 2010. 8

[37] V. Selvamanickam, Y. Chen, *et al.*, "High performance 2G wires: From R&D to pilot-scale manufacturing," *IEEE Trans. Appl. Supercond*, vol. 19, no. 3, pp. 3225–3230, 2009. 8

[38] J. Feighan, A. Kursumovic, and J. MacManus-Driscoll, "Materials design for artificial pinning centres in superconductorPLD coated conductors,"

Superconductor Science and Technology, vol. 30, no. 12, p. 123001, 2017. 8

[39] T. Araki and I. Hirabayashi, "Review of a chemical approach to YBa2Cu3O7- x-coated superconductors-metalorganic deposition using trifluoroacetates," *Superconductor Science and Technology*, vol. 16, no. 11, p. R71, 2003. 8, 13

[40] X. Obradors, T. Puig, S. Ricart, *et al.*, "Growth, nanostructure and vortex pinning in superconducting YBa2Cu3O7 thin films based on trifluoroacetate solutions," *Superconductor Science and Technology*, vol. 25, p. 123001, dec 2012. 8, 13, 50, 182, 223

[41] V. Chepikov, N. Mineev, Degtyarenko, *et al.*, "Introduction of BaSnO3 and BaZrO3 artificial pinning centres into 2G HTS wires based on PLD-GdBCO films. phase i of the industrial R&D programme at superox," *Superconductor Science and Technology*, vol. 30, no. 12, p. 124001, 2017. 9, 128

[42] O. Stadel, J. Schmidt, G. Wahl, F. Weiss, D. Selbmann, J. Eickemeyer, O. Y. Gorbenko, A. Kaul, and C. Jimenez, "Continuous YBCO deposition by mocvd for coated conductors," *Physica C: Superconductivity*, vol. 372, pp. 751–754, 2002. 9, 128

[43] C. Sánchez-Valdés, T. Puig, and X. Obradors, "In situ study through electrical resistance of growth rate of trifluoroacetate-based solution-derived YBa2Cu3O7 films," *Superconductor Science and Technology*, vol. 28, no. 2, p. 024006, 2015. 9, 128

[44] H. J. Scheel, "Introduction to liquid phase epitaxy," *Liquid Phase Epitaxy of Electronic, Optical and Optoelectronic Materials; John Wiley & Sons, Ltd.: Chichester, UK*, pp. 1–19, 2007. 9, 128

[45] K.-W. Benz and W. Neumann, *Introduction to crystal growth and characterization*. John Wiley & Sons, 2014. 9, 106, 108, 111

[46] M. Tachibana, *Beginner's Guide to Flux Crystal Growth*. Springer, 2017. 9

[47] Y. Shiohara and E. A. Goodilin, "Chapter 189 single-crystal growth for science and technology," in *High-Temperature Superconductors - I*, vol. 30 of *Handbook on the Physics and Chemistry of Rare Earths*, pp. 67 – 227, Elsevier, 2000. 10, 113

[48] T. Aselage and K. Keefer, "Liquidus relations in Y-Ba-Cu oxides," *Journal of Materials Research*, vol. 3, no. 6, pp. 1279–1291, 1988. 10, 121

[49] Y. Shiohara and A. Endo, "Crystal growth of bulk high-Tc superconducting oxide materials," *Materials Science and Engineering: R: Reports*, vol. 19, pp. 1–86, apr 1997. 10, 125, 182

[50] D. A. Cardwell, "Processing and properties of large grain (RE) BCO," *Materials Science and Engineering: B*, vol. 53, no. 1-2, pp. 1–10, 1998. 10

[51] K. Salama and D. F. Lee, "Progress in melt texturing of YBa2Cu3Ox superconductor," *Superconductor Science and Technology*, vol. 7, no. 4, p. 177, 1994. 10

[52] X. Obradors, T. Puig, X. Granados, and F. Sandiumenge, "Melt textured YBa2Cu3O7: fundamental properties and current limitation applications," *Physica C: Superconductivity*, vol. 378, pp. 1–10, 2002. 10

[53] A. Kuršumović, Y. Cheng, B. Glowacki, J. Madsen, and J. Evetts, "Study of the rate-limiting processes in liquid-phase epitaxy of thick YBaCuO films," *Journal of crystal growth*, vol. 218, no. 1, pp. 45–56, 2000. 10, 11, 126

[54] N. Chen, S. Rothman, J. Routbort, and K. Goretta, "Tracer diffusion of Ba and Y in YBa 2 Cu 3 O x," *Journal of materials research*, vol. 7, no. 9, pp. 2308–2316, 1992. 10

[55] M. J. Cima, M. C. Flemings, A. M. Figueredo, M. Nakade, H. Ishii, H. D. Brody, and J. S. Haggerty, "Semisolid solidification of high temperature superconducting oxides," *Journal of applied physics*, vol. 72, no. 1, pp. 179–190, 1992. 10

[56] H. Nelson, "Epitaxial growth from the liquid state and its application to the fabrication of tunnel and lasar diodes," *RCA review*, vol. 24, no. 4, pp. 603–615, 1963. 10

[57] Y. Yamada, "Liquid-phase epitaxy processing of RBa2Cu3O7- δ," *Superconductor Science and Technology*, vol. 13, no. 1, p. 82, 2000. 11, 128

[58] J. L. Qi, X MacManus-Driscoll, "Liquid phase epitaxy processing for high temperature superconductor tapes," *Current Opinion in Solid State and Materials Science*, vol. 5, no. 4, pp. 291–300, 2001. 11, 119, 128

[59] T. Ohnishi, J. Huh, R. Hammond, and W. Jo, "High rate in situ YBa2Cu3O7film growth assisted by liquid phase," *Journal of materials research*, vol. 19, no. 4, pp. 977–981, 2004. 11, 148, 205, 228

[60] A. Kursumovic, R. I. Tomov, R. Hühne, J. L. MacManus-Driscoll, B. a. Glowacki, and J. E. Evetts, "Hybrid liquid phase epitaxy processes for YBa2Cu3O7film growth," *Superconductor Science and Technology*, vol. 17, no. 10, pp. 1215–1223, 2004. 11, 112, 117, 119, 128

[61] K. Yun, B. Choi, Y. Matsumoto, *et al.*, "Vapor–liquid–solid tri-phase pulsed-laser epitaxy of RBa 2 Cu 3 O 7- y single-crystal films," *Applied physics letters*, vol. 80, no. 1, pp. 61–63, 2002. 11, 128

[62] Y. Ichino, H. Matsuo, *et al.*, "Possibility of High Deposition Rate in SmBa2Cu3Oy Films Prepared Using the Vapor–Liquid–Solid Growth MODe," *Japanese journal of applied physics*, vol. 45, no. 2R, p. 758, 2006. 11

[63] A. Kursumovic, J. E. Evetts, J. MacManus-Driscoll, *et al.*, "High critical current densities in YBCO films grown at high rates by hybrid liquid phase epitaxy," *Applied Physics Letters*, vol. 87, no. 25, p. 252507, 2005. 11, 119, 120, 126, 128

[64] J.-H. Lee, H. Lee, J.-W. Lee, S.-M. Choi, S.-I. Yoo, and S.-H. Moon, "RCE-DR a novel process for coated conductor fabrication with high performance," *Superconductor Science and Technology*, vol. 27, no. 4, p. 044018, 2014. 11, 161, 180, 205, 228

[65] C. McDonagh, F. Sheridan, T. Butler, and B. MacCraith, "Characterisation of sol-gel-derived silica films," *Journal of Non-Crystalline Solids*, vol. 194, no. 1-2, pp. 72–77, 1996. 11

[66] T. Shimoda, Y. Matsuki, M. Furusawa, T. Aoki, I. Yudasaka, H. Tanaka, H. Iwasawa, D. Wang, M. Miyasaka, and Y. Takeuchi, "Solution-processed silicon films and transistors," *Nature*, vol. 440, no. 7085, p. 783, 2006. 11

[67] T. Schneller, R. Waser, M. Kosec, and D. Payne, *Chemical solution deposition of functional oxide thin films*. Springer, 2013. 11, 17, 52, 55, 57, 60

[68] R. W. Schwartz, T. Schneller, and R. Waser, "Chemical solution deposition of electronic oxide films," *Comptes Rendus Chimie*, vol. 7, pp. 433–461, may 2004. 11, 17, 51

[69] V. C. Tung, M. J. Allen, Y. Yang, and R. B. Kaner, "High-throughput solution processing of large-scale graphene," *Nature nanotechnology*, vol. 4, no. 1, p. 25, 2009. 11

[70] W. C. Chueh, C. Falter, *et al.*, "High-flux solar-driven thermochemical dissociation of CO2 and H2O using nonstoichiometric ceria," *Science*, vol. 330, no. 6012, pp. 1797–1801, 2010. 11

[71] X. Obradors, T. Puig, A. Pomar, F. Sandiumenge, *et al.*, "Progress towards all-chemical superconducting YBa2Cu3O7-coated conductors," *Superconductor Science and Technology*, vol. 19, pp. S13–S26, mar 2006. 11

[72] R. W. Schwartz, "Chemical solution deposition of perovskite thin films," *Chemistry of Materials*, vol. 9, no. 11, pp. 2325–2340, 1997. 12

[73] G. W. Scherer, "Sintering of sol-gel films," *Journal of Sol-Gel Science and Technology*, vol. 8, no. 1-3, pp. 353–363, 1997. 12, 57

[74] F. Lange, "Chemical solution routes to single-crystal thin films," *Science*, vol. 273, no. 5277, pp. 903–909, 1996. 12

[75] M. S. Bhuiyan, M. Paranthaman, and K. Salama, "Solution-derived textured oxide thin films-a review," *Superconductor Science and Technology*, vol. 19, pp. R1–R21, feb 2006. 12

[76] a. Gupta, R. Jagannathan, E. I. Cooper, E. a. Giess, J. I. Landman, and B. W. Hussey, "Superconducting oxide films with high transition temperature prepared from metal trifluoroacetate precursors," *Applied Physics Letters*, vol. 52, no. 24, p. 2077, 1988. 12, 50

[77] V. Solovyov, I. K. Dimitrov, and Q. Li, "Growth of thick YBa2Cu3O7 layers via a barium fluoride process," *Superconductor Science and Technology*, vol. 26, no. 1, p. 013001, 2012. 13, 154

[78] Y. Chen, C. Wu, G. Zhao, and C. You, "An advanced low-fluorine solution route for fabrication of high-performance YBCO superconducting films," *Superconductor Science and Technology*, vol. 25, no. 6, p. 062001, 2012. 13

[79] A. A. Armenio, A. Augieri, L. Ciontea, *et al.*, "Structural and chemical evolution of propionate based metal-organic precursors for superconducting YBCO epitaxial film growth," *Superconductor Science and Technology*, vol. 24, no. 11, p. 115008, 2011. 13

[80] X. Palmer, C. Pop, *et al.*, "Solution design for low-fluorine trifluoroacetate route to YBa CuO films," *Superconductor Science and Technology*, vol. 29, no. 2, p. 24002, 2016. 13, 53, 62

[81] C. Pop, B. Villarejo, F. Pino, B. Mundet, *et al.*, "Growth of all-chemical high critical current YBa2Cu3O7- δ thick films and coated conductors," *Superconductor Science and Technology*, vol. 32, no. 1, p. 015004, 2018. 13

[82] T. Haugan, P. Barnes, R. Wheeler, F. Meisenkothen, and M. Sumption, "Addition of nanoparticle dispersions to enhance flux pinning of the YBa2Cu3O7-x superconductor," *Nature*, vol. 430, no. 7002, p. 867, 2004. 13, 226

[83] A. Llordes, A. Palau, J. Gázquez, M. Coll, R. Vlad, A. Pomar, J. Arbiol, R. Guzman, S. Ye, V. Rouco, *et al.*, "Nanoscale strain-induced pair suppression as a vortex-pinning mechanism in high-temperature superconductors," *Nature materials*, vol. 11, no. 4, p. 329, 2012. 13, 34, 226

[84] F. Parmigiani, G. Chiarello, N. Ripamonti, H. Goretzki, and U. Roll, "Observation of carboxylic groups in the lattice of sintered Ba2YCu3O7-y high-Tc superconductors," *Physical Review B*, vol. 36, no. 13, p. 7148, 1987. 13, 50, 80

[85] P.-Y. Chu and R. C. Buchanan, "Reactive liquid phase sintering of solution-derived YBa2Cu3O7-x superconducting thin films: Part i. ambient and precursor effects on bao–cuo liquid phase formation," *Journal of materials research*, vol. 8, no. 9, pp. 2134–2142, 1993. 13, 81, 85, 129

[86] A. Hamdi, J. Mantese, A. Micheli, R. Laugal, D. Dungan, Z. Zhang, and K. Padmanabhan, "Formation of thin-film high t c superconductors by metalorganic deposition," *Applied physics letters*, vol. 51, no. 25, pp. 2152–2154, 1987. 13

[87] K. Tsukada, M. Furuse, M. Sohma, T. Manabe, I. Yamaguchi, W. Kondo, S. Fuchino, and T. Kumagai, "Preparation of high-jc YBa2Cu3O7-y films on CeO2-buffered yttria-stabilized zirconia substrates by fluorine-free metalorganic deposition," *Japanese journal of applied physics*, vol. 44, no. 7R, p. 4914, 2005. 13

[88] L. Soler, *Chemical solution deposition of YBCO superconducting thin films using fluorine free precursors*. Master thesis, Universitat Autònoma de Barcelona, 2013. 13, 17, 51

[89] X. X. Xu, W. C. Xu, Y. L. Bai, C. B. Cai, and J. H. Fang, "High Performance of YBCO Films Prepared by Fluorine-Free MOD Method and a Direct Annealing Process," *Key Engineering Materials*, vol. 537, pp. 243–246, feb 2013. 13

[90] F. Lu, F. Kametani, and E. E. Hellstrom, "Optimization of a fluorine-free metal-organic deposition to fabricate BaZrO3 -doped YBCO film on RABiTS substrates," *Superconductor Science and Technology*, vol. 26, p. 045016, apr 2013. 13

[91] Y. Zhao, J. Chu, T. Qureishy, W. Wu, Z. Zhang, P. Mikheenko, T. H. Johansen, and J.-C. Grivel, "Structural and superconducting characteristics of YBa2Cu3O7films grown by fluorine-free metal-organic deposition route," *Acta Materialia*, vol. 144, pp. 844–852, 2018. 13

[92] P. Vermeir, I. Cardinael, *et al.*, "Elucidation of the mechanism in fluorine-free prepared YBa2Cu3O(7-delta) coatings.," *Inorganic chemistry*, vol. 49, pp. 4471–7, may 2010. 13, 60, 81

[93] C. Apetrii, H. Schlorb, M. Falter, I. Lampe, L. Schultz, and B. Holzapfel, "YBCO thin films prepared by fluorine-free polymer-based chemical solution deposition," *IEEE transactions on applied superconductivity*, vol. 15, no. 2, pp. 2642–2644, 2005. 13

[94] Y. Patta, D. Wesolowski, and M. Cima, "Aqueous polymer–nitrate solution deposition of YBCO films," *Physica C: Superconductivity*, vol. 469, no. 4, pp. 129–134, 2009. 13

[95] B.-J. Kim, K.-Y. Yi, *et al.*, "Optimization of processing parameters of YBCO films prepared by a dichloroacetic-metalorganic deposition method," *Superconductor Science and Technology*, vol. 20, pp. 428–432, may 2007. 13

[96] T. Motoki, S. Ikeda, G. Honda, T. Nagaishi, S. I. Nakamura, and J. I. Shimoyama, "Dramatic effects of chlorine addition on expanding synthesis conditions for fluorine-free metal-organic decomposition YBa2Cu3Oy films," *Applied Physics Express*, vol. 10, no. 2, 2017. 13

[97] B. Derby, "Inkjet printing of functional and structural materials: fluid property requirements, feature stability, and resolution," *Annual Review of Materials Research*, vol. 40, pp. 395–414, 2010. 19

[98] M. Vilardell Navarro, *Inkjet printing : a flexible manufacturing of functional ceramic coatings by Chemical Solution Deposition.* Phd thesis, Universitat Autònoma de Barcelona, 2014. 19

[99] N. Sahu, B. Parija, and S. Panigrahi, "Fundamental understanding and MODeling of spin coating process: A review," *Indian Journal of Physics*, vol. 83, no. 4, pp. 493–502, 2009. 19

[100] I. Van Driessche, J. Feys, *et al.*, "Chemical solution deposition using inkjet printing for YBCO coated conductors," *Superconductor Science and Technology*, vol. 25, p. 065017, jun 2012. 20

[101] M. Vilardell, X. Granados, S. Ricart, I. V. Driessche, A. Palau, T. Puig, and X. Obradors, "Flexible manufacturing of functional ceramic coatings by inkjet printing," *Thin Solid Films*, vol. 548, pp. 489 – 497, 2013. 20

[102] B. Villarejo Reina, *Synthesis of defect free YBa2Cu3O7-x films over 1μm by CSD using inkjet printing.* PhD thesis, Universitat Autonoma de Barcelona, 2018. 20, 55

[103] K. Zalamova, N. Romà, *et al.*, "Smooth stress relief of trifluoroacetate metal-organic solutions for YBa2Cu3O7 film growth," *Chemistry of materials*, vol. 18, no. 25, pp. 5897–5906, 2006. 22

[104] P. McIntyre, R. Chiu, M. Cima, *et al.*, "High-temperature superconductors: Fundamental properties and novel materials processing," in *Materials Research Society Symposium Proceedings*, vol. 169, pp. 743–746, 1990. 22, 68

[105] Y. Rotenberg, L. Boruvka, and A. Neumann, "Determination of surface tension and contact angle from the shapes of axisymmetric fluid interfaces," *Journal of colloid and interface science*, vol. 93, no. 1, pp. 169–183, 1983. 28

[106] G. Ström, M. Fredriksson, and P. Stenius, "Contact angles, work of adhesion, and interfacial tensions at a dissolving hydrocarbon surface," *Journal of colloid and interface science*, vol. 119, no. 2, pp. 352–361, 1987. 28

[107] A. Calleja, S. Ricart, X. Palmer, R. F. Luccas, T. Puig, and X. Obradors, "Water determination of precursor solutions with oxidant cations by the Karl Fischer method: The YBCO-TFA case," *Journal of Sol-Gel Science and Technology*, vol. 53, no. 2, pp. 347–352, 2010. 28, 73

[108] D. Sanchez-Rodriguez, J. Farjas, P. Roura, S. Ricart, N. Mestres, X. Obradors, and T. Puig, "Thermal analysis for low temperature synthesis of oxide thin films from chemical solutions," *The Journal of Physical Chemistry C*, vol. 117, no. 39, pp. 20133–20138, 2013. 29

[109] P. Roura, J. Farjas, H. Eloussifi, L. Carreras, S. Ricart, T. Puig, and X. Obradors, "Thermal analysis of metal organic precursors for func-

tional oxide preparation: thin films versus powders," *Thermochimica Acta*, vol. 601, pp. 1–8, 2015. 29

[110] Roger Guzman Aluja, *In-depth investigation of the origin, evolution and interaction of structural defects in YBCO nanocomposite thin lms.* PhD thesis, Universitat Autònoma de Barcelona, 2013. 32

[111] M. Birkholz, *Thin film analysis by X-ray scattering.* John Wiley & Sons, 2006. 33

[112] B. B. He, U. Preckwinkel, and K. L. Smith, "Fundamentals of two-dimensional X-ray diffraction (XRD2)," *Advances in X-ray Analysis*, vol. 43, pp. 273–280, 2000. 33, 36

[113] A. Llordes, *Superconducting nanocomposite films grown by chemical solution deposition: synthesis, microstructure and properties.* PhD thesis, Thesis, 2010. 37

[114] F. M. Granozio, M. Salluzzo, U. S. di Uccio, I. Maggio-Aprile, and Ø. Fischer, "Competition between a-axis and c-axis growth in superconducting r ba 2 cu 3 o 7- x thin films," *Physical Review B*, vol. 61, no. 1, p. 756, 2000. 38, 39, 109, 123

[115] P. Roura *et al.*, "Melting of CuO-BaO films prepared by chemical solution deposition (CSD)," *to be published.* 42, 89, 115, 116, 133

[116] A. Grunenwald, C. Keyser, A.-M. Sautereau, E. Crubézy, B. Ludes, and C. Drouet, "Revisiting carbonate quantification in apatite (bio) minerals: a validated ftir methodology," *Journal of Archaeological Science*, vol. 49, pp. 134–141, 2014. 45, 64

[117] C. P. Bean, "Magnetization of hard superconductors," *Physical review letters*, vol. 8, no. 6, p. 250, 1962. 46

[118] G. H. Haertling, "PLZT thin films prepared from acetate precursors," *Ferroelectrics*, vol. 116, no. 1, pp. 51–63, 1991. 51

[119] K. H. Whitmire, J. C. Hutchison, A. Gardberg, and C. Edwards, "Triethanolamine complexes of copper," *Inorganica chimica acta*, vol. 294, no. 2, pp. 153–162, 1999. 51

[120] D. P. Birnie, S. K. Hau, D. S. Kamber, and D. M. Kaz, "Effect of ramping-up rate on film thickness for spin-on processing," *Journal of Materials Science: Materials in Electronics*, vol. 16, no. 11-12, pp. 715–720, 2005. 54

[121] J. D. Bass, C. Boissiere, L. Nicole, D. Grosso, and C. Sanchez, "Thermally induced porosity in CSD MgF2-Based optical coatings: An easy method to tune the refractive index," *Chemistry of Materials*, vol. 20, no. 17, pp. 5550–5556, 2008. 57

[122] A. Pomar, J. Gutiérrez, A. Palau, T. Puig, and X. Obradors, "Porosity induced magnetic granularity in epitaxial YBa2Cu3O7 thin films," *Physical Review B*, vol. 73, no. 21, p. 214522, 2006. 57, 183, 193, 225

[123] K. Tada, J. Yoshida, *et al.*, "Growth process of Ba-poor YBCO film fabricated by TFA-MOD process," *Physica C: Superconductivity*, vol. 468, no. 15-20, pp. 1554–1558, 2008. 59

[124] S. Rasi, S. Ricart, X. Obradors, T. Puig, P. Roura, and J. Farjas, "Thermal decomposition of yttrium propionate: film and powder," *Journal of Analytical and Applied Pyrolysis*, vol. 133, pp. 225–233, 2018. 60

[125] M. Nasui, R. Mos, *et al.*, "Synthesis, crystal structure and thermal decomposition of a new copper propionate [Cu (CH3CH2COO) 2]· 2H2O," *Journal of analytical and applied pyrolysis*, vol. 92, no. 2, pp. 439–444, 2011. 60

[126] M. Nasui, C. B. Pop, L. Ciontea, and T. Petrisor, "Synthesis, crystal structure MODeling and thermal decomposition of yttrium propionate [Y2 (CH3CH2COO) 6· H2O]· 3.5 H2O," *Journal of analytical and applied pyrolysis*, vol. 97, pp. 88–93, 2012. 60

[127] K. D. Dobson and A. J. McQuillan, "In situ infrared spectroscopic analysis of the adsorption of aliphatic carboxylic acids to TiO2, ZrO2, Al2O3, and Ta2O5 from aqueous solutions," *Spectrochimica Acta Part A: Molecular and Biomolecular Spectroscopy*, vol. 55, no. 7-8, pp. 1395–1405, 1999. 62

[128] R. Urlaub, U. Posset, and R. Thull, "FT-IR spectroscopic investigations on sol–gel-derived coatings from acid-modified titanium alkoxides," *Journal of Non-Crystalline Solids*, vol. 265, no. 3, pp. 276–284, 2000. 62

[129] J. W. London and A. T. Bell, "Infrared spectra of carbon monoxide, carbon dioxide, nitric oxide, nitrogen dioxide, nitrous oxide, and nitrogen adsorbed on copper oxide," *journal of catalysis*, vol. 31, no. 1, pp. 32–40, 1973. 64

[130] W. Taifan, J.-F. Boily, and J. Baltrusaitis, "Surface chemistry of carbon dioxide revisited," *Surface Science Reports*, vol. 71, no. 4, pp. 595–671, 2016. 66

[131] C. Yang and C. Wöll, "Ir spectroscopy applied to metal oxide surfaces: adsorbate vibrations and beyond," *Advances in Physics: X*, vol. 2, no. 2, pp. 373–408, 2017. 66

[132] A. Llordes, K. Zalamova, *et al.*, "Evolution of metal-trifluoroacetate precursors in the thermal decomposition toward high-performance YBa2Cu3O7 superconducting films," *Chemistry of Materials*, vol. 22, no. 5, pp. 1686–1694, 2010. 67

[133] A. Górski and A. Kraśnicka, "The importance of the CO22- anion in the mechanism of thermal decomposition of oxalates," *Journal of thermal analysis*, vol. 32, no. 4, pp. 1229–1241, 1987. 67

[134] S. Kramer, K. Wu, and G. Kordas, "The effects of water-to-alkoxide ratio on the properties of gels and sol-gel derived high tc ceramic superconductors," *Journal of electronic materials*, vol. 17, no. 2, pp. 135–137, 1988. 73

[135] I. Garcia, *Control and reduction of water content from YBCO precuror solutions to obtain high-performance superconducting films*. Bachelor thesis, Universitat Autònoma de Barcelona, 2016. 75

[136] R. Strobel, M. Maciejewski, S. E. Pratsinis, and A. Baiker, "Unprecedented formation of metastable monoclinic BaCO3 nanoparticles," *Thermochimica acta*, vol. 445, no. 1, pp. 23–26, 2006. 76

[137] E. Lataste, "Thermochromic behaviour (400 <TC<1200C) of barium carbonate/binary metal oxide mixtures," *Dyes and pigments*, vol. 91, pp. 396–403, 2011. 81

[138] T. Itoh, "Role of CuO for the decarbonation of BaCO 3 and CaCO 3 in the solid-state reaction of CuO with BaCO 3 and that of CuO with CaCO 3," *Journal of materials sicence letters*, vol. 22, pp. 185–189, 2003. 81

[139] J. L. Sobolik, H. Wang, and W. J. Thomson, "Effect of Particle Size on Binary Reactions Common to the Y-Ba-Cu-O System," *Journal of the American Ceramic Society*, vol. 77, no. 10, pp. 2738–2746, 1994. 81

[140] M. T. Buscaglia, V. Buscaglia, and R. Alessio, "Coating of BaCO3 crystals with TiO2: Versatile approach to the synthesis of BaTiO3 tetragonal nanoparticles," *Chemistry of Materials*, vol. 19, no. 4, pp. 711–718, 2007. 81

[141] M. Nevřiva, E. Pollert, L. Matějková, and A. Tříska, "On the determination of the CuO-BaCuO2 and CuO-YCuO2. 5 binary phase diagrams," *Journal of crystal growth*, vol. 91, no. 3, pp. 434–438, 1988. 85, 115, 117, 129

[142] W. Zhang, K. Osamura, and S. Ochiai, "Phase Diagram of the BaO-CuO Binary System," *Journal of the American Ceramic Society*, vol. 73, no. 7, pp. 1958–1964, 1990. 85, 129

[143] T. B. Lindemer and E. D. Specht, "The BaOCuCuO system. Solid-liquid equilibria and thermodynamics of BaCuO2 and BaCu2O2," *Physica C: Superconductivity and its applications*, vol. 255, no. 1-2, pp. 81–94, 1995. 86, 87, 88, 89, 90, 115, 116, 143

[144] T. B. Lindemer, F. A. Washburn, C. S. MacDougall, and O. B. Cavin, "Synthesis of Y-Ba-Cu-O superconductors in subatmospheric oxygen," *Physica C: Superconductivity and its applications*, vol. 174, no. 1-3, pp. 135–143, 1991. 87, 89, 114

[145] M. E. Brown, D. Dollimore, and A. K. Galwey, *Reactions in the solid state*, vol. 22. Elsevier, 1980. 88, 101

[146] T. Lindemer, F. Washburn, and C. MacDougall, "Study of phase behavior in the YBa2Cu3O7- x- BaCuO2+ y- CuO- Ag system," *Physica C: Superconductivity*, vol. 196, no. 3-4, pp. 390–398, 1992. 89, 116

[147] F. Taïr, L. Carreras, J. Camps, J. Farjas, P. Roura, *et al.*, "Melting temperature of YBa2Cu3O7- x and gdba2cu3o7- x at subatmospheric partial pressure," *Journal of Alloys and Compounds*, vol. 692, pp. 787–792, 2017. 89, 116, 117

[148] J. MacManus-Driscoll, J. Bravman, and R. Beyers, "Phase equilibria in the y1b2 cu3 o7-x system and melt processing of ag clad y1ba2cu3o7- x tapes at reduced oxygen partial pressures," *Physica C: Superconductivity*, vol. 241, no. 3-4, pp. 401–413, 1995. 89, 116, 202

[149] K. A. Jackson, *Kinetic Processes: crystal growth, diffusion, and phase transformations in materials*. John Wiley & Sons, 2006. 90

[150] A. Mersmann and K. Bartosch, "How to predict the metastable zone width," *Journal of crystal growth*, vol. 183, no. 1-2, pp. 240–250, 1998. 107

[151] K. Kelton and A. L. Greer, *Nucleation in condensed matter: applications in materials and biology*, vol. 15. Elsevier, 2010. 108, 110, 111

[152] I. Markov, M. Milvidskii, and V. Osvenskii, "Crystal growth," *Crystal Growth for Beginners*, pp. 181–351, 2003. 108

[153] F. M. Granozio and U. S. Di Uccio, "Gibbs energy and growth habits of YBCO," *Journal of alloys and compounds*, vol. 251, no. 1-2, pp. 56–64, 1997. 109, 123

[154] J. Qi, X, MacManus-Driscoll, "Liquid phase epitaxy processing for high temperature superconductor tapes," *Current Opinion in Solid State and Materials Science*, vol. 5, no. 4, pp. 291–300, 2001. 110, 147, 176

[155] D. Turnbull and J. C. Fisher, "Rate of nucleation in condensed systems," *The Journal of chemical physics*, vol. 17, no. 1, pp. 71–73, 1949. 110

[156] I. Avramov, "Relationship between diffusion, self-diffusion and viscosity," *Journal of Non-Crystalline Solids*, vol. 355, no. 10-12, pp. 745–747, 2009. 111, 164

[157] A. Gamalski, J. Tersoff, R. Sharma, C. Ducati, and S. Hofmann, "Formation of metastable liquid catalyst during subeutectic growth of germanium nanowires," *Nano letters*, vol. 10, no. 8, pp. 2972–2976, 2010. 114, 117

[158] G. Voronin and S. Degterov, "Solid state equilibria in the Ba-Cu-O system," *Journal of Solid State Chemistry*, vol. 110, no. 1, pp. 50–57, 1994. 115, 116, 130

[159] P. Cayado, K. De Keukeleere, *et al.*, "Epitaxial YBa2Cu3O7- x nanocomposite thin films from colloidal solutions," *Superconductor Science and Technology*, vol. 28, no. 12, p. 124007, 2015. 116, 183, 227

[160] S. Kodambaka, J. Tersoff, M. Reuter, and F. Ross, "Germanium nanowire growth below the eutectic temperature," *Science*, vol. 316, no. 5825, pp. 729–732, 2007. 117

[161] S. V. Sivaram, H. Y. Hui, M. de la Mata, J. Arbiol, and M. A. Filler, "Surface hydrogen enables subeutectic vapor–liquid–solid semiconductor nanowire growth," *Nano letters*, vol. 16, no. 11, pp. 6717–6723, 2016. 117

[162] Y. Chen, X. Cui, and X. Yao, "Peritectic melting of thin films, superheating and applications in growth of REBCO superconductors," *Progress in Materials Science*, vol. 68, pp. 97–159, 2015. 117

[163] X. Yao and Y. Shiohara, "Process for high growth rate and high superconducting properties of REBCO single crystals," *Materials Science and Engineering: B*, vol. 53, no. 1-2, pp. 11–17, 1998. 119, 140, 213

[164] M. Nakamura, C. Krauns, and Y. Shiohara, "Oxygen partial pressure dependence of the yttrium solubility in y–ba–cu–o solution," *Journal of materials research*, vol. 11, no. 5, pp. 1076–1081, 1996. 119, 120, 212

[165] C. Klemenz and H. Scheel, "Solubility of YBa2Cu3O7- δ and Nd1+ xBa2-xCu3O7$\pm\delta$ in the BaO/CuO flux," *Journal of crystal growth*, vol. 200, no. 3-4, pp. 435–440, 1999. 119, 120, 128, 211, 213

[166] Y. Ichino, K. Sudoh, K. Miyachi, Y. Yoshida, and Y. Takai, "Orientation Mechanism of REBa 2 Cu 3 O y (RE = Nd , Sm , Gd , Y , Yb) Thin Films Prepared by Pulsed," *Thin Films*, vol. 13, no. 2, pp. 2735–2738, 2003. 123

[167] A. A. Chernov, "Notes on interface growth kinetics 50 years after Burton, Cabrera and Frank," *Journal of Crystal Growth*, vol. 264, no. 4, pp. 499–518, 2004. 126

[168] C. Klemenz and H. Scheel, "Flat YBa2Cu3O7- x layers for planar tunnel-device technology," *Physica C: Superconductivity*, vol. 265, no. 1-2, pp. 126–134, 1996. 128

[169] W. Jo, T. Ohnishi, J. Huh, R. Hammond, and M. Beasley, "Thickness dependence of critical currents and depth profiling of transport properties in high rate in-situ grown YBa/sub 2/Cu/sub 3/O/sub 7-x/films," *IEEE transactions on applied superconductivity*, vol. 13, no. 2, pp. 2817–2820, 2003. 128

[170] J. MacManus-Driscoll, A. Kursumovic, B. Maiorov, L. Civale, Q. Jia, S. Foltyn, and H. Wang, "YBa ₂ Cu ₃ O _{7-z} Coated Conductor Grown by Hybrid Liquid Phase Epitaxy," *IEEE Transactions on Applied Superconductivity*, vol. 17, no. 2, pp. 2537–2541, 2007. 128, 140, 154, 161, 180

[171] C. Krauns, M. Tagami, Y. Yamada, M. Nakamura, and Y. Shiohara, "Wetting between prospective crucible materials and the Ba-Cu-O melt," *Journal of materials research*, vol. 9, no. 6, pp. 1513–1518, 1994. 131, 163, 164, 176

[172] B. Kim, J. Tersoff, C.-Y. Wen, M. Reuter, E. Stach, and F. Ross, "Determination of size effects during the phase transition of a nanoscale Au-Si eutectic," *Physical review letters*, vol. 103, no. 15, p. 155701, 2009. 134

[173] J. MacManus-Driscoll, J. Bravman, and R. Beyers, "Phase equilibria in the Y B Cu O system and melt processing of Ag clad Y1Ba2Cu3O7- x tapes at reduced oxygen partial pressures," *Physica C: Superconductivity*, vol. 241, no. 3-4, pp. 401–413, 1995. 143

[174] U. S. di Uccio, F. M. Granozio, *et al.*, "Phase competition between Y2BaCuO5 and Y2O3 precipitates in Y-rich YBCO thin films," *Physica C: Superconductivity*, vol. 321, no. 3-4, pp. 162–176, 1999. 143

[175] M. Coll, J. Gazquez, A. Pomar, T. Puig, F. Sandiumenge, and X. Obradors, "Stress-induced spontaneous dewetting of heteroepitaxial YBa2Cu3O7 thin films," *Physical Review B*, vol. 73, no. 7, p. 075420, 2006. 144, 171

[176] R. M. German, "Chapter nine - sintering with a liquid phase," in *Sintering: from Empirical Observations to Scientific Principles* (R. M. German, ed.), pp. 247 – 303, Boston: Butterworth-Heinemann, 2014. 163, 179

[177] D. Wesolowski, Y. Patta, and M. Cima, "Conversion behavior comparison of tfa–mod and non-fluorine solution-deposited YBCO films," *Physica C: Superconductivity*, vol. 469, no. 13, pp. 766–773, 2009. 164

[178] J. Riches, J. Alarco, and J. Barry, "Effects of PtO2 and CeO2 additives on the microstructures of the quenched melts of Y–Ba–Cu–O materials," *Physica C: Superconductivity*, vol. 336, no. 1-2, pp. 43–56, 2000. 164

[179] T. Izumi, Y. Nakamura, and Y. Shiohara, "Doping effects on coarsening of Y2BaCuO5 phase in liquid," *Journal of materials research*, vol. 8, no. 6, pp. 1240–1246, 1993. 164, 165

[180] S. Pinol, F. Sandiumenge, *et al.*, "Enhanced critical currents by CeO2 additions in directionally solidified YBa2Cu3O7," *Applied physics letters*, vol. 65, no. 11, pp. 1448–1450, 1994. 164

[181] R. Teranishi, J. Yoshida, *et al.*, "Jc properties and microstructures of YBCO films fabricated by low temperature calcination in tfa-mod method," *Physica C: Superconductivity*, vol. 469, no. 15-20, pp. 1332–1335, 2009. 171, 183

[182] X. Obradors, T. Puig, *et al.*, "Chemical solution deposition: a path towards low cost coated conductors," *Superconductor Science and Technology*, vol. 17, no. 8, p. 1055, 2004. 171

[183] J. Gazquez, M. Coll, N. Roma, F. Sandiumenge, T. Puig, and X. Obradors, "Structural defects in trifluoroacetate derived YBa2Cu3O7 thin films," *Superconductor Science and Technology*, vol. 25, no. 6, p. 065009, 2012. 171, 183, 195

[184] I. Bretos, T. Schneller, *et al.*, "Solution-derived YBa 2 Cu 3 O 7- δ (YBCO) superconducting films with BaZrO 3 (BZO) nanodots based on reverse micelle stabilized nanoparticles," *Journal of Materials Chemistry C*, vol. 3, no. 16, pp. 3971–3979, 2015. 171

[185] O. Castano, A. Cavallaro, *et al.*, "Influence of porosity on the critical currents of trifluoroacetate-MOD YBa/sub 2/Cu/sub 3/O/sub 7/films," *IEEE transactions on applied superconductivity*, vol. 13, no. 2, pp. 2504–2507, 2003. 183

[186] H. Hilgenkamp and J. Mannhart, "Grain boundaries in high-t c superconductors," *Reviews of MODern Physics*, vol. 74, no. 2, p. 485, 2002. 183

[187] X. Obradors, T. Puig, Z. Li, *et al.*, "Epitaxial YBa2Cu3O7- x nanocomposite films and coated conductors from BaMO3 (M= Zr, Hf) colloidal solutions," *Superconductor Science and Technology*, vol. 31, no. 4, p. 044001, 2018. 183, 227

[188] A. Goyal, M. P. Paranthaman, and U. Schoop, "The rabits approach: Using rolling-assisted biaxially textured substrates for high-performance YBCO superconductors," *MRS bulletin*, vol. 29, no. 8, pp. 552–561, 2004. 183

[189] J. H. Durrell and N. A. Rutter, "Importance of low-angle grain boundaries in YBa2Cu3O7- δ coated conductors," *Superconductor Science and Technology*, vol. 22, no. 1, p. 013001, 2008. 183

[190] L. J. Van der Pauw, "A method of measuring the resistivity and hall coefficient on lamellae of arbitrary shape," *Philips Technical Review*, vol. 20, pp. 220–224, 1958. 186, 222, 223

[191] A. Palau, T. Puig, *et al.*, "Simultaneous inductive determination of grain and intergrain critical current densities of YBa2Cu3O7-x coated con-

ductors," *Applied physics letters*, vol. 84, no. 2, pp. 230–232, 2004. 193, 225

[192] A. Palau, T. Puig, X. Obradors, and C. Jooss, "Simultaneous determination of grain and grain-boundary critical currents in YBa2Cu3O7 -coated conductors by magnetic measurements," *Physical Review B*, vol. 75, no. 5, p. 054517, 2007. 193

[193] R. Feenstra, J. Sinclair, J. R. Thompson, and D. K. Christen, "Intra-and inter-grain currents in coated conductors with arbitrary grain boundary properties from magnetic measurements," *Superconductor Science and Technology*, vol. 24, no. 6, p. 062001, 2011. 193

[194] E. Bartolome, A. Palau, *et al.*, "Artificial magnetic granularity effects on patterned epitaxial Y Ba 2 Cu 3 O 7- x thin films," *Physical Review B*, vol. 76, no. 9, p. 094508, 2007. 193

[195] A. Palau, F. Vallès, *et al.*, "Disentangling vortex pinning landscape in chemical solution deposited superconducting YBa2Cu3O7- x films and nanocomposites," *Superconductor Science and Technology*, vol. 31, no. 3, p. 034004, 2018. 195

[196] R. Guzman, J. Gazquez, V. Rouco, *et al.*, "Strain-driven broken twin boundary coherence in YBa2Cu3O7- δ nanocomposite thin films," *Applied Physics Letters*, vol. 102, no. 8, p. 081906, 2013. 196

[197] T.-H. Seok, I. Park, and S.-I. Yoo, "Stability diagram of YBa2Cu3O7-δ in low oxygen pressures," *IEEE Transactions on Applied Superconductivity*, vol. 27, no. 4, pp. 1–5, 2017. 202

[198] R. Feenstra, T. Lindemer, J. Budai, and M. Galloway, "Effect of oxygen pressure on the synthesis of YBa2Cu3O7- x thin films by post-deposition annealing," *Journal of Applied Physics*, vol. 69, no. 9, pp. 6569–6585, 1991. 203

[199] A. Patterson, "The scherrer formula for x-ray particle size determination," *Physical review*, vol. 56, no. 10, p. 978, 1939. 215

[200] R. Guzman, J. Gazquez, *et al.*, "Probing localized strain in solution-derived YB a 2 C u 3 O 7- δ nanocomposite thin films," *Physical Review Materials*, vol. 1, no. 2, p. 024801, 2017. 219

[201] T. Puig, J. Gonzalez, *et al.*, "The influence of growth conditions on the microstructure and critical currents of TFA-MOD YBa2Cu3O7 films," *Superconductor Science and Technology*, vol. 18, no. 8, p. 1141, 2005. 219, 225

[202] M. Gibert, T. Puig, and X. Obradors, "Growth of strain-induced self-assembled BaZrO3 nanodots from chemical solutions," *Surface science*, vol. 601, no. 13, pp. 2680–2683, 2007. 221

[203] X. Obradors, T. Puig, A. Palau, A. Pomar, F. Sandiumenge, P. Mele, and K. Matsumoto, "Nanostructured superconductors with efficient vortex pinning," in *Comprehensive Nanoscience and Technology*, pp. 303–349, Elsevier Inc., 2010. 221

[204] P. Abellán, F. Sandiumenge, *et al.*, "Interaction between solution derived BaZrO3 nanodot interfacial templates and YBa2Cu3O7 films leading to enhanced critical currents," *Acta Materialia*, vol. 59, no. 5, pp. 2075–2082, 2011. 221

[205] L. Soler, J. Jareno, J. Banchewski, S. Rasi, N. Chamorro, R. Guzman, R. Yanez, C. Mocuta, S. Ricart, J. Farjas, P. Roura-Grabulosa, X. Obradors, and T. Puig, "Ultrafast transient liquid assisted growth of high current density superconducting films," *Submitted*, 2019. 227